ANALYSIS OF CIRRUS PARTICLE SIZE DISTRIBUTIONS FROM THREE IN SITU FLIGHT CAMPAIGNS: APPLICATIONS TO CIRRUS MICROPHYSICS AND PARAMETERIZATION, REMOTE SENSING, AND RADAR FORWARD MODEL SIMULATORS

by

Michael Christian Schwartz

A dissertation submitted to the faculty of
The University of Utah
in partial fulfillment of the requirements for the degree of

Doctor of Philosophy

Department of Atmospheric Sciences

The University of Utah

August 2014

The University of Utah Graduate School

STATEMENT OF DISSERTATION APPROVAL

The dissertation of **Michael Christian Schwartz**

has been approved by the following supervisory committee members:

Gerald G. Mace	, Chair	**6/3/2013** Date Approved
Steven K. Krueger	, Member	**6/3/2013** Date Approved
Timothy J. Garrett	, Member	**4/2/2014** Date Approved
Zhaoxia Pu	, Member	**6/3/2013** Date Approved
Michael S. Zhdanov	, Member	Date Approved

and by **Kevin D. Perry** , Chair of

the Department of **Atmospheric Sciences**

and by David B. Kieda, Dean of The Graduate School.

ABSTRACT

A database of cirrus particle size distributions (PSDs), with concomitant meteorological variables, has been constructed using data collected with the Two-dimensional Stereo (2D-S) probe. Parametric functions are fit to each measured PSD. Full statistical descriptions are given for unimodal fit parameters. Three statistical tests were developed in order to determine the utility of bimodal fits and the efficacy of unimodal fits, and an investigation into the relationship between the parameterized PSDs and several meteorological variables was made.

Next, a parameterization of a "universal" cirrus PSD is given. This parameterization constitutes an improvement on earlier works due both to the size of the dataset and to updated instrumentation. Despite earlier works that predicted a gamma-distribution tail to the universal ice PSD, it is shown here that the tail is best described by an inverse gamma distribution. A method for predicting any PSD given the universal shape and two independent remote sensing measurements is demonstrated.

The constructed PSD database is then used to address a straightforward question: how similar are the statistics of PSD datasets collected using the recently developed 2D-S probe to cirrus PSD datasets collected using older Particle Measuring Systems (PMS) 2D Cloud (2DC) and 2D Precipitation (2DP) probes? It is seen, given the same cloud field and given the same assumptions concerning ice crystal cross-sectional area, density, and radar cross section, that the parameterized 2D-S and the parameterized 2DC predict

similar distributions of inferred shortwave extinction coefficient, ice water content, and 94 GHz radar reflectivity. However, the parameterized 2DC predicts a statistically significant higher number of total ice crystals and a larger ratio of small ice crystals to large ice crystals.

Finally, the beginnings of two works in their early stages are presented. First, the probability structure of the parameterized PSDs is considered in light of application to the Bayesian inference of cirrus microphysical properties from remote sensing measurements. Then, the collection of measured PSDs, along with a forward model for radar reflectivity, is used to investigate uncertainty in computations of radar reflectivity from modeled moments of cirrus cloud PSDs.

To my parents, Michael Jay and Connie Rae Schwartz, who taught me that to work hard
in the heat and the dirt is not beneath me and that to compromise integrity and purity is
and, most importantly, that to look with an eye of faith is to see what can and will be.
Here's to you—quiet, staunch, and true as you are: my love forever.

TABLE OF CONTENTS

Chapter

Appendices

LIST OF TABLES

ACKNOWLEDGEMENTS

Grateful acknowledgement is given to the members of my committee for their efforts in review and assistance. In particular, I am grateful to my committee chair, Dr. Gerald Mace, for his assistance, guidance, and most of all for his patience. Without his patient help, I would not have come at all near to this point.

Acknowledgement is also given to the following for providing data products used in this work: Paul Lawson of SPEC, Inc., for the 2D-S data products; Andrew Heymsfield of the National Center of Atmospheric Research for the PIP data; Linnea Avallone of the University of Colorado, Boulder, for the CLH data; Paul Bui of the NASA Ames Research Center for the MMS data products; Glenn Diskin of the NASA Langley Research Center for the DLH data products; and James Anderson of Harvard University for the HWV data. Finally, appreciative thanks are given to Andreas Muhlbauer of the University of Washington for the cloud-resolving model output used in this dissertation.

CHAPTER 1

INTRODUCTION

It has been understood for decades that any realistic consideration of the sensitivity of the Earth's climate state must include a physically reasonable treatment within climate models of the effects of clouds (e.g., Wetherald and Manabe, 1988; Tiedke, 1993; Stephens, 2005; Heymsfield et al., 2013). Clouds play a critical role in the hydrological cycle, interacting with the dynamics of the atmosphere through the transport of water and of radiative and latent heating; they are important components in many of the chemical processes that take place in the atmosphere (Wayne, 1991), and the feedbacks due to clouds have far-reaching consequences that are poorly understood. Perhaps the most profound climatic impact of clouds, affecting all the roles they play within the climate system, is their modulation of incoming solar radiation and of outgoing terrestrial radiation.

Attempting more fully to discern the climatic ramifications of clouds has proved a perplexing task, for while answers to some of the questions about their complex roles have come over time, the matter of their proper representation in climate models remains a significant challenge. At one point, a group of authors referred to the representation of clouds within global climate models (GCMs) as "a problem that refuses to die" (Randall et al., 2003), but significant progress has been made in the time since (Li et al., 2012). The problem is complicated by a scantness of data relating to cloud microphysical properties—particularly relating to the particle size distributions (PSDs) upon which their radiative interactions rely (Jensen et al., 2009)—and of the relationships between cloud microphysics and atmospheric state and dynamic variables. The work described in this dissertation will ultimately help to address these complications. In order to provide context, this introduction will first visit some general principles regarding the role of clouds within the Earth's climate system. Thence the discussion will concenter on specific problems addressed within this dissertation.

Clouds in Nature

In various parts of the sky (or in the same part of the sky at various times), a great variety in different shapes, sizes, and heights of clouds can be observed—all of which may be broadly classified into either of two categories (or into a combination of the two categories): cumuliform (convective) or stratiform (layered). Clouds may be further classified by the heights of their bases (Fig. 1.1) and by the phase of water found in them (liquid, ice, or mixed). As an example, two images of the Great Lakes area from two consecutive days (15 May 2008 and 16 May 2008) produced using data from the Moderate-Resolution Imaging Spectroradiometer (MODIS) are shown in Fig. 1.2. The 15th is relatively clear, but clouds associated with an incoming, upper-level trough can be seen on the 16th.

All of this variety is related to the fact that clouds occupy a continuum of temporal and spatial scales. Individual cloud elements may range from hundreds of meters to hundreds of kilometers in size and may last from minutes to days. Within cloud elements, the fundamental physical processes responsible for their formation and decay occur on scales of the size of the cloud itself down to the microscopic and can

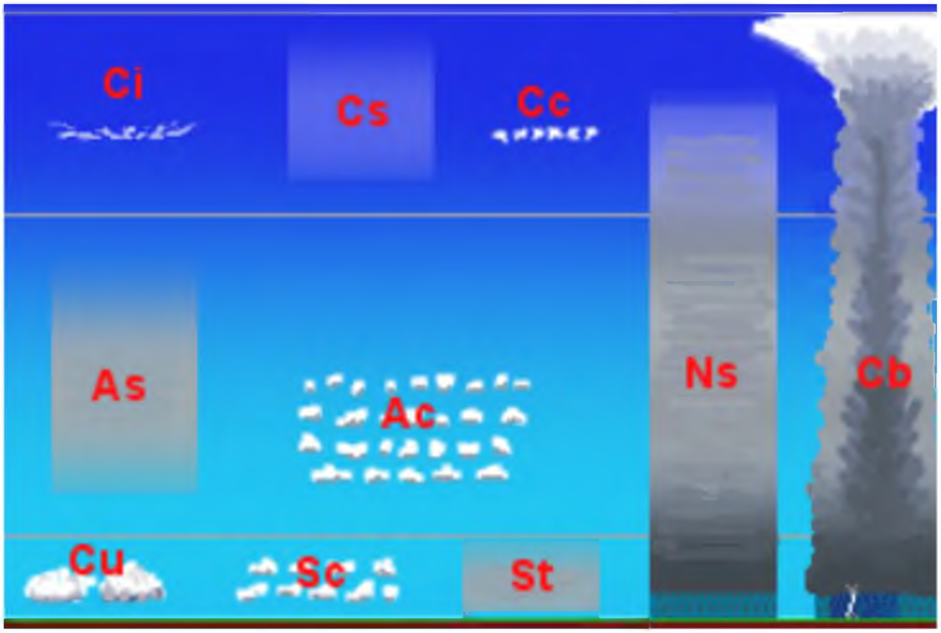

Fig. 1.1: "Schematische Darstellung der Wolkenstockwerke" (Schematic Diagram of Cloud Layer). Source: http://commons.wikipedia.org

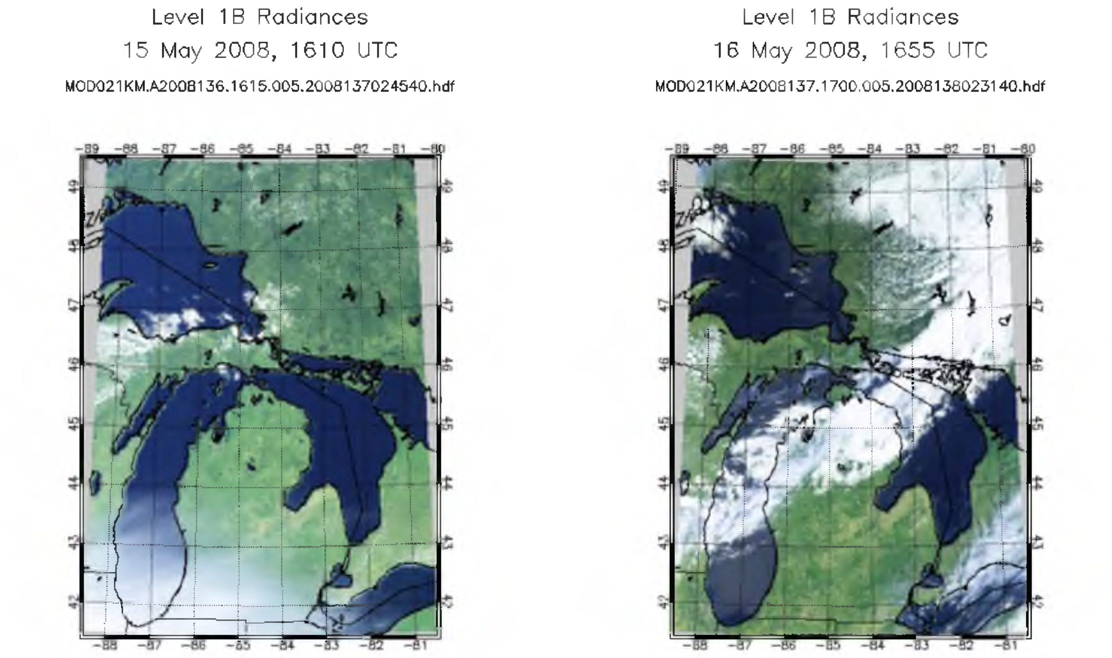

(a) (b)

Fig. 1.2: Terra MODIS images of clouds over the Great Lakes: (a) 15 May 2008, and (b) 16 May 2008. Data for figure provided by NASA.

occur on time scales smaller than the life of the cloud (Wayne, 1991).

Perhaps the simplest statistic relevant to global cloud systems is average global cloud coverage. This statistic has been estimated a number of times, and each estimate is perforce different due to the use of different instruments during different time periods. For one example, Mace et al. (2009) estimated average global cloud coverage (using ~2 km CloudSat footprints) of 76% during 2006 with an associated annual cycle of monthly means approximately 3% in magnitude. Also, using 22 years (1979–2001) of National Oceanic and Atmospheric (NOAA) High Resolution Infrared Radiometer Sounder (HIRS) data, Wylie et al. (2005) estimated fairly steady global cloud coverage of about 75%. However, a reprocessing of the HIRS datasets from 1995 to 2009 by Menzel et al. (2010) suggests downgrading that estimate to about 80% over ocean and about 55% over land (for a total average coverage of about 73%). Stubenrauch et al. (2010), using a 6-year global climatology collected using the Atmospheric InfraRed Sounder (AIRS) instrument aboard the NASA Aqua satellite, estimated global cloud coverage between 66% and 74%—the coverage estimate depending on how partial cloudiness is treated within individual AIRS footprints. This particular study illustrates the fact that cloud coverage estimates depend on instrument-specific factors (such as viewing angle, footprint size, and satellite orbital parameters) and on decisions made regarding the processing of data and the use of ancillary information.

For a further example illustrative of these last effects, consider only the Tropics—specifically, 20°S–20°N latitude. Jacobowitz et al. (2003) estimated, using nearly 20 years of Advanced Very High Resolution Radiometer (AVHRR) measurements merged to form the Pathfinder Atmosphere (PATMOS) dataset, fairly steady average cloud cover at around 50% (with an apparent seasonal cycle). For comparison, they note that a similar estimate based on the International Satellite Cloud Climatology Project (ISCCP) (Rossow and Schiffer, 1999) dataset from 1985 to 1993 had a mean value of 63% for the Tropics with a definite downward trend. However, with regards to this downward trend, Evan et al. (2007) suggest that difficulties in the ISCCP record (such as relate to satellite viewing problems) may mean that the observed trend cannot be taken at face value (see also Amato et al., 2007).

Challenges in reconciling something as seemingly basic as estimates of global average cloud cover from different orbiting measurement systems would seem to indicate that more specific observations related to the climatology and to the climatological effects of clouds encounter similar challenges. However, a number of the basic patterns of cloud systems are well established. The global picture of cloudiness is typified by climatological patterns that vary more or less by latitude (e.g., Bony et al., 2006). A time-averaged view shows large-scale cloud systems determined mainly by dynamical features such as synoptic-scale disturbances in the midlatitudes, areas of deep convection in the Tropics, and large-scale subsidence in the subtropics (Fig. 1.3). It is the statistics of these dynamical features and of their associated cloud patterns that are most important to climate studies (McKague and Evans, 2002). In their largest spatial scales, then, and especially for climatologic time scales, dominant cloud patterns and properties take on different basic, defining characteristics within different climate regimes. These climate regimes may be approximately identified with three geographical divisions: the Tropics, the midlatitudes, and the polar areas.

In their broadest, average sense, Tropical cloud patterns stem from the dominant

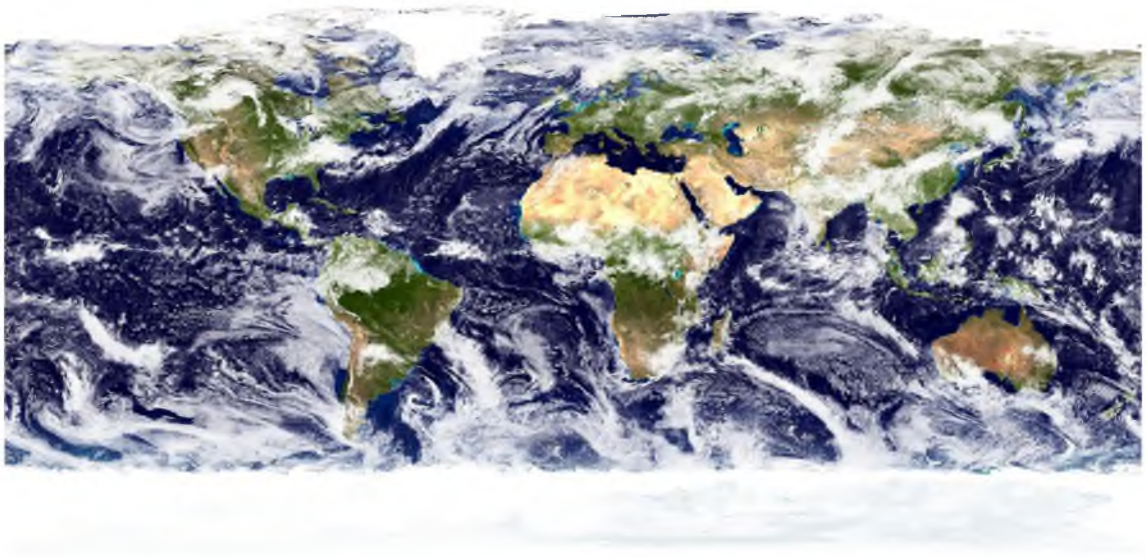

Fig. 1.3: A composite image of typical global cloud conditions from space. (Courtesy of NASA Goddard Space Flight Center).

Hadley circulation (Larson et al., 1999). General rising motion near the equator results in high, convective clouds and in cirrus that are associated either directly or indirectly with detrained water vapor or particles from convective towers, while regions of subsidence are marked by vast areas of boundary-layer trade cumulus clouds (Bony et al., 2006), often with overlying cirrus (Schwartz and Mace, 2010).

Large-scale dynamics are the main drivers of cloudiness in the higher latitudes (Cotton, 1990). Cloud systems are often generated in conjunction with synoptic-scale baroclinic instabilities, the particular forms and distributions of cloudiness depending upon particulars of the dynamical situation (e.g., Norris and Iacobellis, 2005). Clouds in polar areas possess a number of unique features. Here, synoptic-scale systems also generate much of the cloudiness, but in many cases boundary layer stratiform clouds are found where warmer, moister air is entrained from lower latitudes over cold surfaces (Curry et al., 1996). Unique types of polar boundary layer clouds include stable, mixed-phase clouds (often with light ice crystal precipitation) and “clear-sky” ice precipitation in stable winter skies, wintertime ice clouds formed over cracks in the ice, spring and fall mixed-phase clouds, and multilayered summertime stratiform clouds (Curry et al., 1996).

The ubiquity of cloud systems both leads to and stems from the numerous roles they play within the climate system. For instance, as noted, clouds play a major role in Earth’s radiative energy balance: they are, in general, absorbers and radiators of longwave terrestrial radiation (resulting in “greenhouse” warming) and reflectors of shortwave solar radiation (resulting in cooling). Measured at the top of the atmosphere (TOA), these two effects compete with one another, and in areas of tropical deep convection, they nearly cancel one another (Kiehl and Ramanathan, 1990; Kiehl, 1994;

Hartmann et al., 2001; Potter and Cess, 2004; Allan, 2011).

A basic, global description of the modulation of solar and terrestrial radiation streams that focuses on the TOA is cloud radiative effect (CRE), expressed as (Hartmann, 1994)

$$\Delta R = \Delta S_{ABS} - \Delta F^{\uparrow}_{TOA}. \tag{1.1}$$

That is, the change in net radiation at the TOA due to cloudiness (ΔR) is the difference between the change in absorbed shortwave solar radiation (ΔS_{ABS}) and the change in upwelling longwave terrestrial radiation ($F^{\uparrow}_{TOA}$). In the global average, if ΔR is negative, then the Earth experiences a net loss of radiative energy at the TOA and must cool; the opposite is true if ΔR is positive. Using data from the Clouds and Earth's Radiant Energy System (CERES) program (Wielicki et al., 1996; Loeb et al., 2007), Allan (2011) investigated mean CRE at the TOA during the years 2001–2007. That study found the strongest shortwave cloud effects over the maritime continent, over oceanic storm tracks, over large maritime stratocumulus decks, and over the Inter-Tropical Convergence Zone (ITCZ). It also found the strongest longwave cloud effects over the maritime continent (nominally cancelling, as previously discussed, the corresponding shortwave effect) and over equatorial South America and Africa.

On its own, however, CRE at the TOA is probably too simple a description of cloud radiative effects. Longwave heating and shortwave cooling effects at the surface and on an atmospheric column are distributed, depending greatly on such factors as the vertical distribution of cloud and of associated water vapor fields (Paltridge, 1980; Stephens, 2005; Mace et al., 2009), and these effects are important to the coupling of the hydrological cycle with the planetary energy budget (Allan, 2011).

The NASA Surface Radiation Budget (SRB) dataset (Stackhouse et al., 2011) applies radiative transfer models to reanalysis data from the Goddard Earth Observing System Data Assimilation System (GEOS DAS; Bloom et al., 2005) and to ISCCP satellite cloud observations in order to characterize the planet's long- and shortwave radiation budgets from the surface to the TOA. SRB radiative flux estimates are constrained using surface and satellite measurements. Allan (2011) used this data product to sample clear sky fluxes and then to estimate CRE in the atmosphere, at the surface (these two abilities being advantages of this approach), and at the TOA [which produced similar results to TOA CRE as using CERES satellite data from 2001 to 2007—see Figs. 3 and 4 in Allan (2011)]. Using this dataset in a global average over several years, the strongest shortwave cloud radiative effects were found to be approximately −50 Wm^{-2} over the large, maritime stratocumulus cloud decks and over midlatitude storm tracks. The global, average cloud radiative effect was found to be one of cooling. Global, multi-annual values for CRE were found to be approximately −21 Wm^{-2} at the TOA, −20 Wm^{-2} at the surface, and −1 Wm^{-2} within the atmosphere.

Looking at zonal means [see Fig. 5 in Allan (2011)], Tropical clouds cool the surface and heat the atmosphere, thus helping to establish radiative-convective equilibrium (Manabe and Strickler, 1964). Net CRE within the atmosphere is positive in the Tropics and negative everywhere else. At higher latitudes, longwave emission from cloud base to the surface results in cooling the atmosphere and in heating the surface. At most latitudes, net surface CRE is negative, polar latitudes being the exception. Though the analysis of Allan (2011) was not extended to the radiative effects of particular types of cloud systems, it was pointed out therein that it certainly could be.

Considering individual cloud systems, it is found that they are organized on the synoptic and mesoscales, where large-scale weather patterns to a great extent control their types, arrangements, and lifetimes (Stephens, 2005). A preliminary work by Jakob and Tselioudis (2003) used cluster analysis (e.g., Anderberg, 1973) on the ISSCP cloud top pressure-cloud optical depth data product in order to categorize cloud regimes in the Tropical Western Pacific region via the clustering of bivariate histograms of estimated cloud layer top pressure and cloud optical depth. Building on that earlier study, Rossow et al. (2005) performed a statistically rigorous cluster analysis on the same ISCCP dataset (spanning the years 1983–2004) throughout the entire Tropics within 2.5° boxes (which they state to be at the upper end of the mesoscale). In so doing, they categorized observed clouds into six distinct "weather states" throughout the whole Tropics. These weather states span cloud regimes from deep convective to low-level marine stratus and are associated with distinct tropical atmospheric dynamic states (Jakob and Tselioudis, 2003).

More recently, Tselioudis et al. (2013) extended the procedure of Rossow et al. (2005) by using the global ISCCP cloud top pressure-optical depth data from July 1983 to June 2009 in order to identify weather states at all latitudes. The same rigorous K-means clustering approach was applied to joint histograms of cloud top pressure and optical depth, and 11 distinct weather states were found, some of which coincided with states found in the earlier tropical study (Rossow et al., 2005). A 12th, clear-sky state was added which had only a 1.9% relative frequency of occurrence. Concurrent CloudSat radar and Cloud-Aerosol Lidar and Infrared Pathfinder Satellite Observations

(CALIPSO) lidar data (these satellites will be described in more detail later) were used to investigate the statistics of the vertical structures of the identified weather states, the results of which indicated that the weather states were not only distinct but more or less correct in their respective classifications. To summarize briefly the natures of the weather states identified in Tselioudis et al. (2013), States 1 and 2 are convective regimes (State 1 is more characteristic of tropical convective systems and State 2 of midlatitude convective systems). State 3 is comprised more of cumulus congestus, convective anvil clouds, and disordered convective systems. States 4 and 5 are dominated by midlevel clouds. States 9 through 11 are dominated by marine stratocumulus and stratus decks, and State 6 is dominated by cirrus. State 7 is dubbed the "fair weather" state.

The centroids of the clusters given by Tselioudis et al. (2013) are not to be taken as strict guidelines within the individual weather systems on locations of cloud tops, on cloud optical depths, or on the occurrence of the cloud types defined in Rossow and Schiffer (1999), but should rather be thought of as "representing distinctive mesoscale distributions or mixtures of cloud types." [Indeed, difficulties in the ISCCP classification of individual cloud scenes have been identified—see, e.g., Mace and Wrenn (2013).] Use of such weather states makes a better method for tracking trends in clouds than does looking at the occurrence of specific cloud types and of their coverages, and because the states are distinctive, they can be tracked through time and space and can be used to composite other, cloud-related atmospheric variables (Tselioudis et al., 2013). To demonstrate the study of atmospheric dynamics and of CRE in conjunction with the defined weather states, Tselioudis et al. (2013) used them to composite both large-scale 500 mb vertical velocities from the European Centre for Medium-Range Weather

Forecasts (ECMWF) Interim Re-Analysis (ERA) and CRE computed from the ISSCP flux data (see their Figs. 5 and 7). Also, to demonstrate the study of the long-term variability of the weather states, they plotted anomalies in the relative frequencies of occurrence of the states over the study period (see their Fig. 6). Their particular results are of less interest here than is their demonstration of the various analysis capabilities.

Cloud Feedbacks

CRE is the result of a complex set of coupled processes. Where and how clouds form is largely a result of large-scale atmospheric motions. Clouds affect the distribution of atmospheric radiative and latent heating and since, on interannual time scales, atmospheric radiative and convective processes are often considered to be in approximate balance (Manabe and Strickler, 1964), changes in the distribution of cloudiness and of its interaction with the water vapor field affect changes in hydrological processes. By operating on latent and radiative heating distributions and on the hydrological cycle, cloudiness then feeds back on the large-scale circulation (Stephens, 2005). A consideration of the climatic effects of cloudiness thus must involve more than just the radiative properties of clouds: it must also attempt to account for as many of the significant feedback avenues between clouds and the other elements of the climate system as possible.

Feedbacks are often described mathematically in terms of the sensitivity of the globally averaged surface temperature to any one of a number of climatologic forcings. For example, as in Stephens (2005), if in equilibrium the net radiation budget at the TOA is near zero, then it may be stated that

$$\Delta R = \frac{\partial R}{\partial \varepsilon}\Delta\varepsilon + \frac{dR}{dt}\Delta T = 0. \tag{1.2}$$

Two components of ΔR are considered in the expression above: one due solely to a change in some controlling action (such as an increase in atmospheric carbon dioxide levels) $\Delta\varepsilon$ and another due to the total change in ΔR due to the resulting adjustment of surface temperature. Feedbacks between surface temperature and some set of climate factors—$\{x_i\}$, many of them related to clouds—find expression within the total derivative $\frac{\mathrm{d}R}{\mathrm{d}T}$. If an (incomplete) application of the chain rule

$$\frac{dR}{dT} = \frac{\partial R}{\partial T} + \sum_i \frac{\partial R}{\partial x_i}\frac{dx_i}{dT} \tag{1.3}$$

is used and if the radiative effect of the control action is approximated by

$$\Delta Q = \frac{\partial R}{\partial \varepsilon}\Delta\varepsilon, \tag{1.4}$$

then by algebraic manipulation the expression for the total resulting surface temperature change may be written as

$$\Delta T = \frac{\lambda_0 \Delta Q}{1-f}. \tag{1.5}$$

Here

$$\lambda_0 = \frac{\partial T}{\partial R} \tag{1.6}$$

is called the closed-loop gain, and the set

$$\left\{ f_i : 1 - f = 1 - \lambda_0 \sum_i \frac{\partial R}{\partial x_i} \frac{dx_i}{dT} \right\} \qquad (1.7)$$

are called feedback factors. According to this approach, feedback relationships between various aspects of the global cloud field and temperature (often surface temperature) can be expressed via these feedback factors, though there are other ways to formulate them (e.g., Paltridge, 1980). However, the isolation of any of the open loop or feedback effects of clouds (or, in other words, of any of the partial derivative terms in Eq. 1.7) from observations alone is a statistical impossibility, so model-based studies must be used in order to discern these effects (Stephens, 2005).

This view of cloud feedbacks is evidently borrowed from the field of control engineering (a subdiscipline of electrical engineering). Specifically, it is an expression of a linear feedback network (Belanger, 1995). A simple feedback network is shown in Fig 1.4a, and the input, forward, and feedback filters are represented mathematically by their Laplace transforms [C(s), H(s), and F(s), respectively]. It is important to recognize that within this representation is the implicit assumption that all of these filters are both linear and time-invariant. The time-invariant assumption requires the feedback factors and the closed-loop gain both not to be functions of time, which assumption probably would not bear close examination. Figure 1.4b shows Eq. 1.5 in this linear feedback configuration—note that the filter response functions are constant and that they are just the derivative terms from Eq. 1.7. Beside the linear and time-invariant assumptions already mentioned, two other critical assumptions are also implicit in Fig. 1.4b: 1) that the impulse responses of the several filters are memory-less (implied by the use of

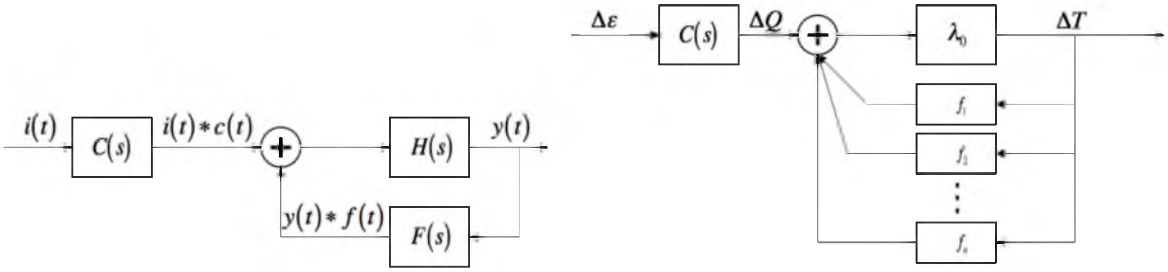

(a) (b)

Fig. 1.4: Liner feedback network theory applied to cloud feedbacks. A general linear feedback network (a), and Eq. (1.5) diagrammed as a linear feedback network (b).

constant-value transfer functions) and 2) that the feedbacks are both independent and parallel to one another (seen in the fact that the derivatives of x_i above are not expanded to include interrelationships among the several x_i's, or also in the placement of the feedback factors f_i within the diagram). Use of this theory therefore involves a number of pitfalls, perhaps the most dangerous being that a linear, memory-less explanation is used for a system that is grossly nonlinear and that has a long memory.

Furthermore, there is a "system identification" problem (Stephens, 2005): a thorough description of the system, including all relevant inputs and outputs, is required but is not accounted for in this representation. An easily seen manifestation of this problem is the independent, parallel treatment of feedbacks that in reality bear nonlinear relationships with one another (Bony et al., 2006). Ultimately, though, the relationship between globally averaged surface temperature and a set of cloud processes that occur and interact on several temporal and spatial scales is certainly not unique. Thus, according to linear feedback control theory, the system as defined in Fig. 1.4 is not "observable" (Belanger, 1995), or, in other words, the state of the system cannot be determined from measurements of average surface temperature but must instead be determined via a multivariate analysis (Aires and Rossow, 2003).

It is therefore difficult to imagine this construction of cloud feedbacks to be truly useful either as a way to predict how a climate model will respond given a disturbance or as a way to diagnose, based upon the response of modeled global cloud systems, the efficacy of climate models given a disturbance. Aires and Rossow (2003) show that it is not and state that the results of an analysis couched in linear feedback theory can be highly misleading and amount at best to a "schematic" representation of feedbacks in an equilibrium climate. As an alternative to using model runs to estimate constant, univariate feedback factors, they lay out a method for estimating the multivariable time- and state-dependent sensitivities (basically, as a Jacobian of the partial derivatives from Eq. 1.3) of a nonlinear, dynamical climate system.

Essentially, the method of Aires and Rossow (2003) applies a nonlinear regression technique (their technique of choice being neural network analysis) to estimate state-dependent system sensitivities by making use of as many observations of a climate system—in as many of its different states and through as many of its possible state transitions—as can be made. They demonstrate the efficacy of their method using a low-order Lorenz atmospheric model (Lorenz, 1984) whose sensitivities can be computed analytically.

Though it would require the manipulation of immense amounts of data, this method would provide a more realistic and therefore a more useful framework for performing intercomparisons of the cloud-related behaviors of either GCMs or of cloud resolving models (CRMs) "by comparing the sensitivities of the variables of the [systems] and their state dependence" (Aires and Rossow, 2003). It would also provide a more realistic framework for evaluating the behavior of models, especially of CRMs, in light of actual cloud data or also a framework for using cloud data to examine the physics underlying sensitivities diagnosed from models (Aires and Rossow, 2003). For the latter two purposes, there needs to exist a massive database of reliable measurements of climatologically relevant cloud micro- and macrophysical observations. In implementing such a framework, use of the full SRB dataset could be helpful in constraining feedback processes [as pointed out by Allan (2011)]. However, that dataset's characterization of clouds derives from ISCCP measurements and is limited in its details of cloud microphysical information, and, as already pointed out, ISCCP classifications of specific cloud scenes are problematic. Considering the former purpose, model intercomparisons for the evaluation of cloud predictions increase in utility as the accuracy of the methods for modeling clouds increases. For this to occur, it will be seen in the next section that, again, there needs to exist a massive database of reliable measurements of climatologically relevant cloud micro- and macrophysical observations.

Cloud Modeling

Many cloud-related processes and effects occur at scales smaller than the resolution of numeric models and must therefore be parameterized in terms of modeled quantities that are resolved. A parameterization expresses the statistical knowledge of the influence of an unresolved quantity on those that are resolved while expressing the unresolved quantity as a function of the resolved quantities (Hack, 1992). A parameterization is thus perforce only an approximation to the actual statistical relationship, utilizing various “idealizations and closure assumptions”; and due to computational costs, it is often the case that only the bulk properties of clouds are parameterized (Randall et al., 2003). What is sought for in a model is a simple parameterization scheme that describes the most important processes—for instance, cloud roles in the water cycle and in radiation (Ryan, 2000) as well as the evolution of cloud systems. Often, the desired quantities include cloud fraction and water content, spatial distribution of water content, precipitation, liquid and water vapor advection, and cloud microphysical properties (such as effective radius). Furthermore, different types of clouds can require different parameterization philosophies. For example, parameterization of broad, stable stratiform layers is often performed as a function of relative humidity, with bulk parameterization of condensed water (Randall et al., 2003). Convective clouds are more complicated to parameterize as they must be tied to convective processes, fluxes of water vapor, and interactions with and creation of other types of clouds such as cirrus anvils and stratus layers (Randall et al., 2003). Furthermore, they do not exist in broad layers, so their partial coverage must somehow be taken into account. There are a number of different approaches to the parameterization of realistic cloud fields.

One of the most basic techniques in use is diagnostic parameterization, wherein cloud bulk properties within a grid cell are diagnosed (specified) from the resolved flow. Bulk properties thus diagnosed can include model grid-box cloud fraction and water content as well as the mixing ratios of both cloud water and precipitating water. This is often performed in terms of large-scale variables such as relative humidity and lapse rate, with convection, cloudiness, and precipitation being triggered according to semi-empirical relationships (Bony and Emmanuel, 2001).

Prognostic parameterization is a second technique. In this approach, the rates of change of quantities such as cloud water mixing ratio and grid-box cloud fraction, rather than the quantities themselves, are diagnosed. These quantities thereby become themselves prognostic (predicted) variables at each model grid point. A classic example of the prognostic parameterization of the two quantities just mentioned is found in Tiedke (1993). In skeletal form, the equations given there are

$$\frac{\partial}{\partial t}\left[\text{cloud water content}\right] = \text{advection} + \text{sources} - \text{sinks} \qquad (1.8)$$

$$\frac{\partial}{\partial t}\left[\text{cloud coverage}\right] = \text{advection} + \text{sources} - \text{sinks} \tag{1.9}$$

Statistical parameterizations constitute a third approach, built upon the first two. In a statistical scheme, the variability of certain conserved quantities is expressed via a joint probability density function (pdf) whose moments must be specified (Xu and Randall, 1996). Desired model quantities, such as cloud fraction, are then derived from the joint pdf. Consider as an example a parameterization of convective cloudiness proposed by Bony and Emanuel (2001). Based on results from Xu and Randall (1996) that indicated the distribution of conservative cloud variables to be skewed according to domain size, cloud regime, and altitude, Bony and Emanuel (2001) describe the variability of total water content with a normalized lognormal distribution. This distribution allows for varying amounts of skew, given an upper limit and a specification of the distribution's moments. Large-scale saturation values, along with water produced by convection within the model grid-box [as computed by a convective model (Emanuel and Zivkovic-Rothman, 1999)], are used to solve a set of simultaneous equations for the normalized distribution's various parameters. From these, the distribution's moments can be computed, and from the moments, the parameterized cloud fractions and average water content can then be computed. Of course, one of the factors determining the efficacy of a statistical approach is an accurate statistical knowledge, from comprehensive observations, of the conserved variables for which pdfs are assumed.

A modern parameterization scheme will likely use elements of all three of these different parameterization types. For example, Wilson et al. (2008) present a scheme for a prognostic grid-box volume cloud fraction and condensate parameterization for the

United Kingdom Met Office's Unified Model. Condensate and cloud fractions are parameterized for liquid, ice, and total cloud (from which may be derived the corresponding quantities for mixed-phase cloud). As an example, the equations for the rates of change of gridbox-mean liquid condensate and liquid cloud fraction from Wilson et al. (2008) are repeated here:

$$\begin{aligned}\frac{\partial \overline{q}_{cl}}{\partial t} = {} & \left.\frac{\partial \overline{q}_{cl}}{\partial t}\right|_{advection} + \left.\frac{\partial \overline{q}_{cl}}{\partial t}\right|_{radiation} + \left.\frac{\partial \overline{q}_{cl}}{\partial t}\right|_{convection} + \left.\frac{\partial \overline{q}_{cl}}{\partial t}\right|_{microphysics} \\ & \left.\frac{\partial \overline{q}_{cl}}{\partial t}\right|_{boundary\ layer} + \left.\frac{\partial \overline{q}_{cl}}{\partial t}\right|_{orographic\ drag} + \left.\frac{\partial \overline{q}_{cl}}{\partial t}\right|_{erosion} + \left.\frac{\partial \overline{q}_{cl}}{\partial t}\right|_{adiabatic\ expansion}\end{aligned} \tag{1.10}$$

$$\begin{aligned}\frac{\partial C_l}{\partial t} = {} & \left.\frac{\partial C_l}{\partial t}\right|_{advection} + \left.\frac{\partial C_l}{\partial t}\right|_{radiation} + \left.\frac{\partial C_l}{\partial t}\right|_{convection} + \left.\frac{\partial C_l}{\partial t}\right|_{microphysics} \\ & \left.\frac{\partial C_l}{\partial t}\right|_{boundary\ layer} + \left.\frac{\partial C_l}{\partial t}\right|_{orographic\ drag} + \left.\frac{\partial C_l}{\partial t}\right|_{erosion} + \left.\frac{\partial C_l}{\partial t}\right|_{adiabatic\ expansion}\end{aligned} \tag{1.11}$$

Briefly, the components of these two equations express total changes in the quantities of interest due to semi-Lagrangian advection from neighboring model grid boxes to the effects of short- and longwave radiation, to convective processes, to cloud and precipitation microphysics, to boundary layer processes, to orographic drag, to erosion of clouds from entrainment, and to pressure changes from large-scale ascent within the grid-box. Wilson et al. (2008) lay out an intricate and detailed parameterization scheme. It is not purposed here to explain it in detail, but instead to illustrate some issues that are relevant to the theme of this introductory chapter. Therefore, a few of the underlying principles of the scheme used by Wilson et al. (2008) will be briefly discussed.

First, though Wilson et al. (2008) formulate a prognostic parameterization, it is built upon an underlying pdf of water [as is, they point out, the scheme of Tiedke (1993)]. Within a grid-box, condensed and total water variables are described both by their mean values and by pdfs describing variations from their respective means. Predicting variables based on physical processes and allowing the water pdf to be governed by the physical processes, as opposed to specifying a fixed water pdf, makes it possible to account for different processes' dominating in different regions of the grid-box (Wilson et al., 2008). Depending on what physical process is being parameterized (see Eqs. 1.10 and 1.11), the water pdfs are explicitly, semi-explicitly, or only implicitly referenced. The ways in which they are used may be examined by looking at certain aspects of the shortwave radiation, convection, and cloud erosion terms (Wilson et al., 2008).

Warming and evaporation due to shortwave radiation are treated by Wilson et al. (2008) as a "homogenous forcing." The result is that temperature and total condensed water change uniformly throughout the model grid-box, and the underlying water pdf (assumed to have a "tophat-like" shape) is unaffected.

Convection results in changes in cloud fraction (liquid, ice, and total) due to detrainment from convective plumes via a process dubbed by Wilson et al. (2008) as "injection forcing." A distinct water pdf is assumed for each of the clear and cloudy portions of a grid-box. The new fraction of cloudy air is computed, which computation implicitly results in a single, adjusted water pdf for the grid-box.

The erosion term is basically the opposite of convective injection and accounts for the entrainment of dry air into cloudy air. Wilson et al. (2008) model this process as resulting in "a slow reduction in width of the background [water] pdf." Relative change in pdf width is explicitly parameterized using various modeled and empirical parameters, and from this comes $\left.\frac{\partial \bar{q}}{\partial t}\right|_{erosion}$ and $\left.\frac{\partial C}{\partial t}\right|_{erosion}$ (the lack of subscripts indicating that similar expressions are used for liquid, ice, and total cloud).

Assumptions made in a parameterization can both lead to and reflect uncertainties in cloud processes. Within the presently discussed parameterization, we see that fundamental assumptions are made relating to the shape and evolution of the grid-box water pdf. As an example of accompanying uncertainty, Wilson et al. (2008) acknowledge that assuming the grid-box water vapor distribution to be uniform for ice processes can have a significant effect on ice-related variables. More assumptions can be seen in their large-scale precipitation scheme, which affects changes in liquid, ice, and total cloud fractions (including transitions from one type of cloud to another) via parameterization of several microphysical processes. These processes include homogenous and heterogenous ice nucleation; ice particle sedimentation; vapor deposition and sublimation; riming; condensation, melting, and evaporation; and precipitation particle growth by accretion and collision/coalescence. Many of these processes are assumed not to change cloud volume fraction within a grid-box. Also, affecting the modeling of mixed phase cloud, changes in ice cloud fraction are assumed to be randomly overlapped with coincident liquid cloud.

Furthermore, in any parameterization, critical uncertainties are introduced through assumptions about ice crystal microphysics. For instance, Wilson et al. (2008) use ice crystal fall speed as a component in computing their large-scale precipitation processes. Parameterizations of ice crystal terminal velocity carry with them significant uncertainties (see, e.g., Mitchell, 1996; Heymsfield et al., 2013). In any case, whenever radiative transfer is to be parameterized, some assumptions concerning cloud PSDs, and in the case of ice clouds concerning ice particle habit, must be made (see, e.g., Ryan, 2000).

As an example of this last point, consider a bulk property parameterization scheme proposed by Ryan (2000) for ice clouds, designed to unify the diagnosis of bulk variables, radiation, and precipitation processes. Within a grid cell, a set of coupled differential equations serve as prognostic equations for the bulk cloud quantities of temperature, water vapor mixing ratio, and cloud and precipitation water mixing ratios. The particle size distributions of nonprecipitating particles are based on an empirical power law fit to data collected by Heymsfield (1977) and processed by Platt (1997), and the size distribution of precipitating particles is described by the Marshall–Palmer distribution (Marshall and Palmer, 1948). The various parameters of these two size distributions are treated as functions of temperature and of cloud type (dry cirrus, frontal cirrus, or midlevel clouds), the functional relationships thereof being based upon in situ observations. The actual numbers of particles in each particle regime are then diagnosed, and from this diagnosis and from the bulk parameters extinction efficiency and particle effective diameter are computed as the main radiative parameters. However, historical datasets [including those used by Ryan (2000)] of cloud ice particle size distributions are rife with uncertainties (Lawson, 2011). Here again, then, we return to a recurring theme: the efficacy of parameterization schemes, such as those of Ryan (2000) and Wilson et al. (2008), depends heavily on obtaining a massive database of reliable measurements of climatologically relevant cloud micro- and macrophysical observations. These observations must be capable of addressing matters such as ice particle sedimentation velocity and ice particle radiative properties, and they must be able to tie cloud microphysics to atmospheric processes.

At this point, it is well to consider a more exhaustive, computationally expensive approach to cloud parameterization called multiscale modeling—or “superparameterization”—described by Randall et al. (2003). The basic idea is to embed a cloud-resolving model (CRM) within the grid-boxes of a coarse-resolution GCM. This concept comes with a number of advantages (Randall et al., 2003). To begin with, many processes that must be parameterized conventionally within a GCM grid-box, such as deep convection, cloud overlap, and distributions of fractional cloudiness and of precipitation, can be explicitly resolved by a CRM. Some of the processes operating on various temporal and spatial scales, such as large-scale dynamics, cloud dynamics, and radiative transfer, can then be explicitly coupled. Furthermore, with their high resolution and their ability to couple scales together, CRMs can be used for the testing and development of conventional parameterizations.

Superparameterization is not a panacea, though. CRMs cannot resolve everything, and so a number of things must still be parameterized within them by conventional means, notably details of cloud microphysics and of radiative transfer. This approach also comes at a very high computational cost since the CRM must be run within every grid-box at time steps that are able to resolve changes in the governing cloud microphysics. For this cause, two-dimensional CRMs that do not span the entirety of a GCM grid cell are typically used along with periodic boundary conditions. Of course, and to return to a now oft-repeated point, in order for CRMs to be used in the development of conventional parameterizations, they must be validated with data to ensure that they are realistic (see, e.g., Khairoutdinov and Kogan, 1999; Polkinghorne et al., 2010; Negri et al., 2014).

Many of the intricacies involved with the modeling of clouds begin to be clear. Parameterizations of the processes that tie the various scales occupied by clouds together, such as turbulence, detrainment, convection, radiative and dynamic interactions, and mesoscale organization (Randall et al., 2003), need to be accurate themselves and to be properly interconnected with one another. Furthermore, in order to compute CRE in a model, the radiative effects derived from the microphysical properties of modeled clouds must be well characterized; for as seen, computing radiative transfer within a modeled cloud as a function of the cloud's bulk quantities requires beginning with correct assumptions about cloud microphysical properties and of the interactions of radiation with the cloud on this scale. In truth, the solidity and completeness of any such set of assumptions currently in use could be reasonably questioned, and this is particularly true for cirrus, for boundary layer clouds, and for convective clouds (e.g., Randall et al., 2003). Though it is a matter of broad agreement that one of the keys to improving numeric models of the Earth's climate is the proper formulation therein of all processes related to the atmospheric hydrological cycle (especially the interactions between aerosols, clouds, and precipitation), beyond this agreement may be found a varied array of proposed parameterization schemes meant to deal with the issue.

Differences in parameterization schemes among models lead as a matter of course to differences in model outputs, manifesting themselves as differences in such outcomes as cloud type frequency, seasonal variation of cloud cover, cloud water content, and, ultimately, predicted global sensitivity to such forcings as increased carbon dioxide (Li et al., 2012). It therefore comes as no surprise that different numeric models give inconsistent values for cloud feedback factors, even when the feedback factors are computed in a consistent manner from model to model (Soden and Held, 2006).

The Particular Problem of Cirrus Clouds

The documented spread in estimated cloud feedback factors (Eq. 1.7) between GCMs is mostly due to inconsistencies (born of uncertainties) between models in their treatments of marine boundary layer clouds (Bony and Dufresne, 2005; Zelinka and Hartmann, 2010). There is, however, a particular problem with the modeling of ice-phase (cirrus) clouds. To begin with, substantial disagreement exists between model simulations on the amount of global ice cloud (Li et al., 2005; Li et al., 2007; Waliser et al., 2009; Li et al., 2012). Using model output from the Coupled Model Intercomparison Project Phase 3 (CMIP3), Waliser et al. (2009) demonstrated differences as high as a factor of 20 between model simulations of globally averaged, annual mean values of cloud ice water path. Even after removing two outlier models from the dataset, the differences are still about a factor of 6 (see their Fig. 3). In contrast, model simulations of global averages of cloud fraction, average precipitable water, and average precipitation fared very well (relatively speaking) in their intercomparison. When geographical distributions of average ice water path were considered, intermodel differences of up to two orders of magnitude were found (see their Fig. 3). An updated study (Li et al., 2012) using model output from the Coupled Model Intercomparison Project Phase 5 (CMIP5) found significant improvements in cloud ice simulations from those in CMIP3—both in the fidelity of the various models one to another and to satellite observations of cloud ice that were not available at time of the Waliser et al. (2009) study. However, Li et al. (2012) yet found factors of 2 to 10 differences in annual mean maps of cloud ice water path among the models and the satellite observations. Both studies note that, in order for the sets of models to simulate correct TOA energy flux balances while nonetheless demonstrating such large inconsistencies in simulated cloud ice, they must suffer from other, compensating errors in order to meet the TOA energy budget constraints imposed on them by the CERES dataset. Furthermore, Waliser et al. (2011), in a prelimary study, showed that the generally poor treatment of precipitating ice in models results in biases in the radiation balance in precipitating regions. The certain result is to cause errors in modeled column heating rates, and therefore, in modeled atmospheric circulation (Waliser et al., 2011). This result being the case for precipitating ice, it is surely also the case for cloud ice. As it was put in that last paper concerning the satisfactory simulation of TOA energy flux balances, it must be that the models are "getting the right answers for the wrong reasons." The particular problem of cirrus is therefore threefold.

First, if model estimates of feedback factors vary widely due to uncertainties in boundary layer clouds, why do models not seem to "care" about how well ice clouds are simulated, even when the difference between simulations is as high as a factor of 6? If models, in order to fit measured TOA energy balance constraints, effectively tune their own cirrus parameterizations (Li et al., 2012) and thereby alter other of their modeled processes (Waliser et al. 2011), then large amounts of ice cloud data are needed in order to diagnose the effects of these shortcomings (Aires and Rossow, 2003).

Second, better model parameterizations of processes involving ice clouds are evidently needed. From the discussion above, it can be seen that reliable measurements of cirrus cloud microphysics (such as accurate information on cloud PSDs and on ice particle fall speeds), in relation to the physical processes that control them, are needed.

Furthermore, even if cirrus processes are both well understood and well modeled, the problem of computing radiative transfer in them is intricate and incompletely characterized (see, e.g., Kristjansson et al., 2000). Computations are dependent on particle sizes, shapes, and orientations, and also upon the complicated geometries of cloud fields that contain multiple types of clouds at multiple levels and with multiple horizontal and vertical extents. Therefore, the needed measurements must also allow for better characterization of radiative transfer within cirrus clouds.

Third, understanding of cloud physical and dynamic processes is most meager for cirrus clouds (Jakob, 2002) due to several challenges that include (Del Genio, 2002): 1) the occurrence of cirrus over a wide range of optical depths and over a wide range of altitudes, 2) the dependence upon geographical location of elements of the dynamic processes involved in cirrus formation and maintenance, and 3) the difficulty in observing cirrus (either directly or indirectly). As Jakob (2002) puts it: "If cirrus occurrence and microphysical and radiative effects were well understood, a parameterization could be designed. However, ice clouds are probably the poorest observed in the entire spectrum of clouds."

To sum up, and to reiterate, addressing the particular problem of cirrus clouds requires the designing of programs specifically designed to produce a massive database of reliable measurements of climatologically relevant cloud micro- and macrophysical observations. These observations must be capable of addressing microphysical matters such as ice particle sedimentation velocity and ice particle radiative properties, they must be able to tie cloud microphysics to atmospheric processes, and they must represent the wide variety of cirrus clouds that occur within different climate regimes and weather systems. In the next section, some important platforms for the observation of cirrus will be described.

Cirrus In Situ Measurement Campaigns

A number of intensive campaigns designed to observe various sorts of cirrus events have been mounted, featuring in situ measurements made by aircraft in conjunction with data taken by various remote sensors. Examples of such campaigns include the Cirrus Regional Study of Tropical Anvils and Cirrus Layers-Florida Area Experiment (CRYSTAL-FACE) in 2002; the Middle Latitude Cirrus Experiment (MidCiX) in 2004; the CALIPSO-CloudSat Validation Experiment (CC-VEx); the NASA African Monsoon Multidisciplinary Analyses (NAMMA) campaigns in 2006; the Tropical Composition, Cloud, and Climate Coupling (TC^4) campaign in 2007; the Small Particles in Cirrus (SPartICus) campaign in 2010; and the Midlatitude Airborne Cirrus Properties Experiment (MACPEx) in 2011. Uses of ice particle in situ data, taken from a wide variety of such campaigns, abound in the literature and are diverse in their scope and objectives. A few examples will help provide context for this work.

A small cross section of the various kinds of ice microphysical studies includes Heymsfield et al. (2004), who used data from CRYSTAL-FACE and from the Department of Energy (DOE) Atmospheric Radiation Measurement (ARM) Intensive Observation Period (IOP) of 2000 to study effective ice particle densities (i.e., the densities of spheres with crystal-equivalent masses and diameters equal to their respective crystal maximum dimensions), and Schmitt and Heymsfield (2005), who used data from CRYSTAL-FACE and from the First ISCCP Research Experiment Phase II (FIRE II) in 1991 as part of a study to model the total surface area of populations of ice crystals based on their projected areas. A number of microphysical studies have focused on ice nucleation; e.g., Prenni et al. (2007) used data from CRYSTAL-FACE and Heymsfield et al. (2009) used data from seven field programs [CRYSTAL-FACE, three NASA Tropical Rain Measuring Mission (TRMM) campaigns in 1998–1999, the Fourth NASA Convection and Moisture Experiment (CAMEX-4) in 2001, the Aerosol and Chemical Transport in Tropical Convection Experiment (ACTIVE) in 2005–2006, and the NASA African Monsoon Multidisciplinary Analyses (NAMMA) in 2006] to study ice nucleation in cumulus updrafts, pertinent to the formation of cirrus anvils. Heymsfield et al. (2006) looked at the interconnection between ice cloud microphysical and radiative properties by studying relationships between particle effective radius, shortwave extinction, and ice water content using measurements taken during CRYSTAL-FACE and MidCiX. Other examples of studies of ice radiative properties include Heymsfield et al. (2006), who used data from CRYSTAL-FACE to study the effective radii of ice PSDs, and Schmitt et al. (2006), who used data from the ARM IOP as part of a study to model the asymmetry parameter of clouds comprised of hollow, bullet-rosette type ice crystals.

Those sorts of studies focus on investigating specific processes that drive cloud formation, maintenance, and radiative effects, as well as on exploring ways wherein such may be modeled. In the work given here, it is purposed to present and apply a climatology of cirrus cloud mode particle size distributions derived from in situ cloud particle probe data taken during three flight campaigns: the NASA Tropical Composition, Cloud, and Climate Coupling (TC^4) and Midlatitude Airborne Cirrus Properties Experiment (MACPEx) campaigns (held in 2007 and in 2011, respectively) and the DOE ARM Small Particles in Cirrus (SPartICus) campaign (held in 2010). This effort and its results will be presented in Chapters 2 through 4 of this dissertation.

Cirrus Observing Platforms

However, while these campaigns yield valuable information about the makeup of cirrus clouds in various parts of the world, they have not yielded a set of statistics that is either temporally or spatially significant in a global sense (Mace et al., 2006a). To complement these periodic campaigns, then, a number of observing platforms have been devised to provide long-term observations of clouds. Two notable examples are the ARM program sites (Stokes and Schwartz, 1994; Ackerman and Stokes, 2003) and the satellite formation known as the Afternoon Constellation (or A-Train) (Stephens et al., 2002; Waliser et al., 2009; Li et al., 2012).

The ARM program, launched in 1989 by the U.S. Department of Energy, occupies sites at a handful of strategic locations around the globe (see Fig. 1.5) aimed at providing a multitude of long-term observations from several representative climate regimes. Each site is heavily instrumented in order to provide a large variety of measurements, both remote and in situ, relevant to the study of clouds, aerosols, atmospheric state and radiation, and surface properties. Measurements are made mainly using ground-based instruments, occasionally in conjunction with data taken from air- or ship-borne instruments. Several data products exist that are the result of merging many of the in situ measurements, remote sensing measurements, and physical retrievals performed using various combinations of these measurements. One example is the "column physical characterization" (CPC), described in Mace et al. (2006b), which combines soundings, microwave brightness temperatures, millimeter Doppler radar moments, and derived cloud microphysical and radiative properties from the ARM

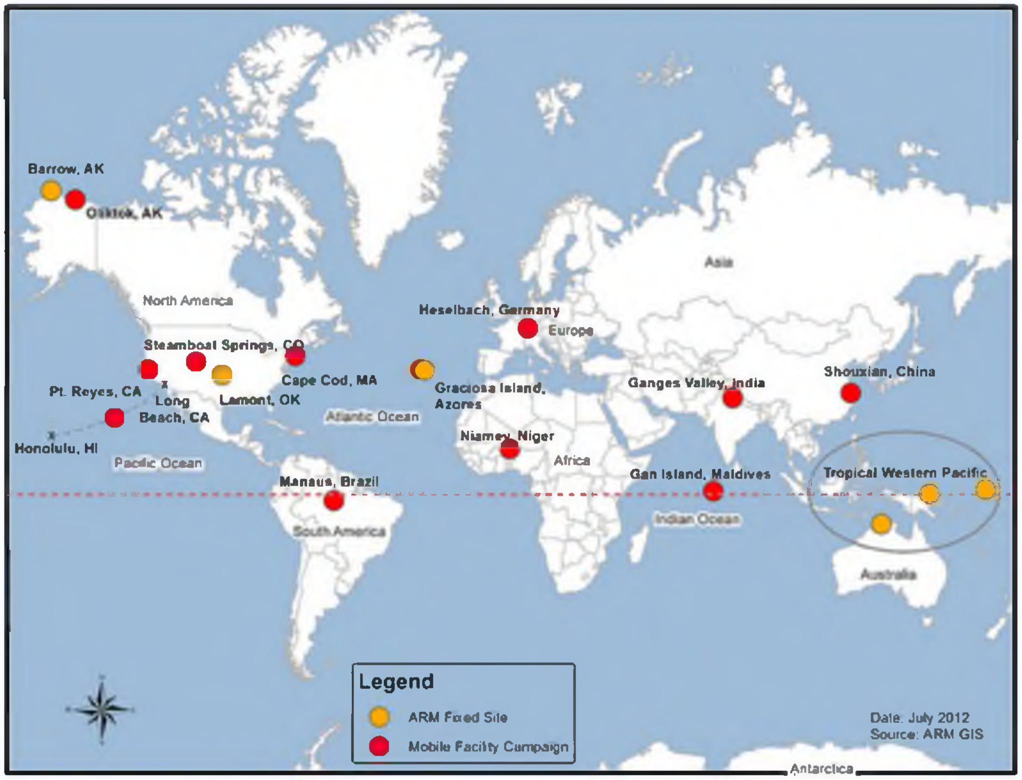

Fig. 1.5: Location of Atmospheric Radiation Measurement program instrumented sites as of July 2012. (Courtesy of ARM Climate Research Facility. For license, see www.flickr.com/photos/armgov/10710922616/.)

Southern Great Plains (SGP) site into a smooth data product with 5-minute temporal resolution and 90-meter vertical resolution.

The A-Train is a constellation (Raymond et al., 2002) of satellites in sun-synchronous orbit, crossing the equator at 1:30 p.m. local time (see Fig. 1.6). The members of the constellation currently active are the NASA CloudSat, Aqua, and Aura satellites; the Japan Aerospace Exploration Agency (JAXA) GCOM-W1 satellite; and the joint NASA/Centre National D'Etudes Spatiales (CNES) Cloud-Aerosol Lidar and Infrared Pathfinder Satellite Observations (CALIPSO) satellite. The instrumentation aboard these satellites is designed to provide remote measurements of atmospheric chemistry and of atmospheric cloud, aerosol, and radiation fields. Three particular instruments of note for the study of clouds are the Cloud Profiling Radar (CPR) aboard CloudSat, the Cloud Aerosol Lidar with Orthogonal Polarization (CALIOP) aboard CALIPSO, and the Moderate Resolution Imaging Spectroradiometer (MODIS) aboard Aqua (King et al., 1992). Synergy occurs when data from these three instruments are combined to produce retrievals of cirrus cloud properties. As they fly within minutes of one another, it is assumed that the different instruments "see" virtually the same air mass. However, each of these three instruments has a unique vertical and horizontal resolution (e.g., Mace et al., 2009) as well as a unique integration time, so each instrument does not see the same volume of air, nor is the frequency of reported data the same for each instrument. Thus, in order for the data from these three instruments to be aligned so that use may be made of this synergy, care must be taken to account for their differing spatial and temporal resolutions as well as for factors such as uncertainty in the nadir direction of each instrument.

Fig. 1.6: The A-Train (Courtesy of NASA Goddard Space Flight Center).

To address this problem, the Radar-Lidar Geometrical Profile (GEOPROF) product has been developed (Mace et al., 2009), the purpose whereof is, through probabilistic means, to properly overlap all CALIOP measurements with concurrent CPR measurements. An example GEOPROF combination from a section of an A-Train orbit north of Papua New Guinea on July 1, 2006, is shown in Fig. 1.7. The three-panel image shows CPR reflectivity and CALIOP backscatter in the top two panels, wherein can be seen a complementary view of the cross section of a large cloud field. The synergy between the two instruments is demonstrated in the third panel, which shows a cloud mask derived by combining the GEOPROF-ovelapped reflectivity and backscatter.

These data sets, like those from the ARM program, have the potential of providing long time-series of cloud observations. There are far fewer instruments aboard the A-Train satellites than are had at the various ARM sites, and such measurements as are had in common between the two observing platforms have coarser resolution when made from space. However, ARM measurements are limited to a handful of fixed locations, whereas A-Train measurements span the globe. Thus, in a handful of ways, the data-streams coming from the two platforms are complementary. Cirrus cloud property retrieval algorithms that make use of data taken by instruments involved with either program abound, but if measurements from these two different sources could be combined with the knowledge gained from the in situ observations provided by flight campaigns, then the relative strengths of each approach could be exploited in order to provide an improved, long-term description of cirrus cloud properties over much of the globe. As a prelude to such a large effort, Chapter 5 of this dissertation will address the beginning of an application of in situ observations of cirrus clouds to inform retrievals of

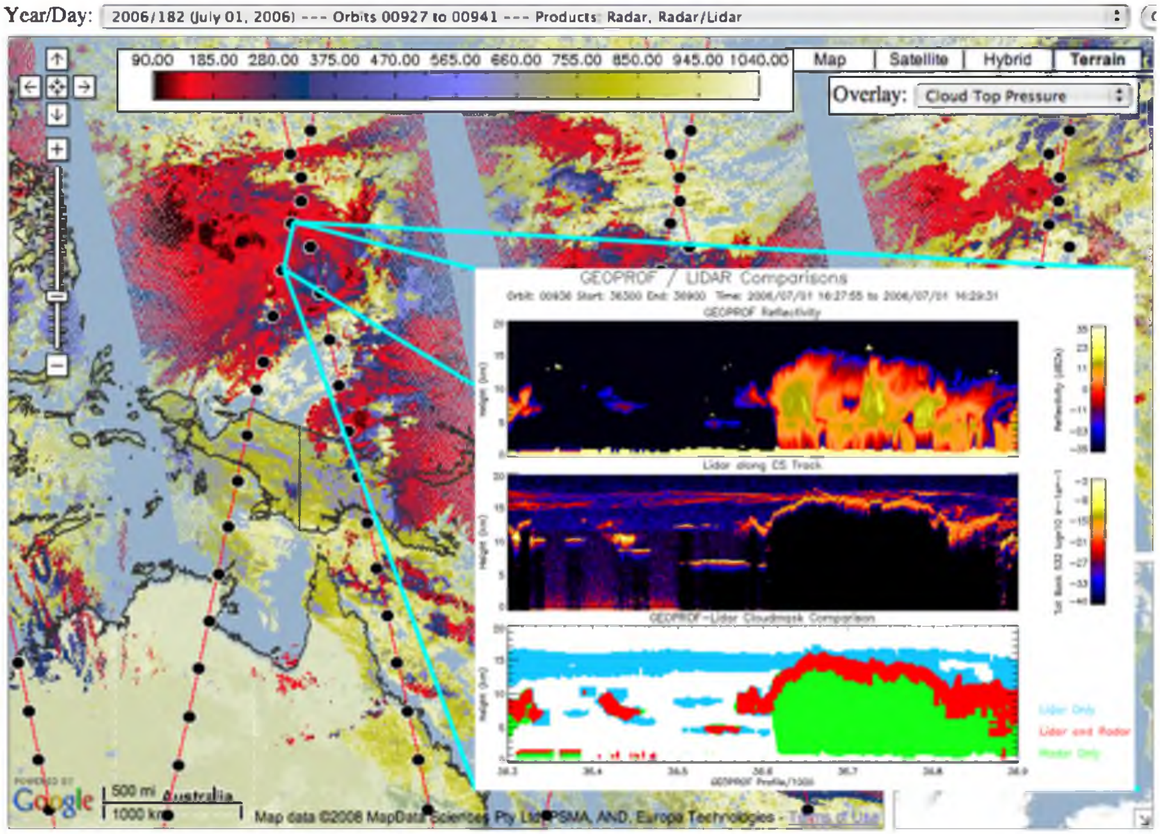

Year/Day: 2006/182 (July 01, 2006) --- Orbits 00927 to 00941 --- Products: Radar, Radar/Lidar

Overlay: Cloud Top Pressure

Developed by Chris Galli for Jay Mace at the University of Utah, Meteorology

Fig. 1.7: A three-panel image from radar-lidar GEOPROF database, showing synergy between CPR and CALIOP in detection of clouds, shown over cloud top pressure field (as derived from MODIS).

cirrus properties from remote sensing measurements generally.

Comparison of Modeled Cirrus Clouds with Remote Observations

Significant efforts are already underway to use the A-Train data for comparison purposes with model outputs (see, e.g., Waliser et al., 2009; Waliser et al., 2011; and Li et al., 2012). One technique that has become popular to this end is the forward modeling of remote sensing observables from GCM and CRM output for comparison with actual remote sensing observations. The third use made of in situ data here is for a beginning of the investigation of remote sensing forward models and the correct comparison of modeled observables to actual observations. This work is in its early stages and will be presented in Chapter 5 along with the remote sensing retrieval work (which is also in a relatively early stage). The proceeding chapters of this dissertation represent papers in various stages of preparation for submission for publication.

CHAPTER 2

DATA AND CIRRUS MICROPHYSICAL ANALYSIS METHOD

Background

The purpose of this and of the following two chapters is to present, examine, and apply a climatology of cirrus cloud mode particle size distributions derived from in situ cloud particle probe data taken during three flight campaigns: the NASA Tropical Composition, Cloud, and Climate Coupling (TC^4) and Midlatitude Airborne Cirrus Properties Experiment (MACPEx) campaigns (held in 2007 and in 2011, respectively) and the Department of Energy (DOE) Atmospheric Radiation Measurement (ARM) Small Particles in Cirrus (SPartICus) campaign (held in 2010). These three campaigns were chosen due to their use of the two-dimensional stereo (2D-S) probe (Lawson et al., 2006b). First, though, a look at some previous work using ice particle in situ data will be taken in order to provide some context for this work described in this chapter.

For studies designed to inspect the nucleation and life cycle of ice clouds, it has been posited that orographic wave clouds constitute a sort of "natural laboratory" (e.g., Heymsfield and Miloshevich, 1993, 1995) because air parcels can be followed as their water and ice microphysics and thermodynamics evolve during the parcel's pass from clear air, through the cloud, and back out into clear air.

Furthermore, in principle, as long as the cloud lasts, this principle of following air parcels can be repeated. Heymsfield and Miloshevich (1995) used microphysical measurements taken in orographic wave clouds during the Wave90 experiment in 1990 to study ice nucleation processes, and then looked at cirrus resulting from large-scale uplift in the First ISCCP Regional Experiment Phase II (FIRE II) in 1991 in order to apply the results from the Wave90 study to more general cirrus. They posited three general zones to exist in cirrus clouds: a highly supersaturated zone near cloud top where ice crystals are produced, a yet-supersaturated zone beneath where PSDs broaden due to growth, and a sublimation zone where crystals fall through subsaturated air. They also proposed a negative feedback between particle number concentration and relative humidity, viz., that relative to areas with lower number concentrations, areas with higher number concentrations may be expected to coincide with lower ice supersaturations due to the excess vapor's being used for particle production.

However, in a study utilizing data from 133 penetrations through 17 wave clouds at various levels within the clouds, Baker and Lawson (2006a) observed that wave clouds often contain features not so easily explained by the simple model thereof given by Heymsfield and Miloshevich (1995), and so not all wave clouds are the ideal "natural laboratory." In broad consistency with the conceptual model of Heymsfield and Miloshevich (1995), though, Baker and Lawson (2006a) found increased concentrations of larger particles in lower cloud levels and a maximum total number concentration higher in the clouds than the ice water content maximum. Furthermore, as Lawson et al. (2006a) similarly found in a more general study of cirrus, various rosette shapes figured most importantly in the mass, while number concentration was determined mainly by small, quasi-spherical particles (droxtals). Though they found only a weak relationship between total number concentration and temperature, they did find that, on average, number concentrations were higher and mass lower in regions where temperature was less than −37°C (see their Table 3). Given favorable humidity conditions, one might expect homogenous nucleation to become appreciable at around this temperature (Sassen and Dodd, 1988; Heymsfield and Miloshevich, 1993). Maximum water content, Baker and Lawson (2006a) stated, is not completely attributable to temperature: they hypothesize that relative humidity over ice (RHi) and vertical velocity must also be accounted for, which measurements they did not have. They found that warmer cloud regions tended to have larger particles, which they attributed to riming and to aggregation.

Heymsfield and Miloshevich (1995) and Lawson et al. (2006a) both point out that, in contrast to the relative ease of studying wave cloud formation, observations of cirrus formation are much more difficult to make: when particles are observed, they are often not observed where they were nucleated, and furthermore, they may have been subjected to secondary ice processes, dynamical processes, fallout, and size sorting. Lawson et al. (2006a) used data from 104 flight legs to investigate 22 midlatitude cirrus clouds, using, as did Baker and Lawson (2006a), particle images from the Stratton Park Engineering Company (SPEC) Cloud Particle Imager (CPI) and from the Particle Measuring Systems (PMS) Forward Scattering Spectrometer Probe (FSSP) and 2DC probe (Knollenberg, 1981). They found temperature and cloud thickness to be important factors in determining ice particle characteristics, but they lacked measurements of RHi and surmised that the fact that particles characteristic of the three zones mentioned earlier can be found at all locations within a cirrus cloud may be due to variability in RHi within the cloud. Thus, they posit, the model of cirrus zones proposed by Heymsfield and Miloshevich (1995) is probably true in a statistical sense, using temperature as a proxy for location within cloud, over a large sample of cirrus. Furthermore, in a wide-ranging study (in temperature, in altitude, and in geographical location), Heymsfield et al. (2013) used 85 000 ice cloud PSD measurements from 10 different in situ field programs: CRYSTAL-FACE, FIRE-II, the ARM IOP, TC^4, the NASA Pre-Aura Validation Experiment (PreAVE) of 2004, the European Commission Integrated Project (IP) Stratospheric-Climate Links with Emphasis on the Upper Troposphere and Lower Stratosphere (SCOUT) tropical aircraft program of 2005, the NASA African Monsoon Multidisciplinary Analyses (NAMMA) field program of 2006, the Aircraft Icing Research Alliance (AIRA) and World Meteorological Organization (WMO) Alliance Icing Research Study II (AIRS-2) of 2003–2004, the Canadian CloudSat/CALIPSO Validation Programme (C3VP) of 2006–2007, and the ARM Mixed-Phase Arctic Cloud Experiment (MPACE) of 2004. For many of the measured PSDs, concurrent measurements of condensed water mass were available. They found that, in the average, ice particle concentrations decrease with temperature while ice water contents (IWCs), PSD widths, and maximum particle dimensions increase with temperature.

The Lagrangian spiral technique (Lo and Passarelli, 1982) is one way to observe microphysical processes in widespread and fairly steady-state cirrus: an aircraft is allowed to descend at a constant bank angle and at a low rate of descent, advecting with the horizontal wind, in order to measure the evolution of cloud and precipitation microphysics in the reference frame wherein they evolve. Using this technique, some similar conclusions to those already sketched out have been drawn. For example, Field

(2000) used Particle Measuring Systems (PMS) 2D Cloud (2DC) and 2D Precipitation (2DP) particle probes to investigate bimodality in ice PSDs in frontal clouds around the United Kingdom in five Lagrangian spiral flights through frontal clouds in 1998 and 1999. Their study pointed toward a universality of high concentrations of the smallest ice crystals and a second mode (as a shoulder) in the PSDs that progressively separated itself from the smaller mode with depth from cloud top, only to have the larger mode disappear as cloud base was neared. It was suggested in that paper that the large mode of PSDs evolved with depth in the cloud via aggregational growth, only to have the larger particles disappear due to particle break-up and melting at warmer temperatures. Field and Heymsfield (2003) used PSDs measured in spiral flights with the PMS probes as well as with the SPEC high-volume precipitation spectrometer (HVPS), covering several cases of synoptically and convectively generated cirrus in both the midlatitudes and the Tropics, during the First ISCCP Regional Experiment Phase I (FIRE I) in 1986, the Atmospheric Radiation Measurement (ARM) Intensive Observation Period (IOP) in 2000, and the Kwajalein Experiment (KWAJEX) and Large Scale Biosphere-Atmosphere Experiment (LBA) [both Tropical Rainfall Measuring Mission (TRMM) field campaigns] in 1999. They concluded that the evolution of the particle size distribution was governed not only by aggregation at larger particle sizes, but also at smaller particle sizes by depositional growth and by the breakup of larger particles. As further confirmation of these hypotheses, Westbrook et al. (2007) used Doppler radar measurements of several fairly steady-state cirrus cases over the Chilbolton Observatory in England and came to the similar conclusion that in the cold, well-developed cirrus clouds they examined, crystal formation and depositional growth appeared to be an important factor in the average mass of particles near cloud top, that aggregational growth appeared to be the dominant growth process through the depth of the clouds, and that evaporative processes leading to smaller particles occurred around cloud base.

Data from a number of spiral descents have furthermore been used to develop microphysical parameterizations for cirrus clouds. Heymsfield et al. (2002) used data from the SPEC CPI and HVPS as well as from the PMS 2DC to look at spiral flights from the TRMM Texas-Florida Underflights (TEFLUN-A and -B), LBA, and KWAJEX campaigns. They developed parameterizations for cirrus PSDs in terms of parametric gamma and exponential distributions, based on temperature, and explored relationships between their fit PSD parameters. As with the other studies that have already been mentioned, they determined that PSDs broadened with depth in cloud, probably due to size sorting and to aggregation. Heymsfield (2003a) and Heymsfield (2003b) used the same parametric fitting approach on ice PSD observations made in Lagrangian spirals and with balloon-borne replicators, made during the ARM IOP, KWAJEX, FIRE I, and FIRE II. The parameterized PSDs were used to study the variation of ice particle size spectra through the depths of clouds, as well as median mass diameters and sedimentation velocities of ice particle size spectra and the relationships of these properties one to another. These sorts of studies can provide microphysical parameterizations of the properties and evolution of ice particle size spectra through the depths of cirrus clouds.

The purpose of this work is the beginning of a global climatology of cirrus cloud PSDs and associated meteorological variables that can be easily added upon as well as a framework for constructing and analyzing it. This dataset forms a statistical set, not a microphysical set; i.e., Lagrangian spirals are not had wherewith to study PSD evolution, nor is (in most cases) information on where in a cloud a sample was taken. However, as hinted at in the literature review above, we are able to draw broader, statistically based conclusions about cirrus cloud microphysics based on the wide-ranging datasets we do have. This chapter proceeds with an exposition and discussion of the data used throughout this dissertation. The fitting of measured PSDs with parametric functions, the statistics of the fit parameters, and the occurrence of bimodality within cirrus PSDs are then discussed. The final section of this chapter describes an inspection of the properties of cirrus PSDs as they relate to meteorological variables.

Data

For this study, PSD data from the two-dimensional stereo (2D-S) probe (Lawson et al., 2006b) are used. The 2D-S probe images ice crystal cross-sections via two orthogonal lasers that illuminate two corresponding linear arrays of 128 photodiodes. Particle size distributions, as well as distributions of cross-sectional area and estimated mass, are reported every second in bins ranging in size from 5 μm up to about 3 millimeters. This instrument features a larger sample volume and improvements in resolution and time response in comparison with older particle imaging probes as well as shattered-particle rejection in the data product based on particle interarrival time (Field et al., 2006; Lawson et al, 2006b; Baker et al., 2009; Jensen et al., 2009).

To be sure, the uncertainty in 2D-S measurements for the smallest ice crystals is unknown (Jensen et al., 2009; Lawson, 2011), and at larger particle sizes, instruments such as the 2DP or the HVPS probably provide more reliable data (Baker et al., 2009). Furthermore, in a nod to the bigger microphysical picture, Wiscombe (2005) wrote about “fantasy drop distributions”: distributions that fit only one class of particles (such as cloud particles) and drop off too quickly to join up with other classes of particles (such as drizzle particles). Acknowledging that these are shortcomings pertinent to a broader analysis, the data are used here toward an inspection of cirrus cloud PSDs. To ensure that this is so, the data are filtered such that only averaged samples (explained below) taken above 6 km, at temperatures colder than –20°C, and with 2D-S estimated ice water contents (Baker and Lawson, 2006b) below 1 gm^{-3} are used in this analysis.

Ancillary measurements used in this study include temperature, water vapor mixing ratio, and bulk ice water content. Temperature was measured during MACPEx and TC^4 using the NASA Ames Meteorological Measurement System (MMS). During SPartICus, temperature was measured using a Rosemount temperature transmitter.

Water vapor mixing ratio measurements from the Diode Laser Hygrometer (DLH) (Weinstock et al., 1994; Diskin et al., 2002) were used for SPartICus and for TC^4. However, only a partial DLH dataset exists for MACPEx, and so for this campaign data from the Harvard Water Vapor (HWV) probe (Weinstock et al., 2009) are used instead. For the relatively small portion of time during MACPEx where measurements from the HWV and the DLH overlap, the relationship between the two instruments was investigated. The left panel of Fig. 2.1 shows the scatter between RHi derived from the HWV and from the DLH, along with a one-to-one line (red) and a curve resulting from a quartic fit between the datasets (gold). The right panel shows the result of predicting the DLH-derived RHi from the HWV-derived RHi. The scatter is not removed, but the nonlinear bias is alleviated. The RMS error in the fit is 5.18% (the percent referring to RHi), and the mean DLH-derived RHi is 100.9%—two orders of magnitude higher than the RMS error. The regression terms were then applied to the entire HWV dataset for

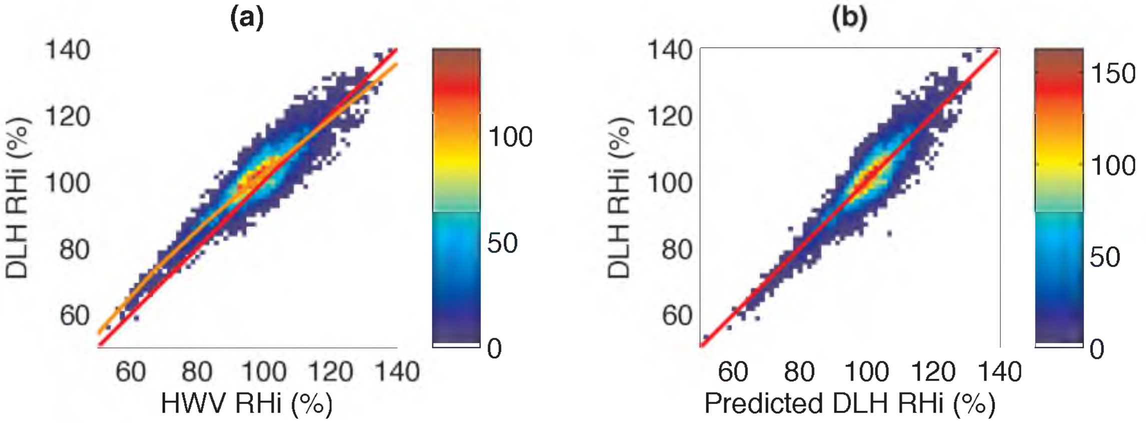

Fig. 2.1: Comparison of DLH- and HWV-derived RHi during MACPEx. (a) Scatter of DLH-derived RHi vs HWV-derived RHi for that portion of MACPEx for which there is overlapping data. The gold curve is a quartic fit between the two datasets. (b) Scatter of DLH-derived RHi vs. predicted (from the HWV) DLH-derived RHi for that portion of MACPEx for which there is overlapping data.

MACPEx.

Vertical velocity was measured using the MMS system during TC^4 and MACPEx and using the Aventech Research Inc. Aircraft-Integrated Meteorological Measurement System (AIMMS-20) during SPartICus. However, these measurements are not taken at face value. Straight, level flight legs are identified from flight navigational data by an automated process that makes use of numerical derivatives of filtered values of aircraft altitude and heading. The average vertical velocity for each flight leg is subtracted from the data to obtain the vertical turbulence for that flight leg. Only values from straight, level flight legs are used (Comstock et al., 2012).

Bulk ice water content measurements are available for MACPEx from the Closed-path tunable diode Laser Hygrometer (CLH) probe (Davis et al., 2007). The basic idea behind the operation of the CLH is that all condensed water that enters the probe is evaporated so that a measurement of total water vapor can be made. The condensed part of total water measured by the CLH is estimated using concurrent PSDs measured by the National Center for Atmospheric Research (NCAR) Video Image Particle Sampler (VIPS) probe: an estimate of condensed water mass is made from the measured PSDs and then subtracted from the measured total water mass.

Parametric Functional Fitting of Binned PSD Data

A number of different parametric distributions have been used for fitting ice PSDs, including exponential and gamma distributions (e.g., Heymsfield et al., 2002), modified gamma distributions (e.g., Delanoe et al., 2005), and lognormal distributions (e.g., Tian et al., 2010). While Tian et al. (2010) found that the lognormal distribution worked best for unimodal PSD fits, only a handful of hours of TC^4 data from tropical, convectively generated cirrus were used in that study, and, as stated in the conclusions of that paper, a more expansive study would be required to determine whether that particular conclusion were universally true. Furthermore, the data used in that study was taken using a 2D Cloud Imaging Probe (CIP) and a Precipitation Imaging Probe (PIP), which when compared with measurements from the 2D-S were only deemed reliable down to 100 μm. Additionally, Tian et al. (2010) found that while the lognormal distribution parameters are more naturally linked to physical properties of cirrus PSDs than are those of the gamma distribution, use of the gamma distribution allows for PSD description using only two parameters, as opposed to three for the lognormal distribution (this point will be elaborated upon later in this paper). In this study, a variant of the gamma distribution is used, though at least part of the fundamental qualitative conclusions of this paper would likely remain the same regardless of what parametric description of the PSDs were used.

The PSDs measured by the 2D-S probe were fit with both unimodal and bimodal parametric gamma distributions. The unimodal distribution is

$$n(D) = N_0 \left(\frac{D}{D_0} \right)^{\alpha} \exp\left(-\frac{D}{D_0} \right), \tag{2.1}$$

where D is particle maximum dimension, D_0 is the scale parameter of the distribution, α is the shape parameter of the distribution, and N_0 is the intercept parameter, i.e., the location where the plotted PSD intercepts the ordinate. The bimodal distribution is simply a mixture of two unimodal distributions:

$$n(D) = N_{01}\left(\frac{D}{D_{01}}\right)^{\alpha_1}\exp\left(-\frac{D}{D_{01}}\right) + N_{02}\left(\frac{D}{D_{02}}\right)^{\alpha_2}\exp\left(-\frac{D}{D_{02}}\right). \tag{2.2}$$

The unimodal fits were performed via the method of moments. Both the method of moments and an expectation maximization algorithm (Moon, 1996) were used for the bimodal fits, the more accurate of those two fits [as determined by whether fit provided the smaller binned Anderson–Darling test statistic (Demortier, 1995)] being kept as the bimodal solution (see Appendices A and B for descriptions of the fitting algorithms, and see Appendix C for descriptions of statistical tests, including the binned Anderson–Darling test).

To determine whether a PSD was satisfactorily fit with the unimodal distribution or if the bimodal distribution were preferable, three different statistical tests were implemented: a maximum likelihood ratio test (Wilks, 2006); a one-sample Anderson–Darling test, adapted for use with binned data (Demortier, 1995); and a goodness-of-fit test based on sample moments, adapted from Gurland and Dahiya (1972). For all three tests, the total number of samples for each PSD was obtained by expressing total number concentrations in number of particles per liter.

The likelihood ratio test speaks to whether enough additional information about the PSD is given by a bimodal fit to warrant its use or whether the extra bimodal parameters are "nuisance parameters." Put differently, this test is based on numbers of particles in size bins—but not on the total number concentration (except for the fact that higher numbers of total samples cause a statistical test to reject smaller imperfections). If the smallest size bins dominate the total number concentration but the bimodal fit is not significantly more likely (given the distribution of samples among the size bins) than the unimodal fit, then the test considers the extra information afforded by the bimodal fit to be unnecessary and the unimodal fit is chosen instead.

The binned, one-sample Anderson–Darling test compares the empirical cumulative distribution function (accumulated particle number density) of a measured PSD with the parametric cumulative distribution function of a unimodal fit. The size of this test statistic is a measure of the deviation of the analytical distribution from the measured distribution and is tested at the 1% significance level. This test speaks to the ability of the unimodal fit to recreate the shape of the empirical PSD.

The third goodness-of-fit test compares the first four noncentral sample moments to the corresponding noncentral population moments suggested by the unimodal fit. In this case, the test statistic's sampling distribution is the generalized chi-squared distribution (Jones, 1983) and is tested at the 1% significance level. This test speaks to the ability of the unimodal fit to reproduce the sample moments of the empirical PSD.

The caution with all of these tests is that higher numbers of samples increase the chance that smaller imperfections in the unimodal fit will cause it to be rejected. This is due to the fact that for each statistical test, and for a given binned PSD shape and corresponding fit, the respective test statistic increases with sample size (i.e., with total measured number concentration). Therefore, other things being equal, an increasing sample size means that the null hypothesis is increasingly likely to be rejected. For the maximum likelihood ratio test, this means that the bimodal fit is more apt to be deemed sufficiently likely to be used in favor of the unimodal fit. For the other two tests, this means that the unimodal fit is more apt to be rejected as nonefficacious.

Before the fits were performed, though, the measured PSDs were both truncated and temporally averaged in order to mitigate counting uncertainties. Though Field et al. (2005) used Poisson counting statistics to estimate counting errors within measured PSD bins, it is here assumed that the length of the eventual temporal average is sufficient to reduce appreciably the need for such error characterization (see, e.g., Gayet et al., 2002). To determine how many of the smallest size bins to truncate and for how many seconds to average in order to make the previous assumption valid, two simple exercises were performed using the MACPEx dataset. In the first exercise, 15-second temporal averages were performed along with truncating zero through three of the smallest size bins, and only the unimodal fits (according to the maximum likelihood ratio test) were kept. Figure 2.2 shows comparisons of distributions of measured and computed (from the fits) total particle concentrations. The difference in the number of samples of computed total particle concentrations between zero bins and one bin truncated is an order of magnitude higher than that between one bin and two bins truncated. This is due to frequent, extraordinarily high numbers of particles recorded in the smallest size bin that at times cause a PSD to be flagged as bimodal by the maximum likelihood ratio test. As this effect lessens greatly after truncating only one bin, and as the computed and measured total particle concentrations are otherwise better matched using a single-bin truncation, the smallest size bin is ignored for all PSD fits (making the smallest size bin used 15–25 μm). Then, IWC was estimated from the fit distributions using the mass-dimensional relationship $m(D) = 0.0065D^{2.25}$ (m denotes mass, D denotes particle maximum dimension, and all units are cgs) given in Heymsfield (2003a) for midlatitude cirrus. The distribution of IWC computed thus is shown in Fig. 2.3, along with distributions of IWC estimated directly from the 2D-S data using mass-projected area relationships (Baker and

Total Number Concentration

(a) 0 bins

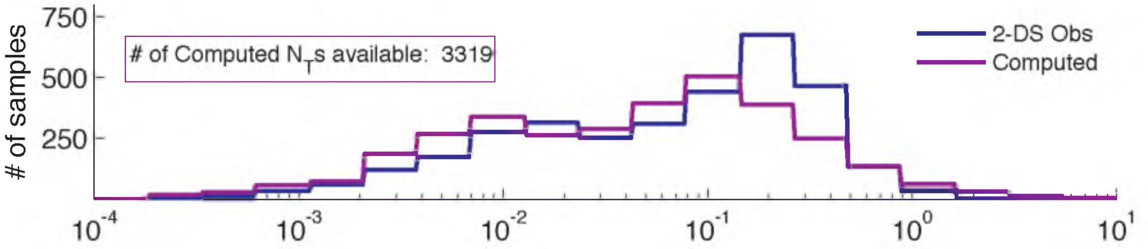

(b) 1 bin

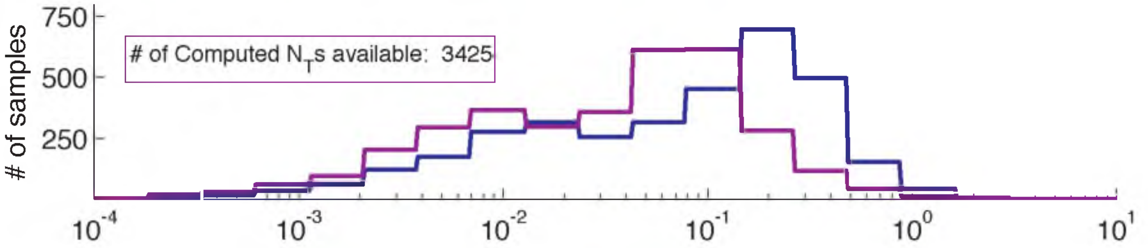

(c) 2 bins

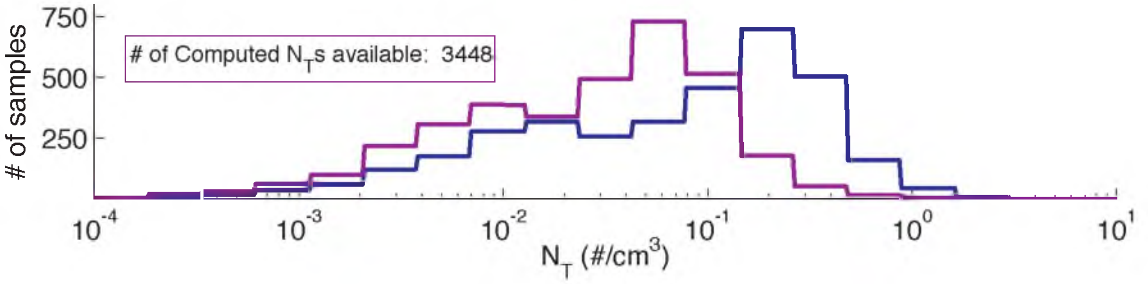

Fig. 2.2: Comparisons of computed and measured total number concentration for 15-second PSD averages and for truncation of none through the first three PSD size bins.

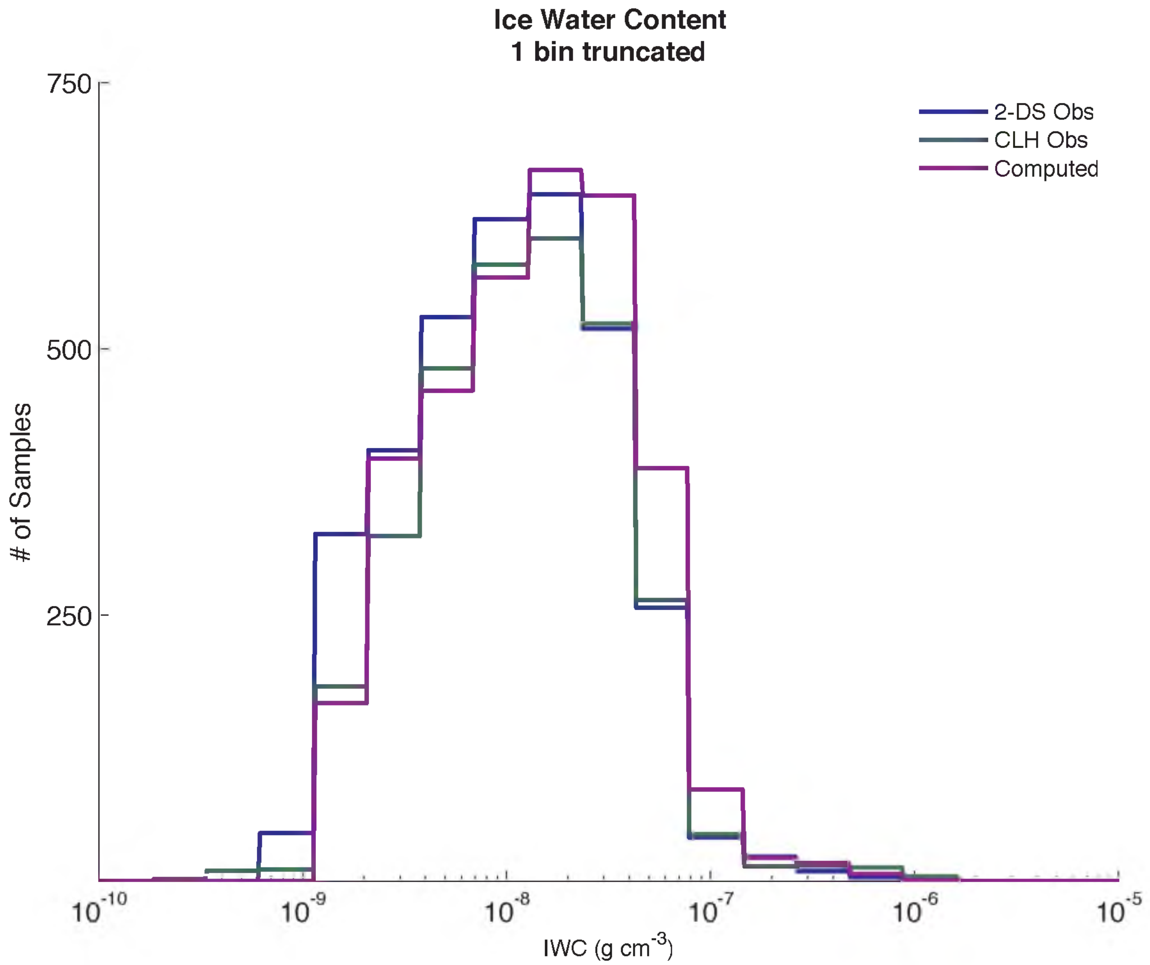

Fig. 2.3: Distributions of IWC from MACPEx provided as part of the 2D-S data product (blue), provided as part of the CLH data product (green), and computed from truncated 2D-S PSDs (the first bin) and the Heymsfield (2003a) mass-dimensional relationship.

Lawson, 2006b) and estimated from the CLH. The fits to the 2D-S data do a fair job, qualitatively, of reproducing ice water content measurements made by the CLH.

For the second exercise, temporal averages from 1 to 20 seconds were performed, truncating the first size bin and again keeping only the unimodal fits. The means and standard deviations of the resulting sets of fit parameters, each normalized by its maximum value, are shown as functions of length of temporal average in Fig. 2.4. The balance to strike in picking a temporal-average length is to acceptably smooth out Poisson counting uncertainties without losing physical information to an overlong average. Qualitatively, the statistics of the fit parameters begin to steady at around 15 seconds, so a 15-second temporal average was chosen. Using the data filters, temporal average, and bin truncation thus far described results in 12 387 PSD fits from MACPEx and SPartICus and 4 562 from TC^4. The MACPEx and SPartICus datasets are considered representative of midlatitude cirrus, and the TC^4 dataset is considered representative of tropical cirrus.

Figures 2.5 and 2.6 show examples of PSD fits. Figure 2.5 shows an A-Train overpass of a SPartICus flight on 3 February 2010: the top panel shows CloudSat reflectivity, masked by the CloudSat 2B-Geoprof-Lidar cloud mask (Mace et al., 2007; Marchand et al., 2008), with the path of the SPEC aircraft overlaid, and the lower panel shows the corresponding PSDs measured by the 2D-S probe aboard the aircraft. Three points along the flight path are labeled (a), (b), and (c). The measured and fit PSDs from these points are shown in the corresponding panels of Fig. 2.6, along with estimates of IWC (provided as part of the 2D-S data product), total number concentration (the zeroth moment of the truncated, binned PSDs), and effective radius (very simply, one-half the

(a) Normalized Mean

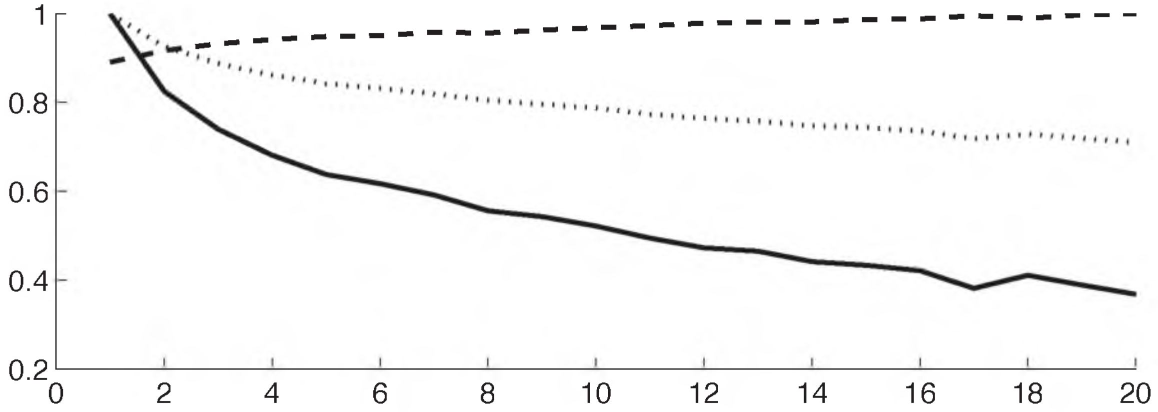

(b) Normalized Standard Deviation

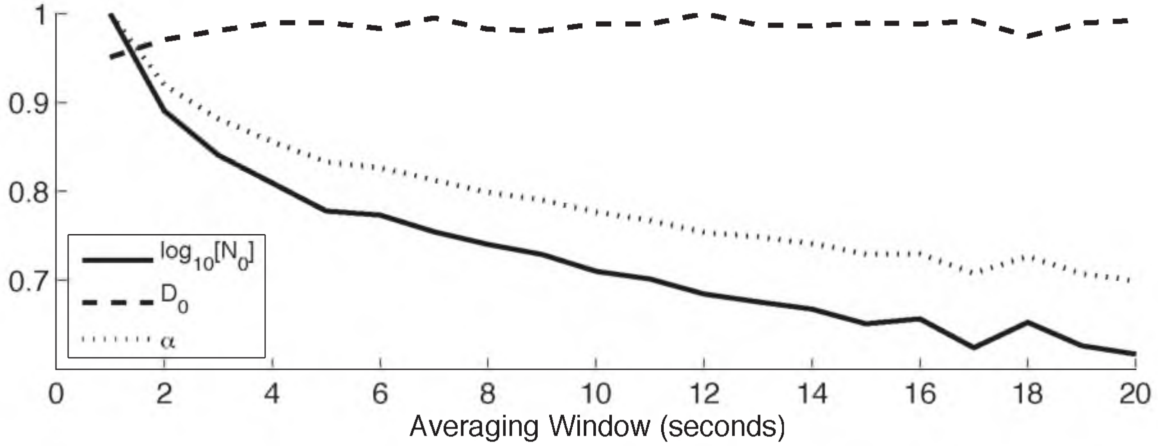

Fig. 2.4: Mean (a), Standard Deviation (b), and Skewness (c) of the computed distributions of fit PSD parameters (unimodal subset only) as a function of flight averaging window. Truncation of the first size bin was used.

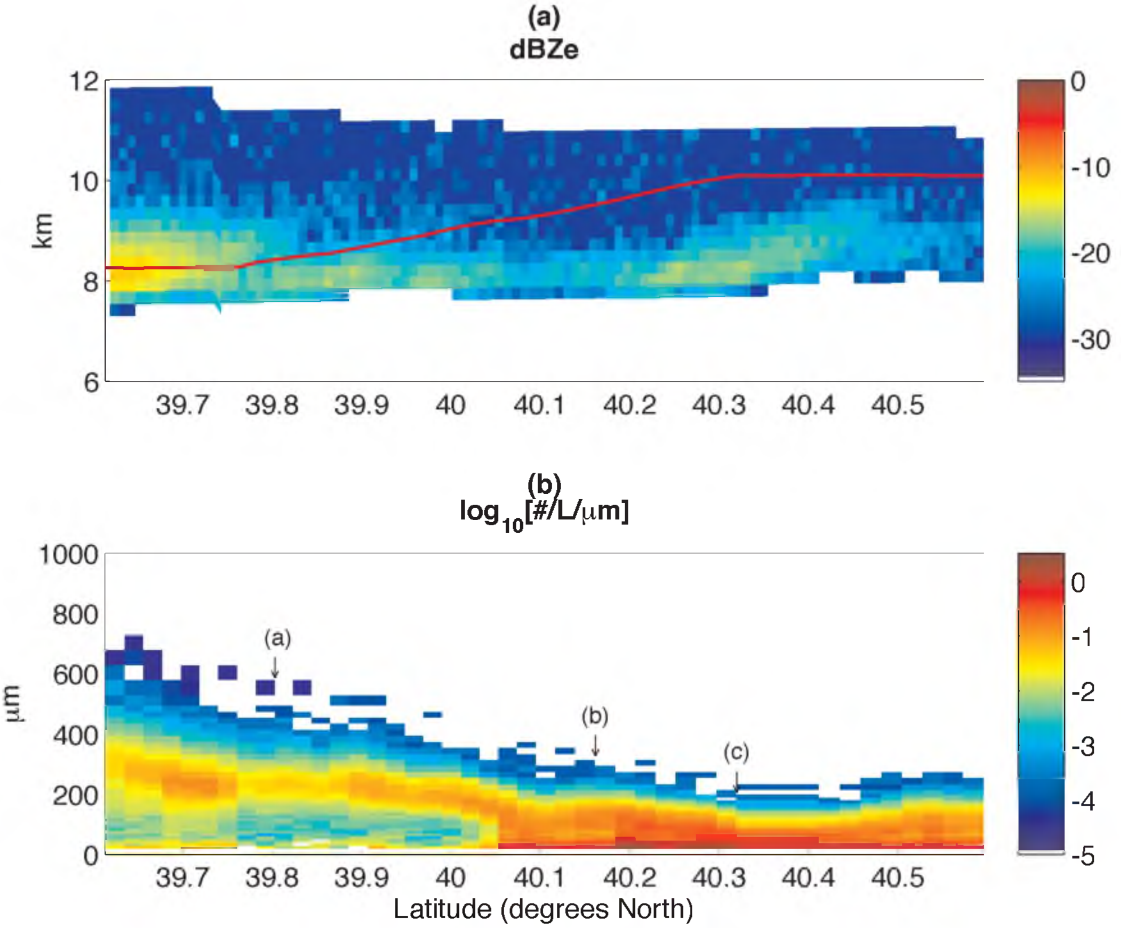

Fig. 2.5: An A-Train overpass of SPartICus on 3 February 2010 shown with measured PSDs. (a) CloudSat reflectivity (masked using the RL-Geoprof cloud mask), with aircraft trajectory in red. (b) Concurrently measured PSDs from the 2D-S. Individually marked PSDs are shown in Fig. 2.6.

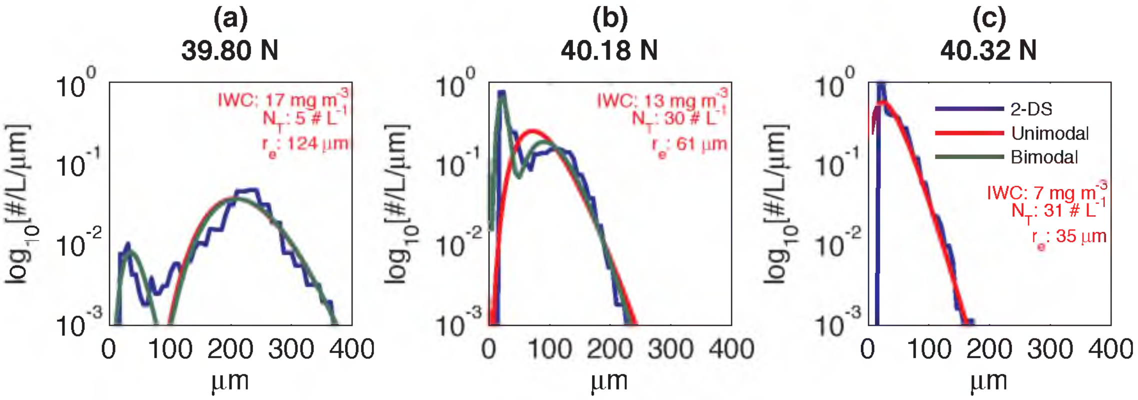

Fig. 2.6: Measured and fit PSDs, each panel a snapshot from the corresponding points labeled in Fig. 2.5. (a) and (b) were deemed bimodal, while (c) was deemed unimodal.

ratio of the third to the second moments of the truncated PSDs). In panel (c), the unimodal fit (shown in red) was deemed sufficient by the maximum likelihood ratio test. In panels (a) and (b), the PSDs were determined to be bimodal (by the maximum likelihood ratio test), which fits are shown by green curves [in panel (a), the unimodal fit is obscured by the large mode of the bimodal fit]. Noting the position within the cloud of the aircraft and the corresponding, measured PSDs, the aforementioned zones are fairly easily discerned within this cirrus cloud: near cloud base, radar reflectivity and effective radius are larger (before tapering off at cloud base), and PSDs contain (mostly) a small mode and a secondary mode of larger, precipitating particles. As the aircraft climbs in the cloud, size sorting and aggregation become less important, and cloud particles are increasingly concentrated in a single mode with smaller effective radius, lower IWC, and higher total number concentration.

Bimodality and the Statistics of Parameterized PSDs

As mentioned before, older cloud probes show high concentrations of very small particles all the time and, hence, very frequent PSD bimodality. Zhao et al. (2011), based on a remote sensing study that inspected the consistency of constantly high concentrations of small particles with radar and lidar measurements, maintained that while bimodality in cirrus PSDs does exist, it does not seem always to be present, nor do the numbers of very small particles seem always to be as high as older datasets suggest. However, whether bimodality is deemed to exist in a given PSD must depend on how bimodality is evaluated. For instance, the frequency of bimodality determined by any particular statistical test might be different from that determined by a qualitative evaluation—made, say, by eye—of each PSD. Indeed, the frequency of bimodality as determined by statistical test depends very much on what test is used. Bimodality, as determined by the maximum likelihood ratio test, occurs ~7% of the time in the midlatitude cirrus and ~3% of the time in tropical cirrus. According to the binned Anderson–Darling test, the unimodal fit is deemed insufficient ~60% of the time in the midlatitudes and ~57% of the time in the Tropics. Using the generalized chi-squared test of moments, the unimodal fit is deemed insufficient ~67% of the time in the midlatitudes and ~53% of the time in the Tropics. Though different numerically, these results qualitatively support the conclusion of Zhao et al. (2011). The reader may wonder, though, why such different results are produced by the different statistical tests. This is because each test, as explained before, examines a different aspect of a PSDs parametric fit. Thus, beyond the qualitative conclusion just made, which statistical test is therefore minded will depend upon what question is being asked of the data.

The likelihood ratio test turns out to be the most forgiving to the unimodal fits, as seen in the previous paragraph. Rather than simply reject a unimodal fit based on its shape or on its ability to reproduce sample moments, this test directly compares bimodal and unimodal fits via their relative likelihood. Thus, if the unimodal fit fails to capture the sample moments or PSD shape sufficiently well (based on the other two tests) but still is "likely enough" when compared with the bimodal fit, the likelihood ratio test accepts the unimodal fit. (How this scenario is possible will be seen shortly.)

However, if bimodality is to be judged strictly on the basis of the reproduction of sample PSD moments, the generalized chi-squared test was designed to select the combination of unimodal and bimodal PSD fits to best produce this overall effect—even for the zeroth moment, which is not incorporated into the test. The unimodal fits produce zeroth moments with a high degree of scatter and a weak relationship with the zeroth moments computed directly from the binned data. However, this scatter is greatly alleviated and a biased relationship emerges if, instead of computing the zeroth moment, a "truncated" zeroth moment is computed: total number concentration is computed from the fits with integration beginning at 15 μm. (Formulae for computing the truncated zeroth moments are given in Appendix D.) Figure 2.7 shows scatter plots of the zeroth through the fourth parameterized versus sample noncentral moments for the midlatitude PSDs, where the zeroth moments computed from fits are truncated, as just described. Figure 2.8 shows the same, but for the Tropics. Apparently, this test commits to a tradeoff: a PSD flagged thereby as more properly unimodal or bimodal does not necessarily result in a unimodal or bimodal parametric fit that gives the best reproduction of each of the zeroth through the fourth sample moments, but in a parametric fit that attempts to give overall the best reproduction of the zeroth through the fourth sample moments. It should be noted, though, that above the second moment, picking a unimodal or bimodal fit based on the generalized chi-squared test results in an increasing low bias in a substantial fraction of the computed parametric moments with respect to their corresponding sample moments. There are then two relevant observations to make from Figs. 2.7 and 2.8.

First, as it turns out, not all of the sample moments of the measured PSDs are of equal certainty because the 2D-S instrument does not make simple counts of particles, but rather measures the occulted area of particles passing through its sample volume. Figure 2.9 shows an example of the images produced by the 2D-S. The zeroth moment is perhaps the least certain of the sample moments due to remaining uncertainties regarding

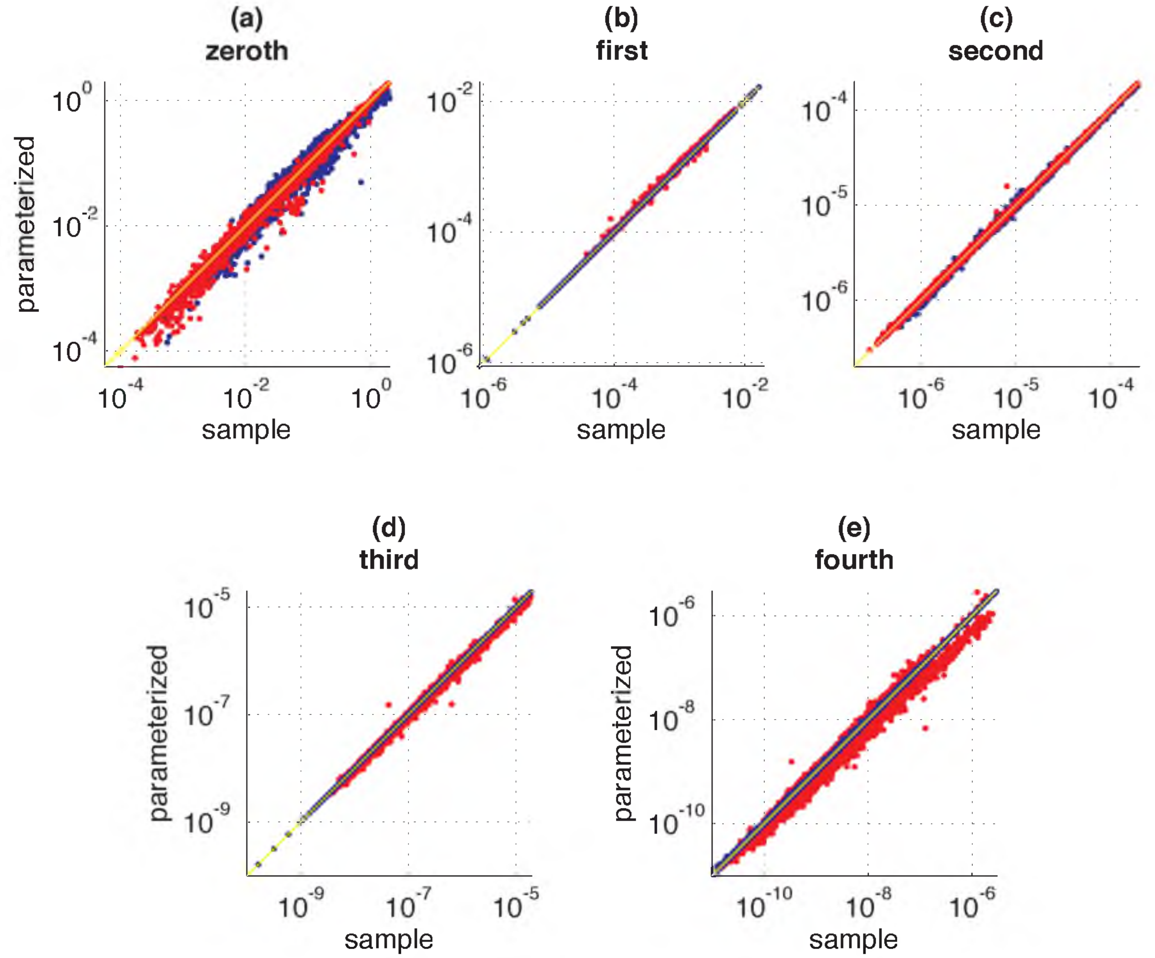

Fig. 2.7: Scatter of the (truncated) zeroth through the fourth parameterized moments vs. the zeroth through the fourth sample moments (in log-space) for the midlatitudes. The blue points indicate where the unimodal fits were used in all cases. The red points indicate where unimodal and bimodal fits were selected based upon the results of the generalized chi-squared test on moments. One-to-one is marked by the yellow line.

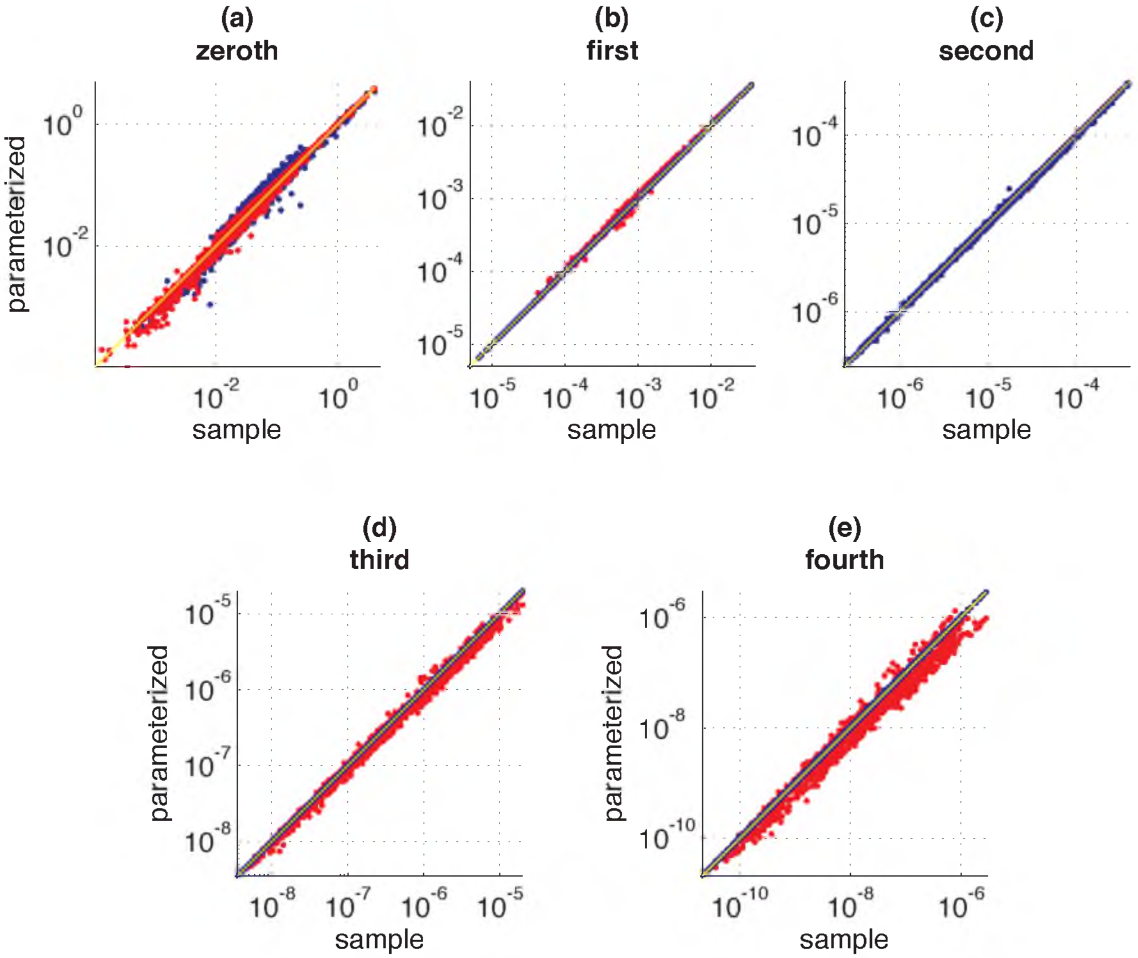

Fig. 2.8: Scatter of the (truncated) zeroth through the fourth parameterized moments vs. the zeroth through the fourth sample moments (in log-space) for the Tropics. The blue points indicate where the unimodal fits were used in all cases. The red points indicate where unimodal and bimodal fits were selected based upon the results of the generalized chi-squared test on moments. One-to-one is marked by the yellow line.

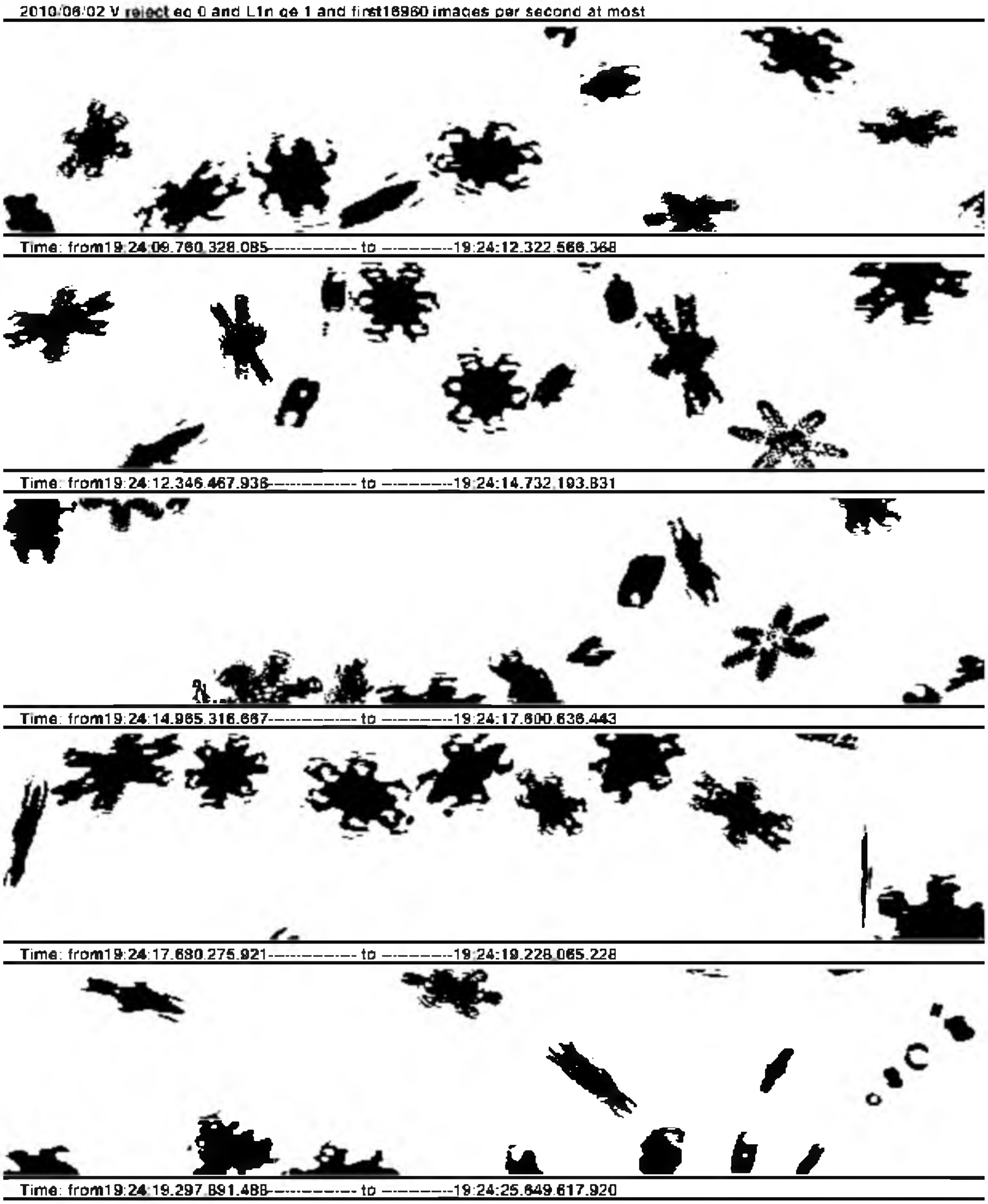

Fig. 2.9: An image of occulted ice crystals made by the 2D-S during SPartICus.

particle shattering (mitigated though it is by recent technological and software advances) as well as to uncertainties in the image processing techniques that infer counts and sizes of particles from occulted instrument pixels. It is for this cause that the selection of either a unimodal or a bimodal parametric PSD based on the generalized chi-squared test causes a growing degradation of reproduced sample moments as the order of the moment increases. Specifically, the expectation-maximization algorithm (which produces a bimodal fit chosen more often than the method of moments fit) is couched in the maximum likelihood estimation method, and it therefore does an admirable job of capturing the shape of bimodality in the measured PSDs (recall Fig. 2.6). Matching what is likely the least certain moment, though, does not ensure that higher-order moments (which are closer to what the 2D-S directly measures) are always well matched. Thus, a bimodal fit may be deemed not sufficiently more likely than a unimodal fit by the maximum likelihood test while the unimodal fit is rejected by either of the other tests. As instrument technology and image processing capabilities continue to improve, it is expected that this discrepancy will be alleviated.

The second observation to make from Figs. 2.7 and 2.8 is that the unimodal fits provide the best overall statistical replication of the first through the fourth PSD sample moments. This is hardly a surprise, given that the first, third, and fifth sample moments are used to make the unimodal fits (see Appendix A); however, ample reproduction of sample moments does not necessarily mean that the unimodal parametric fits have captured the shape of the measured PSDs—only their sample moments. It is true, though, that nearly all the time the second mode is deemed a nuisance by the maximum likelihood ratio test, and for remote sensing applications, fidelity in reproducing the first through the fourth moments, but not necessarily the zeroth moment, is of key importance. Therefore, for an application such as the remote sensing of cirrus bulk properties, the whole dataset may be satisfactorily described as unimodal. In this case, apart from using a truncated zeroth moment as described above, a functional relationship to compute the expected zeroth moment of a PSD given a higher-order moment [such as given in Field et al. (2005)] can be useful. Figure 2.10 shows the zeroth sample moment of the measured PSDs as a function of the first sample moment, both for the midlatitudes (Fig. 2.10a) and for the Tropics (Fig. 2.10b). The functional relationships (in cgs units) are, respectively,

$$M_0 = 463.86 M_1^{1.19} , \tag{2.3}$$

$$M_0 = 63.80 M_1^{0.96} , \tag{2.4}$$

where M_0 is the zeroth sample moment and M_1 is the first sample moment. Though a single power law has been fit to the midlatitude data, Fig. 2.10(a) clearly shows a bimodal relationship between the two moments. Both of these modes exist in both the SPartICus and the MACPEx datasets, and neither mode corresponds to the subset of bimodal or unimodal fits determined by either the binned Anderson–Darling or generalized chi-squared tests (not shown). Using an expectation-maximization routine to decompose the two modes in Fig. 2.10(a) and inspect the meteorological variables concomitant with each mode remains an unfinished work.

The probability density functions (pdfs) of the gamma distribution parameters resulting from fitting the entire dataset as unimodal are shown in Fig. 2.11. Given that the shape parameter must belong to the set $\{\alpha : \alpha > -1\}$ (in order for the zeroth moment

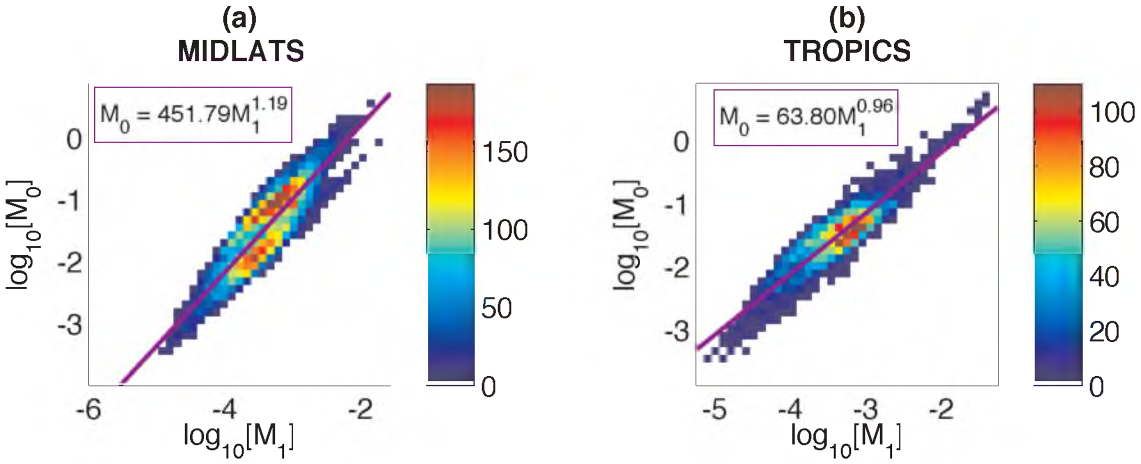

Fig. 2.10: The zeroth sample moment of the measured PSDs as a function of the first sample moment.

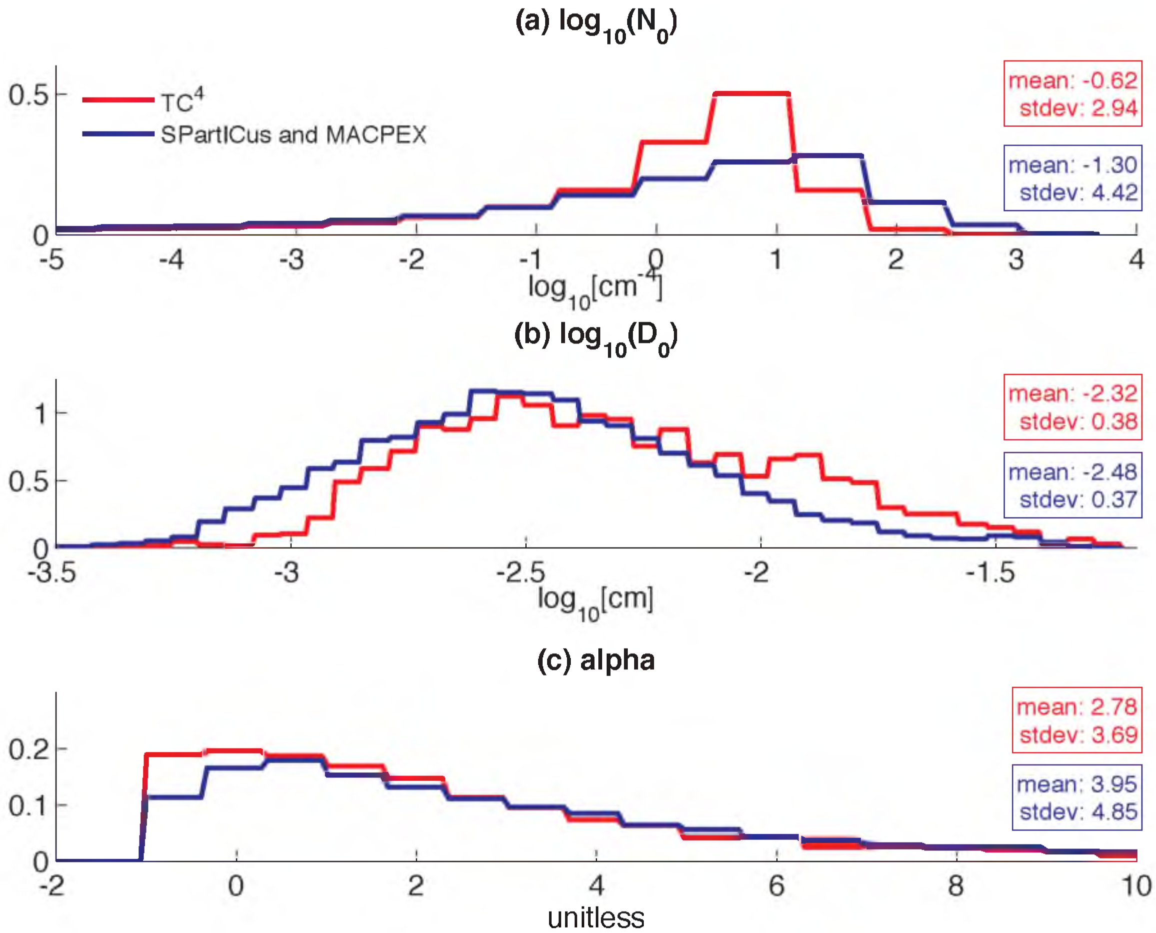

Fig. 2.11: Marginal distributions for unimodally fit PSD parameters.

of the parametric PSD to exist), it is clear that its marginal distribution cannot be normal, and while the marginal distribution of the log-scale parameter can be reasonably modeled as normal (there are, however, two distinct modes in the marginal distribution of the tropical log-scale parameter), the marginal distribution of $\log_{10}\left[N_0\right]$ is noticeably skewed. The pdf of $\log_{10}\left[N_0\right]$ is parameterized as a log-normal distribution that has been reversed and shifted (Oppenheim et al., 1997):

$$\Pr\left(x = \log_{10}\left[N_0\right]\right) = p(x) = \frac{1}{(4-x)\sqrt{2\pi\sigma^2}} \exp\left[-\frac{\left(\ln[4-x]-\mu\right)^2}{2\sigma^2}\right], \qquad (2.5)$$

with a mathematical support of $x \in (-\infty,4)$. The estimators for the parameters (from the method of moments and where the operator E[…] returns the expected value of its argument and where the operator var(…) returns the variance of its argument) are

$$\mu = 2\ln\left\{4-\mathrm{E}\left[\log_{10}(N_0)\right]\right\} - \frac{1}{2}\ln\left(\mathrm{var}\left[\log_{10}(N_0)\right] + \left\{4-\mathrm{E}\left[\log_{10}(N_0)\right]\right\}^2\right), \qquad (2.6)$$

$$\sigma = \sqrt{\ln\left(\mathrm{var}\left[\log_{10}(N_0)\right] + \left\{4-\mathrm{E}\left[\log_{10}(N_0)\right]\right\}^2\right) - 2\ln\left\{4-\mathrm{E}\left[\log_{10}(N_0)\right]\right\}}. \qquad (2.7)$$

The pdf of the log-scale parameter is modeled as normal, with an alternate parameterization of $\log_{10}\left[D_0\right]$ in the Tropics as a mixture of two normal distributions (whose parameters are estimated according to the expectation-maximization algorithm):

$$\Pr\left(x=\log_{10}\left[D_0\right]\right)=\frac{\eta}{\sqrt{2\pi\sigma_1^2}}\exp\left[-\frac{\left(x-\mu_1\right)^2}{2\sigma_1^2}\right]+\frac{1-\eta}{\sqrt{2\pi\sigma_2^2}}\exp\left[-\frac{\left(x-\mu_2\right)^2}{2\sigma_2^2}\right]. \tag{2.8}$$

The pdf of the shape parameter is modeled as a log-normal distribution, shifted one place to the left:

$$\Pr\left(x=\alpha\right)=\frac{1}{\left(x+1\right)\sqrt{2\pi\sigma^2}}\exp\left[-\frac{\left(\ln\left[x+1\right]-\mu\right)^2}{2\sigma^2}\right]. \tag{2.9}$$

with a mathematical support of $x\in\left(-1,\infty\right)$. The estimators for the parameters are

$$\mu=2\ln\left[\mathrm{E}\left(\alpha\right)+1\right]-\frac{1}{2}\ln\left\{\mathrm{var}\left(\alpha\right)+\left[\mathrm{E}\left(\alpha\right)+1\right]^2\right\},\text{ and} \tag{2.10}$$

$$\sigma=\sqrt{\ln\left\{\mathrm{var}\left(\alpha\right)+\left[\mathrm{E}\left(\alpha\right)+1\right]^2\right\}-2\ln\left[\mathrm{E}\left(\alpha\right)+1\right]}. \tag{2.11}$$

The estimated pdfs, for each parameter and for each region, are given in Table 2.1.

The covariance and correlation matrices computed from the distributions of unimodal PSD parameters are given in Table 2.2. Note that the covariance matrices are not diagonal, as is often assumed in remote sensing retrievals of cirrus PSDs. Note also the high degree of correlation between $\log_{10}[N_0]$ and the shape parameter. This correlation suggests a parameterization of $\log_{10}[N_0]$ based on the parameter α or vice versa, and it is for this reason that fitting PSDs with unimodal gamma distributions requires only two free distribution parameters, as mentioned in the previous section.

Table 2.1

Parameters for distributions of unimodal fit parameters (see Eqs. 2.5–2.11).

<table>
<tr><th></th><th colspan="2">MIDLATITUDES</th><th colspan="2">TROPICS</th></tr>
<tr><td rowspan="2">$\log_{10}\left[N_0\right]$</td><td colspan="2">$\mu = 1.4047$</td><td colspan="2">$\mu = 1.3617$</td></tr>
<tr><td colspan="2">$\sigma = 0.7263$</td><td colspan="2">$\sigma = 0.5821$</td></tr>
<tr><td rowspan="2">$\log_{10}\left[D_0\right]$</td><td colspan="2">$\mu = -2.4842$</td><td colspan="2">$\mu = -2.3191$</td></tr>
<tr><td colspan="2">$\sigma = 0.3690$</td><td colspan="2">$\sigma = 0.3792$</td></tr>
<tr><td rowspan="2">α</td><td colspan="2">$\mu = 1.2637$</td><td colspan="2">$\mu = 0.9936$</td></tr>
<tr><td colspan="2">$\sigma = 0.8204$</td><td colspan="2">$\sigma = 0.8184$</td></tr>
<tr><td rowspan="2">tropical, bimodal $\log_{10}\left[D_0\right]$</td><td rowspan="2">$\eta = 0.6751$</td><td colspan="2">$\mu_1 = -2.5345$</td><td>$\mu_2 = -1.8715$</td></tr>
<tr><td colspan="2">$\sigma_1 = 0.2247$</td><td>$\sigma_2 = 0.2020$</td></tr>
</table>

Table 2.2

Covariance and correlation matrices for unimodal fit parameters. The general form of the matrix is given in the top box. In the lower left columns are given covariance matrices for the midlatitude and tropical sets of unimodal fits. The right columns are the same, except that correlation matrices are shown.

<table>
<tr><th colspan="2">General Form of Covariance/Correlation Matrices</th></tr>
<tr><td colspan="2">$$R = \begin{bmatrix} \sigma^2_{\log_{10} N_0} & \sigma_{\log_{10} N_0, \log_{10} D_0} & \sigma_{\log_{10} N_0, \alpha} \\ \sigma_{\log_{10} N_0, \log_{10} D_0} & \sigma^2_{\log_{10} D_0} & \sigma_{\log_{10} D_0, \alpha} \\ \sigma_{\log_{10} N_0, \alpha} & \sigma_{\log_{10} D_0, \alpha} & \sigma^2_{\alpha} \end{bmatrix}$$</td></tr>
<tr><th colspan="2">MIDLATITUDES</th></tr>
<tr><td>$$\begin{bmatrix} 19.55 & 0.59 & -20.62 \\ 0.59 & 0.14 & -0.99 \\ -20.62 & -0.99 & 23.56 \end{bmatrix}$$</td><td>$$\begin{bmatrix} 1.00 & 0.36 & -0.96 \\ 0.36 & 1.00 & -0.55 \\ -0.96 & -0.55 & 1.00 \end{bmatrix}$$</td></tr>
<tr><th colspan="2">TROPICS</th></tr>
<tr><td>$$\begin{bmatrix} 8.62 & 0.46 & -9.99 \\ 0.46 & 0.14 & -0.95 \\ -9.99 & -0.95 & 13.59 \end{bmatrix}$$</td><td>$$\begin{bmatrix} 1.00 & 0.42 & -0.92 \\ 0.42 & 1.00 & -0.68 \\ -0.92 & -0.68 & 1.00 \end{bmatrix}$$</td></tr>
</table>

The PSD parameter pdfs resulting from those fits flagged as bimodal by the generalized chi-squared test are shown in Fig. 2.12. It is seen that these lend themselves even less to simple approximations as normal distributions: while the pdfs for the large-mode parameters show structure similar to that of the corresponding unimodal parameters, the number and shape parameters for the small mode show distinct bimodality in their pdfs. The corresponding covariance and correlation matrices are demonstrated in Tables 2.3 and 2.4. For both the midlatitudes and for the Tropics, there is again a high degree of correlation between $\log_{10}[N_0]$ and the shape parameter for each mode. It is also worth noting that the variances—and hence the uncertainties—of $\log_{10}[N_0]$ and of α for each mode are remarkably larger than those of their unimodal counterparts.

Relationships of Particle Size Distributions with Meteorological Variables

Comparisons between the distributions of measured temperature and RHi for the different datasets are shown in Figs. 2.13 and 2.14. In Fig. 2.13, SPartICus is compared with MACPEx, and in Fig. 2.14, the midlatitude datasets are compared with TC^4. Unlike for SPartICus, the pdf of measured temperatures during MACPEx is bimodal. This is probably due to MACPEx being the smaller dataset and having sampled a more sparse set of altitudes. The differences in distributions of RHi between those two datasets is marked: the RHi's measured during SPartICus belong to a relatively broad distribution with a fairly high average (~118%), while the distribution of RHi's measured during MACPEx is much narrower and has a much lower mean (~101%). Because SPartICus is a significantly larger dataset than MACPEx, it dominates the distributions of midlatitude

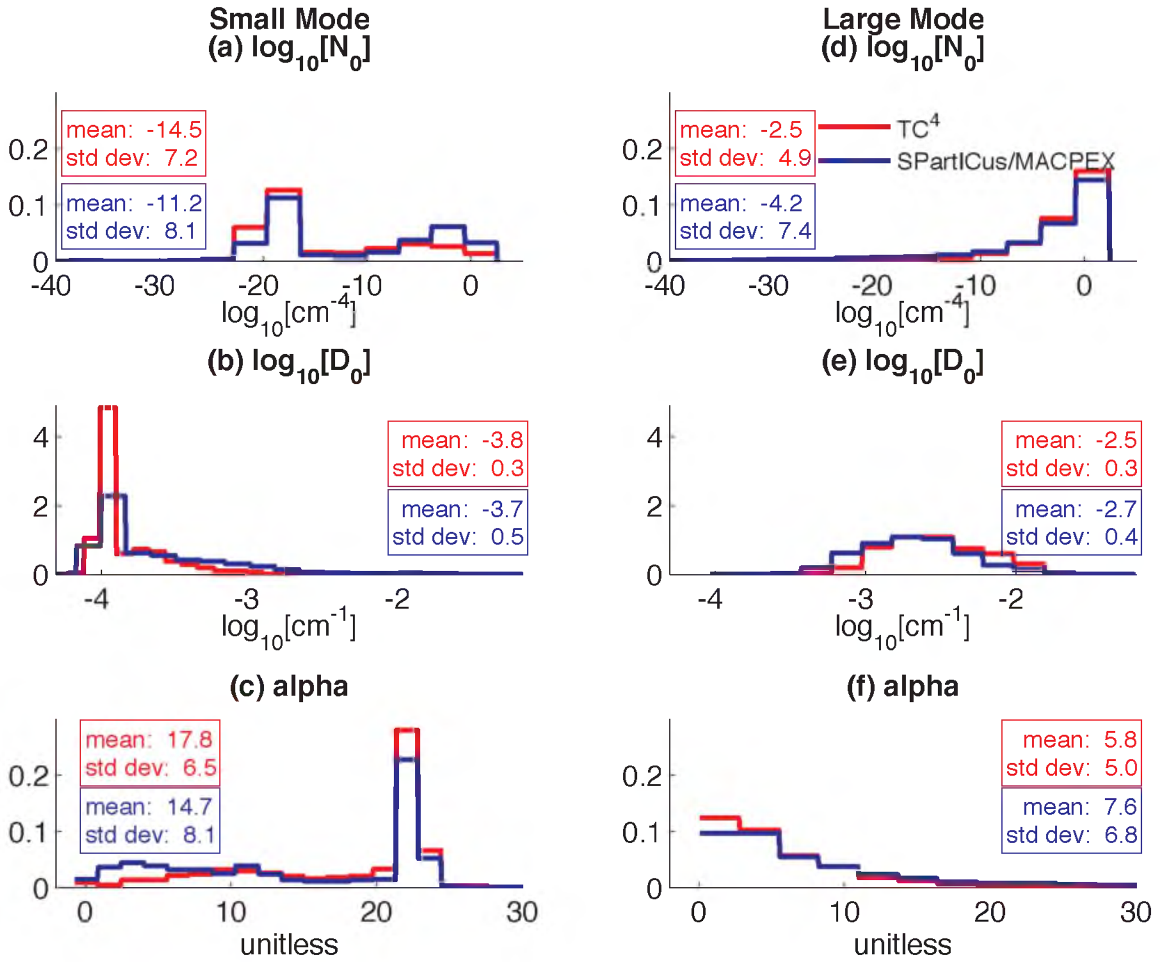

Fig. 2.12: Marginal distributions for the subset of bimodally fit PSD parameters.

Table 2.3

Form of covariance and correlation matrices for bimodal fit PSD parameters.

General Form of Covariance Matrices for Bimodal Fits	
$S = \begin{bmatrix} \sigma_1^2 & \sigma_{1,2} & \sigma_{1,3} & \sigma_{1,4} & \sigma_{1,5} & \sigma_{1,6} \\ \sigma_{1,2} & \sigma_2^2 & \sigma_{2,3} & \sigma_{2,4} & \sigma_{2,5} & \sigma_{2,6} \\ \sigma_{1,3} & \sigma_{2,3} & \sigma_3^2 & \sigma_{3,4} & \sigma_{3,5} & \sigma_{3,6} \\ \sigma_{1,4} & \sigma_{2,4} & \sigma_{3,4} & \sigma_4^2 & \sigma_{4,5} & \sigma_{4,6} \\ \sigma_{1,5} & \sigma_{2,5} & \sigma_{3,5} & \sigma_{4,5} & \sigma_5^2 & \sigma_{5,6} \\ \sigma_{1,6} & \sigma_{2,6} & \sigma_{3,6} & \sigma_{4,6} & \sigma_{5,6} & \sigma_6^2 \end{bmatrix}$	
Parameter Subscript (see matrix)	**Parameter Name (Eq. 2.2)**
1	$\log_{10}\left[N_{01}\right]$
2	$\log_{10}\left[D_{01}\right]$
3	α_1
4	$\log_{10}\left[N_{02}\right]$
5	$\log_{10}\left[D_{02}\right]$
6	α_2

Table 2.4

Covariance and correlation matrices for bimodal fit PSD parameters. (Bimodality determined by the generalized chi-squared test.) In the left column are given covariance and correlation matrices for the midlatitudes, and in the right column the same are given for the Tropics.

MIDLATITUDES						TROPICS					
Covariance Matrices											
65.61	3.24	–65.27	–33.61	–0.30	31.52	51.26	2.01	–46.31	–11.45	–0.11	11.33
3.24	0.22	–3.49	–2.45	–0.03	2.23	2.01	0.12	–1.98	–0.77	–0.01	0.73
–65.27	–3.49	66.42	37.79	0.33	–35.03	–46.31	–1.98	42.68	12.69	0.17	–12.46
–33.61	–2.45	37.79	55.14	1.35	–49.00	–11.45	–0.77	12.69	24.21	1.00	–24.22
–0.30	–0.03	0.33	1.35	0.12	–1.51	–0.11	–0.01	0.17	1.00	0.11	–1.23
31.52	2.23	–35.03	–49.00	–1.51	46.88	11.33	0.73	–12.46	–24.22	–1.23	25.39
Correlation Matrices											
1.00	0.85	–0.99	–0.56	–0.11	0.57	1.00	0.80	–0.99	–0.32	–0.05	0.31
0.85	1.00	–0.91	–0.70	–0.16	0.69	0.80	1.00	–0.87	–0.45	–0.13	0.42
–0.99	–0.91	1.00	0.62	0.12	–0.63	–0.99	–0.87	1.00	0.39	0.08	–0.38
–0.56	–0.70	0.62	1.00	0.52	–0.98	–0.32	–0.45	0.39	1.00	0.60	–0.98
–0.11	–0.16	0.12	0.52	1.00	–0.63	–0.05	–0.13	0.08	0.60	1.00	–0.72
0.57	0.69	–0.63	–0.98	–0.63	1.00	0.31	0.42	–0.38	–0.98	–0.72	1.00

(a) Temperature

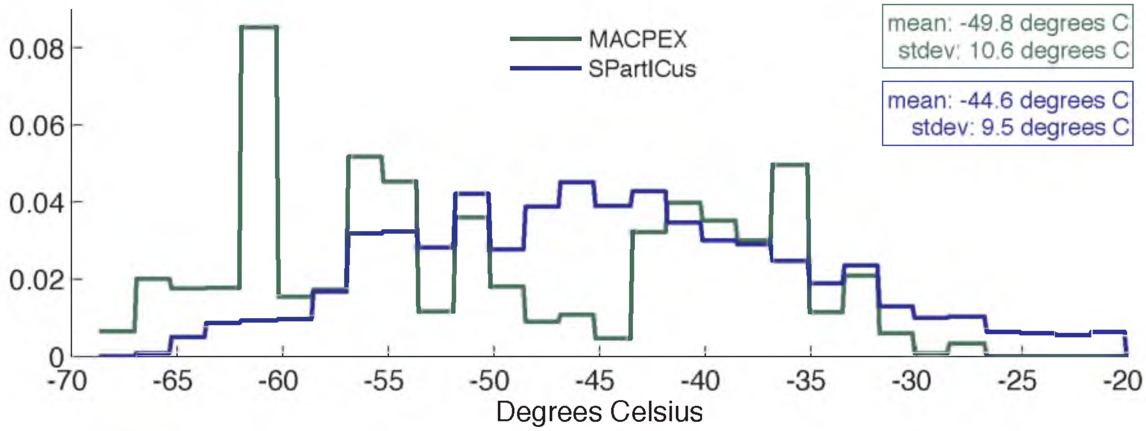

(b) RHi

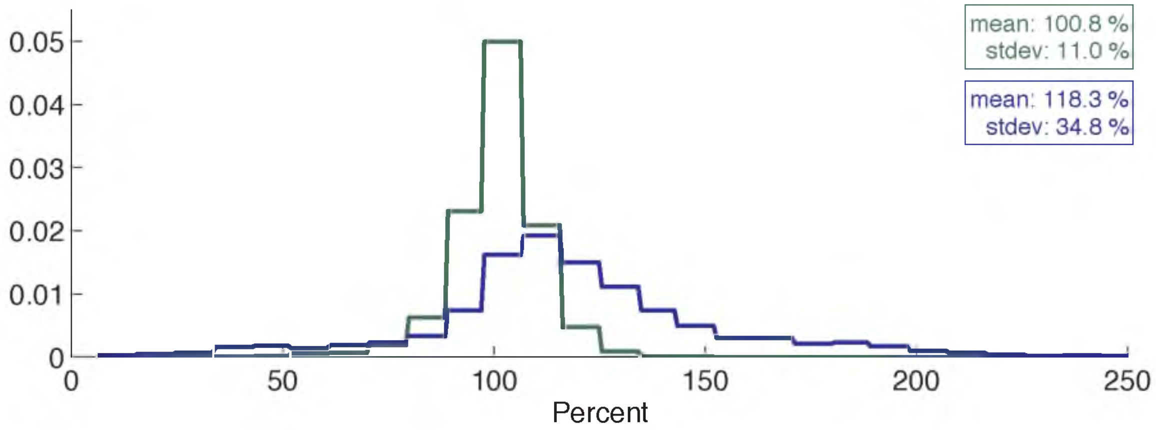

Fig. 2.13: Comparisons of temperature and RHi between SPartICus and MACPEx. (a) Distributions of measured temperature for MACPEx and for SPartICus. (b) Same as (a), but for measured RHi.

(a) Temperature

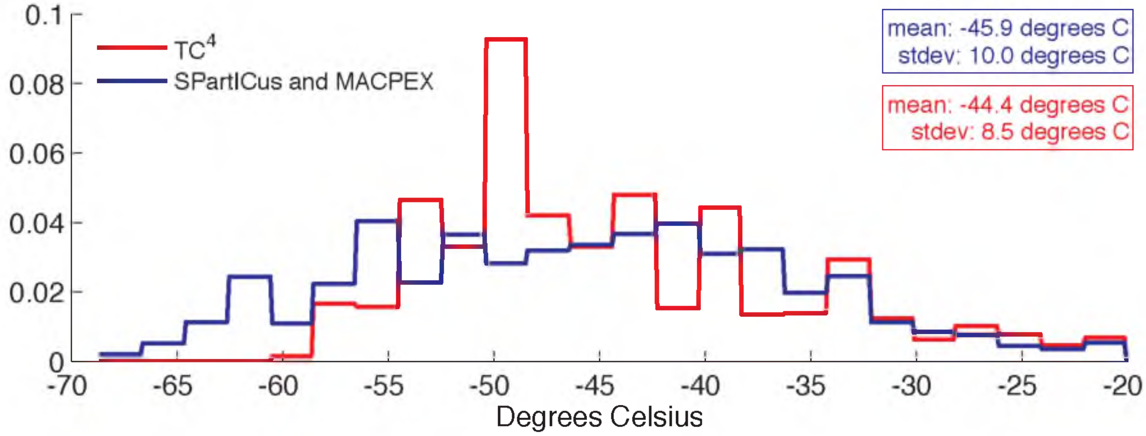

(b) RHi

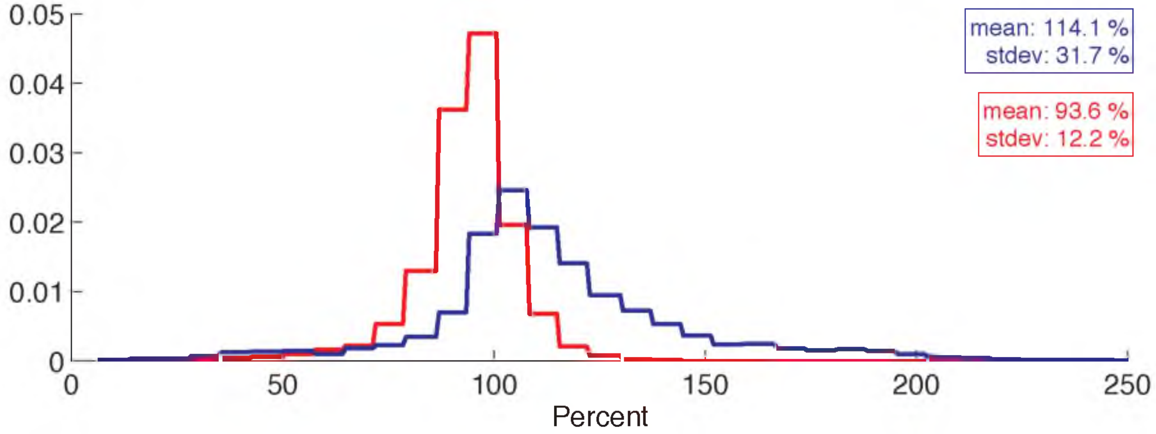

Fig. 2.14: As in Fig. 2.13, but the comparisons here are between the midlatitude data (MACPEx and SPartICus) and the tropical data (TC^4).

temperatures and RHis in Fig. 2.14. Comparing Figs. 2.13 and 2.14, though, one can see that the distributions of RHi for MACPEx and for TC^4 are more alike than are those for MACPEx and for SPartICus: they have approximately the same width, and while the average RHi for MACPEx is in between that for TC^4 and for SPartICus, it is closer to the average for TC^4 (~94%). This is no doubt due to the fact that MACPEx, due to its occurrence in April, focused more on convective cirrus (which form a major share of tropical cirrus) than did SPartICus, which occurred evenly from January into June.

Figure 2.15 shows distributions of temperature, RHi, total particle concentration, and IWC based upon modality as determined by a variant of the binned Anderson–Darling test. Specifically, as all that is being tested is deviation from the empirical cumulative distribution function, each PSD is assumed to have 100 samples so as to put them on equal footing for purposes of statistical testing (for higher numbers of samples, slighter imperfections will be rejected). This test was chosen for this purpose due to its preference for adhering to the shape of the measured PSD and resulted in the rejection of about 91% of the unimodal fits in the midlatitudes and about 85% of the unimodal fits in the Tropics. Looking at the figure, for both the midlatitudes and for the Tropics, bimodality tends to occur at warmer temperatures than does unimodality. The difference between the medians of the temperature distributions is statistically significant, as determined by a Mann–Whitney U-test. This result is consistent with the findings of Zhao et al. (2011). In both geographical areas as well, total number concentrations are quite a bit lower for those PSDs flagged as bimodal. This is in accord with earlier published findings that higher numbers of particles, on average, should be expected to occur in colder, higher parts of clouds where homogenous nucleation is more likely to be

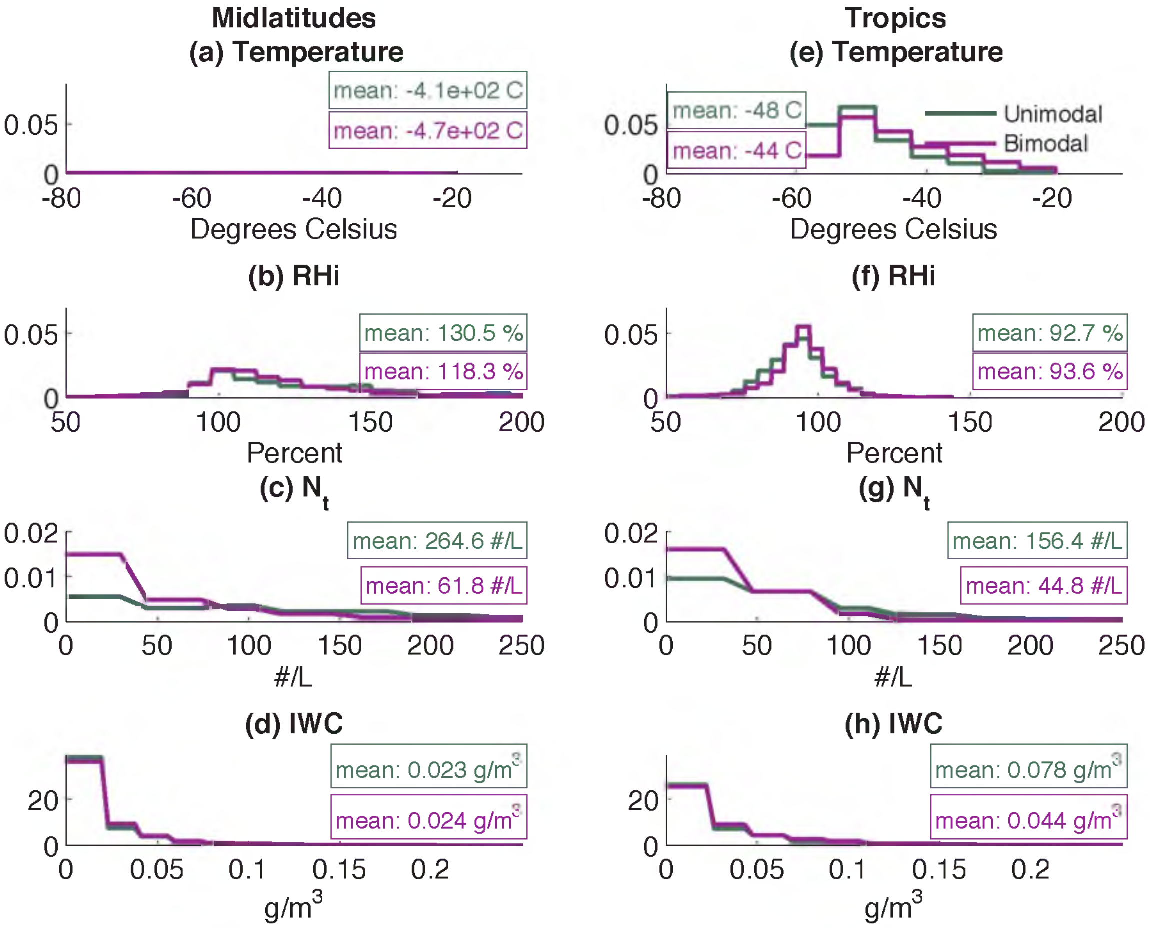

Fig 2.15: Comparisons of distributions of temperature, RHi, total number concentration, and IWC with those corresponding to the bimodal and unimodal fit subsets for the midlatitude data (a)–(d) and for the tropical data (e)–(h).

taking place and that in warmer, lower parts of clouds, where aggregation is a dominant force in shaping PSDs, aggregation tends to scavenge out smaller particles. No explanation is attempted here for the pdfs of IWC and RHi as they seem to be scrambled (in comparison to the pdfs for the other two quantities) by as-yet unidentified cloud processes. Figure 2.15 should buttress the argument in Lawson et al. (2006a) that the findings of Heymsfield and Miloshevich (1995) hold in the average.

Two-dimensional histograms of the unimodal fit parameters $\log_{10}[N_0]$ and $\log_{10}[D_0]$ versus temperature are shown in Fig. 2.16. There are fairly weak relationships between the two parameters and temperature in the midlatitudes, but not in the Tropics. Heymsfield (2002) found relationships between temperature and the scale parameter within individual clouds (see Fig. 12 therein), but in an overall, statistical sense, the relationship is less distinct, as would be expected from combining the relationships from each cloud in Fig. 12 of Heymsfield (2002). No relationship is found between these parameters, RHi, and vertical velocity turbulence (not shown), though it is possible that the 15-second temporal average has filtered information out of the RHi and vertical velocity measurements.

One difficulty pointed out by Field et al. (2005) with parametric distributions such as the gamma distribution is that the parameters vary over many orders of magnitude and do not, on their own, have any physical meaning. (These are two reasons given in that paper for choosing the normalization approach to PSDs, and the former is a major purpose for using the logarithms of N_0 and D_0 here.) Functional combinations of the fit parameters, however, do have physical meaning. For instance, for $\alpha > 0$, a parametric distribution's mode is located at

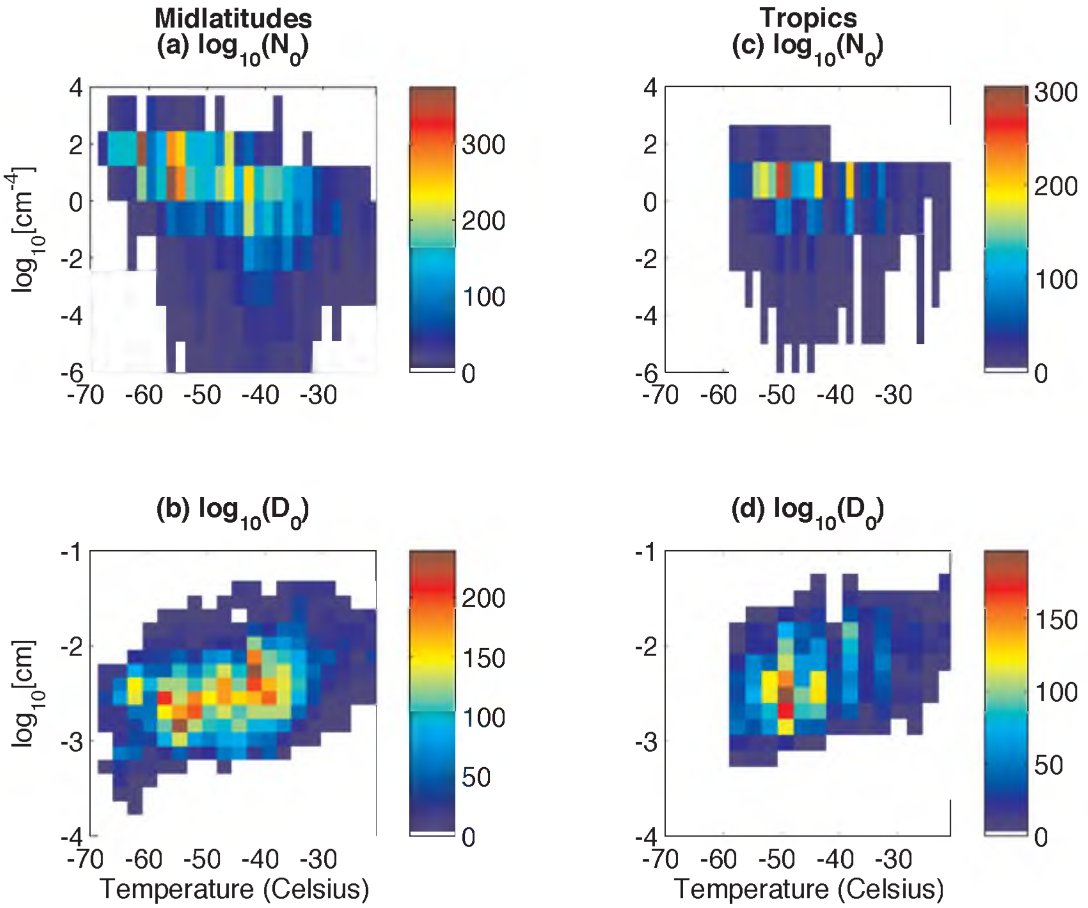

Fig. 2.16: Two-dimensional histograms of $\log_{10}[N_0]$ and $\log_{10}[D_0]$ versus temperature for (a)–(b) the midlatitudes and for (c)–(d) the Tropics.

$$n_{\max}(D_0,\alpha) = D_0\alpha. \tag{2.12}$$

Histograms of temperature versus mode location, with the marginal probability density of finding a mode at any temperature conditioned upon temperature, are shown in Fig. 2.17. Unimodal or bimodal parametric distributions were chosen for each temperature based upon the generalized chi-squared test. There is a faint signature: at the coldest temperatures, there tends to be only one small mode, but as temperature increases, the chances of finding a larger mode further away from the nearly ever-present small mode increase (until the warmest temperatures are reached, at which point the signal fades away). Recall that Field (2000) found that only a small mode tended to exist around cloud top, with a larger mode that moved further from the small mode with descent through the cloud until the lower reaches of the cloud were obtained, where the processes of particle breakup and sublimation became dominant. Information on where in the cloud samples were taken (with respect to top and base) is not had for most of this data, but the findings of Field (2000) and others are confirmed here by using temperature as a rough proxy for location within cloud.

According to the hypothesis of Baker and Lawson (2006a), ice water content is likely a function of RHi and of vertical velocity in some part of the cloud layer as well as of temperature. Two-dimensional histograms of IWC versus temperature are given in Fig. 2.18, both for the midlatitudes and for the Tropics. A definite positive correlation between the two variables is seen in the midlatitude data but is much weaker in the tropical cirrus. This observation also is in accord with Heymsfield et al. (2013). In either case, the spread indicates that IWC must also be a function of other parameters. In making similar histograms of IWC versus both RHi and vertical velocity turbulence, no

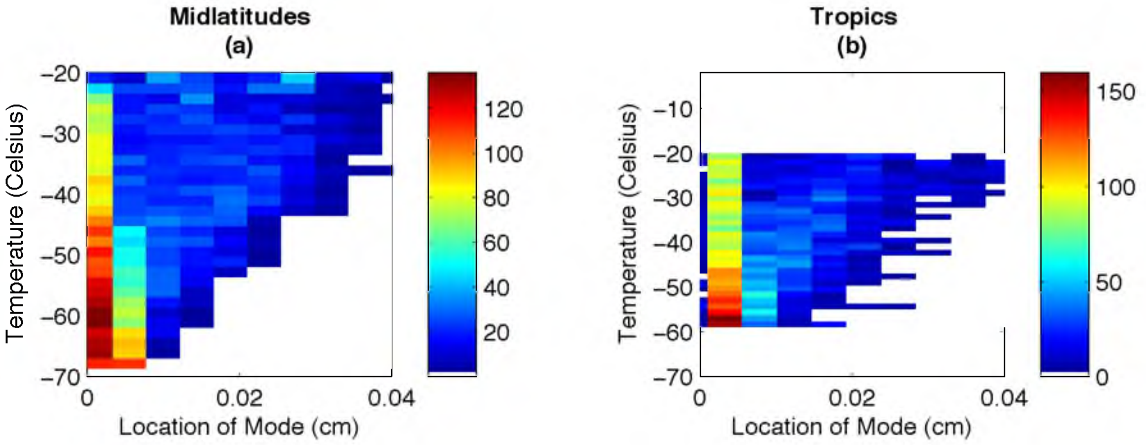

Fig. 2.17: Two-dimensional histograms of fit PSD mode conditioned on temperature for (a) the midlatitudes and for (b) the Tropics.

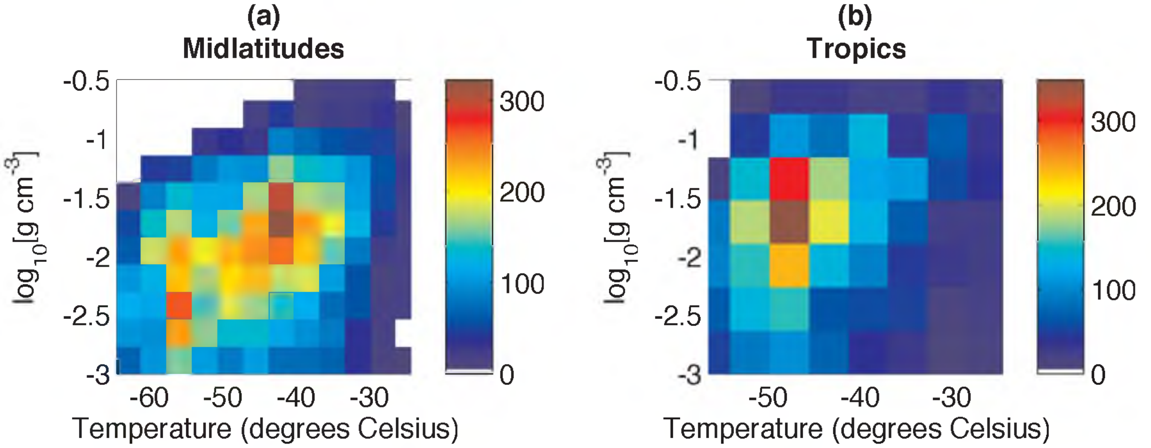

Fig. 2.18: Two-dimensional histograms of $\log_{10}$[IWC] versus temperature for (a) the midlatitudes and for (b) the Tropics.

relationships were found, although this finding does not preclude there being such relationships. Because ice crystals develop on time scales on the order of tens of minutes, where they are measured is typically separated spatially and temporally from where they are nucleated and from where most of their growth has occurred. Therefore, the relationships posited by Baker and Lawson (2006a) would require examination of the properties of the entire layer being studied. This more in-depth probing is not possible with the datasets used in this study.

Figure 2.19 shows two-dimensional histograms of total number concentration (the measured zeroth mode of the PSD) versus both temperature and RHi, for both the midlatitudes and for the Tropics. No relationship between number concentration and RHi is seen in the Tropics, though there is seen a weak relationship in the Tropics between number concentration and temperature. There is a definite relationship between number concentration and temperature in the midlatitudes, whereby, on average, particle number concentration decreases with increasing temperature. If temperature is again considered a rough proxy for location within the cloud layer, this finding is in accord with the previously stated concept of the top zone in cirrus, formed from the results of Lagrangian spiral flights and passes through orographic wave clouds: number concentration is generally highest near cloud top where much of the production of ice crystals is posited to form via homogenous ice nucleation. It is also consistent with the findings of Heymsfield et al. (2013). A weak relationship is seen between number concentration and RHi in the midlatitudes, but it is the opposite of the relationship expected from the negative feedback proposed by Heymsfield and Miloshevich (1995): number concentration increases with increasing supersaturation, rather than vice versa. This is

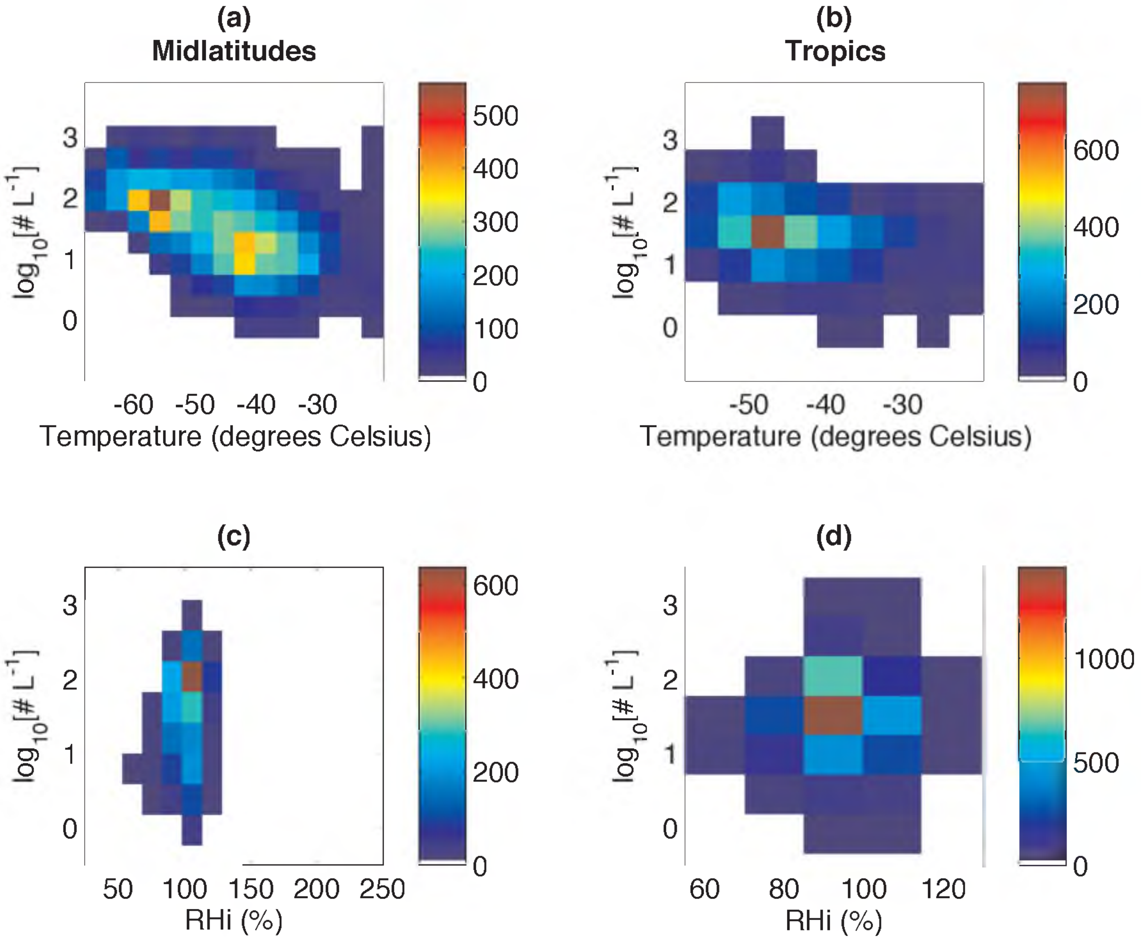

Fig. 2.19: Two-dimensional histograms of $\log_{10}[N_T]$ versus temperature (a)–(b) and RHi (c)–(d) for the midlatitudes and for the Tropics.

not to contradict the observed negative feedback (for, as noted above, the ice crystals used in this study are typically measured away from their nucleation sites), but to point out that it does not show up in a broad, statistical sense. Instead, it would appear that perhaps high supersaturations more often coincide with regions of high number concentration, consistent with the homogenous freezing of large numbers of small, super-cooled water droplets (Lawson et al., 2006a). In neither region is a relationship found between number concentration and vertical velocity turbulence.

Considering that relationships found in the midlatitudes are often seen much more weakly or not at all in the Tropics, it is noted that there are approximately a factor of three more measurements from the midlatitudes than there are from the Tropics. It could simply be that not enough tropical measurements using the updated instruments and processing techniques have been made. In fact, it could be hypothesized that a necessary (but not sufficient) condition for an appropriate sample size would be for the measured temperature pdfs shown in Fig. 2.14 to become clearly normal, or at least smooth.

Summary and Caveat

A database of cirrus particle size distributions, with concomitant meteorological variables, has been constructed using data collected during the TC^4, MACPEx, and SPartICus flight campaigns. These campaigns were chosen due to their use of up-to-date instrumentation as well as due to the measures taken to mitigate ice particle shattering artifacts. Particle size distribution data were averaged for 15 seconds, and it was determined that the 2D-S' first size bin (5 μm–15 μm) is not certain enough to use. Parametric PSDs, both unimodal and bimodal, were fit to each measured PSD, and the fitting procedures developed are demonstrated in Appendices A and B. Functional descriptions (with full covariance matrices) are given for the unimodal fit parameters. These may be used in modeling or remote sensing applications that call for fully described statistics of ice PSDs. It was determined that, at least for certain purposes, the unimodal fits to the measured PSDs are sufficient. Furthermore, due to a high correlation between the two, it was determined that the N_0 parameter can be eliminated by expressing it as a function of the α parameter (or vice versa).

Three statistical tests were developed in order to determine the utility of bimodal fits and the efficacy of unimodal fits: a maximum likelihood ratio test, a modified Anderson–Darling test, and a generalized chi-squared test of moments. While it was found that, from 50% to 60% of time, the Anderson–Darling and generalized chi-squared tests deemed the unimodal fits to be insufficient, the bimodal fits were deemed sufficiently more descriptive of measured PSDs so as not to be nuisances only less than 10% of the time. This inconsistency is attributed to lingering uncertainties in the actual shape of ice PSDs, particularly at the smallest ice crystal sizes.

Properties of the PSDs, including bimodality and various bulk quantities, were examined in relation to meteorological variables such as temperature and RHi. It was found that PSDs identified by the modified Anderson–Darling test as being better served by bimodal representations tend to occur at higher temperatures and with lower total number concentrations than those PSDs that the same test indicates to be unimodal, similar to the findings of Zhao et al. (2011). This finding stands in support of the hypothesis given in Lawson et al. (2006a) that the model of distinct ice growth and particle size zones given in Heymsfield and Miloshevich (1995) holds in the average for cirrus.

Furthermore, a negative correlation was found between temperature and ice particle total number concentration, i.e., that N_T tends to be higher at colder temperatures. A positive correlation was found between temperature and ice water content and a faint, positive correlation in the midlatitudes between N_T and RHi. However, being a study of averages over many clouds rather than a study of individual clouds, what is likely being seen is that areas of high number concentration are tending to occur in highly supersaturated regions where large numbers of small, super-cooled liquid droplets have undergone homogenous freezing (Lawson et al., 2006a).

Here a word of caution is warranted concerning shattered particle removal from the 2D-S data. The removal processing is based upon modeling particle interarrival times according to a Poisson process (Lawson, 2011), and one basic assumption of a Poisson process, as it applies here, is that each particle interarrival time within the optical probe is independent of all other particle interarrival times. Such an assumption's holding for any physical system would require the system's being in a steady, uniform state—which is never truly the case and certainly not so for a cloud. It is sometimes the case in the treatment of cloud and precipitation processes that cloud particles are considered to be independently positioned through the volume of the cloud (Kostinski and Shaw, 2001). However, a number of studies have examined the tendency of cloud particles to cluster nonuniformly in space (Khain et al., 2007). Hobbs and Rangno (1985) found in situ evidence of ice particle clustering both in cumuliform and stratiform clouds. Kostinski and Shaw (2001) found clustering of liquid cloud droplets even in the center of a nominally homogenous cloud core and also determined the "statistics of droplet spacing" to exhibit super-Poissonian variance at increasing length scales. Pinsky and Khain

(2003) also found clustering of liquid cloud droplets on scales the order of a centimeter. All of these studies pointed to the clustering of cloud particles as a result of the interaction of the particles with turbulent eddies: "this mechanism of the preferential concentration acts at all scales of turbulence, increasing toward smaller scales" (Khain et al., 2007).

Thus, the danger with particle removal based on particle interarrival times is that since clouds evolve under the influence of turbulent eddies, the assumption of independent particle interarrival times is not strictly correct and therefore some real, small particles can be expected to have been incorrectly removed from the processed dataset.

That being said, though the shattered particle removal algorithm is imperfect and will be subjected to further testing, the results presented here indicate behaviors in ice crystal concentrations within different regions of cloud that are expected from physical reasoning (as discussed in the first section of this chapter) and that are not always discernible from older datasets where shattering mitigation processing is not possible (Lawson, 2011).

As a first effort, a small experiment is here performed on the sensitivity of the results presented in this chapter to the shatter-correction algorithm. Very simply, the concentrations in size bins up to 55 μm were doubled for the entire MACPEx 2D-S dataset (the first size bin still being truncated). This altered 2D-S dataset constitutes the test set. The rationale for doubling the concentrations in these particular size bins is this: Lawson (2011) reported reductions in small particles due to antishattering processing as great as 90%—mainly at sizes smaller than 50 μm—and a subsequent error in the processing due to imperfections in the application of image processing algorithms of 10% is assumed. Then, the occurrence of PSD bimodality within the test set, as well as shortwave extinction coefficients computed from the test set, were examined. Extinction coefficients were computed as outlined in Appendix D, using a dimensional-cross-sectional area relationship of $A(D) = 0.2285D^{1.88}$ (from Mitchell, 1996; units are cgs).

As a substantial fraction of the total number concentration of ice crystals in a PSD is often found at sizes of 55 μm or smaller (see, e.g., Fig. 2.6), it is freely assumed here that computations of N_T are highly sensitive to the shattering algorithm. The occurrence of PSD bimodality changed significantly from the control set to the test set. Effecting the particle concentration doubling resulted in an apparent increase of PSD bimodality within the MACPEx dataset from 5.5% to 10.4% (as diagnosed by the maximum likelihood ratio test), from 68.8% to 78.7% (as diagnosed by the binned Anderson–Darling test), and from 59.6% to 71.4% (as diagnosed by the generalized chi-squared test). Increasing the numbers of small particles also had an effect on computations of shortwave extinction coefficient, as shown in Fig. 2.20: on average, computed extinction values increased by about 0.02 km^{-1}, and the mean relative increase in extinction coefficient was 9%. It is therefore concluded that the results presented here are sensitive to both the use of as well as the accuracy of the shattered particle removal-processing algorithm.

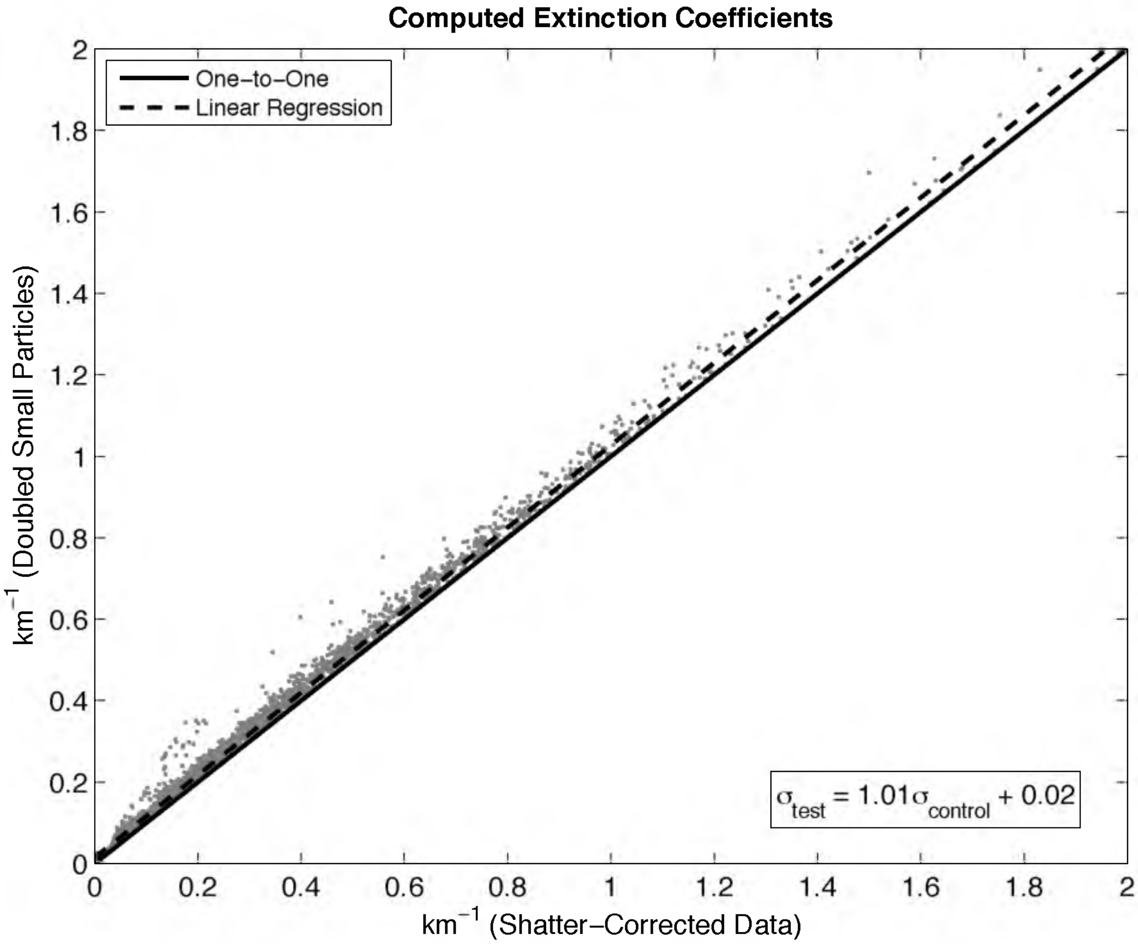

Fig. 2.20: Extinction coefficient computed from the test dataset scattered versus extinction coefficient computed from the control dataset.

CHAPTER 3

PARAMETERIZATION OF A NORMALIZED, UNIVERSAL CIRRUS PSD

Background

Westbrook et al. (2004a) and Westbrook et al. (2004b), through a set of modeling studies and comparisons with data taken during FIRE I (Field and Heymsfield, 2003), concluded that ice PSDs whose dominant mechanism for evolution is aggregation via differential sedimentation asymptotically approach a "universal particle size distribution" when individual PSDs are normalized by two physical quantities directly related to two distribution moments. The idea of underlying universality due to aggregation has been around for some time (see, e.g., Meakin, 1992), and much work has been applied to the scaling of raindrop size distributions (see, e.g., Testud et al., 2001; and Lee et al., 2004). Delanoe et al. (2005) applied the raindrop-scaling framework of Testud et al. (2001) to ice particle systems by converting ice PSDs to equivalent melted diameter drop distributions (assuming an effective density-dimensional relationship) for a large database of cirrus in situ measurements. Tinel et al. (2005) applied the use of normalized, equivalent melted-diameter distributions to the retrieval of ice cloud properties. Using power laws to relate moments of ice PSDs, Field et al. (2005) also scaled ice PSDs to get at a universal size distribution, but they made no assumption about mass-dimensional relationships, normalizing with moments of the PSDs expressed as functions of particle maximum dimension. They point out, however, that for their results to be used, the application of some mass-dimensional assumptions is unavoidable.

One of the attractions of the normalized ice PSD is therefore that, theoretically, normalization allows for the characterization of any PSD using the universal shape along with two of the PSDs moments. Some authors have suggested that the universal shape, along with any two measurements related to any two of a PSDs moments, are sufficient characterization to reconstruct such observables as radar reflectivity (e.g., Field et al., 2005). Despite the fact that PSD normalization is sometimes seemingly given as a panacea for reducing the degrees of freedom in problems related to ice cloud property retrievals and modeling, the natural variability in ice PSDs remains. This is clearly seen in Fig. 11 of Field et al. (2005), where the variation around the mean universal shape spans orders of magnitude. To begin with, the hypothesized universal shape is only an asymptotic limit, and even at that, the theory behind it accounts only for aggregational growth, ignoring other growth/depletion processes (secondary though they may be) such as fragmentation, deposition and sublimation, and turbulent and advective disturbances. Even greater uncertainty is introduced when, inevitably, highly uncertain mass-dimensional relationships (e.g., Mitchell, 1996) are introduced, as in Delanoe et al. (2005). Two moments, it turns out, are not enough to characterize a PSD without avoiding the natural variability inherent in any treatment of ice PSDs

In this chapter, the climatology of cirrus PSDs described in Chapter 2 is normalized after the manner described in Field et al. (2005; hereinafter referred to as F05). A parameterization of cirrus cloud PSDs based on this normalization and on the up-to-date cirrus PSD climatology described in Chapter 2 is then given. The advantages over earlier such parameterizations include 1) that the datasets used here are much larger in both their temporal and spatial coverage and 2) that the more modern two-dimensional stereo (2D-S) probe is used along with advanced shattered particle removal techniques. It will be shown in Chapter 3 that the 2D-S is expected to record a significantly lower number of small ice crystals than the older Particle Measuring Systems (PMS) 2DC probe in identical cloud situations. This chapter proceeds with a brief note regarding the data used and then outlines the normalization process. A method for performing the aforementioned parameterization is then given, and then the performance of the parameterization is demonstrated along with a method for using it in conjunction with a pair of remote sensing observations.

Data

A particular description of the data used in this entire study is given in Chapter 2. Here it is recalled that the unimodal fits did an excellent job of reproducing the first through the fifth sample moments of the measured PSDs. The zeroth moment—total particle number concentration—is best computed by using unimodal fits where the generalized chi-squared fit (see Chapter 2 and Appendix C) indicates that the unimodal fit is sufficient and by using bimodal fits otherwise. Therefore, for computational convenience, all quantities derived from measured 2D-S PSDs—total number concentration, extinction coefficient, etc.—are computed using the parametric fits (with one exception, where total number concentration were computed directly from the binned 2D-S data). Formulae for computing several physical quantities using the parametric fits to the measured PSDs are given in Appendix D.

Normalization of Particle Size Distributions

A PSD is normalized by the scaling of its independent variable and of its abscissa. We begin with PSDs as functions of particle maximum dimension, and following F05, normalize the independent variable by

$$D^* = \frac{M_3}{M_2} \tag{3.1}$$

and the abscissa by

$$N^* = \frac{M_2^4}{M_3^3}, \tag{3.2}$$

where M_n is the n^{th} sample moment of the PSD expressed as a function of particle maximum dimension. The PSD may then be expressed as

$$n(D) = N^* F\left(x = \frac{D}{D^*}\right). \tag{3.3}$$

In Eq. 3.3, $F(x)$ is (ideally) the universal, normalized PSD and may be fit with any of a number of parametric functions. By using numerically computed moments, Eqs. 3.1–3.3 are used to normalize each of the measured PSDs from the combined dataset described in Chapter 2. Each normalized PSD is then grouped into normalized maximum length bins of $\Delta x = 0.10$.

Figure 3.1 shows two-dimensional histograms for the normalized PSDs from each dataset and from all three datasets together with their mean, normalized PSDs overlaid (cf. Fig. 11b of F05). The mean, normalized PSD for all three datasets is shown again

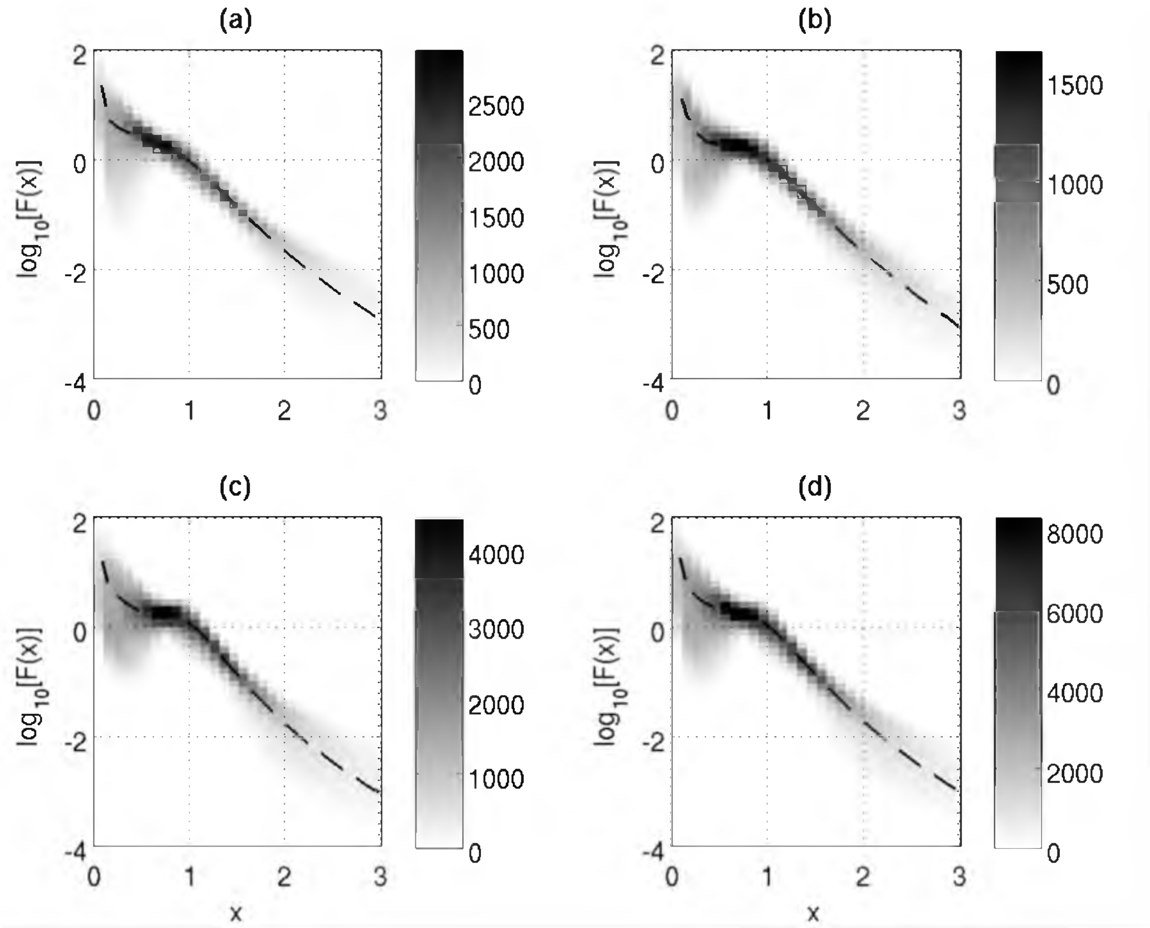

Fig. 3.1: Histograms of normalized PSDs from each flight campaign, overlaid with their mean, normalized PSDs. The color map is truncated at 75% of the highest number of samples in a bin so as to increase contrast. (a) TC^4, (b) MACPEx, (c) SPartICus, (d) all data combined.

in Fig. 3.2 (solid black curve; the other curves will be explained later). This serves as the empirical universal, normalized PSD $F_u(x)$. Comparison of F05's Fig. 11b with Fig. 3.2 shows general similarity in $F_u(x)$, though the shoulder in Fig. 3.2 is more distinct and is closer to a normalized particle size of unity. Given that a great deal more data are used here than in F05 and that the data were collected with a newer instrument, some differences are not unexpected.

In order to check the normalization procedure, it is recognized that total number concentration should be preserved thereby. For all three datasets, the binned, empirical $F(x)$ for each measured PSD was used along with corresponding values of N^* and D^* derived from each PSD in order to compute total number concentration (N_T). These are scattered against N_T computed directly from the binned, nonnormalized PSDs and shown in panel (a) of Fig. 3.3. The agreement is sound and the normalization procedure is validated. In panel (b) of Fig. 3.3, ice water content (IWC) computed from the binned and normalized PSDs against IWC computed from the unimodal fits to the measured PSDs (as described in Chapter 2). The agreement is good, but not quite so good as for N_T in panel (a). The procedure for computing IWC from unimodal PSD fits is described in Appendix D, and the dimensional/density relationship used is that given in Delanoe et al. (2005):

$$\rho(D) = 0.0056 D^{-1.1} \quad \text{(cgs units).} \tag{3.4}$$

Parameterization of the Universal, Normalized PSD

Westbrook et al. (2004b) predict an exponential tail for the normalized PSD. In F05, $F_u(x)$ is fit with a mixture of an exponential distribution and a gamma distribution in

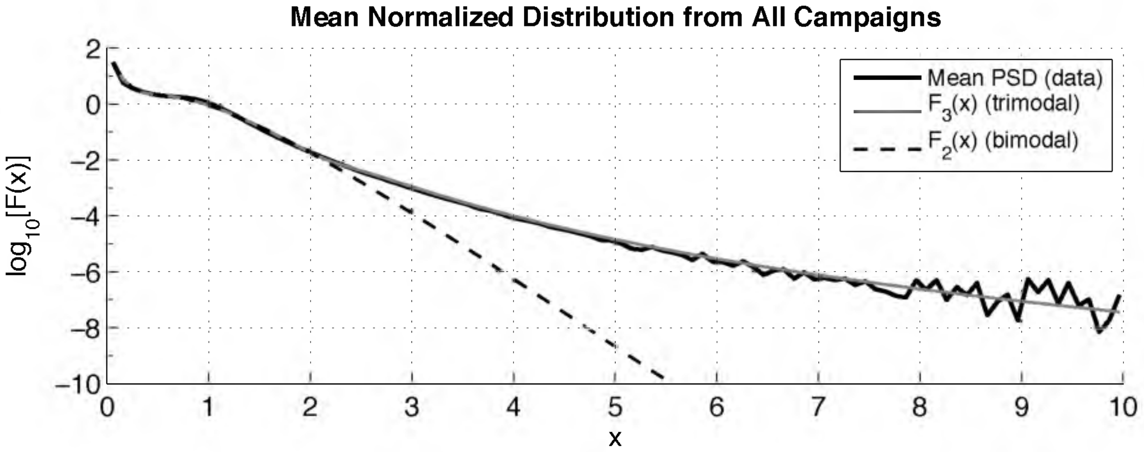

Fig. 3.2: The mean, normalized PSD from all three datasets combined (black curve), overlaid with two parameterizations: a bimodal gamma distribution (dashed curve) and a trimodal function consisting of a bimodal gamma distribution and an inverse gamma distribution (solid gray curve).

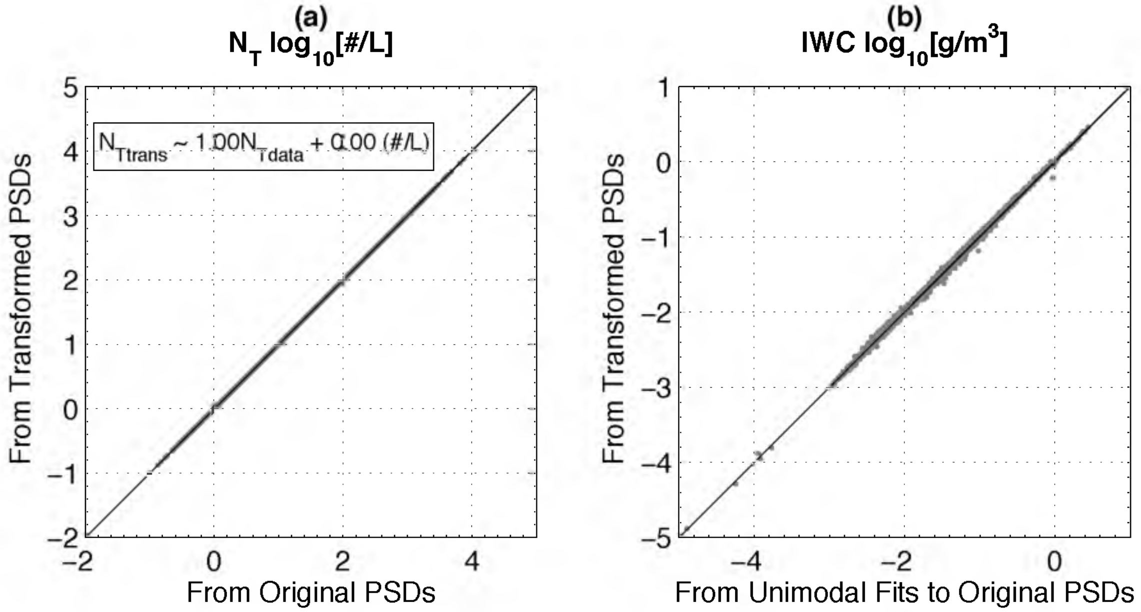

Fig. 3.3: Comparisons of total number concentration and ice water content computed from normalized and measured PSDs. (a) Computations of N_T using the binned, normalized PSDs along with the true values of N^* and D^* from each PSD vs. the true values of N_T computed directly from the binned PSDs. (b) Computations of ice water content using the binned, normalized PSDs along with the true values of N^* and D^* from each PSD vs. the true values of IWC computed directly from the measured PSDs via the unimodal fits described in Chapter 2.

order to describe an observed exponential behavior at small normalized particle sizes, a shoulder around $x \sim 0.5$, and then an approximately exponential drop-off at larger normalized particle sizes (see Fig. 11b in F05). Upon normalizing the 2D-S data, however, it was found that the gamma distribution's tail dropped off too quickly to capture the behavior of $F_u(x)$ at large values of x. Therefore, we here perform two fits to $F_u(x)$: a bimodal mixture of two gamma distributions

$$\begin{aligned} F_2\left[x \mid \mathbf{p}_1 = \left(N_1, D_2, \alpha_1, N_2, D_2, \alpha_2\right)^T\right] = N_1 \left(\frac{x}{D_1}\right)^{\alpha_1} \exp\left(-\frac{x}{D_1}\right) + \\ N_2 \left(\frac{x}{D_2}\right)^{\alpha_2} \exp\left(-\frac{x}{D_2}\right) \end{aligned} \tag{3.5}$$

and a trimodal mixture of two gamma distributions and a shifted, inverse gamma distribution (Johnson et al., 1994)

$$\begin{aligned} F_3\left[x \mid \mathbf{p}_2 = \left(\mathbf{p}_1^T, N_3, \alpha_3, \beta_3\right)\right] = F_2\left(x \mid \mathbf{p}_1\right) + N_3 \frac{\beta_3^{\alpha_3}}{\Gamma\left(\alpha_3\right)} \left(x - 1.55\right)^{-\alpha_3 - 1} \times \\ \exp\left(-\frac{\beta_3}{x - 1.55}\right) H\left(x - 1.55\right) \end{aligned} \tag{3.6}$$

Where $H(x)$ is the Heaviside step function. The inverse gamma distribution, which is simply the distribution of the inverse of a gamma-distributed random variable, was found to capture the tail of the normalized 2D-S data very well. These two parametric functions are fit to the empirical $F_u(x)$ by nonlinear regression via the method of maximum likelihood. Due to its accuracy, this fitting method proved highly useful and will therefore be described, as it will no doubt prove helpful in the future.

First, a remark on a possible simplification to the fitting problem is useful. Let m_k

denote the noncentral moments of $F_u(x)$. By the consistency rule given in F05, it should be that $m_2 = m_3 = 1$, which requirement would allow for elimination of two parameters [N_1 and N_2 in $F_2(x)$, most easily]. In the course of performing the bimodal fit to Eq. 3.5, however, it was found that eliminating those two parameters did not provide enough degrees of freedom for a successful fit. Evidently, the averaged data do not conform well enough with theory for the enforcement of the consistency rule.

Now, let it be recalled that regressions are designed to use a predictor variable in order to fit the mean of a set of measured data (Wilks, 2006). In this case, the predictor variable is $x = D(\mathrm{M}_2/\mathrm{M}_3)$, and the mean of the predicted data $F_u(x)$ is to be set to a parametric function: either the bimodal function $F_2(x)$ in Eq. 3.5 or the trimodal function $F_3(x)$ in Eq. 3.6. Consider the data in each $\Delta x = 0.10$ bin to be described by a gamma probability distribution:

$$\Pr\left(y_{ij}\right) = p\left(y_{ij} \mid \lambda_i, \mu_i, x_i\right) = \frac{1}{\mu_i^{\lambda_i}\Gamma\left(\lambda_i\right)} y_{ij}^{\lambda_i - 1} \exp\left(-\frac{y_{ij}}{\mu_i}\right), \tag{3.7}$$

where y_{ij} are the samples of the normalized PSDs in the i^{th} x_i bin, and μ_i and λ_i are the scale and shape parameters, respectively, of the distribution of normalized PSD samples in the i^{th} bin. Assuming the samples are independent, then, the likelihood function of the samples within an x_i bin is

$$L\left(\lambda_i, \mu_i \mid \mathbf{y}_i\right) = \prod_{j=1}^{K_i} \frac{1}{\mu_i^{\lambda_i}\Gamma\left(\lambda_i\right)} y_{ij}^{\lambda_i - 1} \exp\left(-\frac{y_{ij}}{\mu_i}\right), \tag{3.8}$$

where K_i is the number of samples in the i^{th} x_i bin. Expanding this likelihood function over all x_i bins (and for a total of N normalized size bins) gives

$$\begin{aligned} L\left(\lambda_1,\mu_1,\ldots,\lambda_N,\mu_N \mid \mathbf{y}\right) &= \prod_{i=1}^{N} L\left(\lambda_i,\mu_i \mid \mathbf{y}_i\right) \\ &= \prod_{i=1}^{N}\left[\prod_{j=1}^{K_j}\frac{1}{\mu_i^{\lambda_i}\Gamma\left(\lambda_i\right)} y_{ij}^{\lambda_i-1}\exp\left(-\frac{y_{ij}}{\mu_i}\right)\right]. \end{aligned} \tag{3.9}$$

Rather than use this likelihood function to estimate all of the (λ_i,μ_i) pairs directly, they are parameterized using the nonlinear function $F_u(x)$ such that

$$\lambda_i\mu_i = F_u\left(x_i\right). \tag{3.10}$$

Let var$_i$ denote the sample variance within an x_i bin. Then

$$\mu_i = \frac{\mathrm{var}_i}{F_u\left(x_i\right)}, \text{ and} \tag{3.11}$$

$$\lambda_i = \frac{F_u\left(x_i\right)^2}{\mathrm{var}_i}. \tag{3.12}$$

With these substitutions, the likelihood function of the parameter vector (either $\mathbf{p}_1$ or $\mathbf{p}_2$) becomes

$$L\left(\mathbf{p} \mid \mathbf{y}\right) = \prod_{i=1}^{N}\left\{\prod_{j=1}^{K_i}\frac{y_{ij}^{\frac{F_u(x_i)^2}{\mathrm{var}_i}-1}}{\left[\frac{\mathrm{var}_i}{F_u\left(x_i\right)}\right]^{\wedge}\left[\frac{F_u\left(x_i\right)^2}{\mathrm{var}_i}\right]\Gamma\left[\frac{F_u\left(x_i\right)^2}{\mathrm{var}_i}\right]}\exp\left[-y_{ij}\frac{F_u\left(x_i\right)}{\mathrm{var}_i}\right]\right\}, \tag{3.13}$$

and the log-likelihood function is

$$\begin{aligned}\ln\left[L\right]=\sum_{i=1}^{N}\sum_{j=1}^{K_i}\Bigg\{&\frac{F_u\left(x_i\right)^2}{\mathrm{var}_i}\left(\ln\left[y_{ij}\right]+\ln\left[F_u\left(x_i\right)\right]-\ln\left[\mathrm{var}_i\right]\right)\\&-y_{ij}\frac{F_u\left(x_i\right)}{\mathrm{var}_i}-\ln\left[\Gamma\left(\frac{F_u\left(x_i\right)^2}{\mathrm{var}_i}\right)\right]-\ln\left[y_{ij}\right]\Bigg\}.\end{aligned} \tag{3.14}$$

Maximum likelihood estimation has become a workhorse for parameter estimation. One reason is that under proper conditions (Huber, 2002), the asymptotic sampling distribution of maximum likelihood estimators is multivariate normal (Kotz et al., 2000; Wilks, 2006). An attempt was made to transform the fitting problem here so that the sampling distribution of the fit parameters could be estimated, and though this particular attempt proved unsuccessful, the parameter transformation did aid in the numerical inversion of the likelihood function. Specifically, the mathematical supports of the parameters being estimated are $(N_1,D_1,N_2,D_2,N_3,\alpha_3,\beta_3) \in (0,\infty)$ and $(\alpha_1,\alpha_2) \in (-1,\infty)$. That their mathematical supports might encompass the entire real line, thus eliminating the need for a constrained inversion (Zhdanov, 2002) of Eq. 3.14, the parameters are transformed as shown in Table 3.1. Equations 3.5 and 3.6 therefore change to

$$\begin{aligned}F_2\left[x\,|\,\mathbf{p}_1^*\right]=&\left[\frac{x}{e^{d_1}}\right]^{\exp\left(a_1\right)-1}\exp\left(n_1-e^{-d_1}x\right)+\\&\left[\frac{x}{e^{d_2}}\right]^{\exp\left(a_2\right)-1}\exp\left(n_2-e^{-d_2}x\right).\end{aligned} \tag{3.15}$$

Table 3.1

Variable transformations for the functions $F_2(x)$ and $F_3(x)$.

Parameter	Transformation	Inverse Transformation
N_1	$n_1 = \ln\left[N_1\right]$	$N_1 = \exp\left(n_1\right)$
D_1	$d_1 = \ln\left[D_1\right]$	$D_1 = \exp\left(d_1\right)$
α_1	$a_1 = \ln\left[\alpha_1 + 1\right]$	$\alpha_1 = \exp\left(a_1\right) - 1$
N_2	$n_2 = \ln\left[N_2\right]$	$N_2 = \exp\left(n_2\right)$
D_2	$d_2 = \ln\left[D_2\right]$	$D_2 = \exp\left(d_2\right)$
α_2	$a_2 = \ln\left[\alpha_2 + 1\right]$	$\alpha_2 = \exp\left(a_2\right) - 1$
N_3	$n_3 = \ln\left[N_3\right]$	$N_3 = \exp\left(n_3\right)$
α_3	$a_3 = \ln\left[\alpha_3\right]$	$\alpha_3 = \exp\left(a_3\right)$
β_3	$b_3 = \ln\left[\beta_3\right]$	$\beta_3 = \exp\left(b_3\right)$

$$
\begin{aligned}
F_3\left[x \mid \mathbf{p}_2^* = \left(\mathbf{p}_1^{*T}, n_3, a_3, b_3\right)\right] = F_2\left(x \mid \mathbf{p}_1^*\right) + e^{n_3} \frac{e^{b_3 \exp(a_3)}}{\Gamma\left(e^{a_3}\right)} \left(x - 1.55\right)^{-\exp(a_3) - 1} \times \\
\exp\left(\frac{-e^{b_3}}{x - 1.55}\right) H\left(x - 1.55\right).
\end{aligned}
\tag{3.16}
$$

This nonlinear regression is highly sensitive to the first guess given it. To cope with this sensitivity, 929 280 first guesses were used in fitting $F_2(x)$. This number of first guesses was arrived at simply by dividing the possible solution space for the vector $\mathbf{p_1}$ into fine divisions in each of its six dimensions. Then, each possible combination within the divided solution space was used as a first guess for the transformed vector $\mathbf{p_1}^*$. This suffices as a very large number of first guesses, so that the global maximum of the likelihood function can be found. Out of all the resulting solutions, that with the smallest mean squared error (with respect to the averaged, normalized PSD) was chosen. In fitting $F_3(x_i)$, the fit of $F_2(x)$, along with a method of moments fit of the shifted inverse gamma distribution to the residual for the third mode was used. The fit parameters are shown in Table 3.2.

To demonstrate that the inverse-gamma behavior of the tail of $F_u(x)$ is not an artifact of having used only the 2D-S to measure PSDs, the 2D-S dataset from TC^4 was combined with measurements taken using the Precipitation Imaging Probe (PIP), which probes image particles as large as 6.2 mm. Thus, the PSD measurements were extended to cover the size range 15 μm to 6200 μm. The normalization described above was then performed for the combined dataset, and $F_u(x)$ for the combined dataset is shown in Fig. 3.4. It is seen that the addition of the PIP increases $F_u(x)$ for values of x greater than 2. Since the difficulty with the gamma distribution is that it drops off too fast to catch the

Table 3.2

Values for fit parameters of the normalized PSD. Values for the bimodal form are given on the top, and values for the trimodal form are given on the bottom.

General Bimodal Form
$\mathbf{p}_1 = \left(9, 455, 0.2386, -1.0, 0.4235, 0.1526, 3.8612\right)^T$
General Trimodal Form
$\mathbf{p}_2 = \left(9, 455, 0.2386, -1.0, 0.4235, 0.1526, 3.8612, 0.0023, 6.9673, 6.6952\right)^T$

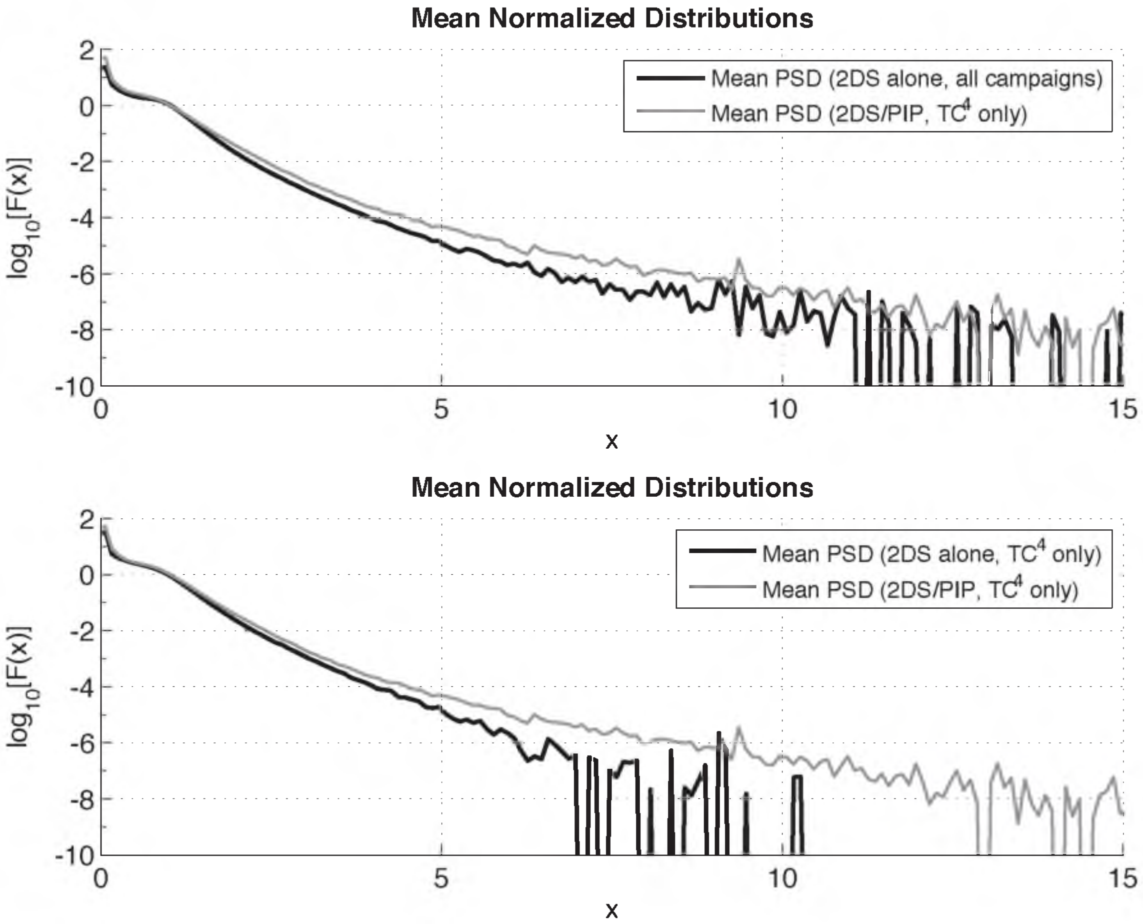

Fig. 3.4: Comparisons of mean, normalized PSDs with and without precipitation probe data included. (a) The mean, normalized PSD from all three datasets combined (black curve), overlaid with mean, normalized PSD from TC^4 derived from the combination of the 2D-S and PIP probes (solid gray curve). (b) The mean, normalized PSD from TC^4 (black curve), overlaid with mean, normalized PSD from TC^4 derived from the combination of the 2D-S and PIP probes (solid gray curve).

tail of $F_u(x)$, it is easily surmised that the addition of the precipitation probe data only reinforces the inverse-gamma behavior of the universal distribution's tail.

It is really the mean of all the possible normalized PSDs that is expressed by $F_u(x)$. For a specific realization of a PSD, then, some uncertainty is introduced by assuming that $F_u(x)$ is its underlying, normalized form. Figure 3.3, however, shows good agreement with measurements when estimating N_T and IWC based on $F_u(x)$ and known values for N^* and D^*. What this really demonstrates is that so long as N^* and D^* are known certainly, and so long as the PSD to be reconstructed belongs to the set of PSDs used to make $F_u(x)$, then using the average $F_u(x)$ is satisfactory, but not perfect (as seen in the case of IWC). It is not shown, but it is expected, that imperfections would also crop up in computations of extinction coefficient and radar reflectivity and that these imperfections are manifestations of the natural variability of real PSDs about their normalized mean $F_u(x)$. Therefore, when using $F_u(x)$ and N^* and D^*, error in reconstructed PSD moments will stem from the error in the parameterization of $F_u(x)$, i.e., from what other realizations of the parameter vectors $\mathbf{p}_1$ and $\mathbf{p}_2$ are possible for a given, measured PSD. This error, however, will not be explored in this work.

Performance of Parameterization and Use with Remote Sensing Observations

In Delanoe et al. (2005), a parameterization scheme based on radar reflectivity was proposed for N^*. Appendix E contains equations for parameterizing the N^* used here, based on radar reflectivity, assuming either a bimodal or a trimodal universal distribution. Figure 3.5 shows the results of computing PSD bulk and radiative quantities using the true D^* and the parameterized N^*, assuming either a bimodal or a trimodal

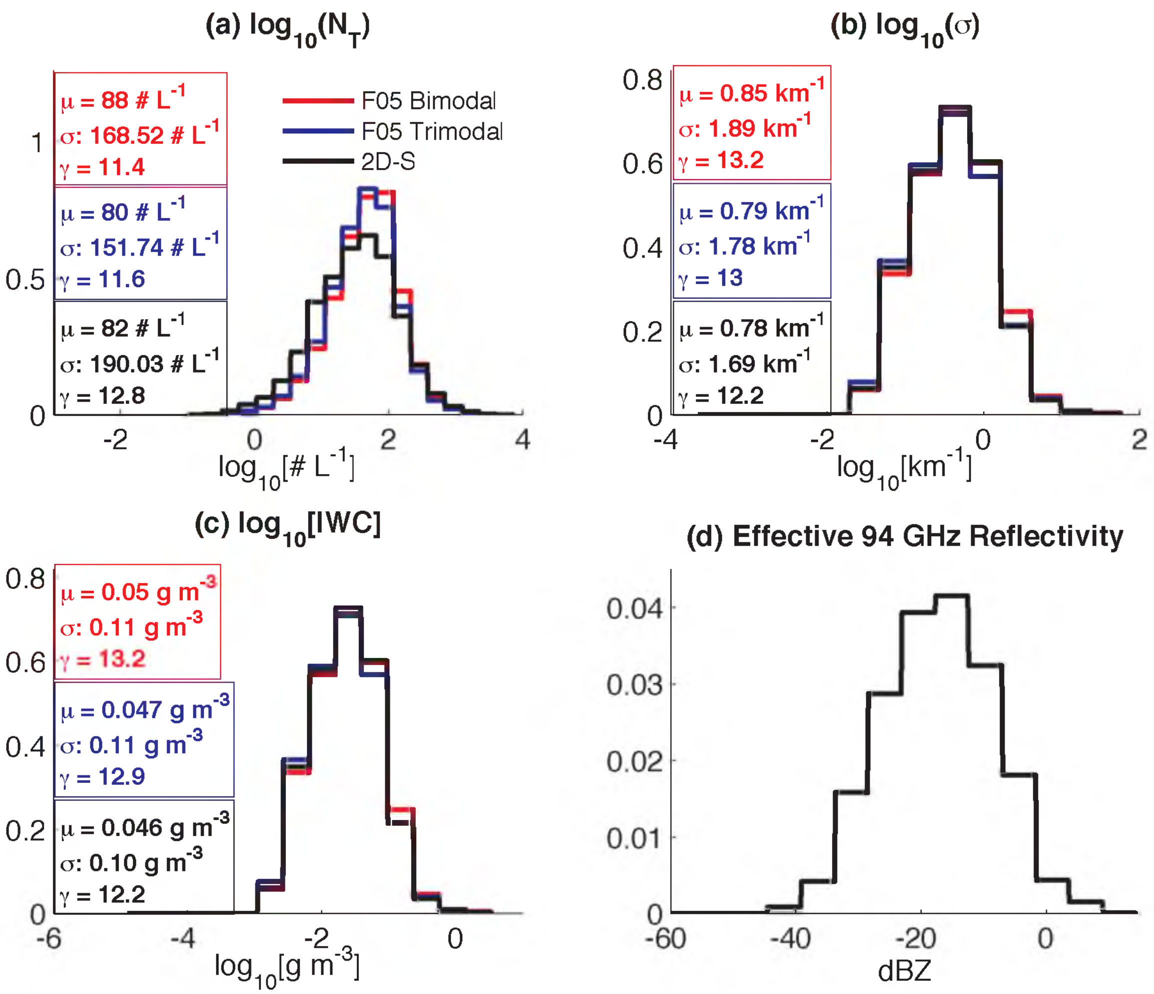

Fig. 3.5: Marginal pdfs of quantities computed directly from 2D-S data (black) as well as computed using the true D_m and a parameterized N_0^* (using reflectivity), via $F_2(x)$ (blue) and $F_3(x)$ (red). (a) total number concentration, (b) shortwave extinction coefficient, (c) ice water content, (d) radar reflectivity.

universal distribution, in comparison to the same quantities computed directly from the 2D-S data (as described in Chapter 2). Recomputed reflectivities match by design since N^* is computed to match the reflectivity. Parameterized number concentrations are closer, in the average (μ), to the data using the trimodal rather than the bimodal parameterization, and distributions of parameterized values for both extinction coefficient and IWC are closer in mean, standard deviation (σ), and skewness (γ) to the 2D-S data when the trimodal parameterization is used. Having pinned down each PSD using only $F_u(x)$ and (approximately, through simulated radar reflectivity) one moment of the PSD, the increasing deviation of measured and parameterized quantities—beginning at IWC and moving down to N_T—is an indication of the natural PSD variability mentioned in the introduction.

In Delanoe et al. (2005), complete parameterization of a PSD is achieved by using the universal shape along with N^* parameterized by radar reflectivity and D^* parameterized by temperature. A similar parameterization scheme is implemented here.

Parameterization of D^* (Eq. 3.1) by temperature is demonstrated in Fig. 3.6, such that

$$D^* = 9.29\exp\left(0.99T\right), \tag{3.17}$$

where T is in °C. Figure 3.7 shows the results of computing PSD quantities using $F_3(x)$ with the true D^* and the reflectivity-parameterized N^* (blue, labeled “semipram”), the temperature-parameterized D^* and the reflectivity-parameterized N^* (red, labeled “pram”), and directly from the 2D-S data (black). The effects of the complete parameterization are to greatly increase the skewnesses, spreads, and means of the recomputed PSD quantities.

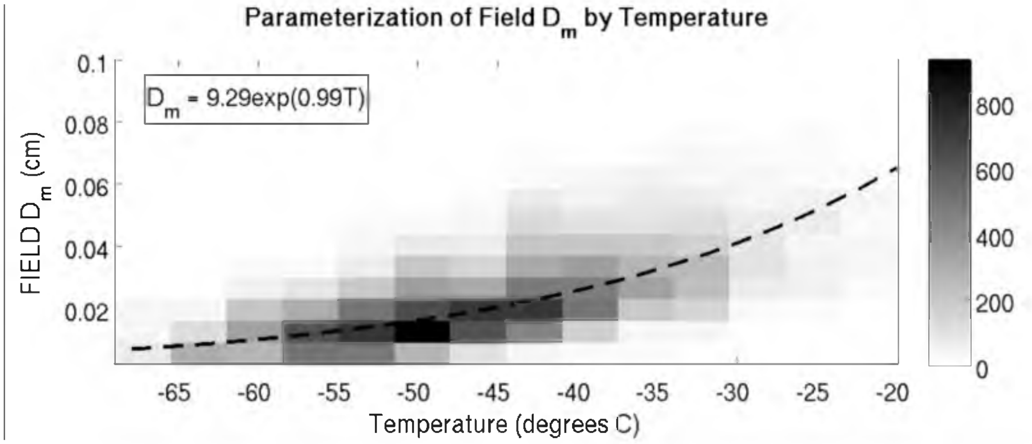

Fig. 3.6: A parameterization of D^* —as defined by Eq. 3.17—by temperature.

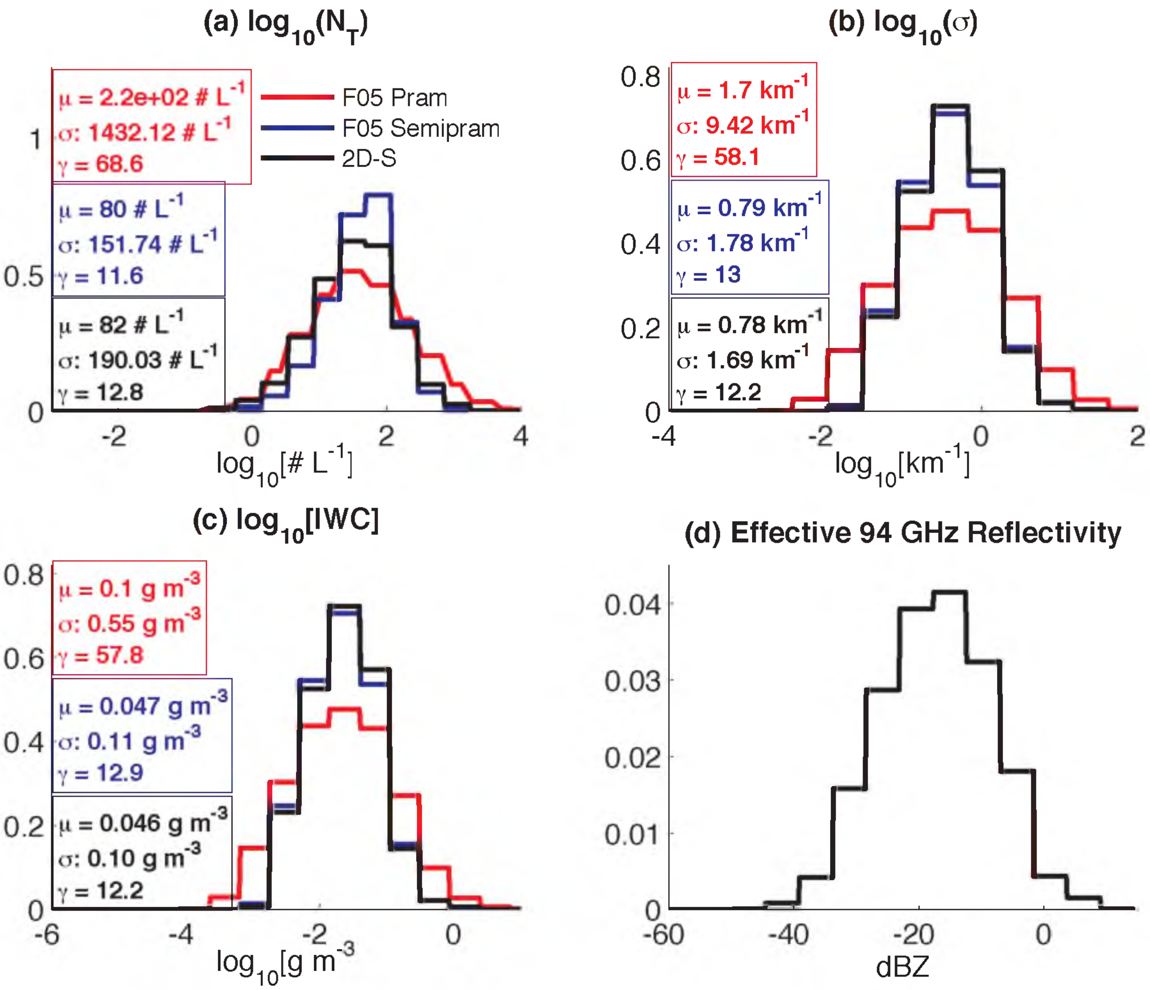

Fig. 3.7: Marginal pdfs of quantities computed directly from 2D-S data (black) as well as computed using the true D_m and a parameterized N_0^* (using reflectivity), via $F_3(x)$ (blue), and parameterized values for both D_m and N_0^* (using temperature and reflectivity), via $F_3(x)$ (red). (a) total number concentration, (b) shortwave extinction coefficient, (c) ice water content, (d) radar reflectivity.

Rather than parameterize D^* by temperature, here is devised a method for parameterizing both N^* and D^* simultaneously by two remote sensing measurements (two modeled moments of the PSD could also be used in a similar fashion). Suppose, for instance, that both radar reflectivity and extinction coefficient measurements were had. The forward models for extinction and reflectivity measurements, based on $F_3(x)$, are given in Appendix E. If we consider the vector of log-parameters

$$\mathbf{m} = (n,d)^T = \left(\ln\left[N^*\right],\ln\left[D^*\right]\right)^T \tag{3.18}$$

and the vector of log-measurements

$$\mathbf{y} = \left(\ln\left[\sigma\right],\ln\left[Z_e\right]\right)^T, \tag{3.19}$$

then we seek to invert the equation

$$\mathbf{y} = G(\mathbf{m}), \tag{3.20}$$

where G is the forward model operator—or, in other words, the set of equations that turns $\mathbf{m}$ into $\mathbf{y}$. Figure 3.8 shows marginal pdfs of quantities computed directly from 2D-S data (black) as well as computed using parameterized values (using the reflectivity/temperature method) for both D^* and N^*, via $F_3(x)$ (red) and parameterized values for both D^* and N^* [using synthetic extinction and radar reflectivity measurements), via $F_3(x)$ blue, labeled "LSE pram"]. The distributions of computed quantities, using the LSE (least-squared error) parameterization, are much closer to the distributions of quantities computed directly from the 2D-S in mean, standard deviation,

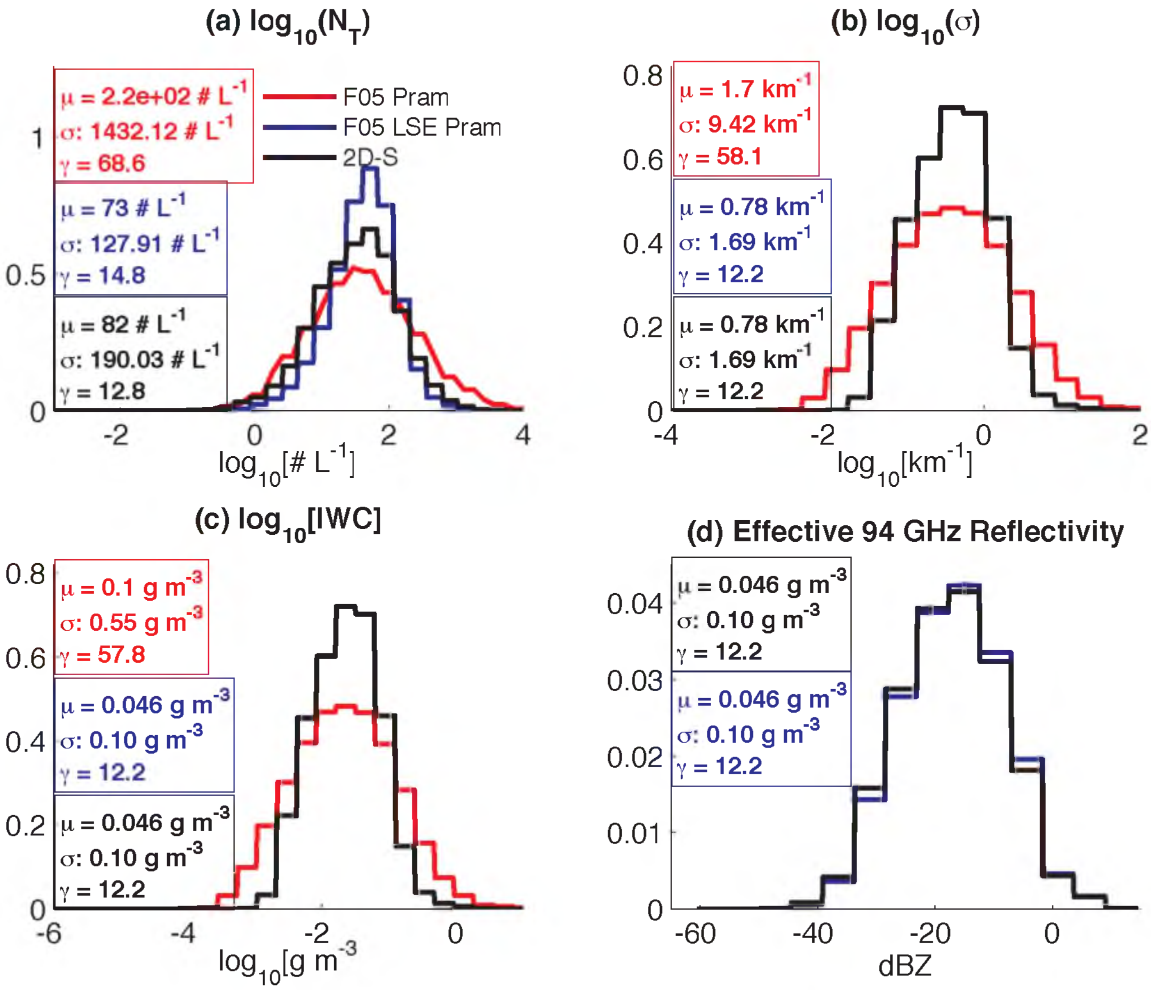

Fig. 3.8: Marginal pdfs of quantities computed directly from 2D-S data (black) as well as computed using parameterized values (using reflectivity and temperature) for both D_m and N_0^*, via $F_3(x)$ (red); parameterized values for both D_m and N_0^* (using synthetic extinction and radar reflectivity measurements), via $F_3(x)$ (blue). (a) total number concentration, (b) shortwave extinction coefficient, (c) ice water content, (d) radar reflectivity.

and skewness than are the distributions of quantities computed using the reflectivity/temperature parameterization.

Summary

A parameterization of a “universal” particle size distribution (PSD), based on F05’s normalization of individual PSDs by their second and third noncentral moments, is given. This parameterization constitutes an improvement on earlier, similar works in that a large database of PSDs is used that was collected with new instrumentation and processed for shattered particle mitigation.

By means of this parameterization, all the measured PSDs are boiled down to one shape. However, the natural variability of ice PSDs remains unavoidable, as seen by the orders-of-magnitude spread in Fig. 3.1. Figures 3.5, 3.7, and 3.8 demonstrate that knowledge of one or two moments (either from a remote measurement or from a model) are not enough to pin down a PSD precisely enough to reproduce all of its moments, even when the moments are known with surety (Fig. 3.5). However, two moments and a universal shape provide a significant improvement over the parameterization scheme of Delanoe et al. (2005), which uses only a radar reflectivity measurement and a temperature to parameterize the normalizing and scaling factors of a universal PSD: the temperature parameterization of D^* adds significant bias to the distributions of reconstructed, PSD-based quantities. It is therefore concluded that, where possible, two independent remote sensing measurements—or two modeled PSD moments—in conjunction with the trimodal, universal PSD presented here, constitute a preferable mechanism for parameterizing cirrus PSDs.

Finally, despite earlier works (e.g., Westbrook et al., 2004a,b), which predict a gamma-distribution tail to the universal, normalized ice PSD, it was found here that the tail is best described by an inverse gamma distribution. Investigating the reason for this is beyond the scope of this work, but, as pointed out earlier in this paper, there are mechanisms at play in a cloud for PSD evolution other than aggregation, and the 15-second temporal averages used to construct the measured PSDs in this study may also play a role in transforming the shape of the universal PSD's tail.

CHAPTER 4

COMPARISON OF THE 2D-S TO OLDER DATASETS

Background

The shattering of ice particles on probe tips and inlets and on aircraft wings (Korolev et al., 2011) has rendered many historical cirrus microphysical datasets suspect [see, e.g., McFarquhar et al. (2007) and Jensen et al. (2009)] due to the possibility of such shattering's leading to artificially inflated measurements of small ice particle concentrations. The important role that would be played in cloud microphysical and radiative properties, if the smallest ice particles were indeed always present in such large numbers as they have been measured, has been noted in a number of studies. For instance, Heymsfield et al. (2002) reported that small particles dominated total particle concentrations at all times in their analysis of data from multiple Tropical Rainfall Measuring Mission (TRMM) field campaigns. The same phenomenon was noted in midlatitude cirrus in Field (2000). Lawson et al. (2006a), using data from midlatitude cirrus clouds, also reported large numbers of small particles, such that particle concentrations ranged from ~ .2 cm^{-3}–1 cm^{-3}. They reported that particles smaller than 50 μm were responsible for 99% of the total number concentration, 69% of the extinction, and 40% of the IWC in their midlatitude dataset. In looking at several representative cirrus cases sampled during the INterhemispheric differences in Cirrus properties from Anthropogenic emissions (INCA) campaign of 2000–2002, Gayet et al.

(2002) found average ice particle concentrations as high as 10 cm^{-1} and estimated that particles having maximum dimensions smaller than 15.8 μm resulted in about 38% of measured shortwave extinction. Gayet et al. (2004) and Gayet et al. (2006), in considering INCA midlatitude cirrus data taken from both the Northern and Southern Hemispheres during March and April, 2000, estimated that particles smaller than 20 μm accounted for about 35% of observed extinction.

The use of particle interarrival times within an optical probe (Cooper, 1978; Field et al., 2003; Field et al., 2006) has become a tool for the removal of shattered ice particles from PSD samples [see Baker et al. (2009) for a simple explanation of this technique with respect to raindrops]. Interarrival time statistics were used to mitigate the effects of shattering on several of the ice particle probes during the NASA TC^4 field campaign, and lower particle number concentrations were reported by Lawson et al. (2010) using that dataset than had been previously reported by Lawson et al. (2006a). However, as indicated in Korolev et al. (2011) and in Jensen et al. (2009), interarrival time statistics alone are not enough to deal with the shattering problem: probes designed with modified probe tips and without inlet shrouds should be used, and they must be placed away from leading aircraft wing edges in order to minimize the entering of shattered ice crystals into the instruments' sample volumes because small particles generated by shattering on aircraft parts will likely not disperse enough to be filtered out by shatter-recognition algorithms (Jensen et al., 2009).

In this chapter, an indirect comparison is made between a climatology of 2D-S-measured cirrus PSDs, described in Chapter 2, and a large collection of older datasets, collected from the early 1990s through the early 2000s (with older Particle Measurement

Systems (PMS) 2DC and 2DP probes) and used in Delanoe et al. (2005; hereinafter referred to as D05), via the normalization scheme detailed in D05. The question to be addressed is whether the older datasets differ statistically from datasets collected with newer and more advanced probes and processing techniques. The comparison is made by applying a cirrus PSD statistical model, developed in D05 using the older datasets, to the newer 2D-S data, thereby effectively simulating 2DC measurements. The statistical model of D05 takes PSD moments as inputs and produces a parameterized 2DC PSD. Therefore, the requisite moments from the 2D-S data are calculated and applied to the D05 model in order to give a parameterized view of what the 2DC would have measured had it been collecting data next to the 2D-S. First, the normalization and parameterization scheme used by D05 will be discussed, and the effects of not using a precipitation probe in this study will then be examined. Finally, the results of the comparison are demonstrated.

Normalization and Parameterization

Though modified probe tips were not consistently used on the 2D-S during the three field campaigns heretofore mentioned, all of the data are corrected for shattering artifacts via particle interarrival time analysis. See Chapter 2 for other details concerning the 2D-S dataset used here. As in Chapter 3, save in one instance, all quantities used here that are derived from 2D-S PSDs are computed using parametric fits to the PSDs (see Appendix D).

Variations on the basic normalization procedure for a PSD may be found in a number of places, including in Chapter 2 and in D05. Here, following D05, a PSD $n_D(D)$, whose independent variable is ice particle maximum dimension, may be transformed to a distribution $n_{De}(D_e)$, whose independent variable is equivalent melted diameter. To do so, the dimensional/density relationship given in Chapter 3 (which relationship was borrowed from D05) is used. This density-dimensional relationship stems from relationships published by Locatelli and Hobbs (1974) and Brown and Francis (1995) for aggregate particles. Setting masses equal as in D05 results in the independent variable transformation

$$D_e = \left(\frac{a_m D^{b_m}}{\rho_w} \right)^{\frac{1}{3}} D, \tag{4.1}$$

where ρ_w is the density of water. This transformation ensures that both total number concentration (N_T) and ice water content (IWC) can be obtained by using the PSD in either form:

$$N_T = \int_0^\infty n_D(D)dD = \int_0^\infty n_{D_e}(D_e)dD_e \tag{4.2}$$

$$\text{IWC} = \frac{\pi}{6}\int_0^\infty aD^{b+3} n_D(D)dD = \frac{\pi}{6}\int_0^\infty \rho_w D_e^3 n_{D_e}(D_e)dD_e. \tag{4.3}$$

Since the number of particles is not changed by the transformation and since the transformation is based on mass-equivalent spheres, these results are to be expected. However, the mass-equivalent spherical transformation will cause computations of other physical quantities using the two different versions of the size distribution to differ one from the other. For example, a distribution of spheres will evidently not produce the same shortwave extinction coefficient as the real distribution; i.e., using an area-dimensional relationship $A(D) = {}_{aA}D^{bA}$ for the nonspherical distribution to arrive at the extinction coefficient (see Appendix F),

$$\sigma = \int_0^\infty 2a_A D^{b_A} n_D\left(D\right)dD \neq \int_0^\infty 2\pi\left(\frac{D_e}{2}\right)^2 n_{D_e}\left(D_e\right)dD_e. \tag{4.4}$$

This problem is noted in D05 in conjunction with the definition given therein of effective radius.

Similarly, radar reflectivity computed under the assumption of spherical particles is also incorrect. This is demonstrated in Fig. 4.1, which contrasts forward-modeled radar reflectivities, computed from 2D-S data taken during MACPEx, SPartICus, and TC^4, using two different 94 GHz radar forward models. For the first model, Mie theory was applied to the PSDs expressed in terms of equivalent mass spheres using the Bohren and Huffman Mie (BHMIE) algorithm (Bohren and Huffman, 1983) and 1.784 – i(0.00228) for the refractive index of ice (Liu and Illingworth, 1997). The second, more realistic model uses PSDs expressed in terms of particle maximum dimension and a set of power-law fits to T-matrix computations of backscatter cross section (Matrosov, 2007; Matrosov et al., 2012; Hammonds, 2013; Posselt and Mace, 2013) to compute reflectivity, assuming an air/ice dielectric mixing model and that all particles are prolate spheroids with aspect ratios of 0.7 (Korolev and Isaac, 2003; Westbrook et al., 2004a; Westbrook et al., 2004b; Hogan et al., 2012). A bias of about 2.2 dBZ is clearly seen between the two models, which is comparable to the measurement error of many radars. Thus, the effective radar reflectivity is more properly modeled using appropriate dimensional-backscatter cross-section power laws suited to the natural PSDs (see

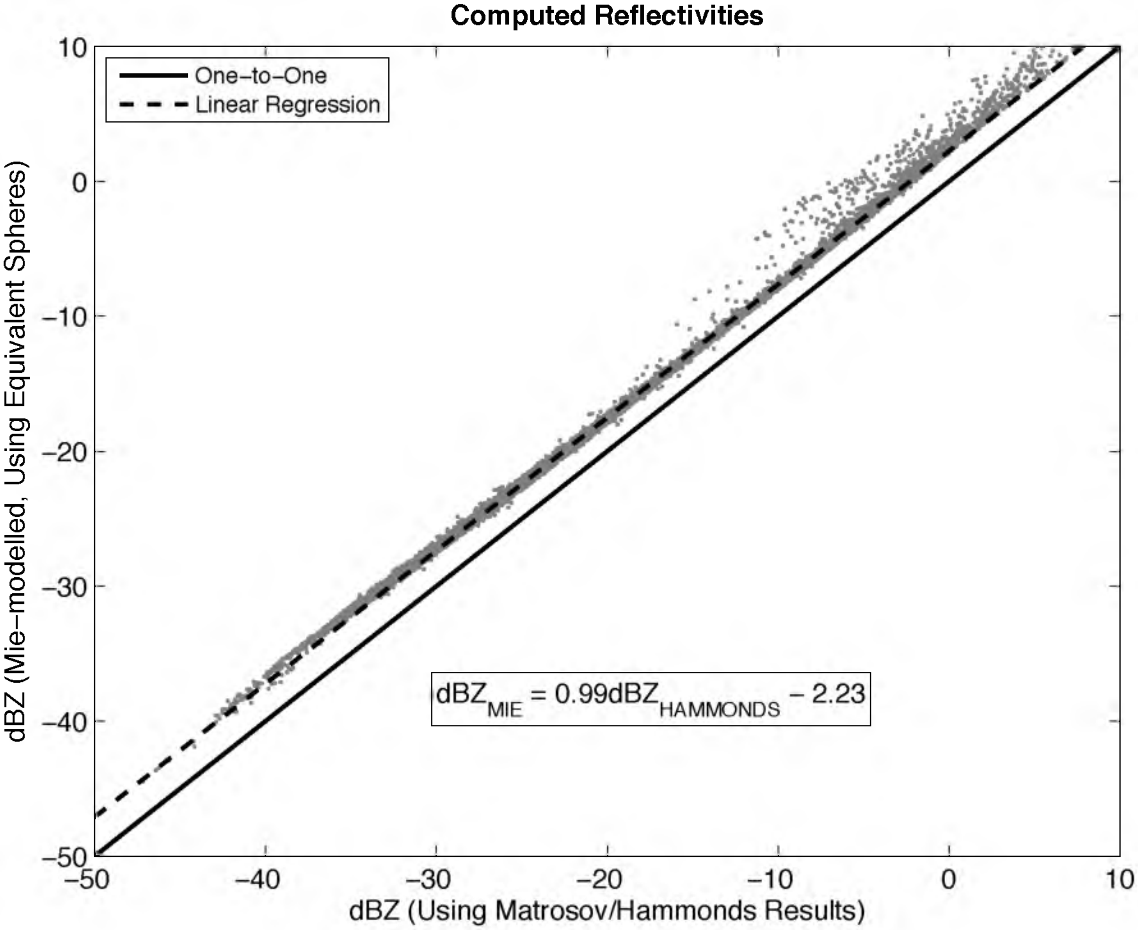

Fig. 4.1: Contrast of forward-modeled 94 GHz radar reflectivity using the spherical assumption versus using an oblate spheroid with mixed permittivity assumption.

Appendix F for details):

$$Z_e = \frac{10^8 \lambda^4}{\left|K_w\right|^2 \pi^5} \int_0^\infty a_z D^{\frac{3b_z+b_m}{3}} n_{D_e} \left[\left(\frac{a_m}{\rho_w}\right)^{\frac{1}{3}} D^{\frac{b_m+3}{3}} \right] \left(\frac{a_m}{\rho_w}\right)^{\frac{1}{3}} \left(\frac{b_m+3}{3}\right) dD, \tag{4.5}$$

where the units of λ are mm, the units of Z_e are mm^6 m^{-3}, and all other units are cgs.

With these caveats, then, and following D05, the transformed PSDs have their independent variable scaled by mass-mean diameter

$$D_m = \frac{\int_0^\infty D_e^4 n_{D_e}\left(D_e\right) dD_e}{\int_0^\infty D_e^3 n_{D_e}\left(D_e\right) dD_e} \tag{4.6}$$

and their ordinates scaled by

$$N_0^* = \frac{4^4}{\Gamma(4)} \frac{\left[\int_0^\infty D_e^3 n_{D_e}\left(D_e\right) dD_e\right]^5}{\left[\int_0^\infty D_e^4 n_{D_e}\left(D_e\right) dD_e\right]^4}, \tag{4.7}$$

so that

$$n_{D_e}\left(D_e\right) = N_0^* F\left(x = \frac{D_e}{D_m}\right). \tag{4.8}$$

In Eq. 4.8, *F(x)* is, ideally, the universal, normalized PSD (see Chapter 3). Via numerically computed moments, Eqs. 4.6–4.8 are used to normalize the measured, mass-equivalent spherical PSDs.

The measured 2D-S PSDs from TC^4, SPartICus, and MACPEx were normalized according to the procedure described in section 4.1 of D05. Two-dimensional histograms of the results, as well as for all three datasets combined, are shown in Fig. 4.2, and from these follow the overall, normalized 2D-S PSD that is to be compared to the simulated 2DC. First, the bin centers and bin widths of the 2D-S were transformed via Eq. 4.1. Then, each measured PSD was transformed by scaling from D-space to D_e-space, attempting to keep N_T and IWC computed using the original and the transformed PSDs the same (see Appendix F). After their transformation, all of the PSDs from the three datasets were normalized and were then grouped into normalized diameter bins of $\Delta x_i = 0.10$. In D05, data taken with the 2DC cloud particle and 2DP precipitation probes were combined to give PSDs ranging from 25 μm to 6400 μm. Here, no precipitation probe data are used. How, then, does not including precipitation probe data affect the comparison here with D05? The answer to this question will be postponed until later in the chapter so as to be given in context of the comparison of D05 with the 2D-S alone.

The two-dimensional histograms shown in Fig. 4.2 are overlaid with their mean normalized PSDs (cf. Figs. 1 and 2 in D05; here the color map is truncated at 75% of the highest number of samples in a bin so as to increase contrast). The mean, normalized PSD for the three datasets is repeated in Fig. 4.3 as the set of solid curves (cf. Fig. 3 of D05). This serves as the empirical universal, normalized PSD $F_{\sim 2DS}(x)$ derived from the 2D-S using the methodology of D05, which distribution and the quantities derived from it serve as the data that represent the more modern 2D-S with shattering artifacts removed using particle interarrival time filtering. The subscript *~2DS* is used hereafter to represent quantities derived using $F_{\sim 2DS}(x)$.

As a check of D05's normalization procedure, the individual normalized and

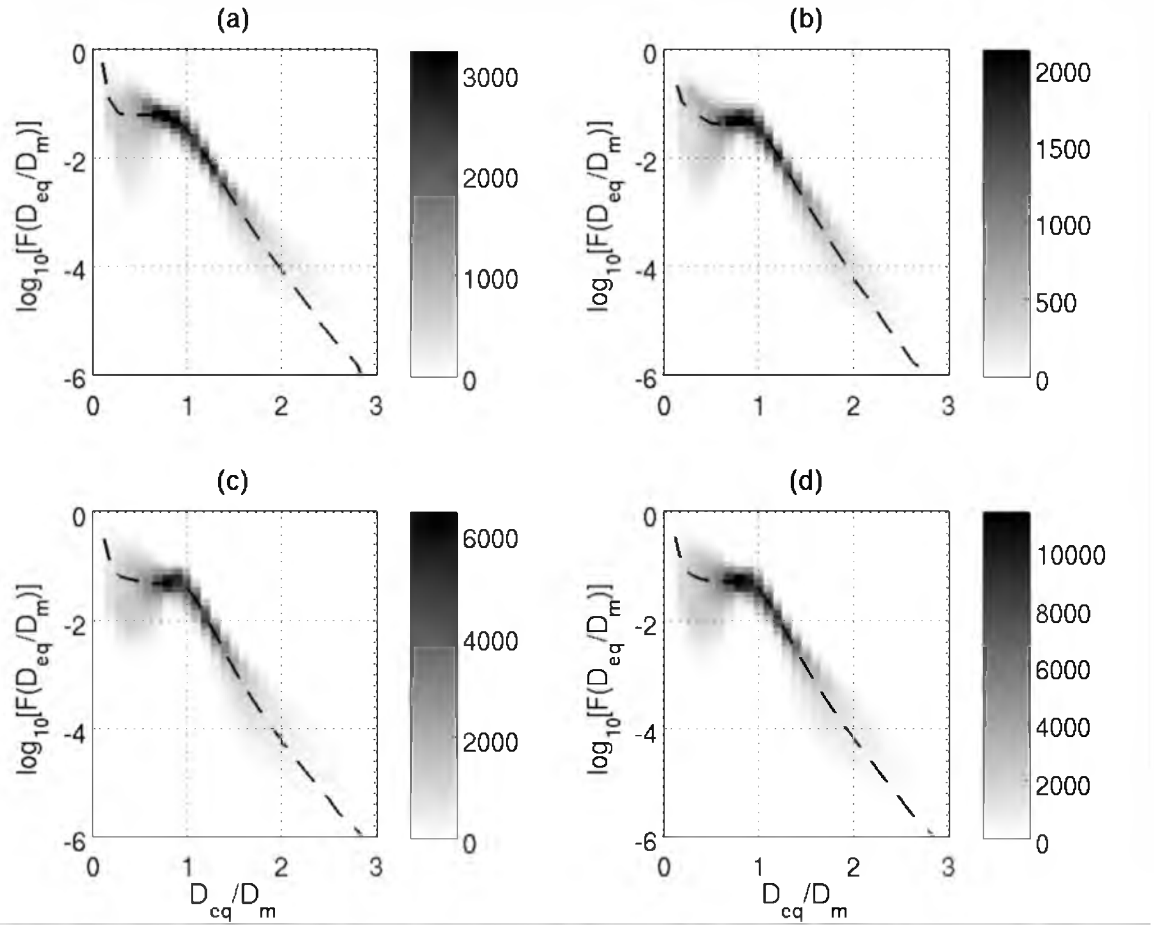

Fig. 4.2: Histograms of normalized PSDs from each flight campaign, overlaid with their mean, normalized PSDs. The color map is truncated at 75% of the highest number of samples in a bin so as to increase contrast. (a) TC^4, (b) MACPEx, (c) SPartICus, (d) all data combined.

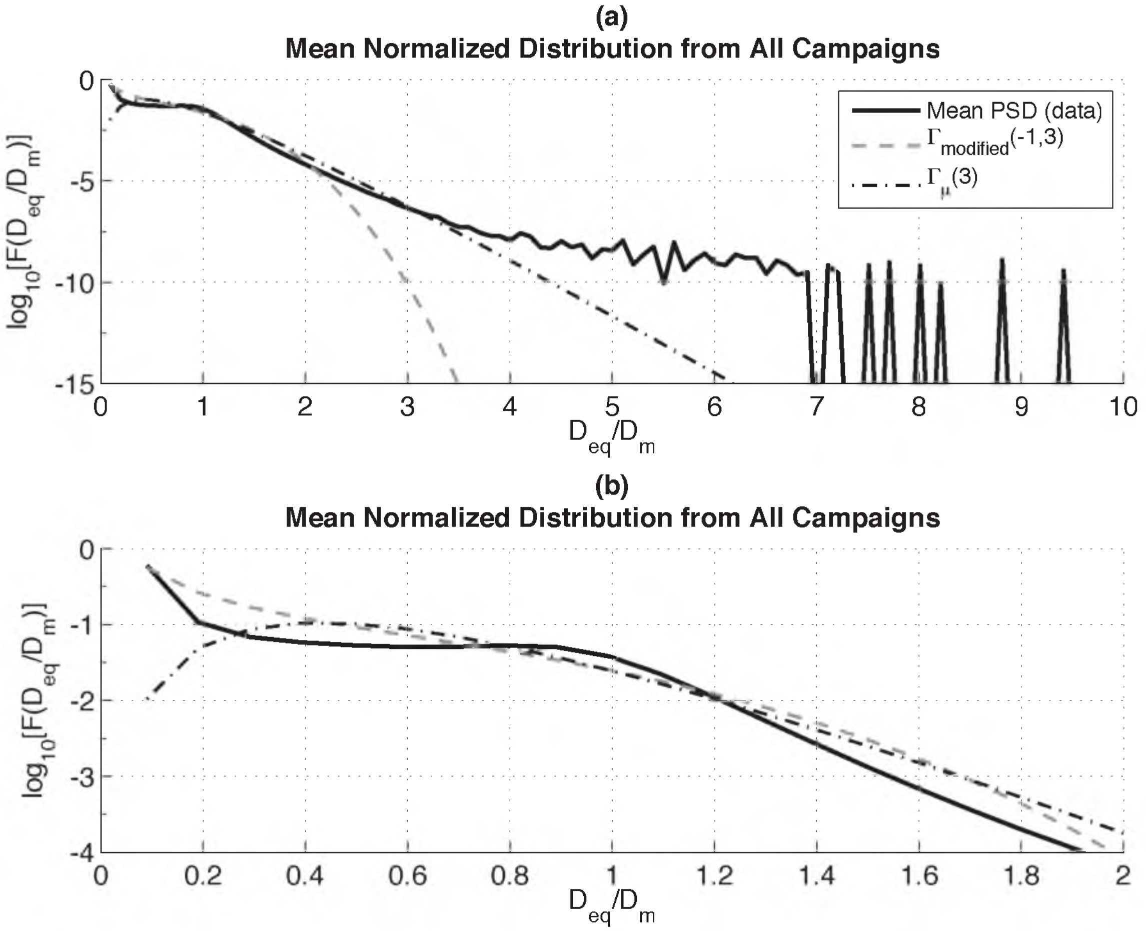

Fig. 4.3: The mean, normalized PSD from all three datasets combined (black curve), overlaid with two parameterizations from D05: the gamma-mu parameterization (dash-dotted curve) and the modified gamma parameterization (dashed curve). Panel (b) is a zoom-in on a portion of panel (a).

transformed PSDs from all three datasets [resulting from the application of Eqs. 4.6–4.8 to each measured and transformed $n_{De}(D_e)$] were used along with their corresponding values of N_0^* and D_m in order to compute values of $\mathrm{N_T}$ and IWC. These computations are scattered against the same quantities, computed directly from the untransformed PSDs (using the binned data to compute $\mathrm{N_T}$ and applying the density-dimensional relationship in Eq. 3.4 to the unimodal PSD fits to compute IWC), as shown in Fig. 4.4. There is a bias in $\mathrm{N_T}$ that is quantified on the figure, but the agreement is sound, and the normalization procedure of the 2D-S data is thus far validated.

Right off the bat, there are some important qualitative observations that can be made from examining the overlaid mean curves in Fig. 4.2 and $F_{\sim 2DS}(x)$ (solid curves) in Fig. 4.3. First, in comparison with Fig. 3 of D05, the concentrations of particles at the smallest scaled diameters are, on average, about an order of magnitude or more lower with data from the 2D-S than they are using data from the older instruments used in D05. From this observation it is surmised that while there continue to be relatively high numbers of small ice particles, the number has decreased in the newer datasets due to the exclusion of shattered ice crystals. It can also be seen in Fig. 4.3 that the shoulder in the normalized PSDs in the vicinity of $x \sim 1.0$ exists in the newer data as it does in the data used in D05. It is worth noting, though, that the shoulder exists in the one tropical dataset used here (TC^4, see Fig. 4.2), whereas it is absent or much less noticeable in the tropical datasets used in D05.

Three parametric fits for $F(x)$ derived from normalized 2DC and 2DP data are given in D05, two of which are repeated here and shown in Fig. 4.3: the gamma-μ form (F_μ) and the modified gamma form ($F_{\alpha\beta}$). Formulae for computing bulk and radiative

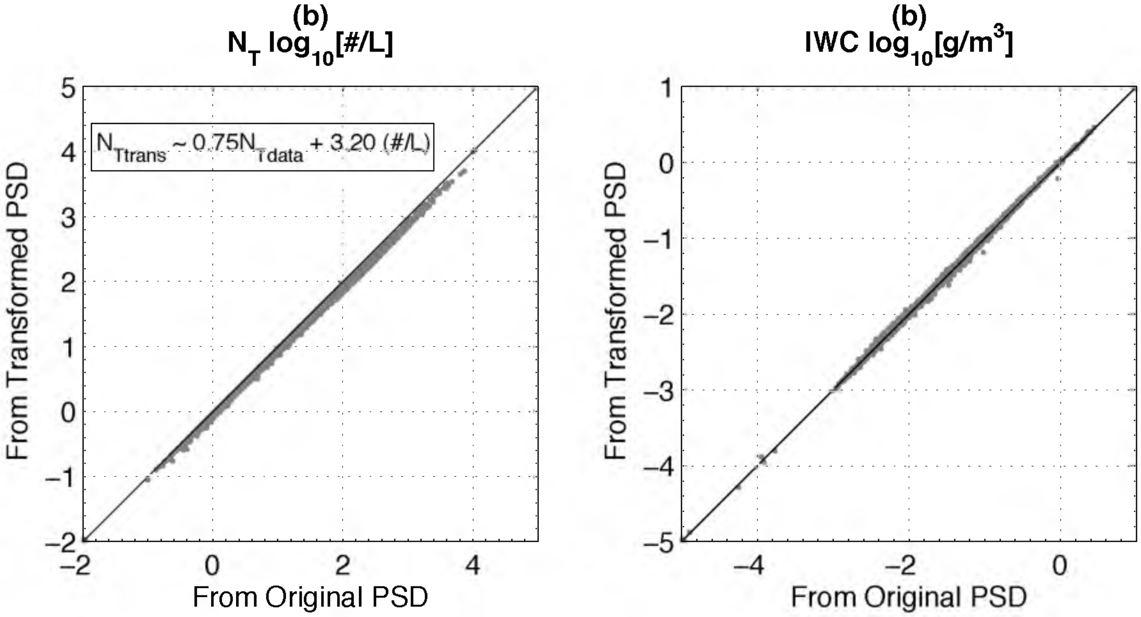

Fig. 4.4: Computation of preserved-upon-transformation quantities using the individual transformed and normalized PSDs along with the true values of N_0^* and D_m from each PSD vs. the true values of the same quantities computed directly from each PSD. (a) Total number concentration, (b) Ice water content.

quantities using these parametric forms are given in Appendix F.

$$F_{\mu}(x) = \frac{\Gamma(4)}{4}\frac{(4+\mu)^{4+\mu}}{\Gamma(4+\mu)}x^{\mu}\exp\left[-(4+\mu)x\right] \tag{4.9}$$

$$F_{\alpha,\beta}(x) = \beta\frac{\Gamma(4)}{4}\frac{\Gamma\left(\frac{\alpha+5}{\beta}\right)^{4+\alpha}}{\Gamma\left(\frac{\alpha+4}{\beta}\right)^{5+\alpha}}x^{\alpha}\exp\left\{-\left[\frac{\Gamma\left(\frac{\alpha+5}{\beta}\right)}{\Gamma\left(\frac{\alpha+4}{\beta}\right)}\right]^{\beta}\right\} \tag{4.10}$$

Fortuitously, D05's modified gamma fits the 2D-S data better than it does the older data at the smallest normalized sizes (cf. Fig. 2 in D05). Notice that neither of D05's parametric shapes correctly catches the shoulder in the newer data, though the modified gamma was formulated to (better) catch a corresponding shoulder in the older data. Since $F_{\alpha,\beta} = F_{(-1,3)}$ (Eq. 4.10) and $F_{\mu} = F_3$ (Eq. 4.9) were formulated to approximate PSDs given by a combined 2DC and 2DP database given two noncentral PSD moments that could be either predicted by a model or otherwise observed, we make the assumption that if we take the same two moments derived from a 2D-S PSD and apply them to Eqs. 4.9 and 4.10 (as in Eq. 4.8), then we have effectively simulated the transformed PSD that a combined 2DC and 2DP would have observed had they been present with the 2D-S. The subscript $\sim 2DC$ is used hereafter to represent quantities that simulate 2DC-2DP data in this way.

A comparison of PSD properties computed directly from the 2D-S with PSD properties computed using the true N_0^* and D_m (derived directly from the binned 2D-S data) applied to Eqs. 4.9 and 4.10 was made. This constitutes a comparison of the 2D-S with a parameterized 2DC-2DP dataset. The extinction coefficient, IWC, and 94 GHz radar reflectivity compare well between the data and both parametric shapes (not shown). IWC matches by design (under the normalization scheme of D05, IWC is independent of normalized PSD shape). Computed and parameterized radar reflectivities have a slightly skewed and slightly non-one-to-one relationship (this is an important consideration in the parameterization of N_0^* by Z given in D05—see Appendix F.) As for total number concentration, it is the least certain computation (see Fig. 4.5), but the gamma-μ shape is entirely wrong in attempting to reproduce this quantity, so this shape is not used hereafter, and $F_{\alpha\beta}(x) = F_{(-1,3)}(x)$ is the shape used to simulate the 2DC-2DP.

Figure 4.6 shows the mean relative error and the standard deviation of the relative error (cf. Fig. 5 of D05) between the 2D-S-derived and parameterized (via $F_{\alpha\beta}(x)$) 2DC-derived quantities mentioned in the previous paragraph as well as between the effective radius (as defined in D05). The mean relative error in total number concentration is rather large at ~51%, and the mean relative error in radar reflectivity Z, at ~23%, is larger than that shown in Fig. 5 of D05 (less than 5% there) but, at about 2 dB, is within the error of most radars. This may well be due to the overestimation of $F(x)$ by $F_{\alpha\beta}(x)$ between normalized sizes of about 1.2 and 2 (see Fig. 4.3b). (Both here and in D05, $F_{\alpha\beta}(x)$ falls off much more rapidly than $F(x)$ above a normalized diameter of two. However, it is deduced from Figs. 2 and 5 in D05 that this roll-off is not responsible for the large mean relative error in Z shown in Fig. 4.6.)

The mean relative error in effective radius shown in Fig. 4.6 is approximately –9%, whereas it is apparently nil in Fig. 5 of D05. Effective radius is defined in D05 as the ratio of the third to the second moments of the spherical-equivalent PSDs and is

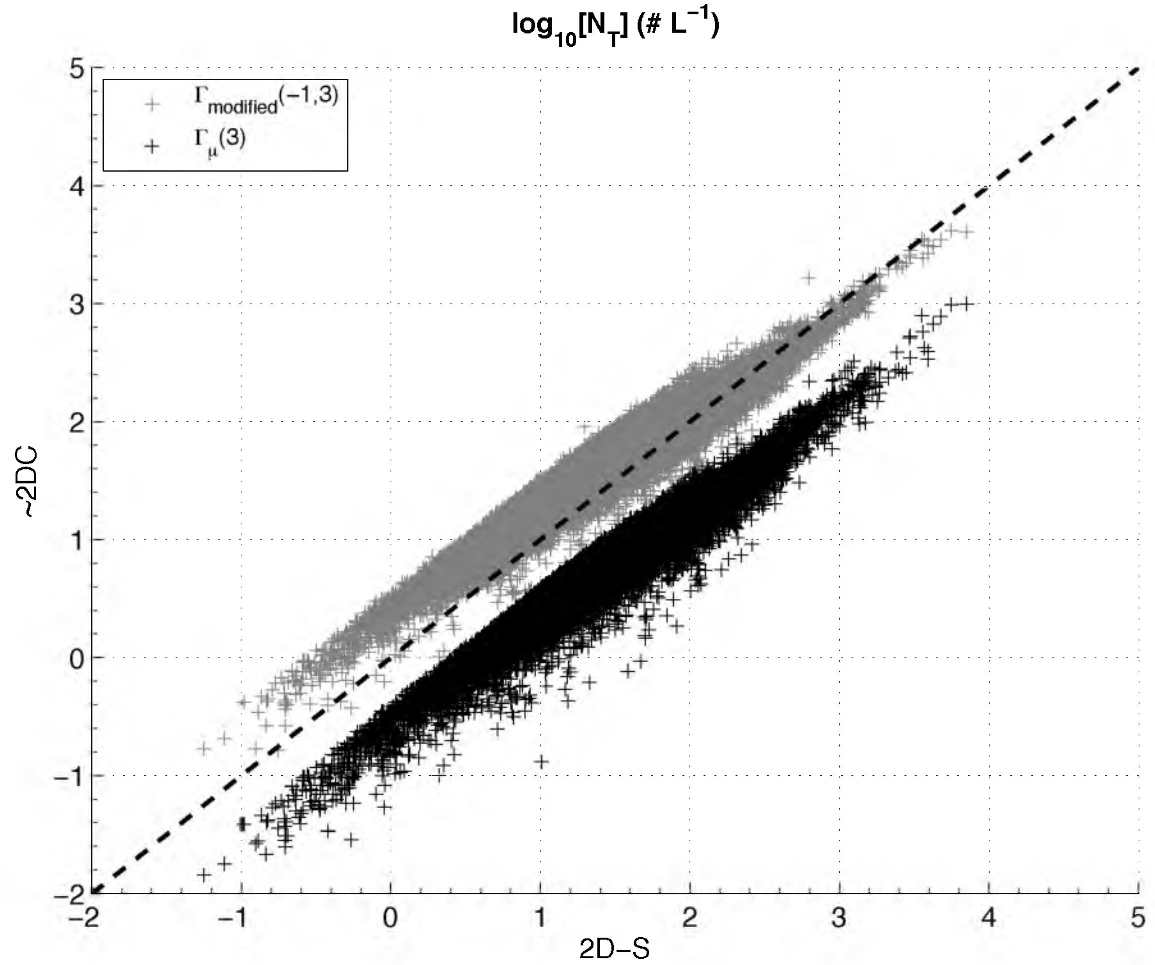

Fig. 4.5: Total number concentration computed using the parameterized universal PSDs from D05 (gamma-μ in black, modified gamma in gray) along with true values of N_0^* and D_m (from the 2D-S data) scattered vs. total number concentration computed directly from untransformed 2D-S data.

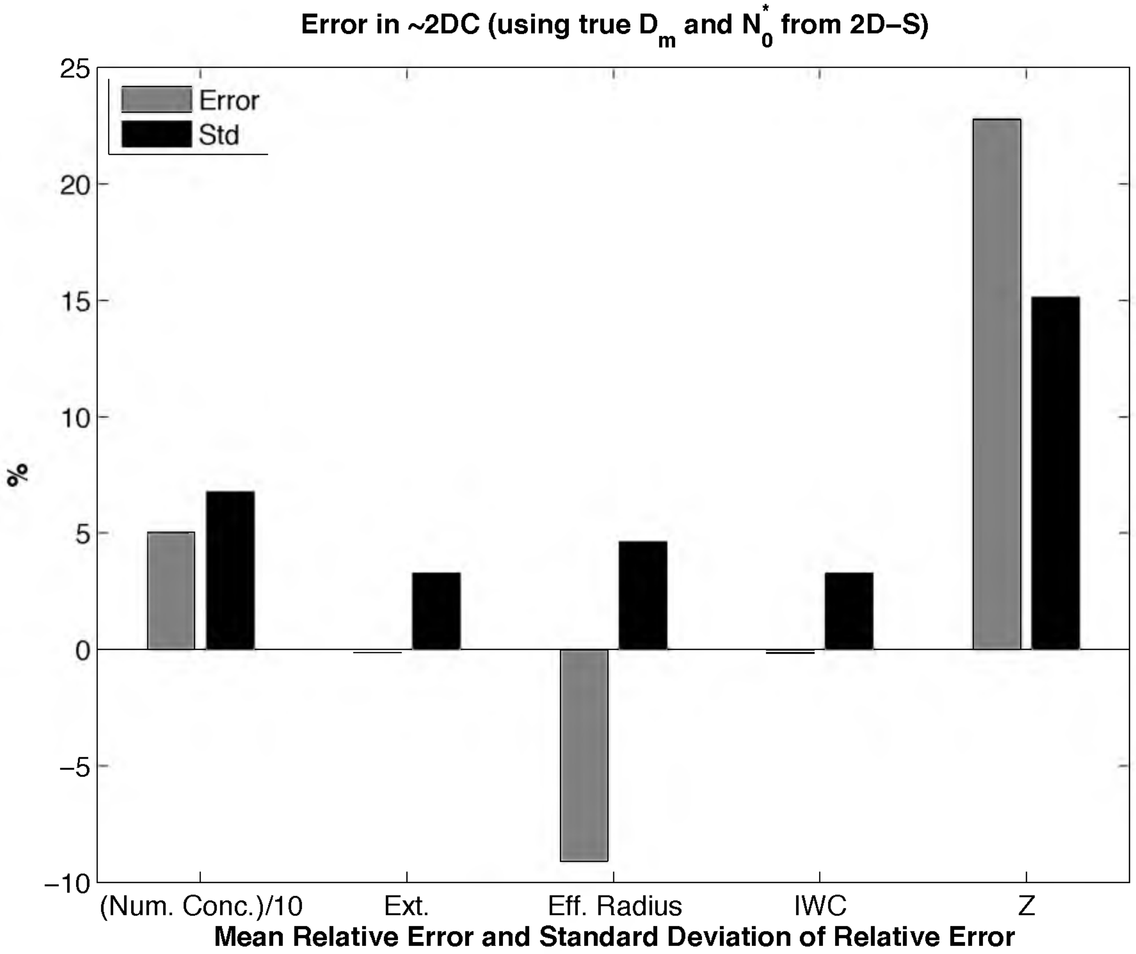

Fig. 4.6: Mean relative error (gray) and standard deviation of the relative error (black) between total number concentration (divided by 10), effective radius, IWC, and Z as computed directly from the 2D-S and as computed from the modified-gamma universal PSD shape and the true N_0^* and D_m computed from the 2D-S data.

therefore a weighted mean of the PSD. The negative sign on the relative error indicates that, on average, $F_{\alpha,\beta}(x)$ is underestimating the effective radius of the PSDs measured by the 2D-S, whereas, for the older datasets used in D05, the effective radius is spot-on in the average. Therefore, there is a significant difference between the new 2D-S datasets and the older 2DC datasets used in D05 in the ratio of large particles to small particles, even when precipitation probe data is not combined with the 2D-S.

Impact of Not Using Precipitation Probe Data

To more formally investigate the impact of not combining precipitation probe data with the 2D-S data, data from the Precipitation Imaging Probe (PIP) were combined with data from the 2D-S using the TC^4 dataset. This campaign was chosen due to its tending to occur at warmer temperatures, in a more convective environment, and at lower relative humidities (Chapter 2): so if large particles are going to matter, they should matter for TC^4. Figure 4.7 shows, similar to Fig. 4.3, the normalized size distribution for the 2D-S alone, the 2D-S combined with the PIP, and $F_{\alpha,\beta}(x)$. The combined data do not show the average, normalized PSD between zero and one digging as low as for the 2D-S alone, but it does show similar numbers of particles at the very smallest normalized sizes, and the shoulder is in the same location. Beginning at about $x = 1.2$, the 2D-S-PIP normalized distribution is higher than the 2D-S-alone normalized distribution, and it continues out to about $x = 10$, whereas the 2D-S-alone distribution ends shy of $x = 5$. In either case, the modified gamma distribution misses what is greater than about $x = 2$. This roll-off, along with the fact that the mean normalized and transformed 2D-S/PIP combination appears to be more similar to $F_{x2DS}(x)$ than it does to $F_{\alpha,\beta}(x)$, would seem to indicate that a parameterization of $F(x)$ based off the 2D-S alone is comparable to the

(a)
Mean Normalized Distribution from TC^4

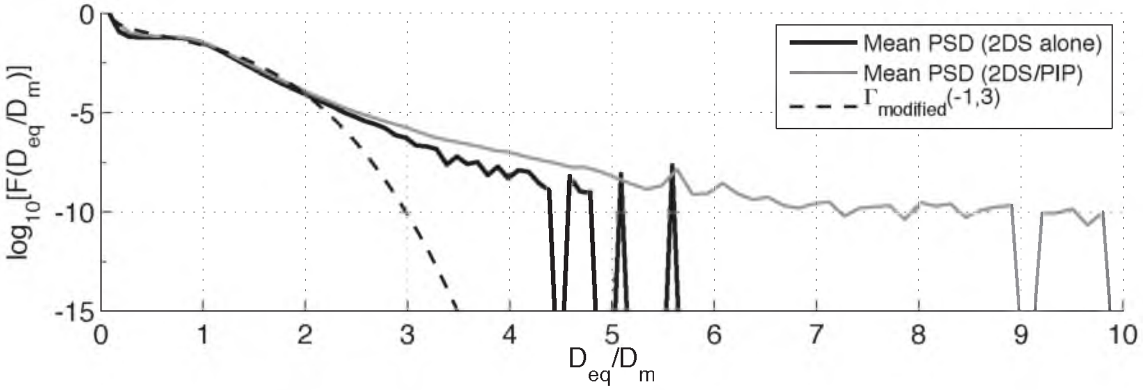

(b)
Mean Normalized Distribution from TC^4

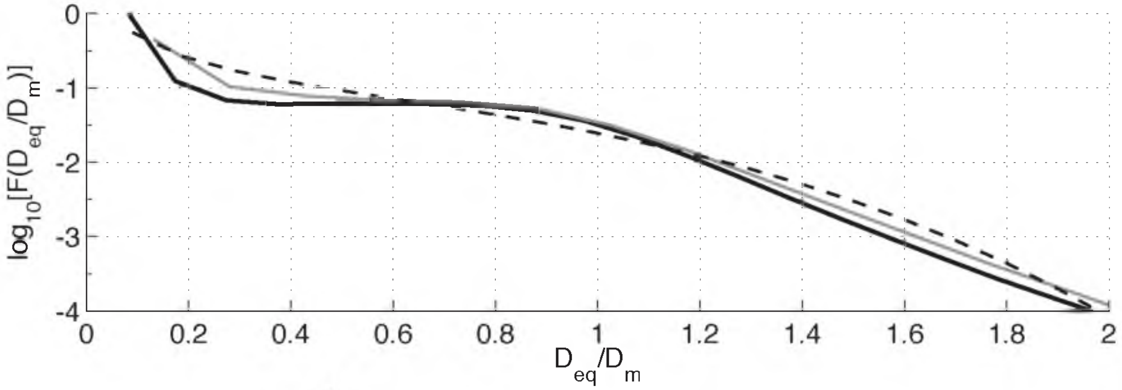

Fig. 4.7: Data from TC^4 alone. The mean, normalized PSD from the 2D-S (black curve) is overlaid with the mean, normalized PSD obtained from combining the 2D-S with the PIP (gray curve) and the modified gamma parameterization from D05 (dashed curve). Panel (b) is a zoom-in on a portion of panel (a).

2DC/2DP-based $F_{\alpha\beta}(x)$ parameterization.

In support of this assertion, Fig. 4.8 shows the penalty in radar reflectivity, computed directly from data using the Hammonds/Matrosov/Posselt/Mace approach described earlier, incurred by using only the 2D-S instead of the combination of the 2D-S and of the PIP (which penalty is in the neighborhood of 1 dB). The true N_0^* and D_m computed from each of the 2D-S PSDs alone and from the combined PSDs from TC^4 were used, along with $F_{\alpha\beta}(x)$, to compute total number concentration, extinction coefficient, IWC, and 94 GHz effective radar reflectivity. This amounts to two different simulations ~2DC: one including the PIP and one not. The results are shown in Fig. 4.9. The distributions are very similar, with the exception of the reflectivity distributions, whose means are separated by less than 1 dBZ. It is concluded that the cloud filtering technique has resulted in PSDs that are satisfactorily described by the 2D-S alone, at least in the case of this comparison.

Final Result and Conclusion

In D05, complete parameterization of a 2DC/2DP-measured PSD is achieved by using the universal shape $F_{\alpha\beta}(x)$ along with N_0^* parameterized by radar reflectivity and D_m parameterized by temperature. A similar parameterization scheme (also based on radar reflectivity and temperature) for the 2D-S (based on Field et al., 2005) is outlined in Chapter 3. Figure 4.10 shows the results of computing PSD-based quantities using the fully parameterized 2D-S (red, labeled "*x2DS*"), the fully parameterized 2DC (blue, labeled "*x2DC*"), and directly from the 2D-S data (black). Again, probability density functions of 94 GHz effective radar reflectivity match because they are forced to by the two instrument parameterizations. Otherwise, biases exist between computations based

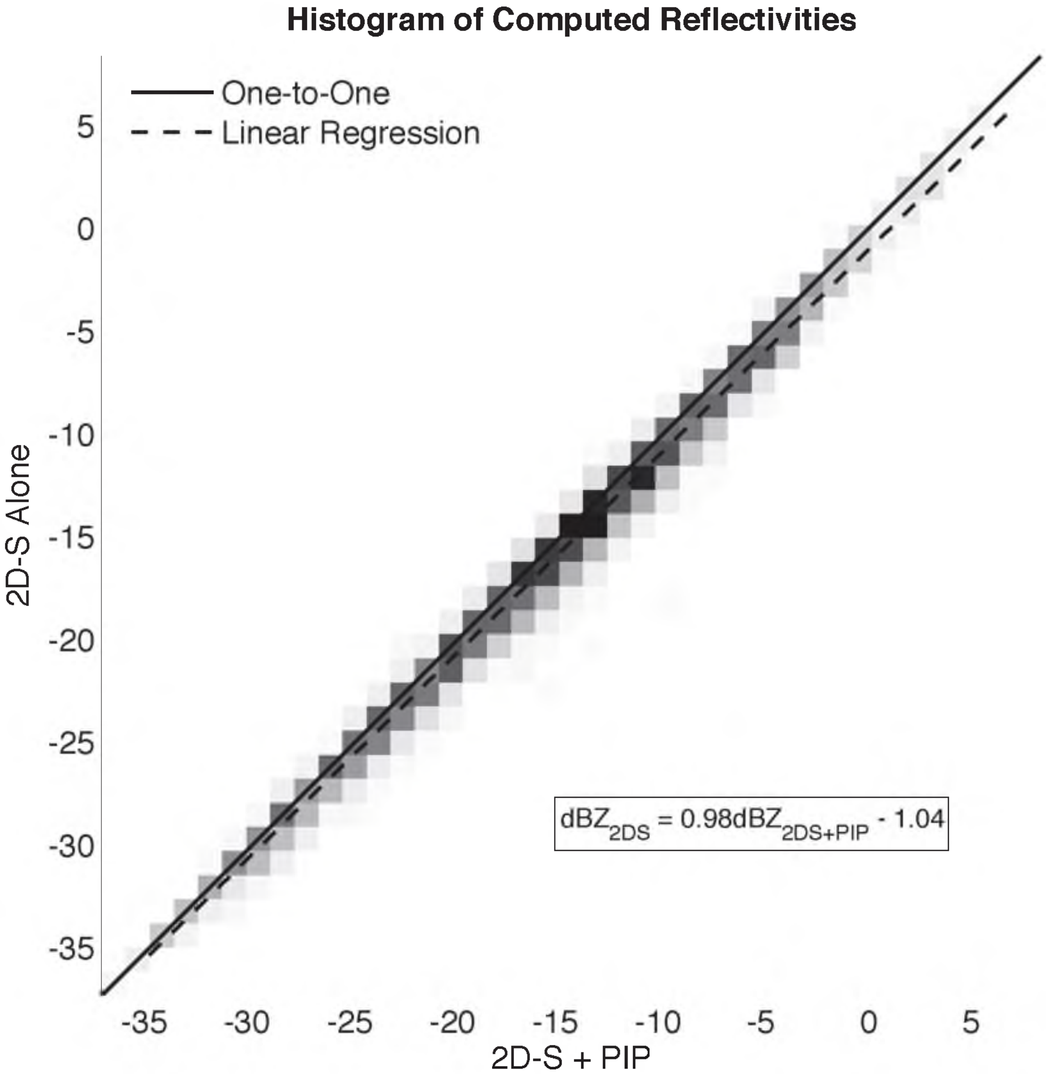

Fig. 4.8: Two-dimensional histogram of 94 GHz effective radar reflectivity computed, using the Hammonds/Matrosov approach, from the 2D-S alone versus that computed from the 2D-S combined with the PIP.

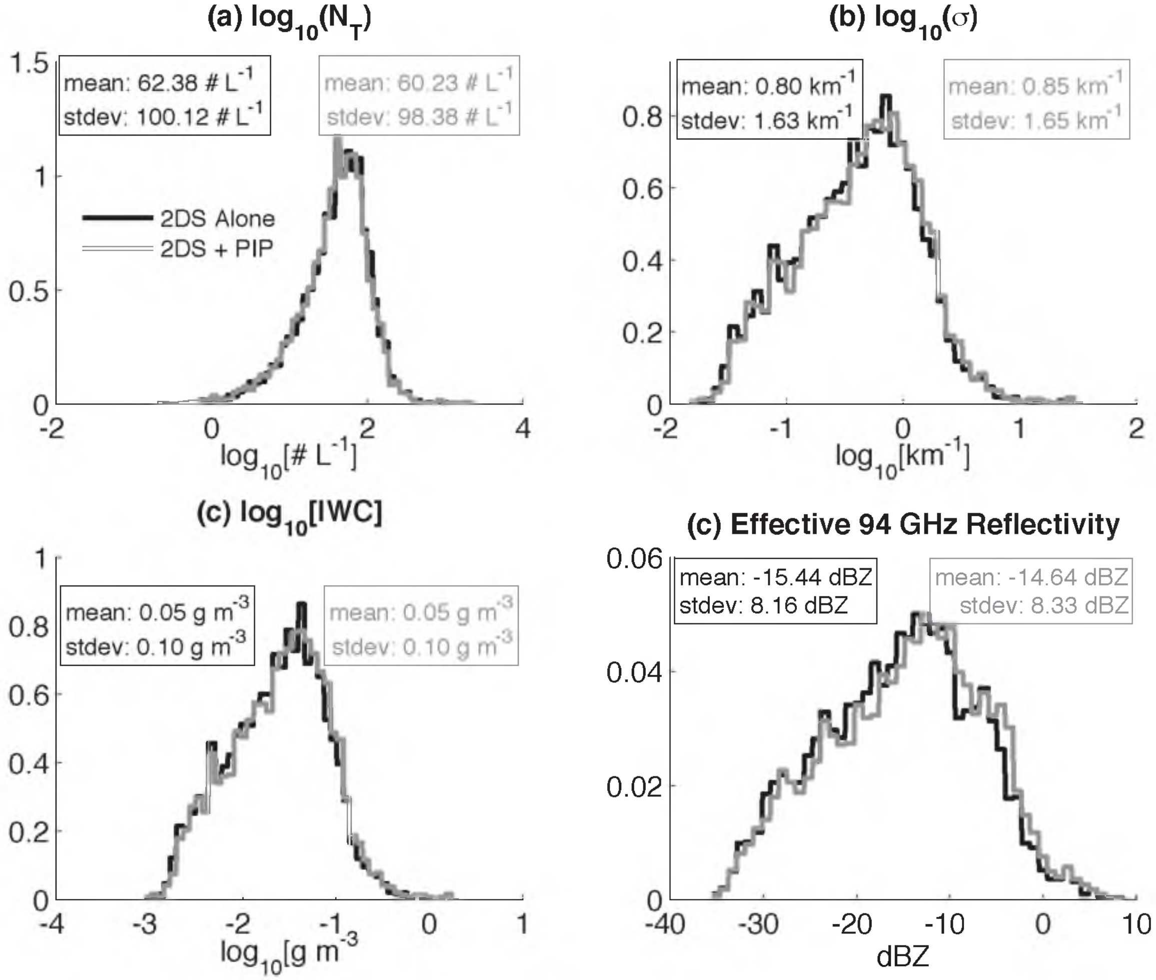

Fig. 4.9: Distributions of quantities computed using the parametric modified gamma distribution along with the true values of N_0^* and D_m computed from the 2D-S alone (black) and from the 2D-S combined with the PIP (gray). (a) N_T, (b) extinction coefficient, (c) IWC, (d) 94 GHz effective radar reflectivity.

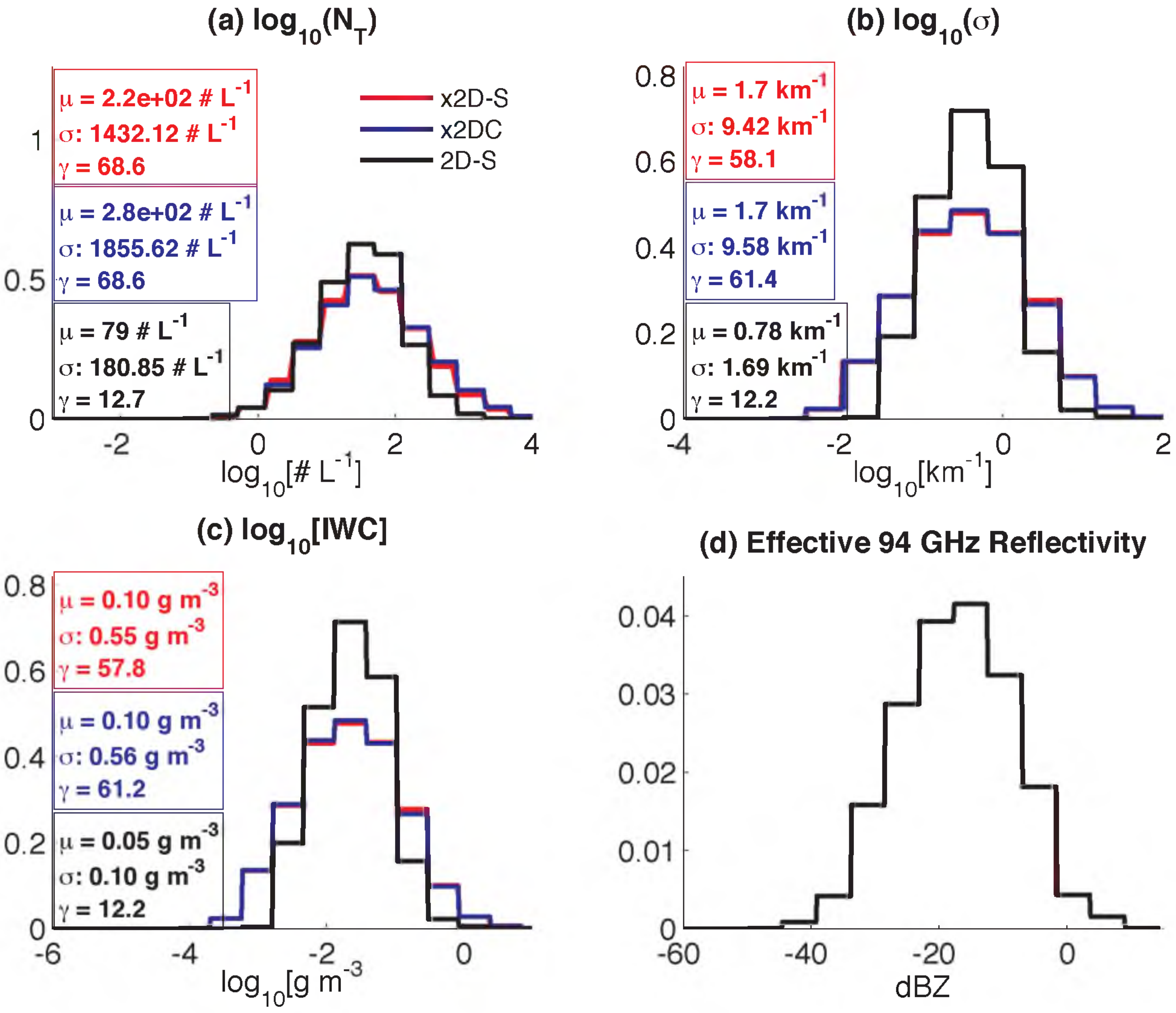

Fig. 4.10: Marginal pdfs of quantities computed directly from 2D-S data (black) as well as computed using the parameterized 2D-S (red) and the parameterized 2DC (blue). (a) total number concentration, (b) shortwave extinction coefficient, (c) ice water content, (d) radar reflectivity

on simulated instruments and computations based on the actual 2D-S. This bias is due mainly to the temperature parameterization of D_m. The density functions of extinction coefficient and IWC for the two parameterized instruments match one another quite well (the differences in their medians are not statistically significant). However, the density function of total number concentration for *x2DC* is shifted to higher number concentrations compared to the density function of total number concentration for *x2DS*: using a Mann–Whitney U test, the difference in their medians is statistically significant at the 95% level. We therefore conclude that the older D05 parameterization based on the 2DC-2DP datasets predicts a statistically significant higher number of total ice crystals than does the parameterized 2D-S (by a factor of about 1.3, or a little over 1 dB) and that, more generally, the 2DC measures a larger ratio of small ice crystals to large ice crystals than does the 2D-S, as shown in the effective radius comparison in Fig. 4.6.

Via an indirect comparison to older, 2DC-based datasets by means of a parameterization given by D05, it is determined that the 2D-S cirrus cloud datasets used here are significantly different from historical datasets in numbers of small ice crystals measured. Furthermore, it is determined that were a 2DC to have been flown alongside a 2D-S in the three flight campaigns utilized and processed with the same methodology as was used in D05, 2DC would have reported significantly higher numbers of the smallest ice crystals. We also note that the differences between the 2D-S and the 2DC databases are relatively small. Our aim was to determine whether the historical datasets analyzed by D05 continue to be scientifically viable given the newer probes and modern processing techniques. Given the modest differences found here between the newer and older data, we conclude that the historical datasets do indeed continue to be useful with the caveats noted above. However, it is surmised that since the 2D-S is superior in response time, resolution, and sample volume to the 2DC and that since steps were taken to mitigate ice particle shattering in the 2D-S data, the newer datasets are more accurate. Therefore, we recommend continuing field investigations of cirrus clouds using the newer particle probes and data processing techniques and, where possible, investigating the possibility of effecting the statistical correction of historical cirrus ice particle datasets using newer datasets.

CHAPTER 5

REMOTE SENSING AND RADAR FORWARD MODEL UNCERTAINTY

A number of algorithms for the retrieval of cirrus properties using instruments from the A-Train or from the ARM program have been devised for combinations of instruments from these remote sensing platforms (see, e.g, Zhang and Mace, 2006). Cloud property retrieval schemes—including those for cirrus—often make assumptions, either implicitly or explicitly, about cloud PSDs (Comstock et al., 2007), and some schemes attempt—at least implicitly—to retrieve parameters of assumed PSDs [e.g., Gossard (1994), Austin and Stephens (2001), Mace et al. (2002), Zhang and Mace (2006), and Zhao et al. (2011)]. Another purpose, then, to be served by data from the three flight campaigns being examined is to provide cirrus PSD data that can be used to inform and to refine remote sensing retrieval algorithms. As an example, Evans et al. (2002) used cloud in situ measurements to construct a database of many possible, hypothetical cloud configurations, each matched to their radiation signatures, for use in a cloud property retrieval scheme. By way of explanation, the manner in which it is proposed that this purpose be fulfilled is now elaborated upon.

The A-Train dataset is able to provide several independent measurements of a volume of cloudy atmosphere, in the form of radar reflectivity and lidar backscatter as well as brightness temperatures from the MODIS instrument. The ARM dataset is able to provide even more independent measurements, such as the full Doppler radar spectrum and in situ measurements of the atmospheric state. In either case, the number of degrees of freedom associated with a volume of cloudy atmosphere is larger than the number of independent measurements that can be made. There are, for instance, three degrees of independent air motion. Also, for whatever analytical distribution function used to approximate the cloud's average PSD for the volume, there are at least two independent parameters. For ice clouds, other degrees of freedom include particle habit, cross-sectional area, density, and so on. A direct solution method for any physical retrieval using either dataset therefore requires the inversion of a set of heavily underconstrained forward model equations.

The strategy then becomes to limit the solution space to some "correctness set" C, which is a subset of the entire solution space, where we expect a priori to be able to find a unique, physically plausible solution to the inversion of the physical retrieval (Zhdanov, 2002). This can be accomplished—and not infrequently is, in atmospheric retrieval problems—by the addition to the inversion problem of physically based and/or ad hoc constraints, such as by the Tikhonov regularization method (Zhdanov, 2002). Many retrieval schemes make use of Bayesian inference (Rodgers, 2000; Press, 2003), which provides a convenient vehicle both for adding constraints in the form of prior statistical knowledge and for estimating the uncertainty in retrieved results. The latter can be accomplished if the method is properly applied.

The Bayesian method is a general approach (Rodgers, 2000): the probability density of the entire set of possible solutions—the posterior solution—is produced; and from this posterior distribution a retrieved value can be chosen (using any of a variety of possible mathematical inversion methods). The application of prior knowledge narrows the posterior distribution, effectively reducing the solution space for the inversion, and the narrowed posterior distribution contains the uncertainty information for whatever solution is eventually chosen. The Bayesian inferential method is rich in the complexity of its depth and in the scope of its applications, but a brief review of the principles thereof relevant to this work is given next.

A Brief Review of Bayesian Inference

The mathematical underpinning for Bayesian inference is Bayes' Theorem:

$$p(\mathbf{x}\mid\mathbf{y})=\frac{p(\mathbf{y}\mid\mathbf{x})p(\mathbf{x})}{p(\mathbf{y})}, \tag{5.1}$$

where p represents the pdf of a random variable. Within this discussion, the vector **x** contains a set of cirrus PSD parameters, and vector **y** contains a set of remote sensing observations. The prior distribution $p(\mathbf{x})$ contains the knowledge of the parameter vector **x** apart from the measurement vector **y**. The conditional distribution $p(\mathbf{y}|\mathbf{x})$, also often written as the likelihood function $L(\mathbf{x}|\mathbf{y})$ (Severini, 2000), contains the forward model that relates the observations **y** to the parameters **x**. The distribution of observations $p(\mathbf{y})$ will not be made use of here. The posterior distribution, $p(\mathbf{x}|\mathbf{y})$, is then used to make inferences about the parameters in **x**.

The likelihood function $L(\mathbf{x}|\mathbf{y})$ is derived from a forward model $f(\mathbf{y}|\mathbf{x})$ (Broemeling, 1985) that can be written generally as

$$f(\mathbf{y}\mid\mathbf{x}):\mathbf{y}=F(\mathbf{x})+\mathbf{e}, \tag{5.2}$$

where F is the forward model operator that transforms a vector **x** in cirrus cloud state space into a vector **y** in measurement space, and **e**, representing measurement noise, is a random vector with zero mean and covariance matrix S_e. A handful of assumptions then allow for the mathematical construction of the likelihood function (Zhdanov, 2002).

The first assumption is that the relationship $\langle \mathbf{y} \rangle = F(\mathbf{x})$ holds true for the mean of observations. The second assumption is that measurement errors are normally distributed random variables. (Measurement errors are also commonly assumed to be independent of one another.) The third assumption is that whatever observations are made are the most likely given the true state of the forward model. Under this third assumption, the optimum values for the model parameter **x** are those that maximize the probability that the observed data are in fact observed. With these three assumptions, the likelihood function becomes

$$L(\mathbf{x} \mid \mathbf{y}) = \frac{1}{(2\pi)^{n/2} |S_e|^{1/2}} \exp\left[-\frac{1}{2} (\mathbf{y} - F(\mathbf{x}))^T S_e^{-1} (\mathbf{y} - F(\mathbf{x})) \right], \tag{5.3}$$

if $\mathbf{y} \in \mathbb{R}^{n \times 1}$.

Beyond the use of prior information, in order to further reduce the number of degrees of freedom of the inversion problem, certain empirical assumptions must be employed that fall under the rubric of "forward model parameters" (Rodgers, 2000). One common group of assumptions, mentioned already, uses a set of power laws to relate ice particle maximum dimension, for a few examples, to particle mass (or density), particle cross-sectional area, and particle radar backscatter cross-section (e.g., Mitchell, 1996; Aydin and Walsh, 1999; Heymsfield and Iaquinta, 2000; Heymsfield et al., 2002, Hammonds, 2013). All such sets of coefficients are highly uncertain, resulting in (ostensibly) quantifiable forward model uncertainties that further aggravate measurement uncertainties. One approach to dealing with these forward model parameter uncertainties is to incorporate them into the measurement covariance matrix (Rodgers, 2000). Following Rodgers' (2000) notation, let the vector **b** contain all such parameters, and let the matrix S_b be its covariance matrix. Furthermore, let K_b be the Frechet derivative of the forward model operator F with respect to **b**. Then the overall error covariance becomes (using a linear approximation)

$$S_y = S_e + K_b^T S_b K_b \, . \tag{5.4}$$

Substitution of this result into the likelihood function results in

$$L(\mathbf{x} \mid \mathbf{y}) = \frac{1}{(2\pi)^{n/2} \left| S_y \right|^{1/2}} \exp\left[-\frac{1}{2} (\mathbf{y} - F(\mathbf{x}))^T S_y^{-1} (\mathbf{y} - F(\mathbf{x})) \right] \tag{5.5}$$

This chapter focuses on the prior distribution of cirrus PSD parameters $p(\mathbf{x})$. Accordingly, the distributions of fit parameters from Chapter 2, as well as their covariance structure, are here examined and used.

Armed with expressions for the likelihood function and for the prior distribution, the posterior distribution may be constructed by combining Eqs. 5.1 and 5.5:

$$p(\mathbf{x} \mid \mathbf{y}) = \frac{1}{(2\pi)^{n/2} \left| S_y \right|^{1/2}} \exp\left[-\frac{1}{2} (\mathbf{y} - F(\mathbf{x}))^T S_y^{-1} (\mathbf{y} - F(\mathbf{x})) \right] \left\{ \frac{p(\mathbf{x})}{p(\mathbf{y})} \right\} . \tag{5.6}$$

Evidently, if the posterior distribution is maximized with respect to **x**, then the maximum is independent of $p(\mathbf{y})$. We are thus left with a maximization problem, assuming we wish to obtain the maximum a posteriori (MAP) solution (Rodgers, 2000).

$$\begin{aligned}\nabla_{\mathbf{x}}\left[p(\mathbf{x}\,|\,\mathbf{y})\right] &= \nabla_{\mathbf{x}}\left\{\frac{1}{(2\pi)^{n/2}\left|S_y\right|^{1/2}}\exp\left[-\frac{1}{2}\left(\mathbf{y}-F(\mathbf{x})\right)^T S_y^{-1}\left(\mathbf{y}-F(\mathbf{x})\right)\right]p(\mathbf{x})\right\} \\ &= 0\end{aligned} \tag{5.7}$$

Cloud retrieval schemes using complete Bayesian inferential approaches have been formulated, some of them numerically integrating a partially analytical posterior distribution [e.g., Evans et al. (2002), McFarlane et al. (2002), and Evans et al. (2005)], and some of them taking a Markov chain Monte Carlo (MCMC) approach (see, e.g., Posselt et al., 2008). However, the particular form of Bayesian inference most often used in atmospheric retrievals is optimal estimation, wherein the likelihood function and prior distributions are assumed to be multivariate normal, thus conveniently producing a multivariate normal posterior distribution that can be maximized with respect to the vector $\mathbf{x}$ (Rodgers, 2000). In this case, the prior distribution takes the form

$$p(\mathbf{x}) = \frac{1}{(2\pi)^{m/2}\left|S_a\right|^{1/2}}\exp\left[-\frac{1}{2}\left(\mathbf{x}-\mathbf{x}_a\right)^T S_a^{-1}\left(\mathbf{x}-\mathbf{x}_a\right)\right] \tag{5.8}$$

if $\mathbf{x} \in \mathbb{R}^{m\times 1}$, S_a is the prior covariance matrix, and $\mathbf{x}_a$ is the expected value of the prior distribution. Often, for a lack of better information, S_a is assumed to be diagonal.

Using the distributions of fit parameters and their covariance structure given in Chapter 2, the utility of the optimal estimation technique for the retrieval of cirrus PSDs is examined here, and a set of questions is considered. First, may the optimal estimation technique be properly applied to the retrieval of cirrus microphysics via the retrieval of cirrus PSDs? Second, if so, is there a penalty for using the normal statistics called for by optimal estimation? Third, what is the penalty for ignoring the off-diagonal elements of the prior covariance matrix? And finally, fourth, can the prior distribution be categorized by meteorological variables?

Transformation to an Optimal Estimation Problem

As discussed in Chapter 2, the use of the unimodal fits to the cirrus PSDs will be sufficient for the purposes of remote sensing. Evidently, a simple look at Tables 2.1 and 2.2 would rule out the use of optimal estimation were it not for the high correlation between $\log_{10}[N_0]$ and the shape parameter. Use of this fact is now made in order to express $\log_{10}[N_0]$ as a function of α and thereby reduce the number of parameters needed to describe a PSD to two. Two-dimensional histograms of $\log_{10}[N_0]$ versus α are shown in Figs. 5.1 and 5.2—one for the midlatitudes and one for the Tropics. Overlaid on each plot (in purple) is a quartic fit between the two parameters. In either case, the parameterization takes the form

$$\log_{10}\left[N_0\right]=c_0+c_1\alpha+c_2\alpha^2+c_3\alpha^3+c_4\alpha^4. \tag{5.9}$$

The coefficients for both geographical regions are listed in Table 5.1.

Using this parameterization, Eq. 2.1 becomes

$$n(D)=\left[10\wedge\left(c_0+c_1\alpha+c_2\alpha^2+c_3\alpha^3+c_4\alpha^4\right)\right]\left(\frac{D}{D_0}\right)^{\alpha}\exp\left(-\frac{D}{D_0}\right). \tag{5.10}$$

Looking back at Fig. 2.11, one PSD parameter has been removed whose marginal pdf is

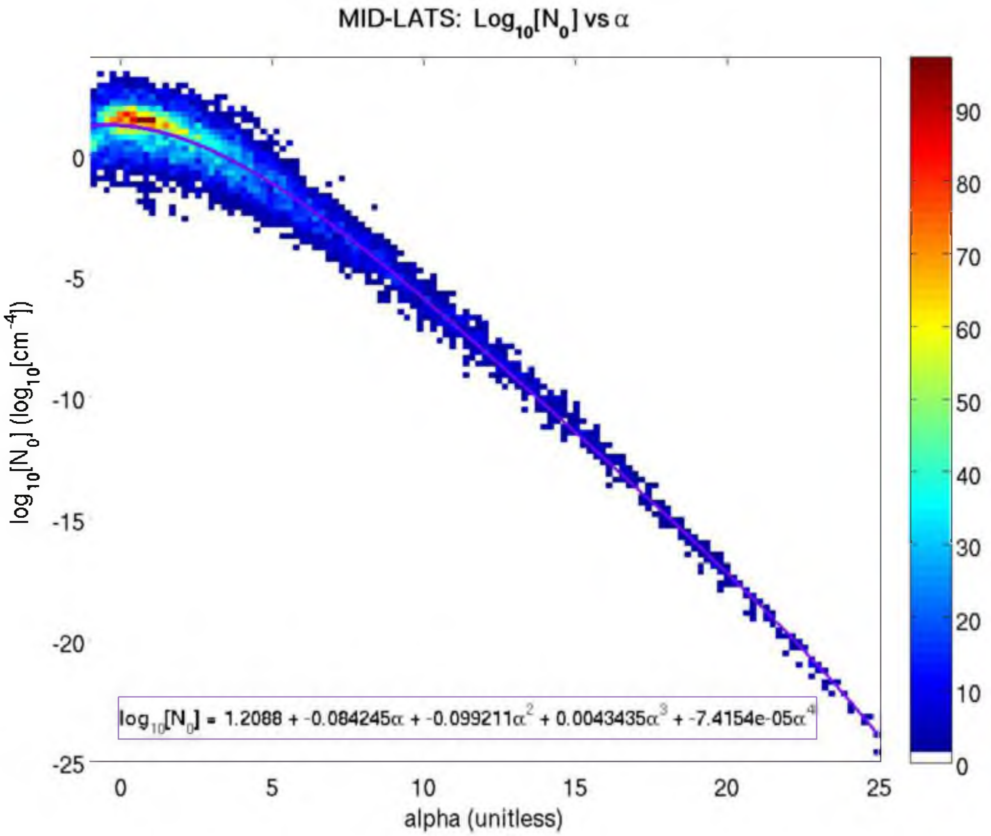

Fig. 5.1: Assuming all fits are unimodal, the scatter between $\log_{10}[N_0]$ and α for the midlatitudes. A quartic fit between the two is shown by the purple curve and given in the purple box.

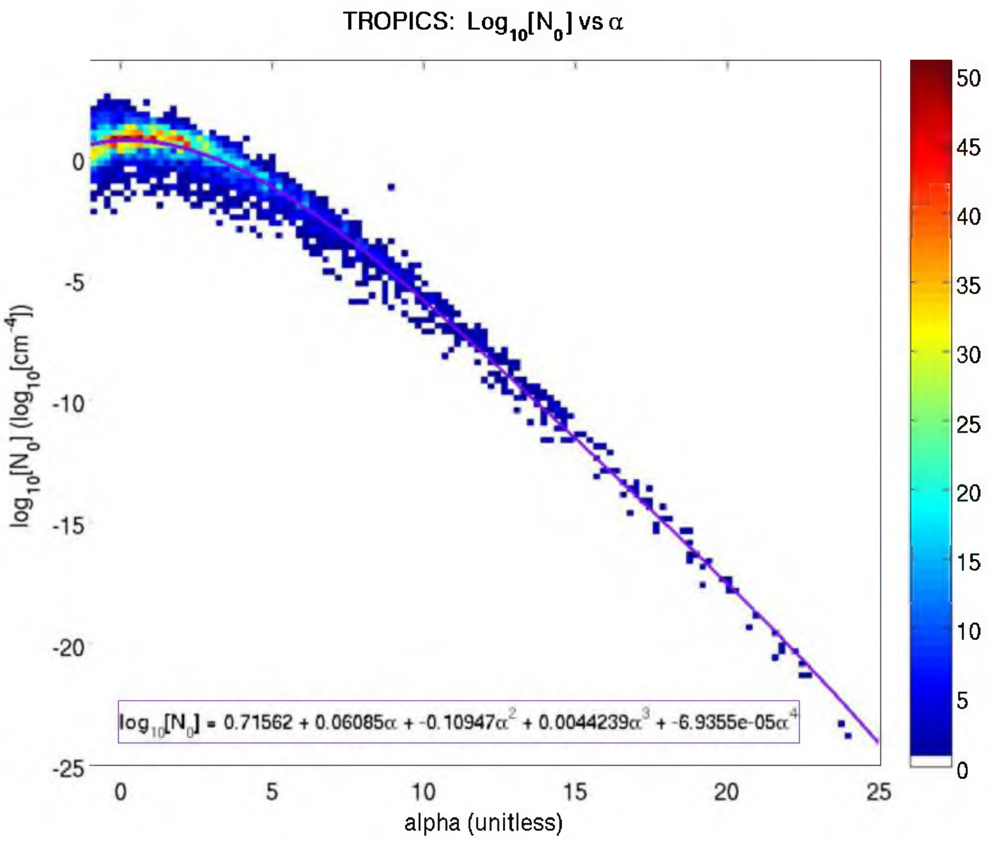

Fig. 5.2: Assuming all fits are unimodal, the scatter between $\log_{10}[N_0]$ and α for the Tropics. A quartic fit between the two is shown by the purple curve and given in the purple box.

Table 5.1

Coefficients for quartic fits shown in Figs. 5.1 and 5.2.

	Midlatitudes	Tropics
c_0	1.2088	0.71562
c_1	–0.084245	0.06085
c_2	–0.099211	–0.10947
c_3	0.0043435	0.0044239
c_4	-7.4154×10^{-5}	-6.9355×10^{-5}

nonnormal. Though the marginal pdf of $\log_{10}[D_0]$ is modeled as normal (albeit sloppily so for the tropical dataset), the marginal pdf of α cannot be. However, if α is transformed according to

$$w = \log_{10}\left[\alpha + 1\right], \tag{5.11}$$

then the distribution of w is skewed (see Fig. 5.3), but its mathematical support is $w \in \left(-\infty, \infty\right)$, and so its marginal pdf may be approximated as normal. Reformulating Eq. 5.10 according to this second parameter transformation gives

$$\begin{aligned} n(D) = &\left\{10 \wedge \left[c_0 + c_1\left(10^w - 1\right) + c_2\left(10^w - 1\right)^2 + c_3\left(10^w - 1\right)^3 + c_4\left(10^w - 1\right)^4\right]\right\} \times \\ &\left(\frac{D}{D_0}\right)^{\left(10^w - 1\right)} \exp\left(-\frac{D}{D_0}\right) \end{aligned} \tag{5.12}$$

The unimodal size distribution is now expressed in terms of two parameters, both of them having quasi-normal marginal pdfs. These pdfs, for both the midlatitudes and for the Tropics, are shown in Fig. 5.3, along with the mean and standard deviations needed in order to parameterize them as normal distributions. Their correlation and covariance matrices are given in Table 5.2. These formulations will allow for the use of optimal estimation for the retrieval of cirrus PSDs, though it should be noted that the nondiagonal prior covariance matrix given in Table 5.2 must be used.

Penalty for Using Optimal Estimation

Using the optimal estimation technique where the prior distribution is not multivariate-normal will perforce result in a penalty in the estimated retrieval uncertainty

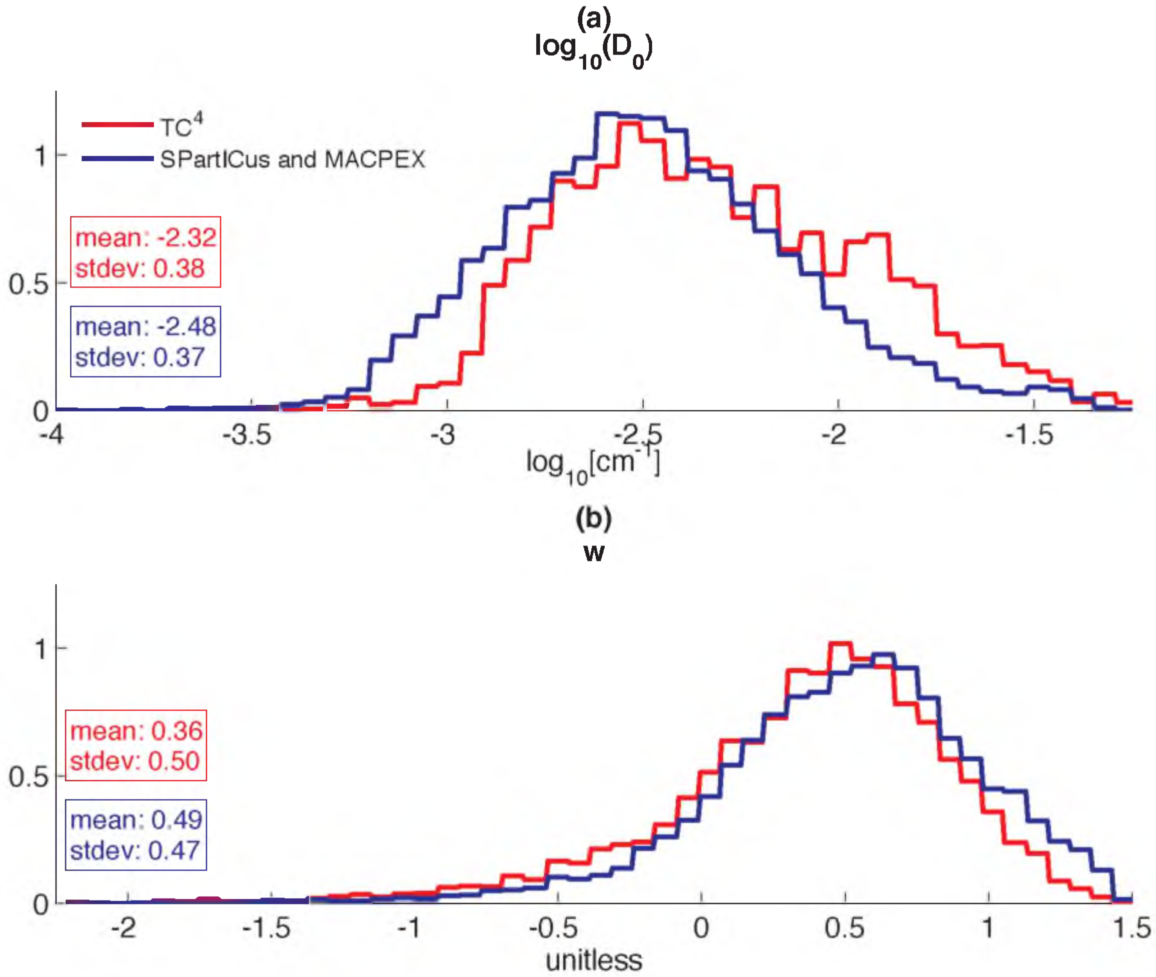

Fig. 5.3: Marginal pdfs of the parameters of the PSD reworked for use with the optimal estimation technique. (a) log$_{10}$[D_0], (b) *w*.

Table 5.2

Covariance and correlation matrices for reduced unimodal fit PSD parameters.

General Form	
$S = \begin{bmatrix} \sigma^2_{\log_{10}[D_0]} & \sigma_{\log_{10}[D_0],w} \\ \sigma_{\log_{10}[D_0],w} & \sigma^2_w \end{bmatrix}$	
MIDLATITUDES	
Covariance Matrix	Correlation Matrix
$\begin{bmatrix} 0.14 & -0.10 \\ -0.10 & 0.22 \end{bmatrix}$	$\begin{bmatrix} 1.00 & -0.60 \\ -0.60 & 1.00 \end{bmatrix}$
TROPICS	
Covariance Matrix	Correlation Matrix
$\begin{bmatrix} 0.14 & -0.15 \\ -0.15 & 0.25 \end{bmatrix}$	$\begin{bmatrix} 1.00 & -0.80 \\ -0.80 & 1.00 \end{bmatrix}$

(Posselt et al., 2008). A rigorous characterization of this penalty will require a comparison of the results of retrieval exercises using the optimal estimation technique with the results of performing the same exercises using the complete, parameterized multivariate prior distribution given in Chapter 2. In order to perform the latter, the Markov chain Monte Carlo (MCMC) approach (Press, 2003) has been settled on. The specific algorithm to be used is an adaptive variant of the Metropolis–Hastings algorithm (Haario et al., 1999; Tamminen and Kyrola, 2001) that was developed for the solution of Bayesian inverse problems involving nonnormal statistics. Application of this method requires the implementation of random number generators, the construction of which is detailed in Ghosh and Henderson (2002), that are capable of producing random vectors with arbitrary marginal distributions and specified covariance matrices. This work is incomplete and is not presented here.

Penalty for Ignoring Off-Diagonal Elements of Prior Covariance Matrix

Because of the narrowing constraint that the nonzero correlations in the prior covariance matrix impose upon the posterior distribution of a Bayesian retrieval algorithm, their use will result in a reduction of retrieval uncertainty. To demonstrate this effect in a simple way, the prior knowledge of ice water content is estimated from the marginal distributions of the reduced, unimodal PSD parameters, and the distribution of these estimates is compared with the distribution of ice water contents estimated directly from the 2D-S (SPartICus dataset only). The estimation is performed in two ways: first, the marginal distributions of PSD parameters are considered uncorrelated and second, their correlations are taken into account. The results are shown in Fig. 5.4, except for the

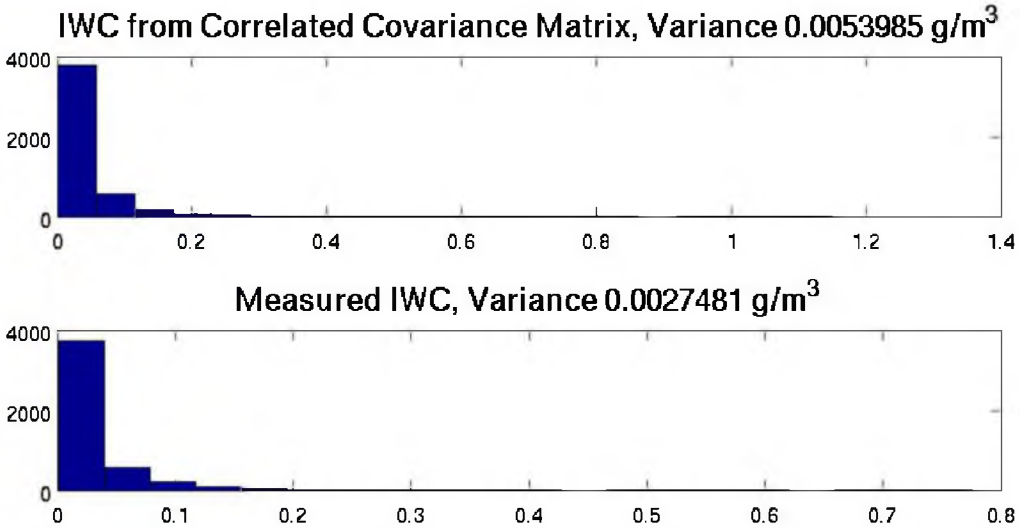

Fig. 5.4: IWC estimated from correlated vectors of unimodal PSD parameters (top) and from 2D-S measurements (bottom).

estimation performed using uncorrelated vectors of PSD parameters: the uncorrelated vectors produce impossible combinations of parameters that lead to unphysical IWC computations that cannot be displayed on a histogram. Thus, not only should the off-diagonal elements produce smaller uncertainties in retrieval results, but they are also necessary if the prior distribution of PSD parameters is to describe the actual distribution of possible bulk cloud parameters.

Partial work (which is not shown here) has been performed to demonstrate the effect in uncertainty estimates of including and of not including the off-diagonal elements of the prior covariance matrix. This is being done using synthetic remote sensing measurables computed using the 2D-S measurements along with a forward model for radar reflectivity and lidar backscatter in cirrus clouds outlined in Zhang and Mace (2006).

Uncertainty in Radar Forward Models

The comparison of simulated radar measurements, computed from simulated cloud microphysics, with actual radar measurements of modeled clouds is emerging as a tool for use in model validation and intercomparison exercises. It is thought that the comparison of simulated and real radar measurements avoids much of the uncertainty involved with comparing modeled cloud microphysics with microphysics derived from inversion algorithms applied to radar measurements. While comparison of real measurements with simulated measurements may seem straightforward to implement, it not only does not completely avoid the inherent uncertainty of microphysical retrievals, but it also introduces new sources of uncertainty.

For example, the Cloud Feedback Model Intercomparison Project (CFMIP)

Observation Simulator Package (COSP) (Bodas-Salcedo et al., 2011) is a multi-instrument simulator package designed to compute via forward model the measurements that a number of orbiting sensors would make were they to view a modeled scene. While the COSP suite of simulations goes to great pains to model things such as subgrid scale variability, instrument beam width, instrument viewing angle, and surface properties, it perforce contains a large number of assumptions concerning cloud microphysics.

The Quickbeam component (Haynes et al., 2007) of COSP is used to model radar reflectivities such as would be measured by CloudSat. Quickbeam models ice particles as spheres and allows for the modeling of ice PSDs using one of a handful of predetermined parametric forms. Given one or two modeled moments of the ice particle size distribution (such as total number concentration and/or ice water content), Quickbeam attempts to discern the corresponding ice PSD and to compute an appropriate effective radar reflectivity.

Ignoring any other considerations at all regarding the forward modeling of radar reflectivities, two concerns based purely in cloud microphysics are immediately raised. First, as seen in Fig. 4.1, error in the Quickbeam forward model is introduced by its assuming that ice particles are spheres and then using Mie theory to compute their radar backscatter cross-sections. Second, and much more importantly, as discussed in Chapter 3 with regards to the normalization of ice PSDs using two moments and as illustrated in Fig. 3.1, there is an unavoidable natural variability in a cirrus PSD when only two of its moments are specified.

Here, uncertainty in forward-modeled radar reflectivity due to incomplete model specification of cloud particle size distributions is inspected. With data from TC^4, MACPEx, and SPartICus, it is found that natural variability in particle size distributions, given only two simulated moments, requires assigning a distribution of radar reflectivities per set of modeled cloud moments.

For a modeled cloud, output from a two-moment CRM (courtesy of Andreas Muhlbauer), initialized with meteorological conditions from an A-Train overpass on 1 April 2010 of the ARM Southern Great Plains site, is used. A two-dimensional histogram of modeled particle number concentration versus modeled ice water content is shown in Fig. 5.5. Figure 5.6 shows the two-dimensional histogram of measured number concentration versus measured ice water content for all three flight campaigns (for reference, the modeled histogram coincides with the pixels outlined in red). The inability of the in situ database to cover the range of modeled N_T-IWC may suggest that nonphysical combinations have been modeled, but it certainly suggests the need for more flight campaigns using the updated particle probes in order to extend the range and statistical significance of the in situ database.

Radar reflectivities for the modeled N_T-IWC pairs are computed three ways. First, Quickbeam is used, and the distribution of results is called "Muhlbauer Quickbeam." Second, the parameterization of $\log_{10}[N_0]$ given above is used, and the two modeled moments are used to solve for D_0 and α. These two parameters are then used to compute a radar reflectivity using the forward model described in Chapter 3. The distribution of these results is called "Mace Deterministic". Third, measured N_T-IWC pairs are grouped into bins of at least 10 samples, and the radar reflectivity for each corresponding measured PSD is computed according to the forward model described in Chapter 3. Thus, each N_T-IWC bin contains a distribution of possible radar reflectivities.

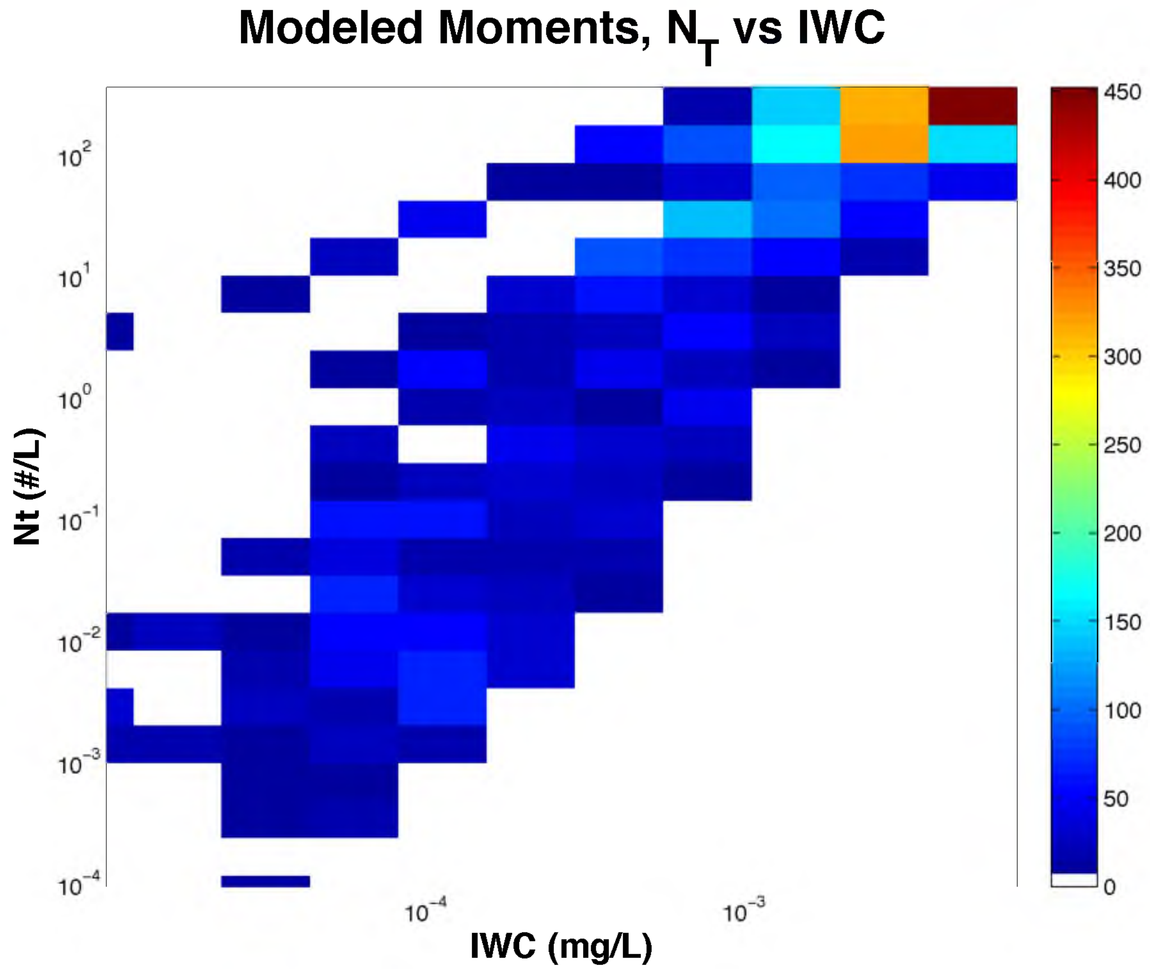

Fig. 5.5: Two-dimensional histogram of modeled number concentration versus modeled ice water content.

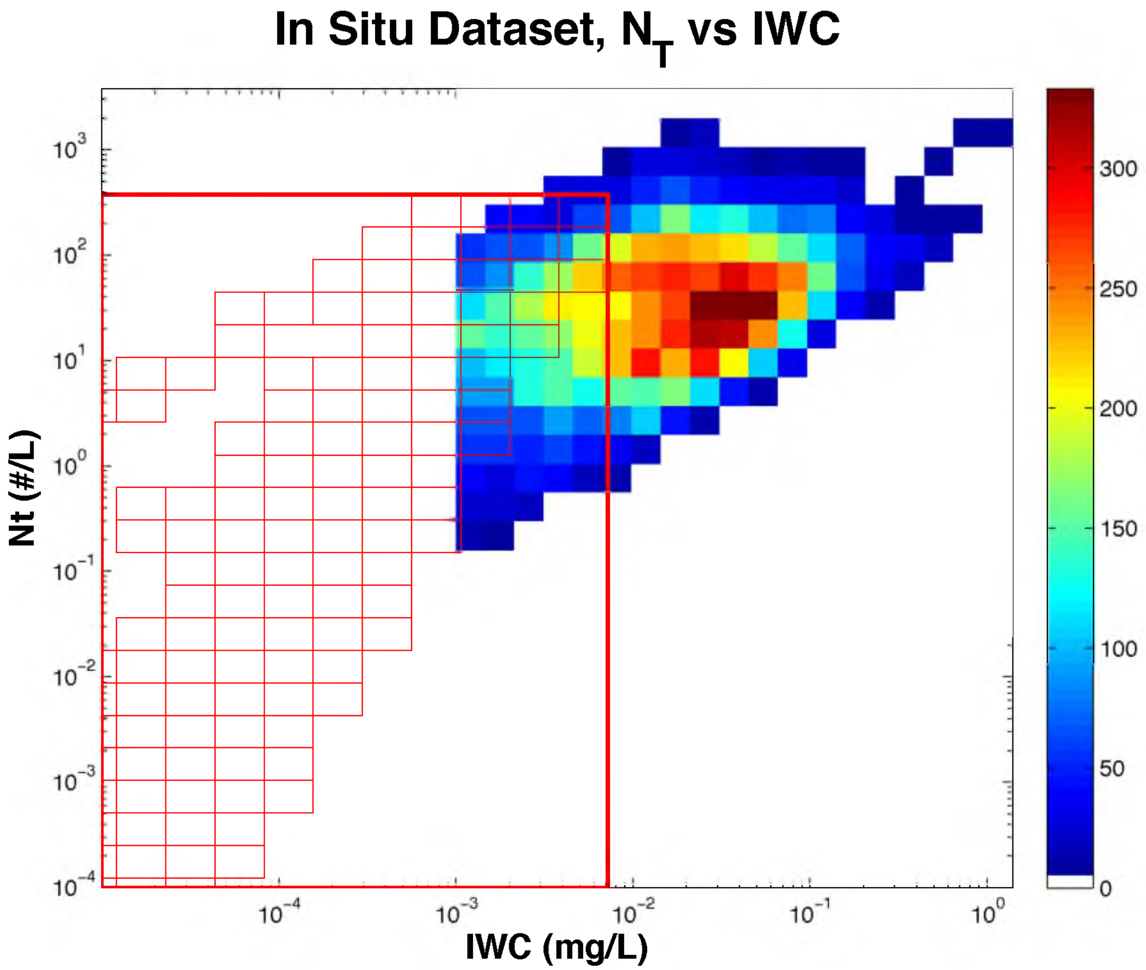

Fig. 5.6: Two-dimensional histogram of measured number concentration versus measured ice water content for the three flight campaigns. For reference, the domain of Fig. 5.5 is indicated by the pixels outlined in red.

(This is illustrated in Figs. 5.7 and 5.8, which show the determined N_T-IWC bins and the means and standard deviations of the radar relectivity distributions contained in each bin.) Then, the measured N_T-IWC bin for each modeled N_T-IWC pair is identified, and the corresponding individual distributions of radar reflectivities are combined via mixture modeling to construct an overall distribution of possible radar reflectivies. This final distribution of reflectivities is called “Stochastic.”

From Fig. 5.7, an overall increase in mean reflectivity with increase in IWC is seen, which is entirely expected, given *Z*-IWC relationships that have reflectivity increasing with ice water content (e.g., Protat et al., 2007). For a given IWC, it is also seen that mean reflectivity decreases with increasing N_T. This also is not an unexpected result as spreading the same amount of mass over more particles results in smaller particles. Figure 5.7 also shows that there is more variation in mean reflectivity for a given N_T than there is for a given IWC. Also, as seen in Fig. 5.8, the current in situ database gives uncertainties in reflectivity distributions of up to several dBZ.

Figure 5.9 shows the three distributions of computed reflectivities for only the modeled N_T-IWC pairs that overlap with the in situ database. The fact alone that the “deterministic” and “Quickbeam” distributions are significantly different indicates that two modeled PSD moments are not enough to definitively determine radar reflectivity. Figures 5.10 and 5.11 show pressure-dBZ histograms for the “deterministic” and “stochastic” reflectivity distributions. These figures clearly demonstrate that natural variability in ice PSDs—which translates into natural variability in radar reflectivity—results in smearing out a deterministically computed histogram of pressure versus dBZ. Thus, to reiterate, natural variability in particle size distributions, given only two

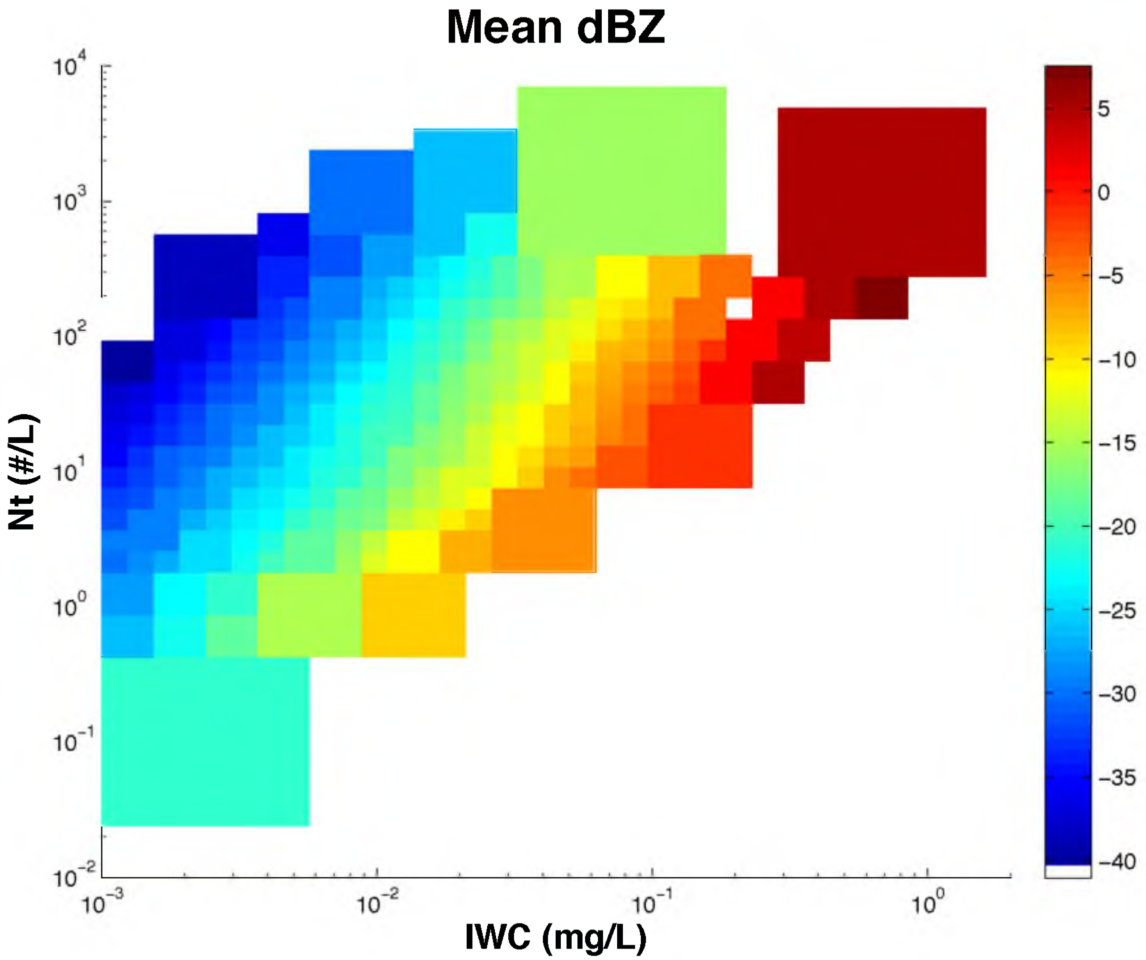

Fig. 5.7: Means of the distributions of radar reflectivity contained in each measured N_T-IWC bin (each bin contains at least 10 PSDs).

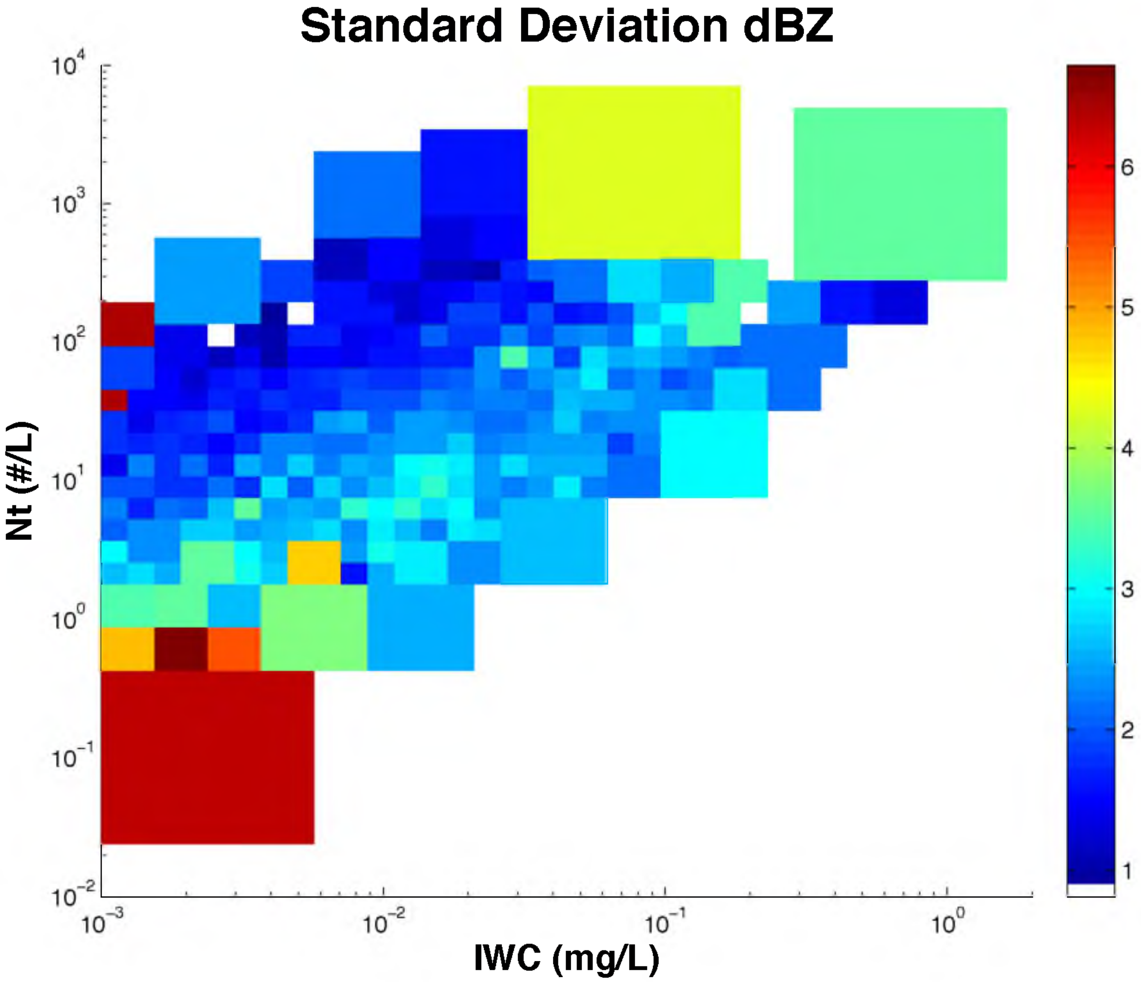

Fig. 5.8: Standard deviations of the distributions of radar reflectivity contained in each measured N_T-IWC bin (each bin contains at least 10 PSDs).

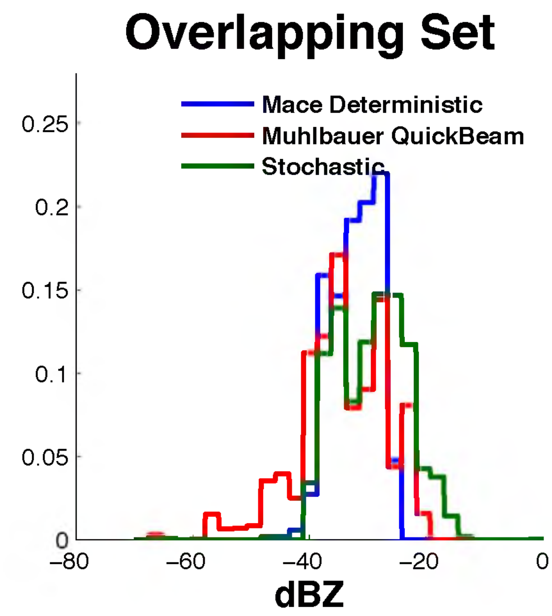

Fig. 5.9: The three distributions of computed reflectivities for only the modeled N_T-IWC pairs that overlap with the in situ database.

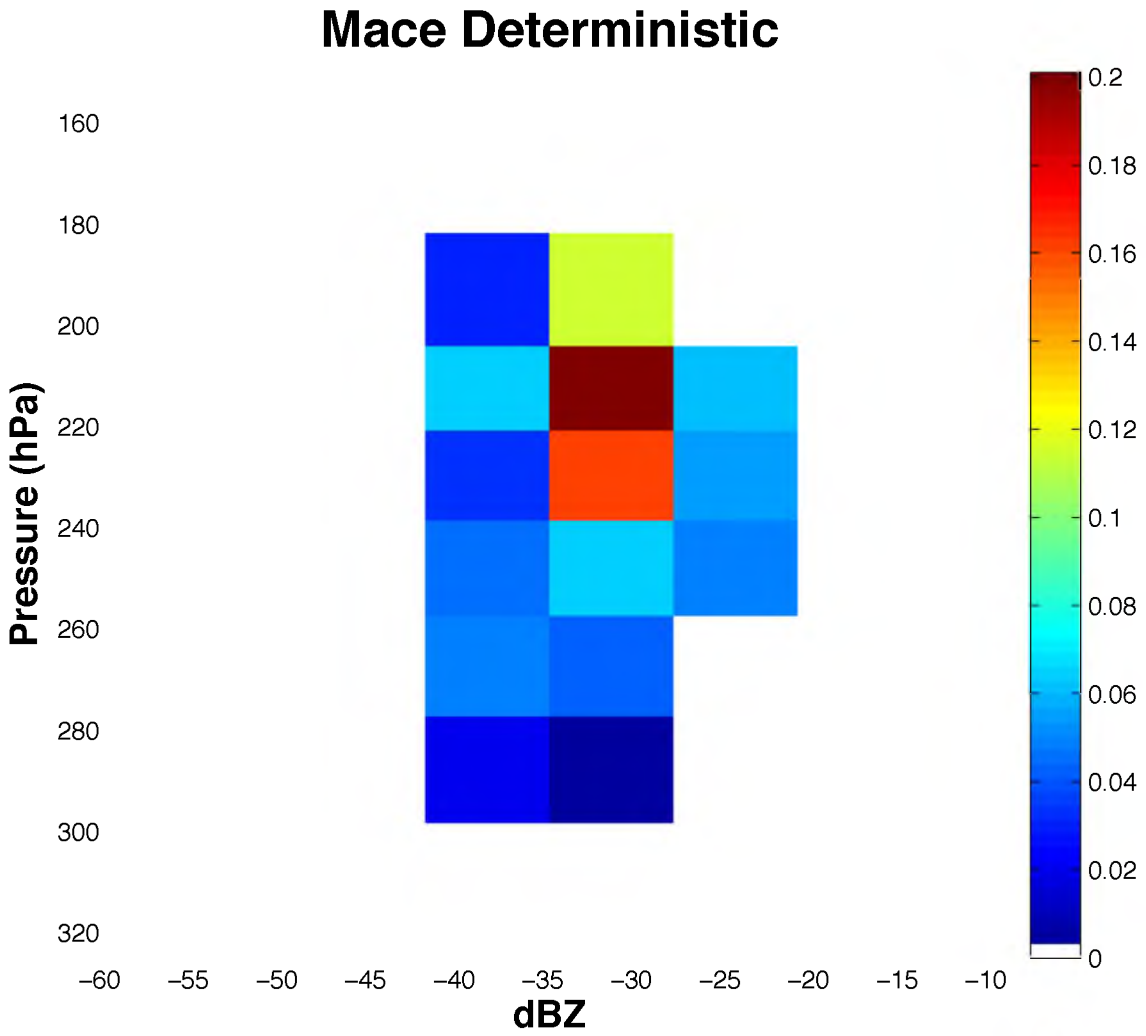

Fig. 5.10: Pressure-dBZ histogram for the distribution of "deterministic" reflectivities.

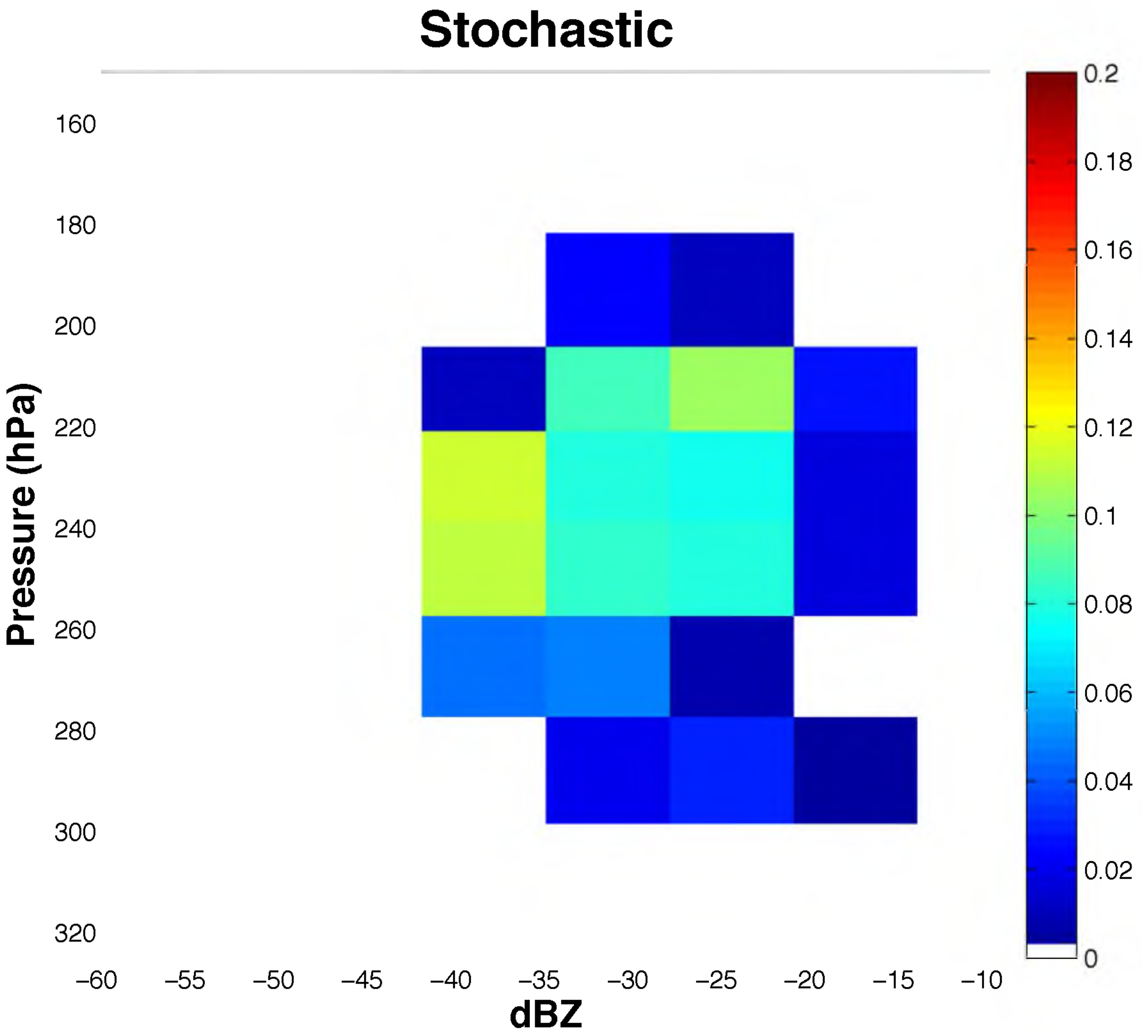

Fig. 5.11: Pressure-dBZ histogram for the distribution of "stochastic" reflectivities.

simulated moments, requires assigning a distribution of radar reflectivities per set of modeled cloud moments. This result is entirely expected in light of the results shown in Chapter 3.

In the estimation of radar reflectivity from modeled PSD moments, from a Bayesian standpoint, what has been shown is the spread in reflectivity computations due to the covariance in prior knowledge of ice PSDs. Other sources of spread will inevitably include variance in aspect ratios used to compute radar backscatter cross sections, variance in the mass-dimensional relationship, and uncertainty in the analytical PSD parameters, especially when one parameter is expressed as a function of another. What remains is to further explore the use of this in situ database by constructing a hierarchical Bayesian model, using latent variables such as temperature, relative humidity, and mass-dimensional relationships, in order to fully express the uncertainty in forward modeled radar reflectivity due to microphysical variability. Information content analysis will also be used to analyze the importance of various modeled moments in the estimation of radar reflectivity.

CHAPTER 6

CONCLUSION

A database of cirrus particle size distributions, with concomitant meteorological variables, has been constructed using data collected during the TC^4, MACPEx, and SPartICus flight campaigns. These campaigns were chosen due to their use of up-to-date instrumentation as well as to the measures taken to mitigate ice particle shattering artifacts. Parametric particle size distributions, both unimodal and bimodal, were fit to each measured particle size distribution, and properties of the PSDs, including bimodality and various bulk quantities, were examined in relation to meteorological variables such as temperature and RHi. It was determined that, at least for certain purposes, the unimodal fits to the measured PSDs are sufficient. Parametric, marginal density functions for each of the unimodal fit parameters, along with their covariances, were given.

Via an indirect comparison to older, 2DC-based datasets by means of a parameterization given by D05, it is determined that 2D-S cirrus cloud data is significantly different from the historical data. It is surmised that since the 2D-S is superior in response time, resolution, and sample volume to the 2DC and since steps were taken to mitigate ice particle shattering in the 2D-S data, the newer datasets are more accurate. That being said, the historical datasets may still be useful, depending on the degree of accuracy needed for a particular application.

A parameterization of the “universal” particle size distribution, based on the method of Field et al. (2005), is also given. Due to the method in which the parameterization was estimated, its sampling distribution is also available.

The work presented in Chapter 2 constitutes a prior distribution for cirrus particle size distribution in the Bayesian estimation of cirrus microphysical properties using remote sensing measurements. It is demonstrated that the unimodal fits are sufficient for remote sensing purposes and that one of the fitting parameters may be eliminated and the parametric particle size distribution reformulated so that the traditional technique of optimal estimation for the retrieval of cirrus microphysical properties may be properly applied. It is critical to point out, though, that this technique may only be properly applied if the proper prior covariance structure, as given in Chapters 2 and 5, is used. Work remains to be completed in this application of the microphysical database, viz., a full-on error analysis via the MCMC method and an analysis of the consequences on the uncertainties in retrieved parameters of the off-diagonal elements of the prior covariance matrix.

Finally, the in situ database was used to investigate the uncertainty in forward models of radar reflectivity based on modeled moments of cirrus cloud particle size distributions. It is concluded that due to natural variability in the ice PSD, a set of modeled PSD moments results in a distribution of possible radar reflectivities rather than in a single, analytically computed radar reflectivity.

This in situ database, as constructed, may be easily added to and the analysis structure given in this dissertation reapplied to continually keep it up to date. In fact, due to the ever-present need for more data for the purposes of informing model parameterizations, refining cirrus retrieval algorithms, and characterizing the forward modeling of remote sensing measurements from model outputs for model validation, the final conclusion of this dissertation is that there is a pressing need for more in situ measurement campaigns with continual improvement in instrumentation and in data processing techniques.

APPENDIX A

FITTING BINNED PSDs USING THE METHOD OF MOMENTS

Before performing a fit, both the measured and parametric PSDs are normalized such that their zeroth moments are unity (thus making them probability density functions). For a unimodal gamma distribution, the normalized parametric form is expressed as

$$\Pr(D) = p(D) = \frac{1}{D_0 \Gamma(\alpha+1)} \left(\frac{D}{D_0} \right)^{\alpha} \exp\left(-\frac{D}{D_0} \right). \tag{A.1}$$

The parameters D_0 and α are estimated in a manner similar to Heymsfield et al. (2002), using the first, third, and fifth noncentral moments of the normalized, measured PSD. The corresponding parametric moments are

$$\mathrm{E}\left[D \right] = D_0 (\alpha+1), \tag{A.2}$$

$$\mathrm{E}\left[D^3 \right] = D_0^3 (\alpha+3)(\alpha+2)(\alpha+1), \tag{A.3}$$

$$\mathrm{E}\left[D^5 \right] = D_0^5 (\alpha+5)(\alpha+4)(\alpha+3)(\alpha+2)(\alpha+1). \tag{A.4}$$

Defining the quantity

$$F=\frac{\mathrm{E}\left[D^{3}\right]^{2}}{\mathrm{E}\left[D^{5}\right]\mathrm{E}\left[D^{1}\right]} \tag{A.5}$$

and using the empirical moments to compute F, it may be shown that α is a solution to the quadratic equation

$$0=\alpha^{2}(1-F)+\alpha(5-9F)+(6-20F). \tag{A.6}$$

As the condition $\alpha>-1$ must be satisfied in order for the zeroth moment of the parametric PSD to exist, the smaller, real solution greater than negative unity is chosen. If none exists, then no unimodal fit for the measured PSD is given. Having a solution for α, the solution for D_0 is

$$D_{0}=\sqrt{\frac{\mathrm{E}\left[D^{3}\right]}{\mathrm{E}\left[D^{1}\right]}\frac{1}{(\alpha+3)(\alpha+2)}}. \tag{A.7}$$

Finally, a solution for N_0 comes from the first noncentral moment of the nonnormalized, measured PSD M_1:

$$N_{0}=\frac{M_{1}}{D_{0}^{2}\Gamma(\alpha+2)}. \tag{A.8}$$

APPENDIX B

FITTING BIMODAL MIXTURE DISTRIBUTIONS TO BINNED PSDs

The Method of Moments

The zeroth moment, or total particle number, of the bimodal distribution is

$$N_T = N_1 D_1 \Gamma(\alpha_1 + 1) + N_2 D_2 \Gamma(\alpha_2 + 1) = N_{T1} + N_{T2}, \tag{B.1}$$

which is the sum of the particles in both modes. Normalized, then, the bimodal distribution (Eq. 2.2) becomes

$$\begin{aligned}\Pr(D) = p(D) = &\frac{1}{D_1 \Gamma(\alpha_1 + 1)} \frac{N_{T1}}{N_T} \left(\frac{D}{D_1} \right)^{\alpha_1} \exp\left(-\frac{D}{D_1} \right) + \\ &\frac{1}{D_2 \Gamma(\alpha_2 + 1)} \frac{N_{T2}}{N_T} \left(\frac{D}{D_2} \right)^{\alpha_2} \exp\left(-\frac{D}{D_2} \right).\end{aligned} \tag{B.2}$$

It is convenient to rewrite this as

$$p(D) = \frac{\eta_1}{D_1 \Gamma(\alpha_1 + 1)} \left(\frac{D}{D_1} \right)^{\alpha_1} \exp\left(-\frac{D}{D_1} \right) + \frac{(1 - \eta_1)}{D_2 \Gamma(\alpha_2 + 1)} \left(\frac{D}{D_2} \right)^{\alpha_2} \exp\left(-\frac{D}{D_2} \right), \tag{B.3}$$

where $\eta_1 \equiv \frac{N_{T1}}{N_T} \in [0,1]$. The distribution parameter vector $\boldsymbol{\theta} = [\eta_1, D_1, \alpha_1, D_2, \alpha_2]^T$ is then estimated using the method of moments, minimizing the misfit functional

$$\phi(\boldsymbol{\theta}) = \left\| \mathbf{E}_{data} - \mathbf{E}(\boldsymbol{\theta}) \right\|^2, \tag{B.4}$$

where $\mathbf{E}_{data}$ and $\mathbf{E}(\boldsymbol{\theta})$ are vectors whose elements are the first through the fifth measured and parametric noncentral moments, respectively. The parametric moments are

$$\mathrm{E}[D^1] = \eta_1 D_1(\alpha_1+1) + (1-\eta_1) D_2(\alpha_2+1), \tag{B.5}$$

$$\mathrm{E}[D^2] = \eta_1 D_1^2(\alpha_1+2)(\alpha_1+1) + (1-\eta_1) D_2^2(\alpha_2+2)(\alpha_2+1), \tag{B.6}$$

$$\mathrm{E}[D^3] = \eta_1 D_1^3(\alpha_1+3)(\alpha_1+2)(\alpha_1+1) + (1-\eta_1) D_2^3(\alpha_2+3)(\alpha_2+2)(\alpha_2+1), \tag{B.7}$$

$$\begin{aligned}\mathrm{E}[D^4] = {} & \eta_1 D_1^4(\alpha_1+4)(\alpha_1+3)(\alpha_1+2)(\alpha_1+1) + \\ & (1-\eta_1) D_2^4(\alpha_2+4)(\alpha_2+3)(\alpha_2+2)(\alpha_2+1),\end{aligned} \tag{B.8}$$

$$\begin{aligned}\mathrm{E}[D^5] = {} & \eta_1 D_1^5(\alpha_1+5)(\alpha_1+4)(\alpha_1+3)(\alpha_1+2)(\alpha_1+1) + \\ & (1-\eta_1) D_2^5(\alpha_2+5)(\alpha_2+4)(\alpha_2+3)(\alpha_2+2)(\alpha_2+1).\end{aligned} \tag{B.9}$$

Finally, solutions for N_1 and N_2 come from the definition of η and from the zeroth moment of the nonnormalized PSD M_0:

$$N_1 = \frac{\eta_1 M_0}{D_1 \Gamma(\alpha_1 + 1)}, \tag{B.10}$$

$$N_2 = \frac{(1-\eta_1) M_0}{D_2 \Gamma(\alpha_2 + 1)}. \tag{B.11}$$

The mode for which the product of the scale and shape parameters is the larger is selected as the large mode.

Expectation-Maximization

For this fitting method, binned counts of cloud particles are modeled as independent samples taken from a multinomial distribution (Bain and Englehardt, 1992), following Johnson et al. (2013). Let y_l be the total number of particle counts in the l^{th} size bin (from a total of L possible size bins). Therefore, if the observed particle size distribution is the vector **y**, then the probability mass function of the counts in its size bins is

$$\Pr(\mathbf{y}) = p_{\mathbf{y}}(\mathbf{y}) = \frac{N_T!}{\prod_{l=1}^{L} y_l!} \prod_{l=1}^{L} p_l^{y_l}, \tag{B.12}$$

where p_l is the probability of obtaining a count in the l^{th} size bin (computed by integrating the assumed mixture distribution) and where N_T is the total number of counts.

Alternatively, the binned counts of cloud particles can be modeled as samples taken from a multinomial distribution with $2L$ bins: a sample may fall in bin l_1 (small particle mode) or in bin l_2 (large particle mode), or, in other words, let x_{1l} be the number of counts in the l^{th} size bin pertaining to the small particle mode, and let x_{2l} be the number of counts in the l^{th} size bin pertaining to the large particle mode. (It must be that the total number of particle counts in a size bin is equal to the numbers of counts in the small and large particle modes.) In this case, the probability mass function of the counts in the particle size distribution is

$$\Pr\left(x_{11},x_{21},\ldots,x_{L1},x_{12},x_{22},\ldots,x_{L2}\right)=p_{\mathbf{x}_1,\mathbf{x}_2}\left(\mathbf{x}_1,\mathbf{x}_2\right) \tag{B.13}$$

and may be expressed in either of two forms:

$$p_{\mathbf{x}_1,\mathbf{x}_2}\left(\mathbf{x}_1,\mathbf{x}_2\right)=\frac{N_T!}{\prod_{l=1}^{L}x_{l1}!x_{l2}!}\prod_{l=1}^{L}p_{l1}^{x_{l1}}p_{l2}^{x_{l2}},\text{ or} \tag{B.14}$$

$$p_{\mathbf{x}_1,\mathbf{x}_2}\left(\mathbf{x}_1,\mathbf{x}_2\right)=\frac{N_T!}{\prod_{l=1}^{L}x_{l1}!x_{l2}!}\exp\left\{\sum_{l=1}^{L}x_{l1}\ln\left[p_{l1}\right]+x_{l2}\ln\left[p_{l2}\right]\right\}. \tag{B.15}$$

Here, p_{l1} is the probability of obtaining a count in the l^{th} size bin of the small mode component of the PSD, and p_{l2} is the probability of obtaining a count in the l^{th} size bin of the large mode component. These probabilities are computed by integrating the large and small modes of the assumed mixture distribution and are given, for example, for the small mode by

$$p_{l1}=\frac{\eta_1}{\Gamma\left(\alpha_1+1\right)}\left[\gamma\left(\alpha_1+1,\frac{D_{l+1}}{D_1}\right)+\gamma\left(\alpha_1+1,\frac{D_l}{D_1}\right)\right], \tag{B.16}$$

where $\gamma\left(\ldots\right)$ is the lower incomplete gamma function.

The expectation-maximization algorithm is an interative algorithm that makes use of two steps: an expectation step and a maximization step. Following Moon (1996), we begin with the function

$$Q\left(\boldsymbol{\theta},\boldsymbol{\theta}^{[k]}\right)=\mathrm{E}\left\{\ln\left[p\left(\mathbf{x}\mid\boldsymbol{\theta}\right)\mid\mathbf{y},\boldsymbol{\theta}^{[k]}\right]\right\}. \tag{B.17}$$

On the right-hand side of Eq. B.17, $p(\mathbf{x},\boldsymbol{\theta})$ denotes the likelihood function of the vector of mixture distribution parameters $\boldsymbol{\theta}$ given the (missing) data vector $\mathbf{x}$. The data vector contains counts of all sampled particles, segregated by mode, and is considered "missing" for two reasons: 1) the data is binned and 2) it is not known to which mode each sample would belong were they had. For the expectation step, the expected value of the log-likelihood function (with respect to $\mathbf{x}$) is computed, given a set of observed data $\mathbf{y}$ (in this application, the binned PSD) and a current estimate of the parameters $\boldsymbol{\theta}^{[k]}$. This expected value becomes the current estimate of the missing data $\mathbf{x}^{[k]}$. Equation B.17 is then maximized with respect to the parameter vector $\boldsymbol{\theta}$ in order to obtain a new estimate $\boldsymbol{\theta}^{[k+1]}$:

$$\boldsymbol{\theta}^{[k+1]}=\arg\max_{\boldsymbol{\theta}}\left[Q\left(\boldsymbol{\theta},\boldsymbol{\theta}^{[k]}\right)\right]. \tag{B.18}$$

As $p_{\mathbf{x}_1,\mathbf{x}_2}\left(\mathbf{x}_1,\mathbf{x}_2\right)$ is a member of the exponential distribution family (see Eq. B.15), it will suffice for the expectation step to estimate $\mathbf{x}_1$ and $\mathbf{x}_2$ (Moon, 1996). To do so, their expected values, conditioned upon the observations $\mathbf{y}$ and on an estimate of the distribution parameters $\boldsymbol{\theta}^{[k]}$, will be found. Equation B.18 is therefore transformed using

$$\mathbf{y}=\left[y_1,\ldots,y_L\right]^T=\left[\left(x_{11}+x_{12}\right),\ldots,\left(x_{L1}+x_{L2}\right)\right]^T=\mathbf{x}_1+\mathbf{x}_2 \tag{B.19}$$

so that

$$p_{\mathbf{x}_1,\mathbf{y}}(\mathbf{x}_1,\mathbf{y}) = p_{\mathbf{x}_1,\mathbf{x}_2}(\mathbf{x}_1,\mathbf{y}-\mathbf{x}_1) = \frac{N_T!}{\prod_{l=1}^{L} x_{l1}!(y_l - x_{l1})!} \prod_{l=1}^{L} p_{l1}^{x_{l1}} p_{l2}^{(y_l - x_{l1})}. \tag{B.20}$$

The conditional distribution of $\mathbf{x}_1$ is therefore (from Eqs. B.12 and B.20)

$$p(\mathbf{x}_1 \mid \mathbf{y}) = \frac{p_{\mathbf{x}_1,\mathbf{y}}(\mathbf{x}_1,\mathbf{y})}{p_{\mathbf{y}}(\mathbf{y})} = \prod_{l=1}^{L} \frac{y_l!}{x_{l1}!(y_l - x_{l1})!} \left(\frac{p_{l1}}{p_l}\right)^{x_{l1}} \left(\frac{p_{l2}}{p_l}\right)^{(y_l - x_{l1})}, \tag{B.21}$$

which is evidently the joint distribution of a sample of independent binomial random variables. Similarly, it may be found that

$$p(\mathbf{x}_2 \mid \mathbf{y}) = \prod_{l=1}^{L} \frac{y_l!}{x_{l2}!(y_l - x_{l2})!} \left(\frac{p_{l1}}{p_l}\right)^{(y_l - x_{l2})} \left(\frac{p_{l2}}{p_l}\right)^{x_{l2}}. \tag{B.22}$$

The conditional expectations are therefore

$$\mathrm{E}[x_{l1} \mid y_l] = x_{l1}^{[k]} = y_l \frac{p_{l1}^{[k]}}{p_l^{[k]}}, \tag{B.23}$$

$$\mathrm{E}[x_{l2} \mid y_l] = x_{l2}^{[k]} = y_l \frac{p_{l2}^{[k]}}{p_l^{[k]}}. \tag{B.24}$$

The maximization step then requires, by Eq. B.18, the maximization of the logarithm of Eq. B.17 with respect to $\boldsymbol{\theta}$, using the estimates $\mathbf{x}_1^{[k]}$ and $\mathbf{x}_2^{[k]}$. Dropping terms that are not functions of the distribution parameters gives

$$\boldsymbol{\theta}^{[k+1]} = \arg\max_{\boldsymbol{\theta}} \left\{ \sum_{l=1}^{L} x_{l1}^{[k+1]} \ln\left[p_{l1}\right] + x_{l2}^{[k+1]} \ln\left[p_{l2}\right] \right\}. \qquad \text{(B.25)}$$

Beginning with an initial estimate for the distribution parameters $\boldsymbol{\theta}^{[0]}$, Eqs. B.23–B.25 are iterated until the distribution parameters converge.

In this case, solutions for N_1 and N_2 come from the definition of η_1 and from the second noncentral sample moment of the nonnormalized PSD M_2:

$$N_1 = \frac{\eta_1 M_2}{D_1 \Gamma(\alpha_1+1)\left[\eta_1 D_1^2 (\alpha_1+2)(\alpha_1+1) + (1-\eta_1)(\alpha_2+2)(\alpha_2+1)\right]} \qquad \text{(B.26)}$$

$$N_2 = \frac{(1-\eta_1) M_2}{D_2 \Gamma(\alpha_2+1)\left[\eta_1 D_1^2 (\alpha_1+2)(\alpha_1+1) + (1-\eta_1)(\alpha_2+2)(\alpha_2+1)\right]} \qquad \text{(B.27)}$$

The second noncentral moment was used to ensure good reproduction of the zeroth through the second noncentral PSD moments by the expectation maximization solution. The mode for which the product of the scale and shape parameters is the larger is selected as the large mode.

First Guesses for Fitting Algorithms

The misfit functional (Eq. B.4) has many local minima, and the log-likelihood function (Eq. B.18) has many local maxima. In either case, then, the iterative search for a global extremum is highly sensitive to the first guess given it. To circumvent this problem, the minimization of Eq. B.4 and the iterative set of Eqs. B.23–B.25 are executed multiple times with multiple first guesses in this manner: the measured PSD is broken up into many first guesses as to which bins might comprise the small and large modes, and the moments scheme described in Appendix A is used to fit parameters for each first guess at each mode. This set of first-guess fit parameters is used as the set of first guesses for the minimization of Eq. B.4 and as the set of first guesses $\boldsymbol{\theta}^{[0]}$ for the expectation-maximization algorithm. Then, for both the method of moments and the expectation-maximization algorithm, the solutions ultimately used as bimodal fits are those which give the minimum Anderson–Darling test statistic for binned data (Demortier, 1995; see Appendix C).

Finally, between the method of moments solution and the expectation-maximization solution, that solution was kept as the bimodal fit that proffered the smaller Anderson–Darling test statistic for binned data (Demortier, 1995). It should be noted that this method has proved successful at modeling bimodality in ice PSDs measured by the 2D-S instrument alone, but if an ice PSD is constructed from a combination of the 2D-S and a precipitation particle imager (such as the HVPS), this method is problematic, and the combined PSD is better modeled as a sum of two distributions contributed by each instrument (however the distribution associated with each instrument is parameterized).

APPENDIX C

STATISTICAL TESTS FOR THE EVALUATION OF FITS

Maximum Likelihood Ratio Test

The likelihood ratio test statistic is twice the natural logarithm of the ratio of the likelihood of the bimodal fit to the unimodal fit (Wilks, 2006):

$$\Lambda = 2\ln\left[\frac{\mathrm{L}(\mathrm{bimodal})}{\mathrm{L}(\mathrm{unimodal})}\right] = 2\ln\left[\mathrm{L}(\mathrm{bimodal})\right] - 2\ln\left[\mathrm{L}(\mathrm{unimodal})\right]. \qquad \text{(C.1)}$$

The asymptotic distribution of Λ is χ^2 with three degrees of freedom. Computation of these likelihoods is performed by treating the PSDs as samples from multinomial random variables (as is done in the expectation-maximization fitting algorithm). First, the proposed unimodal and bimodal parametric fits are converted into probability density functions, as in Eqs. A.1 and B.3. Then, these density functions are integrated over each of the size bins, and the result for each size bin is the probability for each category in the multinomial distribution (unimodal and bimodal probabilities, respectively, shown below, where P is the regularized, lower incomplete gamma function):

$$p_i = \mathrm{P}\left(\alpha + 1, \frac{D_{i+1}}{D_0}\right) - \mathrm{P}\left(\alpha + 1, \frac{D_i}{D_0}\right) \qquad \text{(C.2)}$$

$$p_i = \eta_1\left[\mathrm{P}\left(\alpha_1+1,\frac{D_{i+1}}{D_1}\right)-\mathrm{P}\left(\alpha_1+1,\frac{D_i}{D_1}\right)\right]+ \\ \left(1-\eta_1\right)\left[\mathrm{P}\left(\alpha_2+1,\frac{D_{i+1}}{D_2}\right)-\mathrm{P}\left(\alpha_2+1,\frac{D_i}{D_2}\right)\right]. \tag{C.3}$$

The PSDs' units are converted to *(# of particles)* L^{-1} μm^{-1}, and the total number of counts from all the bins is taken to be the sample size. The likelihood function, in either the unimodal or the bimodal case, thus becomes

$$\mathrm{L} = \prod\nolimits_{i=1}^{N} p_i^{\{\#\ \text{samples in bin}\ i\}}. \tag{C.4}$$

If the p-value is at least 95%, then the null hypothesis that the unimodal fit is sufficient is rejected.

One-Sample Anderson–Darling Test for Binned Data

This is an application of a general algorithm given in Demortier (1995). The one-sample Anderson–Darling statistic, like the corresponding Kolmogorov–Smirnov and Smirnov–Cramer–von Mises statistics, are designed to measure deviations of an empirical cumulative distribution function from a proposed parametric cumulative distribution function. Demortier (1995) adapted these statistics and their corresponding sampling distributions to the case where only a binned version of the original data is had.

Following Demortier's (1995) notation, given that a total of N_T data samples are binned into B bins with contents d_j, the empirical cumulative distribution function is computed according to the following two equations:

$$N_T = \sum\nolimits_{j=1}^{B} d_j, \tag{C.5}$$

$$S_k = \frac{1}{N_T}\sum_{j=1}^{k} d_j,\ \left(k = 1,\dots,B\right). \tag{C.6}$$

The binned, parametric cumulative distribution function (denoted by F) is computed by integrating the unimodal, parametric probability density function from Eq. A.1 over each of the B size bins as follows (where u_j and l_j denote the upper and lower edges of the j^{th} bin, respectively):

$$F\left(u_j\right) = \mathrm{P}\left(\alpha + 1, \frac{u_j}{D_0}\right), \tag{C.7}$$

$$t_j = \mathrm{F}\left(u_j\right) - \mathrm{F}\left(l_j\right), \tag{C.8}$$

$$T = \sum_{j=1}^{B} t_j, \tag{C.9}$$

$$\mathrm{F}_k = \frac{1}{T}\sum_{j=1}^{k} t_j,\ \left(k = 1,\dots,B\right). \tag{C.10}$$

The test statistic is then given by

$$A^2 = N_T \sum_{j=1}^{B} \frac{\left(S_j - \mathrm{F}_j\right)^2}{\mathrm{F}_j\left(1 - \mathrm{F}_j\right)T}. \tag{C.11}$$

The strategy for computing a p-value is as follows:

1) Compute the test statistic A^2 from the data.

2) Generate N_T random numbers D_i according to the theoretical distribution function.
3) Collect the D_i's into a histogram with the same bins as the PSD and form a new empirical distribution function S_k.
4) Calculate the test statistic A^2 between F_k and the new S_k.
5) Repeat steps 2)–4) 1 000 times, and calculate the fraction of times that the simulated test statistic is larger than the measured statistic. This fraction is the p-value.

In order to generate random numbers according to the probability density function given in Eq. A.1, it is necessary to use the method of inverse transform sampling (Devroye, 1986). A total of N_T uniform random numbers a_i are generated on the interval $a \in [0,1]$, and they are transformed via the inverse of the cumulative distribution function of D (or, in other words, via the inverse of Eq. C.7) to random numbers D_i from the desired density function:

$$D_i = D_0 \mathrm{P}^{-1}\left(\alpha + 1, a_i\right). \tag{C.12}$$

Generalized χ^2 Goodness-of-Fit Test Using Sample Moments

Consider the vectors **m** (containing noncentral sample moments) and $\boldsymbol{\mu}$ (containing hypothesized, noncentral population moments). By the multivariate central limit theorem (van der Vaart, 1998),

$$\sqrt{n}\left(\mathbf{m} - \boldsymbol{\mu}\right) \sim N\left(0, \mathrm{Cov}\left(\boldsymbol{\mu}\right)\right), \tag{C.13}$$

for large n, where N here denotes the multivariate normal distribution (Kotz et al., 2000) and where (Gurland and Dahiya, 1972)

$$\mathrm{Cov}(\boldsymbol{\mu}) = \mathbf{G} = \left[g_{ij}\right] = \left[\mu_{i+j} - \mu_i\mu_j\right]. \tag{C.14}$$

The test here described is an adaptation of that given in Gurland and Dahiya (1972). Specifically, whereas they used linear combinations of sample cumulants in order to simplify the statistical test, only the pure sample moments are used here. Thus, given Eq. C.13, the asymptotic distribution of the test statistic

$$Q = n(\mathbf{m} - \boldsymbol{\mu})^T \mathbf{G}^{-1}(\mathbf{m} - \boldsymbol{\mu}) = \mathbf{a}^T\mathbf{G}^{-1}\mathbf{a}^T \tag{C.15}$$

is the generalized χ^2 distribution (Jones, 1983):

$$Q \sim \chi^2\left(\mathbf{G}^{-1}, \mathbf{G}\right). \tag{C.16}$$

The cumulative generalized χ^2 distribution function must be computed numerically. It is evaluated here, at a particular value of Q, according to the algorithm given by Sheil and O'Muircheartaigh (1977), which requires that the matrix $\mathbf{G}^{-1}$ be either symmetric positive definite or positive semidefinite (in the case that it is neither, the test cannot be performed, and it is assumed that the observed PSD cannot appropriately be fit with the hypothesized, parametric distribution). Evaluation of the distribution function proceeds as follows, using the notation of Sheil and O'Muircheartaigh (1977).

First, the Cholesky decomposition of the covariance matrix is performed: $\mathbf{G} = \mathbf{L}^T\mathbf{L}$. Let α_i be the eigenvalues of the matrix $\mathbf{L}\mathbf{G}^{-1}\mathbf{L}$. Then, let $\mathrm{F}(n', y)$ denote the cumulative distribution function of a central generalized χ^2 random variable with n'

degrees of freedom. Then

$$\Pr\left[\left(\mathbf{a}^T\mathbf{G}^{-1}\mathbf{a}\right)\le t\right]=\begin{cases}\sum_{k=0}^{\infty}c_k\mathrm{F}\left(n'+2k,\frac{t}{\beta}\right),t>0\\ 0,t\le 0\end{cases}\tag{C.17}$$

where n' is the rank of the matrix $\mathbf{LG}^{-1}\mathbf{L}^T$. It remains to define β and the coefficients c_k. Following Sheil and O'Muircheartaigh (1977), the value $\beta=0.90625\alpha_{\min}$ is used, $\alpha_{\min}$ being the smallest eigenvalue of the matrix $\mathbf{LG}^{-1}\mathbf{L}^T$. The coefficients c_k are then computed via the following set of equations:

$$A=\prod_{j=1}^{n'}\sqrt{\frac{\beta}{\alpha_j}},\tag{C.18}$$

$$\gamma_i=1-\frac{\beta}{\alpha_j},\ \left(j=1,\ldots,n'\right),\tag{C.19}$$

$$p_m=\frac{1}{2}\sum_{j=1}^{n'}\gamma_j^m,\tag{C.20}$$

$$c_0=A,\tag{C.21}$$

$$c_k=k^{-1}\sum_{r=0}^{k-1}p_{k-r}c_r.\tag{C.22}$$

As for accuracy, the series in Eq. C.17 is terminated when the maximum possible contribution from the remaining terms is less than 10^{-5}. This is determined from the following inequality (Sheil and O'Muircheartaigh, 1977):

$$\sum_{k=Z+1}^{\infty} c_k \mathrm{F}\left(n' + 2k, \frac{t}{\beta} \right) < \left(1 - \sum_{k=0}^{Z} c_k \right) \mathrm{F}\left(n' + 2k, \frac{t}{\beta} \right), \tag{C.23}$$

where Z denotes the number of terms that have already been computed.

In the current practical application, viz., that of testing whether a binned, measured PSD is sufficiently well fit by a unimodal, parametric gamma distribution, the sample size is chosen by scaling the measured PSD so that its units are (# particles) L^{-1} $\mu\mathrm{m}^{-1}$, and the total number of counts from all the bins is taken to be the sample size. The measured PSD is then normalized so that its zeroth moment is unity, and the test is performed, comparing the sample moments of the normalized PSD with the moments of the fit, normalized parametric gamma distribution.

APPENDIX D

COMPUTATION OF PHYSICAL QUANTITIES USING PARAMETRIC PSDs

Physical quantities are computed using the unimodal PSD fits, except for the total number concentration N_T, which is computed using both the unimodal and the bimodal PSD fits. Total number concentration is best estimated by computing a truncated zeroth moment of the PSD, to wit, by integrating the PSD from the smallest used bin edge (15 μm) to infinity. For the unimodal PSD, this is given by (in cgs units)

$$N_T = N_0 D_0 \Gamma\left(\alpha + 1, \frac{0.0015}{D_0}\right), \tag{D.1}$$

where $\Gamma(x, y)$ denotes the upper incomplete gamma function. For the bimodal PSD, it is given by

$$N_T = N_{01} D_{01} \Gamma\left(\alpha_1 + 1, \frac{0.0015}{D_{01}}\right) + N_{02} D_{02} \Gamma\left(\alpha_2 + 1, \frac{0.0015}{D_{02}}\right). \tag{D.2}$$

The shortwave extinction coefficient σ is computed assuming some dimensional/cross-sectional area relationship:

$$A(D) = a_A D^{b_A}, \tag{D.3}$$

$$\sigma = a_A N_0 D_0^{b_A+1} \Gamma\left(\alpha + b_A + 1\right). \tag{D.4}$$

Ice water content is computed assuming some dimensional/density relationship $\rho\left(D\right)$, where ρ is the density a nonspherical particle with maximum dimension D would have were it a sphere with diameter D:

$$\rho\left(D\right) = a_m D^{b_m}, \tag{D.5}$$

$$IWC = a_m \left(\frac{\pi}{6}\right) N_0 D_0^{b_m+4} \Gamma\left(\alpha + b_m + 4\right). \tag{D.6}$$

To compute effective radar reflectivity, a dimensional/backscatter cross-sectional power law is used, but the power law coefficients are defined piecewise-constant over several size intervals. The coefficients come from a set of power-law fits to T-matrix computations of backscatter cross section (Matrosov, 2007; Matrosov et al., 2012; Hammonds, 2013; Posselt and Mace, 2013) to compute reflectivity, assuming an air/ice dielectric mixing model and that all particles are prolate spheroids with aspect ratios of 0.7 (Korolev and Isaac, 2003; Westbrook et al., 2004a; Westbrook et al., 2004b; Hogan et al., 2012).

$$Z_e = \frac{10^8 \lambda^4}{\left|K_w\right|^2 \pi^5} \sum_i \int_{D_i}^{D_{i+1}} a_{zi} D^{b_{zi}} n\left(D\right) dD = \frac{10^8 \lambda^4}{\left|K_w\right|^2 \pi^5} \sum_i J_i, \tag{D.7}$$

where D_i and D_{i+1} are the beginning and the ending of each size interval over which the dimensional/backscatter cross-sectional power law coefficients are defined (for the last size interval, the upper size limit is infinity). The terms J_i are given by

$$J_i = a_{zi} N_0 D_0^{b_{zi}+1} \left[\gamma\left(\alpha + b_{zi} + 1, \frac{D_{i+1}}{D_0} \right) - \gamma\left(\alpha + b_{zi} + 1, \frac{D_i}{D_0} \right) \right], \tag{D.8}$$

except for the last size interval, where

$$J_{end} = a_{zend} N_0 D_0^{b_{zend}+1} \Gamma\left(\alpha + b_{zend} + 1, \frac{D_{end}}{D_0} \right). \tag{D.9}$$

Here, $\gamma(x, y)$ denotes the lower incomplete gamma function, $|K_w|^2$, the square of the magnitude of the complex index of refraction of water and *n(D)*, the particle size distribution. Using the constants given, if the units of λ are millimeters and the units of the particle size distribution are as given in Chapter 2, then the units of Z_e are mm^6 m^{-3}.

APPENDIX E

COMPUTATION USING THE UNIVERSAL PSD FROM CHAPTER 3

Physical quantities are here computed using both the bimodal and the trimodal forms of the universal PSD (shown in Eqs. 3.4 and 3.5) in combination with the appropriate scale factors N^* and D^*. It is important to recall that all other parameters used in this Appendix are as in Table 3.2, that is, they are fixed and do not vary for each PSD as in Chapter 2. For each quantity, the bimodal computation is listed first, followed by the trimodal computation.

Total number concentration N_T is computed by integrating a PSD from the left edge of the smallest size bin (denoted here as a) out to infinity. For this computation, it is critical to note that the shape parameter is negative unity for the smallest mode.

$$N_{T,\mathrm{bimodal}} = N^* D^* \left[N_1 D_1 \mathrm{E}_1\left(\frac{a}{D^* D_1} \right) + N_1 D_1 \Gamma\left(\alpha_2 + 1, \frac{a}{D^* D_1} \right) \right], \qquad \text{(E.1)}$$

$$N_{T,\mathrm{trimodal}} = N^* D^* \left[N_1 D_1 \mathrm{E}_1\left(\frac{a}{D^* D_1} \right) + N_1 D_1 \Gamma\left(\alpha_2 + 1, \frac{a}{D^* D_1} \right) + N_3 \right], \qquad \text{(E.2)}$$

where $\mathrm{E}_1(x)$ denotes the exponential integral and $\Gamma(x,y)$ denotes the upper, incomplete gamma function.

The shortwave extinction coefficient σ is computed by assuming a cross-sectional area/dimensional relationship $A(D) = a_A D^{b_A}$ and an extinction efficiency of two.

$$\sigma_{\text{bimodal}} = 2a_A N^* \left(D^*\right)^{b_A+1} \left[N_1 D_1^{b_A+1} \Gamma\left(\alpha_1 + b_A + 1\right) + N_2 D_2^{b_A+1} \Gamma\left(\alpha_2 + b_A + 1\right) \right], \qquad \text{(E.3)}$$

$$\sigma_{\text{trimodal}} = 2a_A N^* \left(D^*\right)^{b_A+1} \left[N_1 D_1^{b_A+1} \Gamma\left(\alpha_1 + b_A + 1\right) + N_2 D_2^{b_A+1} \Gamma\left(\alpha_2 + b_A + 1\right) \right] + I_\sigma, \qquad \text{(E.4)}$$

where

$$I_\sigma = N_3 \frac{\beta_3^{\alpha_3}}{\Gamma\left(\alpha_3\right)} \int_0^\infty \left(w + 1.55\right)^{b_A} w^{-\alpha_3 - 1} \exp\left(-\frac{\beta_3}{w} \right) dw. \qquad \text{(E.5)}$$

Ice water content is computed via an assumed density/dimensional relationship $\rho(D) = a_m D^{b_m}$ (which relationship gives the density that a nonspherical particle with maximum dimension D would have were it a sphere with diameter D):

$$\begin{aligned} IWC_{\text{bimodal}} = a_m \left(\frac{\pi}{6} \right) N^* \left(D^*\right)^{b_m+4} \Big[& N_1 D_1^{b_m+4} \Gamma\left(\alpha_1 + b_m + 4\right) + \\ & N_2 D_2^{b_m+4} \Gamma\left(\alpha_2 + b_m + 4\right) \Big], \end{aligned} \qquad \text{(E.6)}$$

$$\begin{aligned} IWC_{\text{trimodal}} = a_m \left(\frac{\pi}{6} \right) N^* \left(D^*\right)^{b_m+4} \Big[& N_1 D_1^{b_m+4} \Gamma\left(\alpha_1 + b_m + 4\right) + \\ & N_2 D_2^{b_m+4} \Gamma\left(\alpha_2 + b_m + 4\right) + I_{IWC} \Big], \end{aligned} \qquad \text{(E.7)}$$

where

$$I_{IWC} = N_3 \frac{\beta_3^{\alpha_3}}{\Gamma(\alpha_3)} \int_0^{\infty} (w+1.55)^{b_m+3} w^{-\alpha_3-1} \exp\left(-\frac{\beta_3}{w}\right) dw. \tag{E.8}$$

Effective radar reflectivity is computed piecewise, as in Appendix D. It is first noted, however, in accordance with Eq. 3.3, that

$$Z_e = \frac{10^8 \lambda^4}{|K_w|^2 \pi^5} \sum_i \int_{D_i}^{D_{i+1}} a_{zi} D^{b_{zi}} n(D) dD = \frac{10^8 \lambda^4}{|K_w|^2 \pi^5} \sum_i \int_{D_i}^{D_{i+1}} a_{zi} D^{b_{zi}} N^* F_u\left(\frac{D}{D^*}\right) dD, \tag{E.9}$$

where D_i and D_{i+1} are the beginning and the ending of each size interval over which the dimensional/backscatter cross-sectional power law coefficients are defined (for the last size interval, the upper size limit is infinity). It may then be written that

$$Z_e = \frac{10^8 \lambda^4}{|K_w|^2 \pi^5} \sum_i \int_{D_i}^{D_{i+1}} a_{zi} D^{b_{zi}} N^* F_u\left(\frac{D}{D^*}\right) dD = \frac{10^8 \lambda^4}{|K_w|^2 \pi^5} \sum_i J_i. \tag{E.10}$$

If the bimodal form of the universal PSD is being used, then the terms in the summation are

$$\begin{aligned} J_{i(\mathrm{bi})} = a_{zi} N^* \left(D^*\right)^{b_{zi}+1} \Bigg\{ & N_1 D_1^{b_{zi}+1} \left[\gamma\left(b_{zi}+\alpha_1+1, \frac{D_{i+1}}{D_1 D^*}\right) - \gamma\left(b_{zi}+\alpha_1+1, \frac{D_i}{D_1 D^*}\right) \right] \\ & + N_2 D_2^{b_{zi}+1} \left[\gamma\left(b_{zi}+\alpha_2+1, \frac{D_{i+1}}{D_2 D^*}\right) - \gamma\left(b_{zi}+\alpha_2+1, \frac{D_i}{D_2 D^*}\right) \right] \Bigg\}, \end{aligned} \tag{E.11}$$

($\gamma(x,y)$ denoting the lower incomplete gamma function) with the last term being

$$J_{end(\mathrm{bi})} = a_{zend} N^* \left(D^*\right)^{b_{zend}+1} \left[N_1 D_1^{b_{zend}+1} \Gamma\left(b_{zend} + \alpha_1 + 1, \frac{D_{end}}{D_1 D^*} \right) \right. \\ \left. + N_2 D_2^{b_{zend}+1} \gamma\left(b_{zend} + \alpha_2 + 1, \frac{D_{end}}{D_2 D^*} \right) \right]. \tag{E.12}$$

If the trimodal form of the universal PSD is being used, then the terms in the summation are

$$J_{i(\mathrm{tri})} = a_{zi} N^* \left(D^*\right)^{b_{zi}+1} \left\{ N_1 D_1^{b_{zi}+1} \left[\gamma\left(b_{zi} + \alpha_1 + 1, \frac{D_{i+1}}{D_1 D^*} \right) - \gamma\left(b_{zi} + \alpha_1 + 1, \frac{D_i}{D_1 D^*} \right) \right] \right. \\ \left. + N_2 D_2^{b_{zi}+1} \left[\gamma\left(b_{zi} + \alpha_2 + 1, \frac{D_{i+1}}{D_2 D^*} \right) - \gamma\left(b_{zi} + \alpha_2 + 1, \frac{D_i}{D_2 D^*} \right) \right] + I_{Zi} \right\}, \tag{E.13}$$

with the last term being

$$J_{end(\mathrm{bi})} = a_{zend} N^* \left(D^*\right)^{b_{zend}+1} \left[N_1 D_1^{b_{zend}+1} \Gamma\left(b_{zend} + \alpha_1 + 1, \frac{D_{end}}{D_1 D^*} \right) \right. \\ \left. + N_2 D_2^{b_{zend}+1} \gamma\left(b_{zend} + \alpha_2 + 1, \frac{D_{end}}{D_2 D^*} \right) + I_{Zend} \right]. \tag{E.14}$$

The form of the term I_{Zi} depends upon the range of the size interval over which integration is being performed:

$$I_{Zi} = \begin{cases} 0, & 1.55 > \dfrac{D_{i+1}}{D^*} > \dfrac{D_i}{D^*} \\ N_3 \dfrac{\beta_3^{\alpha_3}}{\Gamma(\alpha_3)} \displaystyle\int_{1.55}^{\frac{D_{i+1}}{D^*}-1.55} w^{-\alpha_3-1} \left(w+1.55\right)^{b_{zi}} \exp\left(-\frac{\beta_3}{w}\right) dw, & \dfrac{D_{i+1}}{D^*} > 1.55 > \dfrac{D_i}{D^*}, \\ N_3 \dfrac{\beta_3^{\alpha_3}}{\Gamma(\alpha_3)} \displaystyle\int_{\frac{D_{end}}{D^*}-1.55}^{\infty} w^{-\alpha_3-1} \left(w+1.55\right)^{b_{zend}} \exp\left(-\frac{\beta_3}{w}\right) dw, & \dfrac{D_{i+1}}{D^*} > \dfrac{D_i}{D^*} > 1.55 \end{cases} \tag{E.15}$$

Again, for the last size interval, the upper size limit is infinity, and so

$$I_{Zend} = N_3 \frac{\beta_3^{\alpha_3}}{\Gamma\left(\alpha_3\right)} \int_{\frac{D_{end}}{D^*}-1.55}^{\infty} w^{-\alpha_3-1} \left(w+1.55\right)^{b_{zend}} \exp\left(-\frac{\beta_3}{w}\right) dw. \tag{E.16}$$

Given a measured radar reflectivity, the scale parameter N^* may be parameterized by solving Eq. E.10 for N^*:

$$N^* = \frac{\left|K_w\right|^2 \pi^5 Z_e}{10^8 \lambda^4 \sum_i \int_{D_i}^{D_{i+1}} a_{zi} D^{b_{zi}} F_u\left(\frac{D}{D^*}\right) dD}. \tag{E.17}$$

APPENDIX F

ON THE TRANSFORMATION AND NORMALIZATION OF CIRRUS PSDs

Transforming PSDs by Scaling from D-Space to D_e-Space

Due to the uncertainty in the zeroth mode of the measured PSDs, scaling from D-space to D_e-space so that Eqs. 4.2 and 4.3 are both satisfied is not possible. Since for the sake of estimating D_m and N_0^* it is more important that the IWCs be matched, this was done while matching the N_T's to within a factor of approximately 0.75. The scale factor, then, is derived based on this simple consideration: if the number of particles within a size bin is conserved upon the bin's transformation from D-space to D_e-space, then, given that the transformation is from maximum dimension to mass-equivalent spheres, so also is the mass of the particles within a size bin conserved. That is,

$$n_{D_e}\left(D_{e_i}\right)=n_D\left(D_i\right)\frac{a_m D_i^{b_m+3}\Delta D_i}{\rho_w D_{e_i}^3\Delta D_{e_i}}. \tag{F.1}$$

It is surmised that a similar conundrum was encountered in the analysis performed by Delanoe et al. (2005). Though it is not shown here, the scaling was also performed so as to match N_T rather than IWC, and the result that concentrations of particles with the smallest scaled diameters were in the neighborhood of an order of magnitude smaller than those shown in Delanoe et al. (2005) still held true.

Using the Transformed Distribution to Compute Shortwave Extinction Coefficient

A spherically equivalent PSD will not produce the same extinction as the real PSD because the cross-sectional area of the distribution has been altered by the transformation to mass-equivalent spheres. Instead, to compute extinction from the spherical distribution, the variable transformation given in Eq. 4.1 must be used to transform the spherical distribution back into its nonspherical form (Bain and Englehardt, 1992).

$$\int_0^\infty 2a_A D^{b_A} n_D\left(D\right)dD = \int_0^\infty 2a_A D^{\frac{3b_A+b_m}{3}} n_{D_e}\left[\left(\frac{a_m}{\rho_w}\right)^{\frac{1}{3}} D^{\frac{b_m+3}{3}}\right]\left(\frac{a_m}{\rho_w}\right)^{\frac{1}{3}}\left(\frac{b_m+3}{3}\right)dD. \qquad \text{(F.2)}$$

Computation of Effective Radar Reflectivity Using Transformed PSDs

The appropriate transformation for computing effective radar reflectivity is given in Eq. 4.5. The dimensional-backscatter cross-section power law coefficients are defined piecewise constant over several size intervals (Hammonds, 2013) as in the previous two Appendices, so that Eq. 4.5 is rewritten as

$$Z_e = \frac{10^8 \lambda^4}{\left|K_w\right|^2 \pi^5} \sum_i J_i, \qquad \text{(F.3)}$$

where

$$J_i = \int_{D_i}^{D_{i+1}} a_{zi} D^{\frac{3b_{zi}+b_m}{3}} n_{D_e}\left[\left(\frac{a_m}{\rho_w}\right)^{\frac{1}{3}} D^{\frac{b_m+3}{3}}\right]\left(\frac{a_m}{\rho_w}\right)^{\frac{1}{3}} D^{\frac{b_m+3}{3}} dD. \qquad \text{(F.4)}$$

The index variable *i* iterates through the set of power law coefficients, and the integrations J_i are performed piecewise over the corresponding size ranges.

Given that the spherical-equivalent PSD, when normalized, takes the form given in Eq. 4.8, the parameter N_0^* can be retrieved with a radar reflectivity measurement if D_m is known (D05). Substituting Eq. 4.8 into Eq F.4 and defining

$$I_i = \int_{D_i}^{D_{i+1}} a_{Zi} D^{\frac{2b_{Zi}+b_m}{3}} \mathrm{F}\left[\frac{\left(\frac{a_m}{\rho_w}\right)^{1/3} D^{\frac{b_m+3}{3}}}{D_m} \right] \left(\frac{a_m}{\rho_w}\right)^{1/3} D^{\frac{b_m+3}{3}} dD, \tag{F.5}$$

then the formula for effective reflectivity becomes

$$Z_e = \frac{10^8 \lambda^4 N_0^*}{\left|K_w\right|^2 \pi^5} \sum_i I_i . \tag{F.6}$$

Then, for any form of the universal distribution, N_0^* is found using

$$N_0^* = \frac{Z_e \left|K_w\right|^2 \pi^5}{10^8 \lambda^4 \sum_i I_i} . \tag{F.7}$$

The parameterization for N^* defined in Appendix E works equally well, given an estimated 94 GHz effective radar reflectivity and a value for D^*. D_m (from D05) and D^* are both parameterized by temperature, as follows:

$$D_m = 1802.05 \exp\left[0.0326\left(T - 32.5\right)\right], \tag{F.8}$$

$$D^* = 9.29\exp\left(0.99T\right), \tag{F.9}$$

where T is temperature, given in ℃.

Computations of Physical Quantities Using Parameterized PSDs from D05

The total number concentration is computed by integrating Eq. 4.2 from the left edge of the smallest transformed size bin out to infinity for each parametric, universal PSD form. The results are shown here, with the subscript indicating whether the result corresponds to the gamma-μ distribution or to the modified gamma distribution. For this computation, it is critical to note that the α parameter is negative unity for the modified gamma distribution.

$$N_{T\mu} = N_0^* D_m \frac{\Gamma(4)}{4^4}\frac{(4+\mu)^3}{\Gamma(4+\mu)}\Gamma\left(1+\mu,(4+\mu)\frac{D_{e_1}}{D_m}\right), \tag{F.10}$$

where $\Gamma\left(x,y\right)$ denotes the upper incomplete gamma function, and

$$N_{T\alpha,\beta} = N_0^* D_m \frac{\Gamma(4)}{4^4}\frac{\Gamma\left(\frac{\alpha+5}{\beta}\right)^3}{\Gamma\left(\frac{\alpha+4}{\beta}\right)^4}\mathrm{E}_1\left\{\left[\frac{D_{e_1}}{D_m}\frac{\Gamma\left(\frac{\alpha+5}{\beta}\right)}{\Gamma\left(\frac{\alpha+4}{\beta}\right)}\right]^{\beta}\right\}, \tag{F.11}$$

where $E_1\left(x\right) = \int_x^\infty \frac{e^{-t}}{t}dt$ is the exponential integral.

The extinction coefficient is obtained via Eq. F.2.

$$\sigma_{\mu} = 2a_{A}N_{0}^{*}D_{m}^{\frac{3b_{A}+b_{m}+3}{b_{m}+3}}\left(\frac{\rho_{w}}{a_{m}}\right)^{\frac{b_{A}}{b_{m}+3}}\frac{\Gamma(4)}{4^{4}}\left[\frac{(4+\mu)^{\frac{3b_{m}+9-3b_{A}}{b_{m}+3}}}{\Gamma(4+\mu)}\right]\Gamma\left(\frac{3b_{A}}{b_{m}+3}+\mu+1\right), \tag{F.12}$$

$$\sigma_{\alpha,\beta} = 2a_{A}N_{0}^{*}D_{m}^{\frac{3b_{A}+b_{m}+3}{b_{m}+3}}\left(\frac{\rho_{w}}{a_{m}}\right)^{\frac{b_{A}}{b_{m}+3}}\frac{\Gamma(4)}{4^{4}}\left[\frac{\Gamma\left(\frac{\alpha+5}{\beta}\right)^{\frac{3b_{m}+9-3b_{A}}{b_{m}+3}}}{\Gamma\left(\frac{\alpha+4}{\beta}\right)^{\frac{4b_{m}+12-3b_{A}}{b_{m}+3}}}\right]\times$$
$$\Gamma\left(\frac{3b_{A}}{\beta(b_{m}+3)}+\frac{\alpha+1}{\beta}\right). \tag{F.13}$$

For effective radar reflectivity, solutions of Eq. F.6 for each of the parameterized, universal distributions from D05 are given next.

$$I_{i\mu} = a_{Zi}\frac{\Gamma(4)}{4^{4}}\frac{(4+\mu)^{\frac{3b-3b_{Zi}+9}{b+3}}}{\Gamma(4+\mu)}\left(\frac{\rho_{w}}{a}\right)^{1/3}D_{m}^{2}\left[\left(\frac{\rho_{w}}{a}\right)^{1/3}D_{m}\right]^{\frac{3b_{Zi}-b-3}{b+3}}\times$$
$$\left[\gamma\left(\frac{3b_{Zi}-b-3}{b+3}+\mu+2,\frac{(4+\mu)\left(\frac{aD_{i+1}^{b}}{\rho_{w}}\right)^{1/3}D_{i+1}}{D_{m}}\right)-\gamma\left(\frac{3b_{Zi}-b-3}{b+3}+\mu+2,\frac{(4+\mu)\left(\frac{aD_{i}^{b}}{\rho_{w}}\right)^{1/3}D_{i}}{D_{m}}\right)\right] \tag{F.14}$$

$$I_{end\mu} = a_{Zend} \frac{\Gamma(4)}{4^4} \frac{(4+\mu)^{\frac{3b-3b_{Zend}+9}{b+3}}}{\Gamma(4+\mu)} \left(\frac{\rho_w}{a}\right)^{1/3} D_m^2 \left[\left(\frac{\rho_w}{a}\right)^{1/3} D_m\right]^{\frac{3b_{Zend}-b-3}{b+3}} \times$$

$$\Gamma\left(\frac{3b_{Zi}-b-3}{b+3}+\mu+2, \frac{(4+\mu)\left(\frac{aD_{end}^b}{\rho_w}\right)^{1/3} D_{end}}{D_m}\right) \tag{F.15}$$

$$I_{i\alpha,\beta} = a_{Zi} \frac{\Gamma(4)}{4^4} \frac{\Gamma\left(\frac{\alpha+5}{\beta}\right)^{\frac{3b-3b_{Zi}+9}{b+3}}}{\Gamma\left(\frac{\alpha+4}{\beta}\right)^{\frac{4b-3b_{Zi}+12}{b+3}}} D_m \left[\left(\frac{\rho_w}{a}\right)^{1/3} D_m\right]^{\frac{3b_{Zi}}{b+3}} \times$$

$$\left\{ \gamma\left[\frac{3b_{Zi}}{\beta(b+3)}+\frac{\alpha+1}{\beta}, \left(\frac{\left(\frac{aD_{i+1}^b}{\rho_w}\right)^{1/3} D_{i+1}}{D_m} \frac{\Gamma\left(\frac{\alpha+5}{\beta}\right)}{\Gamma\left(\frac{\alpha+4}{\beta}\right)}\right)^{\beta}\right] - \gamma\left[\frac{3b_{Zi}}{\beta(b+3)}+\frac{\alpha+1}{\beta}, \left(\frac{\left(\frac{aD_i^b}{\rho_w}\right)^{1/3} D_i}{D_m} \frac{\Gamma\left(\frac{\alpha+5}{\beta}\right)}{\Gamma\left(\frac{\alpha+4}{\beta}\right)}\right)^{\beta}\right] \right\} \tag{F.16}$$

$$I_{end\alpha,\beta} = a_{Zend}\frac{\Gamma\left(4\right)}{4^4}\frac{\Gamma\left(\frac{\alpha+5}{\beta}\right)^{\frac{3b-3b_{Zend}+9}{b+3}}}{\Gamma\left(\frac{\alpha+4}{\beta}\right)^{\frac{4b-3b_{Zend}+12}{b+3}}}D_m\left[\left(\frac{\rho_w}{a}\right)^{1/3}D_m\right]^{\frac{3b_{Zend}}{b+3}}\times$$

$$\gamma\left[\frac{3b_{Zend}}{\beta\left(b+3\right)}+\frac{\alpha+1}{\beta},\left(\frac{\left(\frac{aD_{i+1}^{b}}{\rho_w}\right)^{1/3}D_{end}}{D_m}\frac{\Gamma\left(\frac{\alpha+5}{\beta}\right)}{\Gamma\left(\frac{\alpha+4}{\beta}\right)}\right)^{\beta}\right] \tag{F.17}$$

REFERENCES

Ackerman, T. P. and G. M. Stokes, 2003: The Atmospheric Radiation Measurement program. *Physics Today*, **56**, 38–44.

Aires, F., and W. B. Rossow, 2003: Inferring instantaneous, multivariate and nonlinear sensitivities for the analysis of feedback processes in a dynamical system: Lorenz model case-study. *Quart. J. Roy. Meteor. Soc.*, **129**, 239–275.

Allan, R. P., 2011: Combining satellite data and models to estimate cloud radiative effect at the surface and in the atmosphere. *Meteor. Appl.*, **18**, 324–333.

Amato, T. E., A. K. Heidinger, and D. J. Vimont, 2007: Arguments against a physical long-term trend in global ISCCP cloud amounts. *Geophys. Res. Lett.*, **34**, L04701, doi:10.1029/2006/GL028083.

Anderberg, N. R., 1973: *Cluster Analysis for Applications*. Elsevier, 359 pp.

Austin, R. T. and G. L. Stephens, 2001: Retrieval of stratus cloud microphysical parameters using millimeter-wave radar and visible optical depth in preparation for CloudSat 1. Algorithm formulation. *J. Geophys. Res.*, **106**, 28,233–28,242.

Aydin, K., and T. M. Walsh, 1999: Millimeter wave scattering from spatial and planar bullet rosettes. *IEEE Trans. Geosci. Remote Sens.*, **37**, 1138–1150.

Bain, L. J. and M. Englehardt, 1992: *Introduction to Probability and Mathematical Statistics, 2nd Ed.* Duxbury Press, 644 pp.

Baker, B. A., and R. P. Lawson, 2006a: In situ observations of the microphysical properties of wave, cirrus, and anvil clouds. Part I: Wave clouds. *J. Atmos. Sci.*, **63**, 3160–3185.

Baker, B. A., and R. P. Lawson, 2006b: Improvement in determination of ice water content from two-dimensional particle imagery. Part I: Image-to-mass relationships. *J. Appl. Meteor. Climatol.*, **45**, 1282–1290.

Baker, B., Q. Mo, R. P. Lawson, D. O'Connor, and A. Korolev, 2009: Drop size distributions and the lack of small drops in RICO rain shafts. *J. Appl. Meteor. Climatol.*, **48**, 616–623.

Belanger, P., 1995: *Control Engineering: A Modern Approach.* Saunders College Publishing, 471 pp.

Bloom, S. J., and Coauthors, 2005: *Documentation and validation of the Goddard Earth Observing System Data Assimilation System—version 4.* TM-2005-104606. NASA, Washington, DC, 166 pp.

Bodas-Saldeco, A., and Coauthors, 2011: COSP: Satellite simulation software for model assessment. *Bull. Amer. Meteor. Soc.*, **92**, 1023–1043.

Bohren, C. F., and D. R. Huffman, 1983: *Absorption and Scattering of Light by Small Particles.* John Wiley and Sons, Inc., 530 pp.

Bony, S. and K. Emanuel, 2001: A parameterization of the cloudiness associated with cumulus convection; evaluation using TOGA COARE data. *J. Atmos. Sci.*, **58**, 3158–3183.

Bony, S., and J. L. Dufresne, 2005: Marine boundary layer clouds at the heart of tropical cloud feedback uncertainties in climate models. *Geophys. Res. Lett.*, **32**, L20806, doi:10.1029/2005GL023851.

Bony, S., and Coauthors, 2006: How well do we understand and evaluate climate change feedback processes? *J. Climate*, **19**, 3445–3482.

Broemeling, L., 1985: *Bayesian Analysis of Linear Models.* STATISTICS: Textbooks and Monographs, Vol. 60, Marcel Dekker, Inc., 472 pp.

Brown, P. R. A., and P. N. Francis, 1995: Improved measurements of the ice water content in cirrus using a total water probe. *J. Atmos. Oceanic. Technol.*, **12**, 410–414.

Comstock, J. M., and Coauthors, 2007: An intercomparison of microphysical retrieval algorithms for upper-tropospheric ice clouds. *Bull. Amer. Meteor. Soc.*, **88**, 191–204.

Comstock, J. M., M. Wang, K. Zhang, X. Liu, and K. Ginsberg, 2012: Influence of dynamics and thermodynamics on cirrus microphysical properties during SPartICus. *MACPEx/SPartICus Science Team Meeting*, Salt Lake City, UT, NASA Earth Science Project Office.

Cooper, W. A., 1978: *Cloud Physics Investigations by the University of Wyoming I nHIPLEX 1977.* Department of Atmospheric Science, University of Wyoming, Rep. AS119, 320 pp.

Cotton, W. R., 1990: *Storms.* Geophysical Science Series, Vol. 1, *ASTeR Press, Fort Collins, CO, 158 pp.

Curry, J., and Coauthors, 1996: Overview of arctic cloud and radiation characteristics. *J. Climate*, **9**, 1731–1764.

Davis, S. M., A. G. Hallar, L. M. Avallone, and W. Engblom, 2007: Measurements of ice water content with a tunable diode laser hygrometer: Calibration procedure and inlet analysis. *J. Atmos. Oceanic. Technol.*, **24**, 463, doi:10.1175/JTECH1975.1.

Delanoe, J., A. Protat, J. Testud, D. Bouniol, A. J. Heymsfield, A. Bansemer, P. R. A. Brown, and R. M. Forbes, 2005: Statistical properties of the normalized ice particle size distribution. *J. Geophys. Res.*, **110**, D10201, doi:10.1029/2004JD005405.

Del Genio, A. D., 2002: GCM simulation of cirrus for climate studies. *Cirrus*, D. K. Lynch et al., Eds., Oxford University Press, 310–326.

Demortier, L., 1995: Assessing the Significance of a Deviation in the Tail of a Distribution. Collider Detector at Fermilab note 3419.

Devroye, L., 1986: *Non-Uniform Random Variate Generation.* Springer-Verlag, 857 pp.

Diskin, G. S., J. R. Podolske, G. W. Sachse, and T. A. Slate, 2002: Open-path airborne tunable diode laser hygrometer. *Proc. SPIE*, Volume 4817, Seattle, WA, the International Society for Optical Engineering, 196–204.

Emanuel, K. A. and M. Zivkovic-Rothman, 1999: A scheme for representing cumulus convection in large-scale models. *J. Atmos. Sci.*, **56**, 1766–1782.

Evan, A. T., A. K. Heidinger, and D. J. Vimont, 2007: Arguments against a physical long-term trend in global ISCCP cloud amounts. *Geophys. Res. Lett.*, **34**, L04701, doi:10.1029/2006GL028083.

Evans, K. F., S. J. Walter, A. J. Heymsfield, and G. M. McFarquhar, 2002: Submillimeter-Wave Cloud Ice Radiometer: Simulations of retrieval algorithm performance. *J. Geophys. Res.*, **107**, doi:10.1029/2001JD000709.

Evans, K. F., J. R. Wang, P. E. Racette, and G. Heymsfield, 2005: Ice cloud retrievals and analysis with the Compact Scanning Submillimeter Imaging Radiometer and the Cloud Radar System during CRYSTAL FACE. *J. Appl. Meteor.*, **44**, 839–859.

Field, P. R., 2000: Bimodal ice spectra in frontal clouds. *Quart. J. Roy. Meteor. Soc.*, **126**, 379–392.

Field, P. R., and A. J. Heymsfield, 2003: Aggregation and scaling of ice crystal size distributions. *J. Atmos. Sci.*, **60**, 544–560.

Field, P. R., R. Wood, P. R. A. Brown, P. H. Kay, E. Hirst, R. Greenaway, and J. A. Smith, 2003: Ice particle interarrival times measured with a Fast FSSP. *J. Atmos. Oceanic. Technol.*, **20**, 249–261.

Field, P. R., R. J. Hogan, P. R. A. Brown, A. J. Illingworth, T. W. Choularton, and R. J. Cotton, 2005: Parameterization of ice-particle size distributions for midlatitude stratiform cloud. *Quart. J. Roy. Meteor. Soc.*, **131**, 1997–2017.

Field, P. R., A. J. Heymsfield, and A. Bansemer, 2006: Shattering and particle interarrival times measured by optical array probes in ice clouds. *J. Atmos. Oceanic Technol.*, **23**, 1357–1371.

Gayet, J.-F., F. Auriol, A. Minikin, J. Stroem, M. Seifert, R. Krejci, A. Petzold, G. Febvre, and U. Schumann, 2002: Quantitative measurement of the microphysical and optical properties of cirrus clouds with four different in situ probes: Evidence of small ice crystals. *Geophys. Res. Lett.*, **29**, doi:10.1029/2001GL014342.

Gayet, J.-F., J. Ovarlez, V. Shcherbakov, J. Stroem, U. Schumann, A. Minikin, F. Auriol, A. Petzold, and M. Monier, 2004: Cirrus cloud microphysical and optical properties at southern and northern midlatitudes during the INCA experiment. *J. Geophys. Res.*, **109**, D20206, doi:10.1029/2004JD004803.

Gayet, J.-F., V. Shcherbakov, H. Mannstein, A. Minikin, U. Schumann, J. Stroem, A. Petzgold, J. Ovarlez, and F. Immler, 2006: Microphysical and optical properties of midlatitude cirrus clouds observed in the southern hemisphere during INCA. *Quart. J. Roy. Meteor. Soc.*, **132**, 2719–2748.

Ghosh, S., and S. G. Henderson, 2002: Chessboard distributions and random vectors with specified marginals and covariance matrix. *Operations Research*, **50**, 820–834.

Gossard, E., 1994: Measurement of cloud droplet size spectra by doppler radar. *J. Atmos. Oceanic Technol.*, **11**, 712–726.

Gurland, J. and R. C. Dahiya, 1972: A test of fit for continuous distributions based on generalized minimum chi-square. *Statistical Papers in Honor of George W. Snedecor*, T. A. Bancroft, Ed., Iowa State University Press, 115–128.

Haario, H., E. Saksman, and J. Tamminen, 1999: Adaptive proposal distribution for random walk Metropolis algorithm. *Computational Statistics*, **14**, 375–395.

Hack, J., 1992: Climate system simulation: Basic numerical and computational concepts. *Climate System Modeling*, Kevin E. Trenberth, Ed., Cambridge University Press, 283–318.

Hammonds, K. D., 2013: *Impact of Ice Crystal Habit on the Parameterization of Cloud Microphysical Properties When Using 94GHz Polarimetric Scanning Cloud Radar During StormVEx*. M.S. thesis, Dept. of Atmospheric Sciences, the University of Utah, 91 pp.

Hartmann, D. L., 1994: *Global Physical Climatology*. International Geophysics Series, Vol. 56, Academic Press, 411 pp.

Hartmann, D. L., L. A. Moy, and Q. Fu, 2001: Tropical convection and the energy balance at the top of the atmosphere. *J. Climate.*, **14**, 4495–4511.

Haynes, J. M., Z. Luo, G. L. Stephens, R. T. Marchand, and A. Bodas-Salcedo, 2007: A Multipurpose Radar Simulator Package: Quickbeam. *Bull. Amer. Meteor. Soc.*, **88**, 1723–1727.

Heymsfield, A. J., 1977: Precipitation development in stratiform ice clouds: A microphysical and dynamical study. *J. Atmos. Sci.*, **34**, 367–381.

Heymsfield, A. J., and L. M. Miloshevich, 1993: Homogenous ice nucleation and supercooled liquid water in orographic wave clouds. *J. Atmos. Sci.*, **50**, 2335–2353.

Heymsfield, A. J., and L. M. Miloshevich, 1995: Relative humidity and temperature influences on cirrus formation and evolution: Observations from wave clouds and FIRE II. *J. Atmos. Sci.*, **52**, 4302–4326.

Heymsfield, A. J., and J. Iaquinta, 2000: Cirrus crystal terminal velocities. *J. Atmos. Sci.*, **57**, 916–942.

Heymsfield, A. J., A. Bansemer, P. R. Field, S. L. Durden, J. L. Stith, J. E. Dye, W. Hall, and C. A. Grainger, 2002: Observations and parameterizations of particle size distributions in deep tropical cirrus and stratiform precipitating clouds: Results from in situ observations in TRMM field campaigns. *J. Atmos. Sci.*, **59**, 3457–3491.

Heymsfield, A. J., 2003a: Properties of tropical and midlatitude ice cloud particle ensembles. Part I: Median mass diameters and terminal velocities. *J. Atmos. Sci.*, **60,** 2573–3591.

Heymsfield, A. J., 2003b: Properties of tropical and midlatitude ice cloud particle ensembles. Part II: Applications for mesoscale and climate models. *J. Atmos. Sci.*, **60**, 2592–2611.

Heymsfield, A. J., A. Bansemer, C. Schmitt. C. Twohy, and M. R. Poellot, 2004: Effective ice particle densities derived from aircraft data. *J. Atmos. Sci.*, **61**, 982–1003.

Heymsfield, A. J., C. Schmitt, A. Bansemer, G.-J. van Zadelhoff, C. Twohy, and D. Baumgardner, 2006: Effective radius of ice cloud particle populations derived from aircraft probes. *J. Atmos. Oceanic. Technol.*, **23**, 361–380.

Heymsfield, A. J., A. Bansemer, G. Heymsfield, and A. O. Fierro, 2009: Microphysics of maritime tropical convective updrafts at temperatures from -20° to -60°C. *J. Atmos. Sci.*, **66**, 3530–3562.

Heymsfield, A. J., C. Schmitt, and A. Bansemer, 2013: Ice cloud particle size distributions and pressure-dependent terminal velocities from in situ observations at temperatures from 0° to -86°C. *J. Atmos. Sci.*, **70**, 4123–4154.

Hobbs, P. V. and A. L. Rangno, 1985: Ice particle concentrations in clouds. *J. Atmos. Sci.*, **42**, 2523–2549.

Hogan, R. J., L. Tian, P. R. A. Brown, C. D. Westbrook, A. J. Heymsfield, and J. D. Eastment, 2012: Radar scattering from ice aggregates using the horizontally aligned oblate spheroid approximation. *J. Appl. Meteor. Climatol.*, **51**, 655–671.

Huber, P. J., 2002: The behavior of maximum likelihood estimates under nonstandard conditions. *Proc. of the Fifth Berkeley Symposium on Mathematical Statistics and Probability, Vol. 1: Theory of Statistics*, Berkeley, CA, the University of California, 221–233.

Jacobowitz, H., L. L. Stowe, G. Ohring, A. Heidinger, K. Knapp, and N. R. Nalli, 2003: The Advanced Very High Resolution Radiometer Pathfinder Atmosphere (PATMOS) climate dataset: A resource for climate research, *Bull. Am. Meteorol. Soc.*, **84**(6), 785–793.

Jakob, C., 2002: Cloud parameterization—progress, problems and prospects. *ECMWF Seminar on Key Issues in Parameterization*, ECMWF, November 2001, 327–338.

Jakob, C. and G. Tselioudis, 2003: Objective identification of cloud regimes in the Tropical Western Pacific. *Geophys. Res. Lett.*, **30**, 2082, doi:10.1029/2003GL018367.

Jensen, E. J., and Coauthors, 2009: On the importance of small ice crystals in tropical anvil cirrus. *Atmos. Chem. Phys.*, **9**, 5519–5537.

Johnson, N. L., S. Kotz, and N. Balakrishnan, 1994: *Continuous Univariate Distributions, Volume 1, 2nd Ed.* Wiley Series in Probability and Mathematical Statistics: Applied Probability and Statistics Section, John Wiley & Sons, Inc., 747 pp.

Johnson, R. W., D. V. Kliche, and P. L. Smith, 2013: Maximum likelihood estimation of gamma parameters for coarsely-binned and truncated raindrop size data. *Quart. J. Roy. Meteor. Soc.*, doi:10.1002/qj.2209.

Jones, D. A., 1983: Statistical analysis of empirical models fitted by optimization. *Biometrika*, **70**, 67–88.

Khain, A., M. Pinsky, T. Elperin, N. Kleeorin, I. Rogachevskii, and A. Kostinski, 2007: Critical comments to results of investigations of drop collisions in turbulent clouds. *Atmospheric Research*, **86**, 1–20.

Khairoutdinov, M. F. and Y. L, Kogan, 1999: A large eddy simulation model with explicit microphysics: Validation against aircraft observations of a stratocumulus-topped boundary layer. *J. Atmos. Sci.*, **56**, 2115–2131.

Kiehl, J. T., and V. Ramanathan, 1990: Comparison of cloud forcing derived from Earth Radiation Budget Experiment with that simulated by the NCAR Community Climate Model. *J. Geophys. Res.*, **95**, 1679–1698.

Kiehl, J. T., 1994: On the observed near cancellation between longwave and shortwave cloud forcing in tropical regions. *J. Climate.*, **7**, 559–565.

King, M. D., Y. J. Kaufman, W. P. Menzel, and D. Tanre, 1992: Remote sensing of cloud, aerosol, and water vapor properties from the Moderate Resolution Imaging Spectroradiometer (MODIS). *IEEE Trans. Geosci. Remote Sens.*, **30**, 2–27.

Knollenberg, R. G., 1981: Techniques for probing cloud microstructure. *Clouds, Their Formation, Optical Properties, and Effects*, P. V. Hobbs and A. Deepak, Eds., Academic Press, 15–91.

Korolev, A. V., and G. Isaac, 2003: Roundness and aspect ratio of particles in ice clouds. *J. Atmos. Sci.*, **60**, 1795–1808.

Korolev, A. V., E. F. Emery, J. W. Strapp, S. G. Cober, G. A. Isaac, M. Wasey, and D. Marcotte, 2011: Small ice particles in tropospheric clouds: Fact or artifact?. *Bull. Amer. Meteor. Soc.*, **92**, 967–973.

Kostinski, A. B., and R. A. Shaw, 2001: Scale-dependent droplet clustering in turbulent clouds. *J. Fluid. Mech.*, **434**, 389–398.

Kotz, S., N. Balakrishnan, and N. L. Johnson, 2000: *Continuous Multivariate Distributions, Volume 1: Models and Applications, 2nd Ed.* Wiley Series in Probability and Mathematical Statistics: Applied Probability and Statistics Section, John Wiley & Sons, Inc., 722 pp.

Kristjansson, J. E., J. M. Edwards, and D. L. Mitchell, 2000: Impact of a new scheme for optical properties of ice crystals on climates of two GCMs. *J. Geophys. Res.*, **105**, 10,063–10,079.

Larson, K., D. L. Hartmann, and S. A. Klein, 1999: The role of clouds, water vapor, circulation, and boundary layer structure in the sensitivity of the tropical climate. *J. Climate*, **12**, 2359–2374.

Lawson, R. P., B. Baker, B. Pilson, and Q. Mo, 2006a: In situ observations of the microphysical properties of wave, cirrus, and anvil clouds. Part II: Cirrus clouds. *J. Atmos. Sci.*, **63**, 3186–3203.

Lawson, R. P., D. O'Connor, P. Zmarzly, K. Weaver, B. Baker, Q. Mo, and H. Jonsson, 2006b: The 2D-S (Stereo) probe: Design and preliminary tests of a new airborne, high speed, high-resolution particle imaging probe. *J. Atmos. Oceanic Technol.*, **23**, 1462–1476.

Lawson, R. P., E. Jensen, D. L. Mitchell, B. Baker, Q. Mo, and B. Pilson, 2010: Microphysical and radiative properties of tropical clouds investigated in TC4 and NAMMA. *J. Geophys. Res.*, **115**, doi:10.1029/2009JD013017.

Lawson, R. P., 2011: Effects of ice particles shattering on the 2D-S probe. *Atmos. Meas. Tech.*, **4**, 1361–1381.

Lee, G., I. Zawadzki, W. Szyrmer, D. Semper-Torres, and R. Uijlenhoet, 2004: A general approach to double-moment normalization of drop size distributions. *J. Appl. Meteor.*, **43**, 264–281.

Li, J.-L., and Coauthors, 2005: Comparisons of EOS MLS cloud ice measurements with ECMWF analyses and GCM simulations: Initial results. *Geophys. Res. Lett.*, **32**, L18710, doi:10.1029/2005GL023788.

Li, J.-L., J. H. Jiang, D. E. Waliser, and A. M. Tompkins, 2007: Assessing consistency between EOS MLS and ECMWF analyzed and forecast estimates of cloud ice. *Geophys. Res. Lett.*, **34**, L08701, doi:10.1029/2006GL029022.

Li, J.-L. F., and Coauthors, 2012: An observationally based evaluation of cloud ice water in CMIP3 and CMIP5 GCMs and contemporary reanalyses using contemporary satellite data. *J. Geophys. Res.*, **117**, D16105, doi:10.1029/2012JD017640.

Liu, C.-L., and A. J. Illingworth, 1997: Error analysis of backscatter from discrete dipole approximation for different ice particle shapes. *Atmospheric Research*, **44**, 231–241.

Lo, K. K., and R. E. Passarelli, Jr., 1982: The growth of snow in winter storms: An airborne observational study. *J. Atmos. Sci.*, **39**, 697–706.

Locatelli, J. D., and P. V. Hobbs, 1974: Fall speed and masses of solid precipitation particles. *J. Geophys. Res.*, **79**, 2185–2197.

Loeb, N. G, S. Kato, K. Loukachine, N. Manalo-Smith, D. R. Doelling, 2007: Angular distribution models for top-of-atmosphere radiative flux estimation form the Clouds and the Earth's Radiant Energy System instrument on the Terra Satellite. Part II: Validation. *J. Atmos. Oceanic. Technol.*, **24**, 564–584.

Lorenz, E. N., 1984: Irregularity: A fundamental property of the atmosphere. *Tellus*, **36A**, 98–110.

Mace, G. G, A. J. Heymsfield, and M. R. Poellot, 2002: On retrieving the microphysical properties of cirrus clouds using the moments of the millimeter-wavelength Doppler Spectrum. *J. Geophys. Res.*, **107**, doi:10.1029/2001JD001308.

Mace, G. G., S. Benson, and E. Vernon, 2006a: Cirrus clouds and the large-scale atmospheric state: Relationships revealed by six years of ground-based data. *J. Climate*, **14**, 3257–3278.

Mace, G. G., and Coauthors, 2006b: Cloud radiative forcing at the Atmospheric Radiation Measurement program Climate Research Facility: 1. Technique, validation, and comparison to satellite-derived diagnostic quantities. *J. Geophys. Res.*, **111**, D11S90, doi:10.1029/2005JK005921.

Mace, G. G., R. Marchand, Q. Zhang, and G. Stephens, 2007: Global hydrometeor occurrence as observed by CloudSat: Initial observations from summer 2006. *Geophys. Res. Lett.*, **34**, doi:10.1029/2006GL029017.

Mace, G., Q. Zhang, M. Vaughan, R. Marchand, G. Stephens, C. Trepte, and D. Winker, 2009: A description of hydrometeor occurrence statistics derived from the first year of merged CloudSat and CALIPSO data. *J. Geophys. Res.*, **114**, doi:10.1029/2007JD009755.

Mace, G. G., and F. J. Wrenn, 2013: Evaluation of hydrometeor layers in the East and West Pacific within ISCCP cloud top pressure-optical depth bins using merged CloudSat and CALIPSO data. *J. Climate*, **26**, 9429–9444.

Manabe, S. and R. F. Strickler, 1964: Thermal equilibrium of the atmosphere with a convective adjustment. *J. Atmos. Sci.*, **21**, 361–385.

Marchand, R., G. G. Mace, T. Ackerman, and G. Stephens, 2008: Hydrometeor detection using Cloudsat—an earth-orbiting 94-GHz cloud radar. *J. Atmos. Oceanic Technol.*, **25**, 519–532.

Marshall, J. S., and W. M. K. Palmer, 1948: The distribution of raindrops with size. *J. Meteor.*, **5**, 165–166.

Matrosov, S. Y., 2007: Modeling backscattering properties of snowfall at millimeter wavelengths. *J. Atmos. Sci.*, **64**, 1727–1736.

Matrosov, S. Y., G. G. Mace, R. Marchand, M. D. Shupe, A. G. Hallar, and I. B. McCubbin, 2012: Observations of ice crystal habits with a scanning polarimetric W-band radar at slant linear depolarization ratio mode. *J. Atmos. Oceanic Technol.*, **29**, 989–1008.

McFarlane, S. A., K. F. Evans, and A. S. Ackerman, 2002: A Bayesian algorithm for the retrieval of liquid water cloud properties from microwave radiometer and millimeter radar data. *J. Geophys. Res.*, **107**, doi:10.1029/2001JD001011.

McFarquhar, G. M., J. Um, M. Freer, D. Baumgardner, G. L. Kok, and G. Mace, 2007: Importance of small ice crystals to cirrus properties: Observations from the Tropical Warm Pool International Cloud Experiment (TWP-ICE). *Geophys. Res. Lett.*, **34**, doi:10.1029/2007GL029865.

McKague, D. and F. Evans, 2002: Multichannel satellite retrieval of cloud parameter probability distribution functions. *J. Atmos. Sci.*, **8**, 1371–1382.

Meakin, P., 1992: Aggregation kinetics. *Physica Scripta*, **46**, 295–331.

Menzel, W. P., and Coauthors, 2010: Inferring global cloud cover properties and trends from 30 years of HIRS data. *The Seventeenth International TOVS Study Conference*, Monterey, CA, the International Association of Meteorology and Atmospheric Sciences and the Coordination Group for Meteorological Satellites.

Mitchell, D. L., 1996: Use of mass- and area-dimensional power laws for determining precipitation particle terminal velocities. *J. Atmos. Sci.*, **53**, 1710–1723.

Moon, T. K., 1996: The expectation-maximization algorithm. *IEEE Signal Processing Magazine*, **13**, 47–60.

Negri, R. G., L. A. T. Machado, S. English, and M. Forsythe, 2014: Combining a cloud-resolving model with satellite for cloud process model simulation validation. *J. Appl. Meteor. Climatol.*, **53**, 521–533.

Norris, J. R., and S. F. Iacobellis, 2005: North Pacific cloud feedbacks inferred from synoptic-scale dynamic and thermodynamic relationships. *J. Climate*, **18**, 4862–4878.

Oppenheim, A. V., A. S. Willsky, and S. H. Nawab, 1997: *Signals & Systems.* 2nd Ed. Prentice Hall Signal Processing Series, Prentice Hall, 957 pp.

Paltridge, G.W., 1980: Cloud-radiation feedback to climate. *Quart. J. Roy. Meteor. Soc.*, **106**, 367–380.

Pinsky, M. and A. Khain, 2003: Fine structure of cloud droplet concentration as seen from the Fast-FSSP measurements. Part II: Results of in situ observations. *J. Appl. Meteor. Climatol.*, **42**, 65–73.

Platt, C., 1997: A parameterization of the visible extinction coefficient in terms of the ice/water content. *J. Atmos. Sci.*, **54**, 2083–2098.

Polkinghorne. R., T. Vukicevic, and K. F. Evans, 2010: Validation of cloud-resolving model background data for cloud data assimilation. *Mon. Wea. Rev.*, **138**, 781–795.

Posselt, D. J., T. S. L'Ecuyer, and G. L. Stephens, 2008: Exploring the error characteristics of thin ice cloud property retrievals using a Markov chain Monte Carlo algorithm. *J. Geophys. Res.*, **113**, doi:10.1029/2008JD010832.

Posselt, D. and G. G. Mace, 2013: The influence of parameter uncertainty on snowfall retrievals using Markov Chain Monte Carlo solution methods. *J. Appl. Meteor. Climatol.*, Accepted.

Potter, G. L., and R. D. Cess, 2004: Testing the impact of clouds on the radiation budgets of 19 atmospheric general circulation models. *J. Geophys. Res.*, **109**, D02106, doi:10.1029/2003JD004018.

Prenni, A. J., and Coauthors, 2007: Examinations of ice formation processes in Florida cumuli using ice nuclei measurements of anvil ice crystal particle residues. *J. Geophys. Res.*, **112**, D10221, doi:10.1029/2006JD007549.

Press, S. J., 2003. *Subjective and Objective Bayesian Statistics: Principles, Models, and Applications*. Wiley, 552 pp.

Protat, A., J. Delanoe, D. Bouniol, A. J. Heymsfield, A. Bansemer, and P. Brown, 2007: Evaluation of ice water content retrievals from cloud radar reflectivity and temperature using a large airborne in situ microphysical database. *J. Appl. Meteor. Climatol.*, **46**, 557–572.

Randall, D., M. Khairoutdinov, A. Arakawa, and W. Grabowski, 2003: Breaking the cloud parameterization deadlock. *Bull. Amer. Meteor. Soc.*, **84**, 1547–1564.

Raymond, C., J. Bristow, and M. Schoeberl, 2002: Needs for an intelligent distributed spacecraft infrastructure. *IEEE International Geoscience and Remote Sensing Symposium*, **1**, 371–374, Toronto, Canada, the Institute of Electrical and Electronics Engineers.

Rodgers, C., 2000: *Inverse Methods for Atmospheric Sounding: Theory and Practice*. Series on Atmospheric, Oceanic and Planetary Physics, Vol. 2, World Scientific, 238 pp.

Rossow, W. B., and R. A. Schiffer, 1999: Advances in understanding clouds from ISCCP. *Bull. Amer. Meteor. Soc.*, **80**, 2261–2288.

Rossow, W. B., G. Tselioudis, A. Polak, and C. Jakob, 2005: Tropical climate described as a distribution of weather states indicated by distinct mesoscale cloud property mixtures. *Geophys. Res. Lett.*, **32**, L21812, doi:10.1029/2005GL024584.

Ryan, B. F., 2000: A bulk parameterization of the ice particle size distribution and the optical properties in ice clouds. *J. Atmos. Sci.*, **57**, 1436–1451.

Sassen, K., and G. C. Dodd, 1988: Homogenous nucleation rate for highly supercooled cirrus cloud droplets. *J. Atmos. Sci.*, **45**, 1357–1369.

Schmitt, C. G., and A. J. Heymsfield, 2005: Total surface area estimates for individual ice particles and particle populations. *J. Appl. Meteor.*, **44**, 467–474.

Schmitt, C. G., J. Iaquinta, and A. J. Heymsfield, 2006: The asymmetry parameter of cirrus clouds composed of hollow bullet rosette-shaped ice crystals from ray-tracing calculations. *J. Appl. Meteor. Climatol.*, **45**, 973–981.

Schwartz, M. C. and G. G. Mace, 2010: Co-occurrence statistics of tropical tropopause layer cirrus with lower cloud layers as derived from CloudSat and CALIPSO data. *J. Geophys. Res.*, **115**, D20215, doi:10.1029/2009JD012778.

Severini, T., 2000: *Likelihood Methods in Statistics*. Oxford University Press, 392 pp.

Sheil, J. and I. O'Muircheartaigh, 1977: Algorithm AS106: The distribution of non-negative quadratic forms in normal variables. *Journal of the Royal Statistical Society, Series C (Applied Statistics)*, **26**, 92–98.

Soden, B. and I. Held, 2006: An assessment of climate feedbacks in coupled ocean-atmosphere models. *J. Climate.*, **19**, 3354–3360.

Stackhouse, P. W. Jr., S. K Gupta, S. J. Cox, T. Zhang, J. C. Mikovitz, and L. M Hinkelman, 2011: 24.5-year SRB data set released. *GEWEX News*, **21**, 10–12.

Stephens, G. L. and Coauthors, 2002: The Cloudsat mission and the A-Train: A new dimension of space-based observations of clouds and precipitation. *Bull. Amer. Meteor. Soc.*, **83**, 1771–1790.

Stephens, G. L., 2005: Cloud feedbacks in the climate system: A critical review. *J. Climate*, **18**, 237–273.

Stokes, G. and S. Schwartz, 1994: The Atmospheric Radiation Measurement (ARM) program: Programmatic background and design of the Cloud and Radiation Test Bed. *Bull. Amer. Meteor. Soc.*, **75**, 1201–1221.

Stubenrauch, C. J., S. Cros, A. Guignard, and N. Lamquin, 2010: A 6-year global cloud climatology form the Atmospheric InfraRed Sounder AIRS and a statistical analysis in synergy with CALIPSO and CloudSat. *Atmos. Chem. Phys.*, **10**, 7197–7214.

Tamminen, J., and E. Kyrola, 2001: Bayesian solution for nonlinear and non-Gaussian inverse problems by Markov chain Monte Carlo method. *J. Geophys. Res.*, **106**, 14,377–14,390.

Testud, J., S. Oury, R. A. Black, P. Amayenc, and X. Dou, 2001: The concept of "normalized" distributions to describe raindrop spectra: A Tool for Cloud Physics and Cloud Remote Sensing. *J. Appl. Meteor.*, **40**, 1118–1140.

Tian, L., G. M. Heymsfield, A. J. Heymsfield, A. Bansemer, L. Li, C. H. Twohy, and R. C. Srivastava, 2010: A study of cirrus ice particle size distributions using TC4 observations. *J. Atmos. Sci.*, **67**, 195–216.

Tiedke, M., 1993: Representation of clouds in large-scale models. *Mon. Wea. Rev.*, **121**, 3040–3061.

Tinel, C., J. Testud, J. Pelon, R. J. Hogan, A. Protat, J. Delanoe, and D. Bouniol, 2005: The retrieval of ice-cloud properties from cloud radar and lidar synergy. *J. Appl. Meteor.*, **44**, 860–875.

Tselioudis, G., W. Rossow, Y. Zhang, and D. Konsta, 2013: Global weather states and their properties from passive and active satellite cloud retrievals. *J. Climate.*, **26**, 7734–7746.

van der Vaart, A. W., 1998: *Asymptotic Statistics. Cambridge Series in Statistical and Probablistic Mathematics,* No. 3, R. Gill, B. D. Ripley, S. Ross, M. Stein, and D. Williams, Eds., Cambridge University Press, 443 pp.

Waliser, D. E., and Coauthors, 2009: Cloud ice: A climate model challenge with signs and expectations of progress. *J. Geophys. Res.*, **114**, D00A21, doi:10.1029/2008JD010015.

Waliser, D. E., J.-L. F. Li, T. S. L'Ecuyer, and W.-T Chen, 2011: The impact of precipitating ice and snow on the radiation balance in global climate models. *Geophys. Res. Lett.*, **38**, L06802, doi:10.1029/2010GL046478.

Wayne, R. P., 1991: *Chemistry of Atmospheres, 2^{nd} Ed.* Oxford University Press, 447 pp.

Weinstock, E. M., E. J. Hintsa, A. E. Dessler, J. F. Oliver, N. L. Hazen, J. N. Demusz, N. T. Allen, L. B. Larson, and J. G. Anderson, 1994: A new fast response photofragment fluorescence hygrometer for use on the ER-2 and Perseus remotely piloted aircraft. *Rev. Sci. Instrum.*, **65**, 3544-3554, doi:10.1063/1.1144536.

Weinstock, E. M., and Coauthors, 2009: Validation of the Harvard Lyman-α in situ water vapor instrument: Implications for the mechanisms that control stratospheric water vapor. *J. Geophys. Res.*, **114**, doi:10.1029/2009JD012427.

Westbrook, C. D., R. C. Ball, P. R. Field, and A. J. Heymsfield, 2004a: Universality in snowflake aggregation. *Geophys. Res. Lett.*, **31**, L15104, doi:10.1029/2004GL020363.

Westbrook, C. D., R. C. Ball, P. R. Field, and A. J. Heymsfield, 2004b: Theory of growth by differential sedimentation, with application to snowflake formation. *Physical Review E*, **70**, 021403, doi:10.1103/PhysRevE.70.021403.

Westbrook, C. D., R. J. Hogan, A. J. Illingworth, and E. J. O'Connor, 2007: Theory and observations of ice particle evolution in cirrus using Doppler radar: Evidence for Aggregation. *Geophys. Res. Lett.*, **34**, L02824, doi:10.1029/2006GL027863.

Wetherald, R. T. and S. Manabe, 1988: Cloud feedback processes in a general circulation model. *J. Atmos. Sci.*, **45**, 1397–1415.

Wielicki, B. A., B. R. Barkstrom, E. F. Harrison, R. B. Lee III, G. L. Smith, and J. E. Cooper, 1996: Clouds and the Earth's Radiant Energy System (CERES): An Earth Observing System experiment. *Bull. Amer. Meteor. Soc.*, 77, 853–868.

Wilks, D. S., 2006: *Statistical Methods in the Atmospheric Sciences, 2nd Ed.* Academic Press, 627 pp.

Wilson, D. R., A. C. Bushell, A. M. Kerr-Munslow, J. D. Price, and C. J. Morecrette, 2008: PC2: A prognostic cloud fraction and condensation scheme. I: Scheme description. *Quart. J. Roy. Meteor. Soc.*, **134**, 2093–2107.

Wiscombe, W. J., 2005: Scales, Tools, and Reminiscences. *3D Radiative Transfer in Cloudy Atmospheres, Physics of Earth and Space Environments*, A. Marshak and A. B. Davis, Eds., Springer, 3–92.

Wylie, D., D. L. Jackson, W. P. Menzel, and J. J. Bates, 2005: Trends in global cloud cover in two decades of HIRS observations. *J. Climate*, **18**, 3021–3031.

Xu, K.-M. and D. Randall, 1996: Evaluation of statistically based cloudiness parameterizations used in climate models. *J. Atmos. Sci.*, **53**, 3103–3119.

Zelinka, M. D., and D. L. Hartmann, 2010: Why is longwave cloud feedback positive? *J. Geophys. Res.*, **115**, D16117, doi:10.1029/2010JD013817.

Zhang, Y. and G. G. Mace, 2006: Retrieval of cirrus microphysical properties with a suite of algorithms for airborne and spaceborne lidar, radar, and radiometer data. *J. Appl. Meteor. Climatol.*, **45**, 1665–1689.

Zhao, Y., G. G. Mace, and J. M. Comstock, 2011: The occurrence of particle size distribution bimodality in midlatitude cirrus as inferred from ground-based remote sensing data. *J. Atmos. Sci.*, **68**, 1162–1176.

Zhdanov, M. S., 2002: *Geophysical Inverse Theory and Regularization Problems.* Methods in Geochemistry and Geophysics, Vol. 36, Elsevier, 609 pp.